Ollscoil na hÉireann, Corcaigh

National University of Ireland, Cork

Synthesis of Nanomaterials for Applications in Heterogeneous Catalysis

Thesis presented by

Éadaoin Casey, MSc, BSc

ORCID: 0000-0002-1482-3599

for the degree of

Doctor of Philosophy

University College Cork

School Of Chemistry

Head of School: Prof. Anita Maguire

Supervisors: Dr. Gillian Collins, Prof. Justin D. Holmes

2022

Declaration

I, Éadaoin Casey, declare that the work I am submitting is my own and has not been submitted for another degree, either at University College Cork or elsewhere. All external references and sources are clearly acknowledged and identified within the contents. I have read and understood the regulations of University College Cork concerning plagiarism and intellectual property.

Éadaoin Casey

Éadaoin Casey

Abstract

The purpose of this thesis was to synthesise nanomaterials with a variety of chemical and physical properties to find the optimum design of heterogeneous catalysts for a variety of applications in heterogeneous catalysis. The aim for chapter 3 was to synthesise support free Pd NPs which are stabilised by a range of small organic ligands and polymers for the application in the pharmaceutical synthesis. It was vital to identify the correct capping ligand to stabilise the NP to find the optimal catalyst for the reductive amination reaction. A range of material characterisation methods were used to evaluate the impact of ligands and the role of steric and electronic effects on the selectivity behaviour of the Pd NPs when they were stabilised by different capping ligands which helped identify the best catalytic system. PVP stabilised Pd NPs was found to be the best performing catalyst displaying the best overall yield of the desired product. XPS and FTIR revealed that the presence of PVP ligands at the NP surface gives rise to combination of steric and electronic effects and it was shown that electron donation from the PVP carbonyl group to the Pd NP occurred.

Chapter 4 focused on plasmonic photocatalysis which allows harvesting of visible light as an abundant and renewable energy source to drive a myriad of chemical reactions. The novelty of this work is that it combines a two- dimensional (2D) metal catalyst and plasmonic photocatalysis which has not been reported in literature. The high proportion of exposed surface atoms and large surface area of ultrathin 2D nanosheets results in high atom efficiency. Light-harvesting catalysts allow lower reaction temperatures and enhanced reaction rates, enabling more energy efficient and greener routes to chemical synthesis. The chapter developed a new synthesis method for 2D alloyed PdAu nanosheets using long chain surfactants to template the growth. Tuning the surface chemistry was critical to controlling the two-dimensional growth and maintaining high catalytic activity. The catalysts display outstanding activity for visible-light driven room-temperature Suzuki cross coupling reactions, greatly outperforming commercial Pd catalysts.

The need for the development of efficient catalysts for the chemical recycling of PET to tackle the global issue of plastic waste was the motivation of Chapter 5. Designing the optimum heterogenous catalyst

was the main aim of this work with particular focus on immobilisation of metal ion and nanoparticle based catalysts. Surface modification of a catalyst support with organic linkers is a suitable strategy to immobilise transition metal ions onto a SiO_2 support material. The nature of the organic ligand being connected to the ion influences the steric and electronic effects which influences the catalytic behaviour. The NP catalysts were found to be superior than the ion immobilsed catalysts in the degradation of PET to its monomer BHET, due to synergistic effects between the NP and the organic ligand. The aim for chapter 6 was to find the optimum metal free heterogeneous catalyst anchored on SiO_2 support. This work was inspired by the findings in chapter 5. Three guanidine catalyst with a range of nitrogen environments were synthesised as potential metal free catalysts for the degradation of PET and PLA. The catalysts were evaluated under conventional, and microwave assisted heating methods to find the best method for converting these plastics to their monomers with high yields. The catalysts were evaluated using material characterisation methods such as XPS, TEM and FTIR. It was discovered that the best performing catalyst had the most nitrogen environments eluding that the nitrogen availability was an important feature for the catalyst activity for both PET and PLA degradation. Microwave assisted heating methods outperformed the conventional heating methods yielding high conversions with less energy and time being required.

Acknowledgements

I would firstly like to thank my supervisors Dr. Gillian Collins and Prof. Justin Holmes for giving me the opportunity to undertake this PhD. All the knowledge, support and guidance over the last few years has been hugely impactfully. I have thoroughly enjoyed working alongside you both, the confidence you both have given me professional and personally is astounding and I will be forever grateful.

I would like to give a huge thanks to the members past and present from the Materials and analysis Group (MCAG). The endless chats, advice and all those coffee breaks really made my time during the PhD so much fun.

I would like to thank all the administration and technical staff in UCC for everything they do. As PhD students we would be lost without you all. I would like to especially thank Dr. Ian O'Connor, Dr. Trevor Carey and Dr. Anna Hogan for all their support and guidance.

Lastly, I would like to thank all my family especially my Mam, Dad and brother Conor. You are all my biggest supports and for that I owe you all a debt of gratitude.

Abbreviations

AC	Activated carbon
AEAPTMS	3-(2 aminoethyl-aminopropyl)trimethoxysilane
APTES	3-Aminopropyltriethoxysilane
APTMS	3-Aminopropyltrimethoxysilane
ATR	Attenuated total reflectance
BE	Binding Energy
BET	Brunauer-Emmett-Teller
BHET	Bis(hydroxyethyl)terephthalate
CONS	CO-assisted nanosheets
CTAB	Hexadecyltrimethylammonium bromide
D-$CDCl_3$	Deuterated Chloroform
D_6-DMSO	Deuterated Dimethyl sulfoxide
DDA	Dodecylamine
DDT	Dodecanethiol
DFT	Density Functional Theory
DLS	Dynamic Light Scattering
DMT	Dimethyl terephthalate
EDX	Energy Dispersive X-Ray Analysis
EG	Ethylene Glycol
FTIR	Fourier-transform Infrared Spectroscopy
ICP-MS	Inductively Coupled Plasma Mass Spectroscopy
MASNMR	Magic Angle Spinning Nuclear Magnetic Resonance
MCF	Mesoporous Cellular Foam (silica)
MCM	Mobil composition of matter (silica)

MHA	Mercaptohexanoic acid
MOF	metal organic frameworks
MW	Microwave
Mw	Molecular weight
NMP	N-Methyl-2-Pyrrolidone
NMR	Nuclear Magnetic Resonance
NP	Nanoparticle
NSs	Nanosheets
PAA	polyacrylic acid
PAH	Polyallylamine hydrochloride
PAN	Polyacrylonitrile
PC	Polycarbonate
PE	Polyethylene
PET	Polyethylene terephthalate
PLA	Polylactic acid
PMMA	Poly(methacrylic acid)
PP	Polypropylene
PTC	Phase transfer catalyst
PVA	Polyvinyl alcohol
PVP	Polyvinylpyrrolidone
SANS	Surfactant assisted nanosheets
SBA	Santa Barbara amorphous (silica)
SEM	Scanning Electron Microscopy
ssNMR	Solid State Nuclear Magnetic Resonance
TEM	Transmission Electron Microscopy

TGA	Thermogravimetric Analysis
TMS	Tetramethylsilane
TOF	Turn over frequency
TON	Turn over number
TOABr	Tetraoctylammonium bromide
TPA	Terephthalic acid
XPS	X-Ray Photoelectron Spectroscopy
XRD	X-Ray Diffraction

Table of Contents

Chapter 1

Introduction

Introduction

Catalysis plays a very important role in the chemical industries that impact our everyday lives. Homogeneous catalysts offer a range of advantages, including, mild reaction conditions, high activity/selectivity, and tuneable reaction sites. Heterogeneous catalysis offers advantages such as higher thermal stability, easy separation of the catalyst from reaction mixture, and potential for recyclability. Commercial heterogeneous catalyst such as Pt or Pd on activated carbon, are widely used catalyst in industrial settings, but the major drawback of these catalysts is the lack of uniformity in nanoparticle size, shape and dispersion. Nanostructured materials show great promise and opportunities for the development of new catalyst materials with controlled and optimized properties that can be used diverse catalytic applications for chemical synthesis to electrocatalysis. Nanostructures can be classed into zero dimensional (0D), one dimensional (1D), two dimensional (2D) and three dimensional (3D) nanostructures as illustrated in Figure 1. Zero dimensional nanostructures, such as metal nanoparticles (NPs) have been studied in many organic transformations including Suzuki cross coupling[1-3], heck[4-5], and hydrogenation reactions[6-8], electrocatalytic applications[9] and photocatalysis.[10] The use of metal nanoparticles in green chemistry has also become very popular in recent years. Using natural resources to drive chemical reactions such as light, is advantageous as it is an eco-friendlier and cost effective method when compared to traditional methods of enhancing performance such as higher reaction temperatures which is not energy efficient. While zero dimensional (0D) nanostructures, have been the most common type of nanostructure employed for catalytic applications, there are many innovative examples of using the wide of nanomaterials as illustrated in Figure 1. One dimensional (1D) ultrafine Pt nanowires are rich high-index facets and coupled with their high conductivity have excellent electrocatalytic properties.[11] Two dimensional (2D) nanostructures such as nanosheets have been used extensively as both catalyst supports and as the active catalyst.[12] Three-dimensional (3D) nanostructure encompasses a wide variety of well known catalyst nanomaterials such as metal-organic frameworks (MOFs). The use of 3D nanostructures has been particularly well explored in the synthesis of electrodes for

electrochemical energy conversion and storage devices.[13] There are myriad of chemical and physical properties that can be tuned when designing a heterogeneous catalyst. The below section outlines some of the main features that can be tailored to influence catalytic properties including size, shape, chemical composition, and the catalytic support.

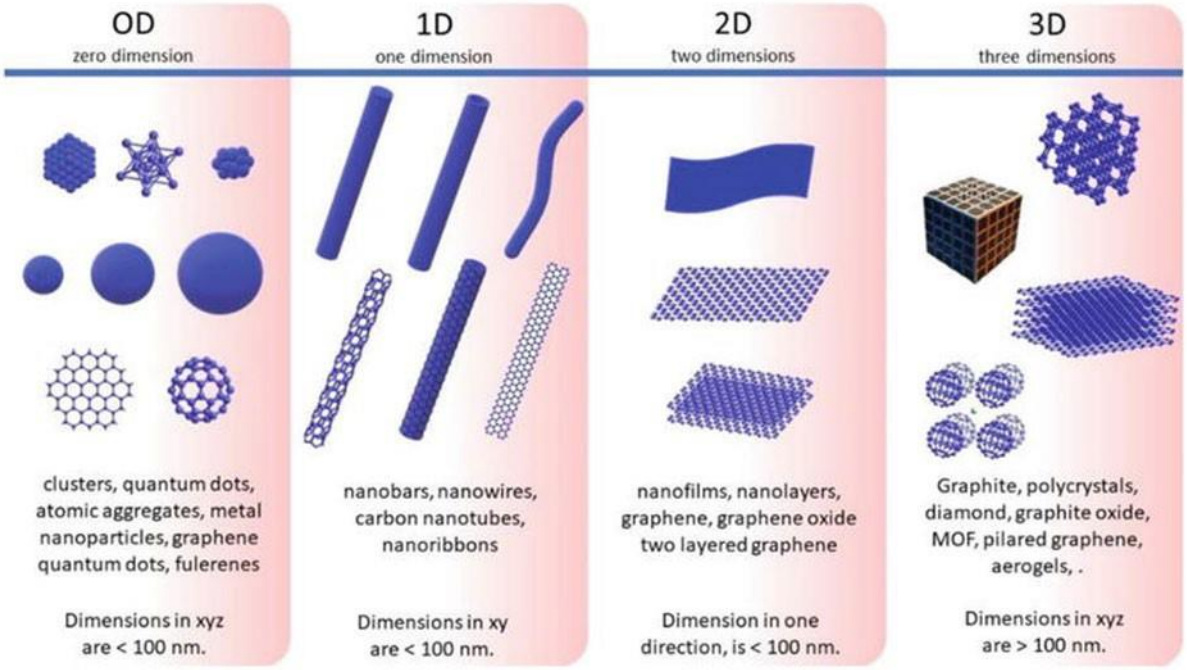

Figure 1: Schematic of the classification of nanostructures, zero- dimensional (0D), one-dimensional (1D), two-dimensional (2D) and three-dimensional (3D).[14]

1 Designing nanomaterials for heterogeneous catalysis

1.1 Tuning Nanoparticle Size

Solution based colloidal synthesis is most common method used to prepare colloidal NPs as it allows for easy tuning of the synthesis parameters to alter the size and shape of NPs. A typical solution-based method involves the reduction or decomposition of a metal precursor in the presence of stabilising ligands. Stabilising ligands play an important role in directing particle growth and restricting particle size by interacting with the metal surfaces during the reaction. The types of stabilising ligands used range from organic molecules to polymers, to ionic salts.

The LaMer model is widely used to explain the formation mechanism of colloidal NPs which describe three stages for the formation of NPs (i) super-saturation of the monomers, (ii) burst nucleation, and

(iii) controlled growth. The LaMer model is shown in Figure 2, where in the first stage, the concentration of monomers increases steadily as a reaction proceeds until it reaches the critical point of supersaturation. These monomers are formed from the metal precursor which is typically a metal salt and are stabilised by the capping ligands. The next stage, nucleation, begins once the concentration of monomers reaches supersaturation, after which small clusters are spontaneously generated. Nucleation causes a decrease in monomer concentration. When the concentration of monomers drops below the critical saturation, the nucleation of new particles stops and the monomers are now used for particle growth, marking the final stage. During the nucleation phase, growth may also occur simultaneously, resulting in size broadening of the NP diameter. Therefore, to achieve narrow NP size distributions, a short nucleation phase and slow growth kinetics are desirable. The nucleation and growth kinetics are controlled by regulating experimental parameters such as precursor concentrations, surfactant ratio, strength of reducing agent and reaction temperature.

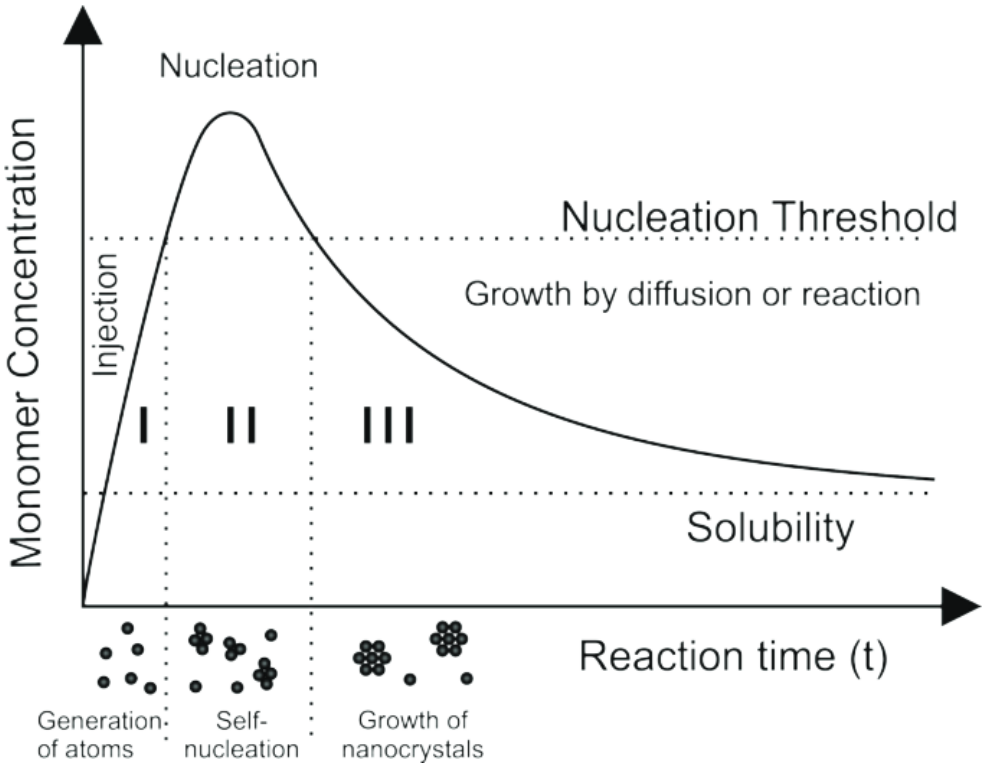

Figure 2: The LaMer model showing the three stages of the NP growth.[15]

One of the earliest reports of modern colloidal synthesis was in 1951 when Turkevich and co-workers[16], developed a method to prepare Au NPs by treating an aqueous $HAuCl_4$ solution with citric

acid. Citric acid acted as both the stabilising agent and reducing agent in an aqueous solution. From this discovery, Frens and co-workers[17] were able to modify the method and found that the size of Au NPs obtained by citrate reduction can be tuned by altering the sodium citrate concentration and the Au precursor to citrate ratio, indicating that the Au NPs were formed and grown through a rapid nucleation process followed by diffusion growth.[18] In 1994, the seminal paper by Brust *et al.*[19], reported organically soluble alkanethiol-stabilised Au NPs via reduction using a phase transfer reagent tetraoctylammmonium bromide (TOABr) and reducing agent sodium borohydride. This synthesis method produced small diameter NPs with the ability to tune the mean NP diameter from 1.5 to 5 nm by simply altering reaction conditions, such as reaction temperature, and ratio of Au precursor to alkanethiol.[20] Similar synthesis methods emerged for other key catalyst methods such as Pt and Pd. In particular, the polyol method which involves suspending the metal precursor in a glycol solvent and subsequently heating the solution to a refluxing temperature is very successful in preparing monodisperse metal NPs such as Ru[21], Pt[22] and Ag.[23] A polyol process is a convenient method for metal NPs as a reducing agent is not required because the polyalcohols e.g. ethylene glycol act as the solvent and reducing agent. Teranishi et al.[24] reported an elegant demonstration of this method to synthesize Pt NPs with tuneable diameters of 1.5–5.0 nm. The method used chloroplatinic acid as a Pt precursor in the presence of PVP and an alcohol solvent, that also acted as the reducing agent. The NP size was controlled by regulating the nucleation rate through the choice solvent. The particle size decreased with an increasing reducing power of the alcohol solvent (methanol > ethanol > IPA), as more nuclei were generated by faster reduction rate. The NP size could also be tuned by the PVP:Pt precursor ratio. Decreasing the PVP concentration increased the NP diameter due to faster NP growth enabled by the lower concentration stabiliser.

Teranishi *et al.*[25] later reported a similar synthesis for size controlled Pd NPs NPs with diameters of 2-3 nm by altering the amount of protective polymer (PVP) and then by changing the alcohol solvent. They reported that increasing the amount of PVP decreased the Pd NPs diameter and that the type of solvent also determined the diameter of the NPs. The NPs diameter was smallest using methanol as a

solvent, and increased in the order of methanol > ethanol > IPA. This trend correlates with the lower reducing power of the alcohol solvent, suggesting that a rapid reduction rate of $[PdCl_4]^{2-}$ ions was a vital factor to produce smaller diameter NPs. The conditions which produced the ~2 nm NPs was PVP:Pd ration of 10:1 and a 40 vol% ethanol in water solvent. They were also able to obtain larger NPs using seeded growth mechanism.

1.2 Shape Control

In catalysis, it is well-established that the activity of a metal NP can be enhanced by reducing its size, as this increases the surface area to volume ratio and also maximises the atom efficiency of the catalyst metal, which can be important for expensive noble metals typically used in catalysis. The selectivity, however, is usually most sensitive to the packing of atoms on the surface, which is determined by the exposed facets of a NP. The facets exposed on a nanostructure have a strong correlation with its shape. In the early 2000's a new phenomenon of shape-controlled synthesis of nanostructures emerged which enabled unprecedented control of nanocrystal morphology. There are a vast range of shapes that have been produced to date these including spheres[26-27], cubes[28-29], tetrahedrons[30], octahedrons[31], icosahedral[32-33], sheets[34-35], rods[36-37], wires[38-39], plates[40], and tetrapods[41]. To obtain such structures synthesis conditions are altered to control nucleation and growth, including the ratio of precursors, the use of surfactants and other capping ligands, temperature, and time.

The NP seed formed at the last stage of nucleation, which is a cluster with well-defined structures, is critical in determining the overall final shape of the NP. In addition to the NP seeds, the presence of shape-directing ligands such as surfactants or ions, also determine the final shape of metal NPs. Shape control of metal nanostructures can be achieved by either homogeneous or heterogeneous nucleation. In homogeneous nucleation, seed particles are formed *in situ* and, typically, nucleation and growth proceed by the same chemical process. To obtain a high uniformity in shape-controlled

nanocrystals, nucleation must occur rapidly and instantaneously, as if nucleation proceeds over an extended time period, reactants would be unevenly depleted from solution leading to variations in the growth rate for seed particles formed at different reaction times. Fast nucleation can be achieved by slowly building up the concentration of metal ions in solution through serial injections of the precursor solution until nucleation occurs. The use of stabilising agents and coordinating ligands between metal precursor and surfactant also plays an important role. Another condition required for homogeneous nucleation is that it must produce seed particles that are single crystalline or possess single-crystalline surfaces. This requirement can be difficult to achieve with the common noble metal such as Pt, Pd, Au and Ag which tend to possess a high degree of twinning and produce seeds particles with numerous crystal defects. One successful strategy to prevent this is oxidative etching which refers to the presence of species e.g. dissolve oxygen or Cl^- ions, that effectively etch particles with high-energy defect planes to produce single-crystalline seed particles. A successful application of this approach is the synthesis of Ag nanocrystalline octahedra polyhedral nanocrystals.[42]

While homogenous nucleation is a simple one step process, its success does require several conditions to be met, as outlined above. In contrast, in heterogeneous nucleation, the nucleation and growth stages occur as separation synthesis steps and it can often be easier to obtain controlled growth. Shape control synthesis under these conditions can be considered as an overgrowth process where seed particles, prepared in a previous step are added to a growth medium to facilitate the reduction of metal ions. If the seed particles possess well-defined shapes, NP growth by heterogeneous nucleation can produce nanostructures with monodisperse sizes and exceptional shape control (>95 % uniformity). This synthesis approach has been well developed for many key catalytic metals such as Pt, Pd, Ru, Rd.[43-45]

The use shape-controlled NPs has also allowed for a meaningful study of their shape-property relationships in catalysis. There have been some reports on how shape of NPs can influence the selectively of reactions and the corresponding turnover frequencies.[46-47] For example, Bratlie *et al.*[48]

studied the facet dependent reactivity of Pt NPs on the selectivity of benzene hydrogenation using Pt cubes and cuboctahedra NPs. Both cyclohexane and cyclohexene were formed using cuboctahedra catalysts, whereas only cyclohexane was produced using the cubic shaped NPs. The specific selectivity effect was attributed to the presence of a single facet type on the Pt cubes *i.e.* the (100) facet, whereas cuboctahedra possess both (100) and (111) facets leading to poor selectivity in benzene hydrogenation.

Since the discovery of graphene in 2004 by Geim *et. al*,[49] the use of 2D materials has attracted a lot of attention in catalysis, for in their use a catalyst support[12]. More recently the use of 2D metallic nanostructures have seen much interest in catalysis and electrocatalysis as the active catalytic component. 2D materials like graphene are made from layered materials and can be synthesised by mechanical or chemical exfoliation of the bulk material.[50] However, metals are not layered materials therefore this method is not applicable. 2D metal nanosheets can be formed using surfactants and stabilisers to direct the growth.[51-52] Using this synthesis method, ultrathin metal nanosheets have been used in a range of applications such as supercapacitors[53], batteries[54] and as efficient catalysts for organic reactions.[55-57] Xu *et al*.[58] reported the bottom-up synthesis of Pd nanosheets via a surfactant template-assisted solution- phase growth whereby the nanosheet surface facets could be controlled by changing the capping ligand. By using capping ligands with different terminal functional head group, nanosheets with (111), (100) or (110) facets could be obtained. Yang *et al*.[59] synthesised ultrathin Pd nanosheets via a surfactant assisted method using hexadecyltrimethylammonium bromide (CTAB) and $Mo(CO)_6$ as catalysts for electrooxidation of ethanol. They reported that the presence of both CTAB and $Mo(CO)_6$ was vital for the formation of the Pd nanosheets structure. The $Mo(CO)_6$ acted as a CO source where the strong binding to the Pd (111) surface promotes 2D growth into nanosheets. The nanosheets displayed 60% higher catalytic performance in ethanol oxidation compared to commercial Pd/C. Along with this result, the nanosheets showed better catalytic stability proving that these Pd nanosheets are efficient catalysts for this reaction. Kong *et al.*[60] synthesised ultrathin Ru metal nanosheets which

displayed high activity toward water splitting. The nanosheets were synthesised using a solvothermal method, which they nucleated and grew into nanosheets with the aid of IPA and urea. IPA influenced the anisotropic growth into sheet-like structures, and urea stabilised them by preventing aggregation and enabled their growth into larger sheets. 2D Ru based catalysts displayed significantly better activity for water splitting compared with the commercial Pt/C and Ru/C powder. Atomically thick Au nanosheets were excellent catalyst for next-generation transparent and conducting electrodes.[61] Single-atom-thick Rh nanosheets were highly active catalyst for hydrogenation and hydroformylation reactions. The activity of the Rh nanosheets was superior to that of commercial Rh/C and PVP capped Rh NPs (four and seven times more active respectively), in both the hydrogenation of phenol and the hydroformylation of 1-octene. [62]

1.3 Alloy and Bimetallic Nanoparticles in Catalysis

In addition to controlling NP size and morphology, tuning the chemical composition through mixing with other metals is another key method for manipulating the catalytic behaviours of catalysts. Alloying is used extensively to alter the chemical properties of metal surfaces, and alloys often have catalytic properties that are substantially different from those of the individual constituents. Alloying effects in heterogeneous catalysis can be divided into ligand effects and ensemble effects. Ligand effects refer to changes in the chemical properties of the atoms as a result of alloying *e.g.* charge transfer effects and electronic effects. Ensemble effects are associated with particular arrangements of the active constituents and how they alter reactivity when the chemical composition of the ensemble changes.[63] Bimetallic nanomaterials can be split into four general categories[64], as shown in Figure 3 (a-d). Mixed alloyed nanostructures (Figure 3 (a)) is where the arrangement of the constituent metals can be random or ordered. Randomly mixed alloys are generally called alloyed NPs and ordered NP are usually referred to as intermetallics. Core shell alloyed NPs are composed of an inner core made from one metal and the outer shell comprised of another metal (Figure 3 (b)). Figure 3 (c) shows sub-cluster segregated alloyed NPs, which are made up of two small clusters of each metal, with either a shared inner interface or shared outer interface.

The advance of shape controlled nanocrystal synthesis has led to the development of multiple core-shell alloyed NPs, which can form complex arrangements, with two or more shells as illustrated in Figure 3 (d).[64]

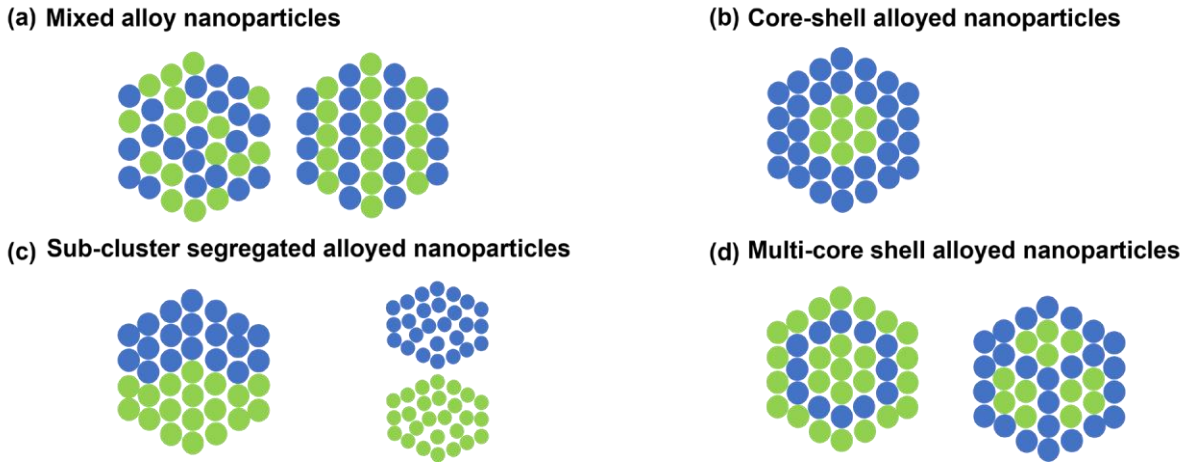

Figure 3: Different classification types of alloyed nanoparticles.

Co-reduction is the simplest method to synthesise bimetallic (or trimetallic) alloyed NPs where simultaneous reduction of two metal precursors occurs in the presence of a stabilising agent(s). This method is particularly useful when the two metals have similar reduction potentials, that allows reduction to occur simultaneously, thereby creating an alloy NP. [65] This facile co-reduction method is robust approach and has been applied to many bimetallic alloys including Pt-Ru[66] Pd-Cu[67-68], Pt-Pd[69], Pd-Au[70], and PtFe.[71] Seed mediated synthesis involving a two-step synthesis method where the preparation of seed NP are mixed with a second (or third) metal species can also been used for the synthesis of size and shape controlled alloy NPs. There have been a number of reports in the literature on the production of seed mediated synthesis of bimetallic nanoparticles.[72-74]

Another common synthesis method for alloy NPs is galvanic replacement method which is particularly is popular for the synthesis of hollow NP displaying ultrathin walls in aqueous media and with relatively short reaction times (< 60 min). The galvanic replacement reaction consists of a redox process between a metal, used as a sacrificial template, and metal ions in the solution. The difference in the reduction potential between the sacrificial template and the metal ions in solution provide the driving force for the reaction. Oxidation and dissolution of the template together with reduction of metal

ions from solution and deposition at the surface of the template occur simultaneously. The classic example of galvanic replacement is the reaction between Ag NPs and $AuCl_4^-$ ions. When a Ag NP is in contact with a $AuCl_{4\,(aq)}^-$ solution, the Ag atoms from the surface are oxidised to $Ag^+_{(aq)}$ ions and dissolved by $AuCl_{4\,(aq)}^-$ ions. This leads to the formation of small cavities at the NP surface. Simultaneously, Au atoms are deposited on the NP surface bu reduction of $AuCl_{4\,(aq)}^-$. As Au and Ag are miscible at the nanoscale, with the same face-centred cubic (fcc) crystal structure and similar lattices constants, uniform AgAu alloy NPs form.[75] The composition of this alloy can be tuned by changing the amount of $AuCl_{4\,(aq)}^-$ ions employed in the reaction relative to the amount of Ag metal.[76] This galvanic replacement synthesis method has also been applied to the synthesis Cu-Pd[77], Pd-Pt[78] and Ag-Pt[79] NPs.

The synergistic effects between the two metals in a bimetallic NP can result in increased activity, selectivity, and stability when compared to their monometallic counterparts.[80-81] Wu *et al.*[82] compared the catalytic activity of monometallic Pd catalysts against their PdIn catalysts in a ethane dehydrogenation reaction performed at 600 °C. They found that the alloyed PdIn NPs had excellent catalytic behaviour which was far superior to that of monometallic Pd catalyst. It was found the Pd–In bond formation modified the electronic properties of Pd atoms, leading to an increase in the turnover rate by almost 10 times compared with monometallic Pd. The turnover frequency was 0.03 and 0.26 s^{-1} for Pd and Pd-In, respectively. Another advantage of alloy NP has been the ability of combine expensive precious metals (Pt, Pd, Rh) with cheaper transition metals to reduce the cost of the catalyst while also maintaining or improving the catalytic ability, such as Pd, were it has been alloyed with many first row transition metals (Co, Cu, Fe and Ni).[83-85] For example, Pd was alloyed with Ni and displayed good activity in an oxygen reduction reaction while also reducing the cost of the catalyst.[86] PtNi alloyed NPs are ten times more catalytic active in an oxygen reduction reaction compared to monometallic Pt NPs.[87] Troutman *et al.*[88] synthesised PdAg NPs which lower the overall catalyst cost while simultaneously increasing the catalytic activity 3.4 times for the NO_2^- hydrogenative reduction reaction. They reported that by alloying the Pd and Ag, a more favourable surface binding energy was created which is the reason for the increased activity.

1.4 Catalysis for sustainable chemistry – green chemistry and circular chemistry

Catalysis is essential for many processes in sustainable chemistry as it is a vital part of chemical processes in industrial economies which rely on catalysts to lower energy outputs, cost and increase rate of reactions. Green chemistry has a relatively long history, with the twelve principles of Green Chemistry first in proposed by Anastas and Warner in the 1990s,[100] illustrated in table 1. Green chemistry refers to the design of chemical products and processes that reduce or eliminate the generation of hazardous substances. Catalysis is directly addressed as one of the twelve principles 'Catalytic reagents (as selective as possible) are superior to stoichiometric reagents.' The term 'sustainable chemistry' has been introduced more recently and in contrast to green chemistry has countless definitions. Sustainable chemistry was defined in the 90's by The Organisation for Economic Co-operation and Development (OECD) as "a scientific concept that seeks to improve the efficiency with which natural resources are used to meet human needs for chemical products and services".[101] It outlines that it increases economic output while simultaneously protecting human and environmental health. For example, replacing an environmentally harmful organic solvent with water in a chemical process would align with the principles of green chemistry, however, if replacing the solvent requires excess water from natural sources to be used, then the process would be green but not sustainable.

Noble metal NP catalysts with photo enhancement using visible light has become popular in the area of green chemistry in recent years. Monometallic and bimetallic nanostructures have been used for a range of organic transformations driven by visible light such as Suzuki cross coupling reactions. Using light as a source to drive chemical reactions aids the use of lower reaction temperatures compared to conventional thermal reactions, enhances reaction rates and improves selectivity which are the main advantages of using light-harvesting catalysts that enable more energy efficient and greener route to chemical synthesis.

A key factor distinguishing green and sustainable chemistry is the concept of circularity. The circular economy takes into account the full cycle of a material *i.e.* how it is used, re-used and disposed, how to minimise waste and maximise resources in that process. Chemistry is central to the ideal of the

circular economy and Keijer *et al.*[102] defined the twelve principles of circular chemistry which provide a useful framework from a chemistry perceptive, which are illustrated in table 1 and compared with the principles of green chemistry from Anastas.

When compared together it is clear that green and circular chemistry are assigned as two separate economic models, linear and circular. The linear economy model is based on a "take, make and dispose" system where profitability is the priority and does not take into account the life cycle of the product. The aim of a circular economy is to develop a sustainable strategy of "make, use and recycle" as represented in figure 4. The twelve principles also illustrate the need for a holistic or life-cycle (system) thinking approach to achieve a transition to a circular economy. This is reflected in later principles that highlight the importance of government policy to implement chemical and environmental regulations and support sustainable supply chains, so circular chemistry innovations can be readily adopted by industry.

Table 1: Principles of green and circular chemistry based off the work reported by Anastas *et al.*[100] and Keijer and co-workers.[102]

Principles of Green Chemistry	Principles of Circular chemistry
Prevention	Collect & use waste
Atom Economy	Maximise atom circulation
Less hazardous chemical synthesis	Optimise resource efficiency
Designing safer chemicals	Strive from energy persistence
Safer solvents & auxiliaries	Enhance process efficiency
Design for energy efficiency	No out of plant toxicity
Use of renewable feedstock	Target optimal design
Reduce derivatives	Access sustainability
Catalysis	Apply ladder of circularity
Design for degradation	Sell service, not product
Real time analysis for pollution prevention	Reject lock in
Inherently safer chemical for accident prevention	Unify industry & provide coherent policy framework

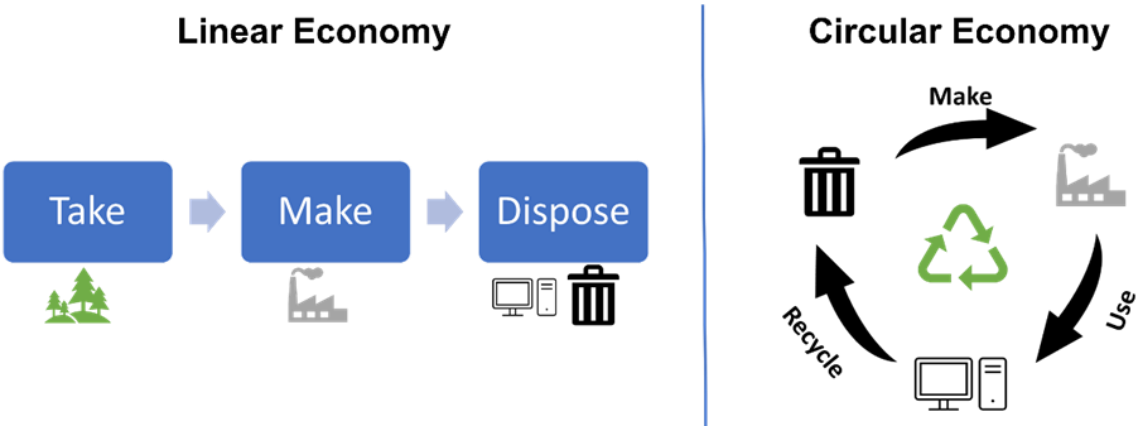

Figure 4: Linear vs circular economy

Using waste as a resource presents a huge challenge which requires the development of new chemical conversions that can deal with complex waste streams and use them as feedstocks for high value products. For example, plastic waste streams are to be often cross contaminated with other plastic types due to insufficient physical sorting. The presence of additives such a colorants and stabilisers can impact on the chemistry developed for their degradation. The development of chemical processes that can convert waste materials into higher value products is a key corner of enabling a materials circular economy.

1.5 Surface immobilisation of catalysts

The use of a support material is often an essential component of a heterogeneous catalyst. Commonly used support materials include carbon-based materials e.g. carbon black, carbon fibres, graphite and metal oxides such as alumina and silica. In general, a support material should have a large specific surface area, high porosity, and relative chemical inertness.[89-91] Colloidal synthesis methods allows for the formation of the well-defined catalytic NPs that can then be immobilised onto a suitable support material. One of the easiest methods for immobilising NPs is based on surface adsorption, where NPs are preformed in a solution phase, are left in contact with a porous catalyst supports such as alumina or activated carbon for a period of time resulting in adsorption.[92] The solvent layer should become colourless indicating adsorption of the metal NP to the support. The solvent layer is then decanted and the metal on the support is the dried in an oven.

Metal NPs can also be immobilized on molecularly modified surfaces. The presence of molecular functionalities grafted on the surface of the support material can have a significant influence on the stabilization and reactivity of the NP. Strong synergistic effects can arise from interactions between the NPs and the molecular ligand. For example, Hou and co-workers[93] demonstrated Ru NPs immobilised on sulfonic acid-functionalized silica produces a bifunctional catalyst with high activity for the hydrogenolysis of cellulose into sorbitol. Their bifunctional catalyst was more selective toward the formation of sorbitol than a physical mixture of its individual components. XPS and FTIR analysis showed strong interaction between the Ru NP and SO_3-OH groups. Many examples of enhanced catalyst activity or selectivity of NPs is due to the presence of surface organic ligands are emerging in the literature and are nicely summarised in a recent review by Bordet *et al.*[94]

Another important strategy in the design of heterogeneous catalysts is to immobilize a homogeneous catalyst or ion species on an insoluble support. Ordered mesoporous silicas such as FSM-16, MCM-41, and SBA-15, are particularly attractive due to the wide variety of structures and pore size available. Common methods for the immobilization of homogeneous catalysts, based on the interaction between the catalyst and the solid support include electrostatic interaction and covalent binding adsorption. Electrostatic interaction is a relatively simple method but often suffers from poor catalyst stability. It also requires the presence of a charged surface so can be limited in its application. Wager *et al.*[95] report a highly successful demonstration of this method by immobilisation of cationic diphosphine Rh complexes on Al-containing MCM-41 materials. This catalyst displayed superior catalytic performance in asymmetric hydrogenation of dimethylitaconate compared to any commercial catalyst.

Covalent modification is by far the most common approach of catalyst immobilisation and silica provides excellent opportunities for immobilization of organic ligands onto the surface. Jeongmyeong *et al.*[96] adopted mesoporous cellular foam (MCF) SiO_2 as a support for Pt catalysts and synthesised amine functionalised MCFs by attaching primary, secondary and tertiary amines on the SiO_2 surface. They used the functionalised catalysts in an enantioselective hydrogenation of an α-keto ester (methyl pyruvate), and they compared their catalysts against Pt/Al_2O_3. The Pt/NH_2 MCF catalyst gave superior

results despite the loading being 10 times lower than Pt/Al_2O_3. Pt/NH_2-MCF yielded 100% conversion and 96% at 0.1 MPa H_2 pressure and showed excellent reusability. The increased catalytic performance was due of the presence of electron-deficient Pt species originating from charge transfer between the amine and Pt. Huerta *et al.*[97] grafted Au NPs onto modified SBA-15 SiO_2 support modified with thiol groups where the strong thiol-Au interaction gave good catalyst stability. SBA-15 modified with (3-aminopropyl)triethoxysilane (APTES) was used as a support for Au NP as a catalyst for the hydrogenation of quinoline to 1,2,3,4-tetrahydroquinoline.[98] The Au-SBA-15 modified catalyst converted 97.6% of quinoline with 99.8% selectively towards 1,2,3,4-tetrahydroquinoline under mild conditions using an autoclave reactor with 0.1 g catalyst and temperature of 100 °C. The high specific surface area of the SBA-15 and low Au concentrations aided the formation of small diameter Au NP which led to high activity of the Au catalyst.

Silylation chemistry allows the surface SiO_2 to be functionalised with a range of organic ligands via condensation reactions. The first step in the silylation reaction is the physisorption of the organosilane molecule on to the hydrated Si surface. The silane head groups (Si-OR) react with the surface Si-OH groups through a condensation reaction forming a new Si-O-Si bond. This method of surface modification is attractive as there are a wide variety of commercially available precursor with different terminal functional group e.g. amines, thiols, epoxides and carboxylic acids. Step-wise reactions can be used to build up more complex organic functional layers on the SiO_2 surface. One of the most commonly used silanes is APTMS. The terminal amine groups can be used to immobilise metals ions and NPs onto the SiO_2 surface. Although the surface chemistry of the attached amine is often illustrated to be that as shown in Figure 5a the true surface is typically more complex with a variety of different surface coordination types possible, as shown in figure 5.

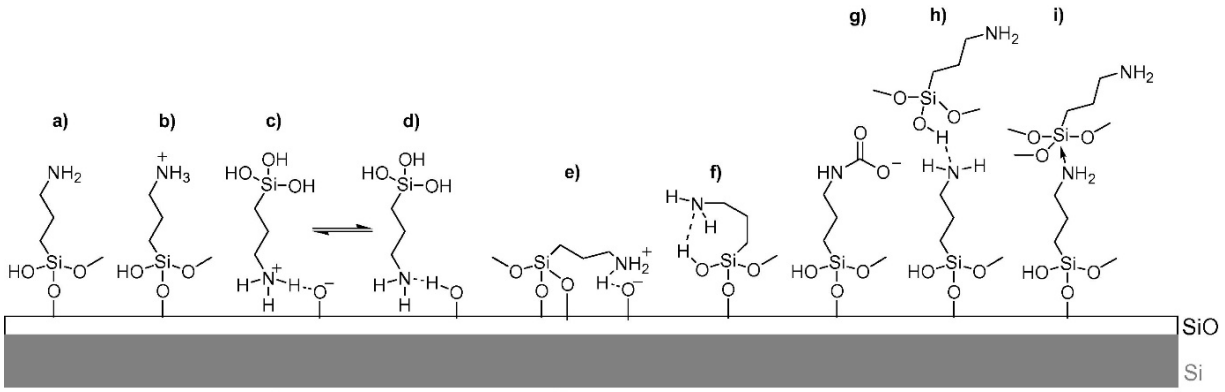

Figure 5: Bonding possibilities of 3-aminopropylsiliane on oxidised Si.[99]

1.6 Chemical depolymerisation of PET

The development of a plastics circular economy has become an important research topic in recent years. Plastics are a cheap, light weight, and durable materials with excellent thermal properties, that play a major role in everyday life for the vast majority of people around the world.[103-104] Their multi-use properties are advantageous and therefore it is not surprising that are one of the most used materials in the sectors from healthcare and laboratory settings to retail and transport.[103] What is sometimes overlooked is the amount of waste that is generated from plastic, and how it is disposed. Improper waste management strategies, particularly in less well developed countries can result in massive scale environmental pollution. Roughly, 4.8 to 12 million tons of plastic waste is generate and lost to the environment each year[105], with 16 million tons of CO_2 equivalents were emitted from the incineration of plastic packaging in 2015.[106] Our current methods for recycling are to send waste to our landfills, incineration, and plastic recycling.[107] The use of landfills and incineration are detrimental to the environmental as hazardous components are released into the environment.[108] Most plastic that is used for packaging are non-degradable and takes hundreds of years to degrade. Therefore, it is not surprising that there has been an increase in reports of banning the uses of such plastic materials. The global production of plastic is growing exponentially and there needs to be a solution.

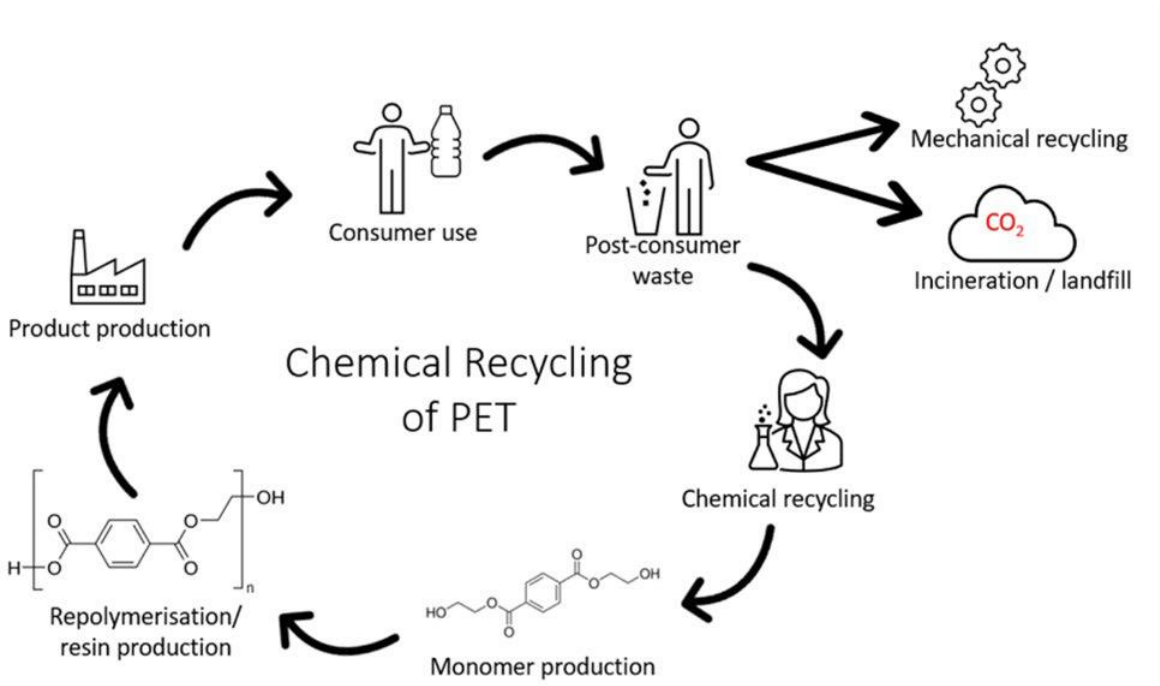

Figure 6: Chemical recycling of PET – a plastics circular economy.

Polyethylene terephthalate (PET) is a high-volume thermoplastic polyester and is one of the most commonly used polymers for single use plastics such as, cups, cutlery, bottles, and packaging for food. The recycling of PET can be carried out by either mechanical or chemical processes.[109] Mechanical recycling consists of sorting, washing, drying, reduction of size, filtration and then reforming of the plastic.[110] This process produces a plastic melt that can then be reformed into other plastic products. The main problem with mechanical recycling of PET is that the reforming process produces PET with inferior properties to virgin PET, therefore the economic demand for this type of product is low and mechanical recycling more accurately describes downcycling of PET. Chemical recycling of PET refers to conversion of PET into it monomeric compounds such as bis(2-hydroethyl) terephthalate (BHET) and terephthalic acid (TPA) that can then be used to make new PET with no loss in product quality.[111] Figure 6 demonstrates the chemical recycling of PET, which represents the goal of achieving a circular economy in the polymer life cycle.

There are a variety of chemical recycling methods reported for the recycling of post-consumer plastics waste and these include, hydrolysis, methanolysis, glycolysis and aminolysis. Figure 7 details the different types of solvolysis of PET depolymerisation. Hydroylsis[112-114] of PET can be carried out under

basic, acidic, or neutral conditions at high temperatures. The acidic hydrolysis occurs with usually concentrated sulfuric acid. Alkaline hydrolysis usually occurs using aqueous sodium hydroxide and the neutral hydrolysis occurs with water and a metal salt as the catalyst. [115] Hydrolysis reaction is quite slow in comparison to other chemical recycling methods.[116] Typically due to the high energy consumed during hydrolysis reactions are deemed inadequate in an industrial scale.[112] Methanolysis[117] of PET is a process whereby methanol is used at high temperatures and high pressures to degrade PET into dimethyl terephthalate (DMT) and ethylene glycol (EG). The most common catalyst used for this transesterification reaction is zinc acetate. For example, Hofmann *et al*.[118] reported a simple methodology to depolymerise PET to produce DMT and EG., which was able to be used as monomers to resynthesise PET with the use of zinc acetate as the catalyst. They obtained excellent isolated yield of 95% DMT. There have been reports in literature for other catalysts used for the methanolysis of PET.[117, 119] The methanolysis process is high costing for the production due to the need for separation and refining of the end products and when compared with other methods. Aminolysis form of chemical degradation which has not been researched as well as other methods.[116] The process of degrading PET through an aminolytic chain cleavage forms diamides of terephthalic acid (TPA), known as terephthalamide (TPM), this method involves the use different amines such as allylamine, ethylamine, and ethanolamine under low reaction temperatures of 20-100°C. Catalysts commonly used for this reaction are zinc acetate, lead acetate and other metal salts.[120-121] Glycolysis is another effective method for depolymerisation of PET to its monomer BHET as it can be achieved under mild conditions with a relatively low cost. PET with excess ethylene glycol and the catalyst undergoes a transesterification reaction producing BHET at relatively high temperatures (~190°C). The typical catalyst used for the degradation of PET to BHET is a zinc acetate salt.[118, 122-123]

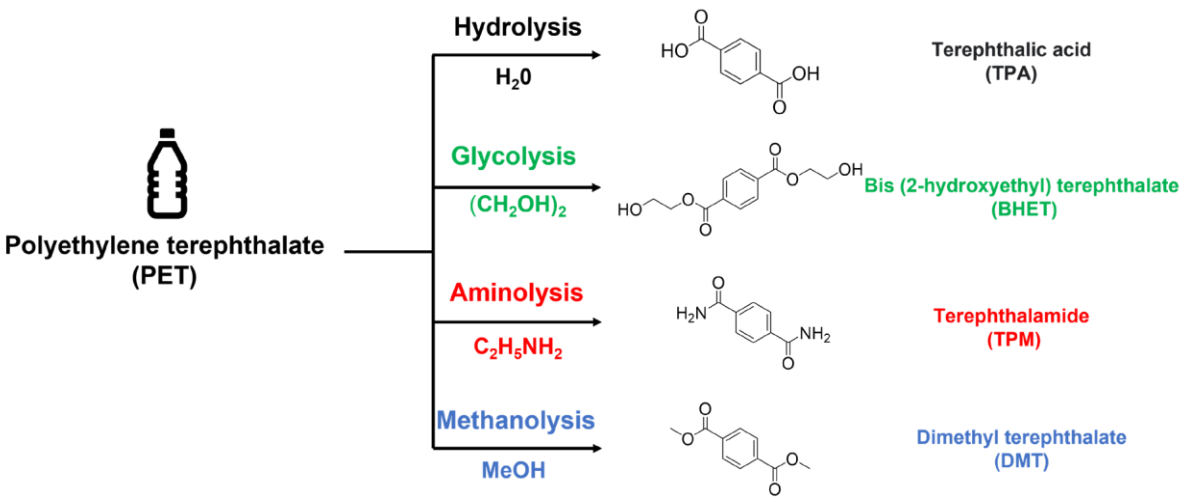

Figure 7: Different solvolysis methods for PET depolymerization.

There are a variety of factors which influence the activity of the glycolysis reaction, these include choice of catalyst, catalyst loading, time, temperature, and ratio of PET: glycol. As for the choice of catalysts, homogenous catalysts are often used to efficiently convert PET to its monomers. However, issues arise regarding recovery and recycling of the catalyst as it is common for metal salts to leach into the product.[124] Metal salts[125-127], metal oxides[128-129] and ionic liquids.[111, 130-131] are the most common homogeneous catalysts for the degradation of PET. The use of heterogeneous catalysts in the glycolysis reaction avoids this issue and are capable of being recovered and recycled which from a sustainability point of view is very attractive.

1.7 Aims and Objectives

This introduction chapter presents a general overview in the design of nanomaterials for the application in heterogeneous catalyst such as size and shaped control nanostructures, alloy NPs, and the immobilisation of the catalysts onto support materials. The aim of this thesis is to design optimum catalysts for a range of pharmaceutical and chemical recycling applications. In Chapter 1, the aim was to illustrate the use of well-defined catalytic NPs for the application to important pharmaceutically relevant reactions for maintaining high activity and selectivity. Materials characterisation was used to reveal information about the pre and post reaction catalyst along with the interaction of steric and electronic effects. The aim for the chapter 2 was to develop a new one-pot method for the synthesis of alloy AuPd nanosheets and their application to light enhanced Suzuki cross coupling reaction. The study of combining 2D morphology and photocatalysis was an important feature of this work as it is not reported well in literature. The aim final two chapters was to focus the development of heterogeneous catalysts for the depolymerisation of PET and PLA. This work displays a combination of using material synthesis and characterization, solid state NMR and DFT calculations to find the optimum design for metal and metal free heterogenous catalysts.

1.8 References

1. Bej, A.; Ghosh, K.; Sarkar, A.; Knight, D. W., Palladium nanoparticles in the catalysis of coupling reactions. *RSC Advances* **2016,** *6* (14), 11446-11453.
2. Collins, G.; Schmidt, M.; O'Dwyer, C.; Holmes, J. D.; McGlacken, G. P., The Origin of Shape Sensitivity in Palladium-Catalyzed Suzuki–Miyaura Cross Coupling Reactions. *Angewandte Chemie International Edition* **2014,** *53* (16), 4142-4145.
3. Han, J.; Liu, Y.; Guo, R., Facile Synthesis of Highly Stable Gold Nanoparticles and Their Unexpected Excellent Catalytic Activity for Suzuki−Miyaura Cross-Coupling Reaction in Water. *Journal of the American Chemical Society* **2009,** *131* (6), 2060-2061.
4. Yu, L.; Huang, Y.; Wei, Z.; Ding, Y.; Su, C.; Xu, Q., Heck Reactions Catalyzed by Ultrasmall and Uniform Pd Nanoparticles Supported on Polyaniline. *The Journal of Organic Chemistry* **2015,** *80* (17), 8677-8683.
5. Bhakta, S.; Ghosh, T., Nickel Nanocatalysis: An Efficient Tool for Heck Reaction. *ChemCatChem* **2021,** *13* (3), 828-835.
6. Mitsudome, T.; Kaneda, K., Gold nanoparticle catalysts for selective hydrogenations. *Green Chemistry* **2013,** *15* (10), 2636-2654.
7. Luza, L.; Rambor, C. P.; Gual, A.; Alves Fernandes, J.; Eberhardt, D.; Dupont, J., Revealing Hydrogenation Reaction Pathways on Naked Gold Nanoparticles. *ACS Catalysis* **2017,** *7* (4), 2791-2799.
8. Reina, A.; Favier, I.; Teuma, E.; Gómez, M.; Conte, A.; Pichon, L., Hydrogenation reactions catalyzed by colloidal palladium nanoparticles under flow regime. *AIChE Journal* **2019,** *65* (11), e16752.
9. Wu, L.; Xi, Z.; Sun, S., Chapter 4 - Well-Defined Metal Nanoparticles for Electrocatalysis. In *Studies in Surface Science and Catalysis*, Fornasiero, P.; Cargnello, M., Eds. Elsevier: 2017; Vol. 177, pp 123-148.
10. Nasrallah, H.; Douma, F.; Hamoud, H. I.; El-Roz, M., Chapter 5 - Metal nanoparticles in photocatalysis: Advances and challenges. In *Nanostructured Photocatalysts*, Nguyen, V.-H.; Vo, D.-V. N.; Nanda, S., Eds. Elsevier: 2021; pp 119-143.
11. Xu, H.; Shang, H.; Wang, C.; Du, Y., Ultrafine Pt-Based Nanowires for Advanced Catalysis. *Advanced Functional Materials* **2020,** *30* (28), 2000793.
12. Kumar, A.; Xu, Q., Two-Dimensional Layered Materials as Catalyst Supports. *ChemNanoMat* **2018,** *4* (1), 28-40.
13. Zhao, H.; Lei, Y., 3D Nanostructures for the Next Generation of High-Performance Nanodevices for Electrochemical Energy Conversion and Storage. *Advanced Energy Materials* **2020,** *10* (28), 2001460.
14. García-Betancourt, M.; Jiménez, S.; González-Hodges, A.; Salazar, Z.; Escalante-Garcia, I.; Aparicio, J., Low Dimensional Nanostructures: Measurement and Remediation Technologies Applied to Trace Heavy Metals in Water. 2020.
15. Zhao, Y. Quantum Dots and Doped Nanocrystals: Synthesis, Optical Properties, and Bio-applications. 2013.
16. Turkevich, J.; Stevenson, P. C.; Hillier, J., A study of the nucleation and growth processes in the synthesis of colloidal gold. *Discussions of the Faraday Society* **1951,** *11*, 55-75.
17. Frens, G., Controlled nucleation for the regulation of the particle size in monodisperse gold suspensions. *Nature physical science* **1973,** *241* (105), 20-22.
18. Ji, X.; Song, X.; Li, J.; Bai, Y.; Yang, W.; Peng, X., Size Control of Gold Nanocrystals in Citrate Reduction: The Third Role of Citrate. *Journal of the American Chemical Society* **2007,** *129* (45), 13939-13948.
19. Brust, M.; Walker, M.; Bethell, D.; Schiffrin, D. J.; Whyman, R., Synthesis of thiol-derivatised gold nanoparticles in a two-phase Liquid–Liquid system. *Journal of the Chemical Society, Chemical Communications* **1994,** (7), 801-802.
20. Yeh, Y. C.; Creran, B.; Rotello, V. M., Gold nanoparticles: preparation, properties, and applications in bionanotechnology. *Nanoscale* **2012,** *4* (6), 1871-80.

21. Yan, X.; Liu, H.; Liew, K. Y., Size control of polymer-stabilized ruthenium nanoparticles by polyol reduction. *Journal of Materials Chemistry* **2001,** *11* (12), 3387-3391.
22. Hei, H., Controlled Synthesis and Characterization of Nobel Metal Nanoparticles. *Soft Nanoscience Letters* **2012,** *02*, 34-40.
23. Silvert, P.-Y.; Herrera-Urbina, R.; Duvauchelle, N.; Vijayakrishnan, V.; Elhsissen, K. T., Preparation of colloidal silver dispersions by the polyol process. Part 1—Synthesis and characterization. *Journal of Materials Chemistry* **1996,** *6* (4), 573-577.
24. Teranishi, T.; Hosoe, M.; Tanaka, T.; Miyake, M., Size Control of Monodispersed Pt Nanoparticles and Their 2D Organization by Electrophoretic Deposition. *The Journal of Physical Chemistry B* **1999,** *103* (19), 3818-3827.
25. Teranishi, T.; Miyake, M., Size Control of Palladium Nanoparticles and Their Crystal Structures. *Chemistry of Materials* **1998,** *10* (2), 594-600.
26. Yan, C. C.; Zhang, D. H.; Li, D. D., Spherical metallic nanoparticle arrays for super-resolution imaging. *Journal of Applied Physics* **2011,** *109* (6), 063105.
27. Pustovalov, V. K.; Astafyeva, L. G.; Fritzsche, W., Analysis of optical properties of spherical metallic nanoparticles for effective absorption of solar radiation and their heating. *Solar Energy* **2015,** *122*, 1334-1341.
28. Khaywah, M.; Potdevin, A.; Réveret, F.; Mahiou, R.; Ouerdane, Y.; Désert, A.; Parola, S.; Chadeyron, G.; Centeno, E.; Smaali, R.; Moreau, A., Large and Versatile Plasmonic Enhancement of Photoluminescence Using Colloidal Metallic Nanocubes. *The Journal of Physical Chemistry C* **2021,** *125* (14), 7780-7790.
29. Clark, B. D.; Jacobson, C. R.; Lou, M.; Renard, D.; Wu, G.; Bursi, L.; Ali, A. S.; Swearer, D. F.; Tsai, A.-L.; Nordlander, P.; Halas, N. J., Aluminum Nanocubes Have Sharp Corners. *ACS Nano* **2019,** *13* (8), 9682-9691.
30. Zhang, Y.; Wang, M.; Zhu, E.; Zheng, Y.; Huang, Y.; Huang, X., Seedless Growth of Palladium Nanocrystals with Tunable Structures: From Tetrahedra to Nanosheets. *Nano letters* **2015,** *15* (11), 7519-7525.
31. Figueroa-Cosme, L.; Gilroy, K. D.; Yang, T.-H.; Vara, M.; Park, J.; Bao, S.; da Silva, A. G. M.; Xia, Y., Synthesis of Palladium Nanoscale Octahedra through a One-Pot, Dual-Reductant Route and Kinetic Analysis. *Chemistry – A European Journal* **2018,** *24* (23), 6133-6139.
32. Zhou, S.; Wang, C.; Xia, Y., Polyol Synthesis of Pd Icosahedral Nanocrystals: Insights into the Growth Mechanism and Size Control. *Chemistry of Materials* **2022,** *34* (11), 5065-5073.
33. Xu, M.; Zhang, L.; Zhao, F., One-Pot Aqueous Synthesis of Icosahedral Au as Bifunctional Candidates for Enhanced Glucose Electrooxidation and Surface-Enhanced Raman Scattering. *ACS Applied Materials & Interfaces* **2020,** *12* (10), 12186-12194.
34. Wang, J.; Du, C.; Wei, Q.; Shen, W., Two-Dimensional Pd Nanosheets with Enhanced Catalytic Activity for Selective Hydrogenation of Nitrobenzene to Aniline. *Energy & Fuels* **2021,** *35* (5), 4358-4366.
35. Zhang, Y.; Cui, Z.; Li, L.; Guo, L.; Yang, S., Two-dimensional structure Au nanosheets are super active for the catalytic reduction of 4-nitrophenol. *Physical Chemistry Chemical Physics* **2015,** *17* (22), 14656-14661.
36. Zheng, J.; Cheng, X.; Zhang, H.; Bai, X.; Ai, R.; Shao, L.; Wang, J., Gold Nanorods: The Most Versatile Plasmonic Nanoparticles. *Chemical Reviews* **2021,** *121* (21), 13342-13453.
37. Ganji, M.; Paulk, A. C.; Yang, J. C.; Vahidi, N. W.; Lee, S. H.; Liu, R.; Hossain, L.; Arneodo, E. M.; Thunemann, M.; Shigyo, M.; Tanaka, A.; Ryu, S. B.; Lee, S. W.; Tchoe, Y.; Marsala, M.; Devor, A.; Cleary, D. R.; Martin, J. R.; Oh, H.; Gilja, V.; Gentner, T. Q.; Fried, S. I.; Halgren, E.; Cash, S. S.; Dayeh, S. A., Selective Formation of Porous Pt Nanorods for Highly Electrochemically Efficient Neural Electrode Interfaces. *Nano letters* **2019,** *19* (9), 6244-6254.
38. Valério Neto, E. S.; Almeida, C. V. S.; Colmati, F.; Ciapina, E. G.; Salazar-Banda, G. R.; Eguiluz, K. I. B., Pt nanowires as electrocatalysts for proton-exchange membrane fuel cells applications: A review. *Journal of Electroanalytical Chemistry* **2022,** *910*, 116185.

39. Cheng, C.; Gonela, R. K.; Gu, Q.; Haynie, D. T., Self-Assembly of Metallic Nanowires from Aqueous Solution. *Nano letters* **2005,** *5* (1), 175-178.
40. Hwang, A.; Kim, E.; Moon, J.; Lee, H.; Lee, M.; Jeong, J.; Lim, E.-K.; Jung, J.; Kang, T.; Kim, B., Atomically Flat Au Nanoplate Platforms Enable Ultraspecific Attomolar Detection of Protein Biomarkers. *ACS Applied Materials & Interfaces* **2019,** *11* (21), 18960-18967.
41. Zhao, R.; Liu, Y.; Liu, C.; Xu, G.; Chen, Y.; Tang, Y.; Lu, T., Pd@Pt core–shell tetrapods as highly active and stable electrocatalysts for the oxygen reduction reaction. *Journal of Materials Chemistry A* **2014,** *2* (48), 20855-20860.
42. Tao, A.; Sinsermsuksakul, P.; Yang, P., Polyhedral Silver Nanocrystals with Distinct Scattering Signatures. *Angewandte Chemie International Edition* **2006,** *45* (28), 4597-4601.
43. Danilenko, M. V.; Guterman, V. E.; Vetrova, E. V.; Metelitsa, A. V.; Paperzh, K. O.; Pankov, I. V.; Safronenko, O. I., Nucleation/growth of the platinum nanoparticles under the liquid phase synthesis. *Colloids and Surfaces A: Physicochemical and Engineering Aspects* **2021,** *630*, 127525.
44. Ungureanu, S.; Deleuze, H.; Babot, O.; Achard, M. F.; Sanchez, C.; Popa, M. I.; Backov, R., Palladium nanoparticles heterogeneous nucleation within organically grafted silica foams and their use as catalyst supports toward the Suzuki–Miyaura and Mizoroki–Heck coupling reactions. *Applied Catalysis A: General* **2010,** *390* (1), 51-58.
45. Anumol, E. A.; Kundu, P.; Deshpande, P. A.; Madras, G.; Ravishankar, N., New Insights into Selective Heterogeneous Nucleation of Metal Nanoparticles on Oxides by Microwave-Assisted Reduction: Rapid Synthesis of High-Activity Supported Catalysts. *ACS Nano* **2011,** *5* (10), 8049-8061.
46. Somorjai, G. A.; Park, J. Y., Molecular Factors of Catalytic Selectivity. *Angewandte Chemie International Edition* **2008,** *47* (48), 9212-9228.
47. Liang, C.; Cheong, J. Y.; Sitaru, G.; Rosenfeldt, S.; Schenk, A. S.; Gekle, S.; Kim, I. I. D.; Greiner, A., Size-Dependent Catalytic Behavior of Gold Nanoparticles. *Advanced Materials Interfaces* **2022,** *9* (4), 2100867.
48. Bratlie, K. M.; Lee, H.; Komvopoulos, K.; Yang, P.; Somorjai, G. A., Platinum nanoparticle shape effects on benzene hydrogenation selectivity. *Nano letters* **2007,** *7* (10), 3097-101.
49. Novoselov, K. S.; Geim, A. K.; Morozov, S. V.; Jiang, D.; Zhang, Y.; Dubonos, S. V.; Grigorieva, I. V.; Firsov, A. A., Electric Field Effect in Atomically Thin Carbon Films. *Science* **2004,** *306* (5696), 666-669.
50. Yi, M.; Shen, Z., A review on mechanical exfoliation for the scalable production of graphene. *Journal of Materials Chemistry A* **2015,** *3* (22), 11700-11715.
51. Butler, S. Z.; Hollen, S. M.; Cao, L.; Cui, Y.; Gupta, J. A.; Gutiérrez, H. R.; Heinz, T. F.; Hong, S. S.; Huang, J.; Ismach, A. F.; Johnston-Halperin, E.; Kuno, M.; Plashnitsa, V. V.; Robinson, R. D.; Ruoff, R. S.; Salahuddin, S.; Shan, J.; Shi, L.; Spencer, M. G.; Terrones, M.; Windl, W.; Goldberger, J. E., Progress, challenges, and opportunities in two-dimensional materials beyond graphene. *ACS Nano* **2013,** *7* (4), 2898-926.
52. Chen, Y.; Fan, Z.; Zhang, Z.; Niu, W.; Li, C.; Yang, N.; Chen, B.; Zhang, H., Two-Dimensional Metal Nanomaterials: Synthesis, Properties, and Applications. *Chem Rev* **2018,** *118* (13), 6409-6455.
53. Wang, C.-H.; Zhang, D.-W.; Liu, S.; Yamauchi, Y.; Zhang, F.-B.; Kaneti, Y. V., Ultrathin nanosheet-assembled nickel-based metal–organic framework microflowers for supercapacitor applications. *Chemical Communications* **2022,** *58* (7), 1009-1012.
54. Yang, J.; Gao, M.; Lei, J.; Jin, X.; Yu, L.; Ren, F., Surfactant-assisted synthesis of ultrathin two-dimensional Co3O4 nanosheets for applications in lithium-ion batteries and ultraviolet photodetector. *Journal of Solid State Chemistry* **2019,** *274*, 124-133.
55. Yim, D.; Raza, F.; Park, J. H.; Lee, J.-H.; Kim, H.-I.; Yang, J.-K.; Hwang, I.-J.; Kim, J.-H., Ultrathin WO3 Nanosheets Converted from Metallic WS2 Sheets by Spontaneous Formation and Deposition of PdO Nanoclusters for Visible Light-Driven C–C Coupling Reactions. *ACS Applied Materials & Interfaces* **2019,** *11* (40), 36960-36969.
56. Fan, H.; Huang, X.; Shang, L.; Cao, Y.; Zhao, Y.; Wu, L.-Z.; Tung, C.-H.; Yin, Y.; Zhang, T., Controllable Synthesis of Ultrathin Transition-Metal Hydroxide Nanosheets and their Extended

Composite Nanostructures for Enhanced Catalytic Activity in the Heck Reaction. *Angewandte Chemie International Edition* **2016,** *55* (6), 2167-2170.
57. Zhang, J.; Gong, W.; Yin, H.; Wang, D.; Zhang, Y.; Zhang, H.; Wang, G.; Zhao, H., In Situ Growth of Ultrathin Ni(OH)(2) Nanosheets as Catalyst for Electrocatalytic Oxidation Reactions. *ChemSusChem* **2021,** *14* (14), 2935-2942.
58. Xu, D.; Liu, X.; Lv, H.; Liu, Y.; Zhao, S.; Han, M.; Bao, J.; He, J.; Liu, B., Ultrathin palladium nanosheets with selectively controlled surface facets. *Chemical science* **2018,** *9* (19), 4451-4455.
59. Yang, M.; Pang, M.; Chen, J.; Gao, F.; Li, H.; Guo, P., Surfactant-Assisted Synthesis of Palladium Nanosheets and Nanochains for the Electrooxidation of Ethanol. *ACS Applied Materials & Interfaces* **2021,** *13* (8), 9830-9837.
60. Kong, X.; Xu, K.; Zhang, C.; Dai, J.; Norooz Oliaee, S.; Li, L.; Zeng, X.; Wu, C.; Peng, Z., Free-Standing Two-Dimensional Ru Nanosheets with High Activity toward Water Splitting. *ACS Catalysis* **2016,** *6* (3), 1487-1492.
61. Niu, J.; Wang, D.; Qin, H.; Xiong, X.; Tan, P.; Li, Y.; Liu, R.; Lu, X.; Wu, J.; Zhang, T.; Ni, W.; Jin, J., Novel polymer-free iridescent lamellar hydrogel for two-dimensional confined growth of ultrathin gold membranes. *Nature Communications* **2014,** *5* (1), 3313.
62. Duan, H.; Yan, N.; Yu, R.; Chang, C.-R.; Zhou, G.; Hu, H.-S.; Rong, H.; Niu, Z.; Mao, J.; Asakura, H.; Tanaka, T.; Dyson, P. J.; Li, J.; Li, Y., Ultrathin rhodium nanosheets. *Nature Communications* **2014,** *5* (1), 3093.
63. Liu, P.; Nørskov, J. K., Ligand and ensemble effects in adsorption on alloy surfaces. *Physical Chemistry Chemical Physics* **2001,** *3* (17), 3814-3818.
64. Huynh, K. H.; Pham, X. H.; Kim, J.; Lee, S. H.; Chang, H.; Rho, W. Y.; Jun, B. H., Synthesis, Properties, and Biological Applications of Metallic Alloy Nanoparticles. *International journal of molecular sciences* **2020,** *21* (14).
65. Kim, H.; Yoo, T. Y.; Bootharaju, M. S.; Kim, J. H.; Chung, D. Y.; Hyeon, T., Noble Metal-Based Multimetallic Nanoparticles for Electrocatalytic Applications. *Advanced science (Weinheim, Baden-Wurttemberg, Germany)* **2022,** *9* (1), e2104054.
66. Rakap, M., Hydrogen generation from hydrolysis of ammonia borane in the presence of highly efficient poly(N-vinyl-2-pyrrolidone)-protected platinum-ruthenium nanoparticles. *Applied Catalysis A: General* **2014,** *478*, 15-20.
67. Kunz, M. R.; McClain, S. M.; Chen, D. P.; Koczkur, K. M.; Weiner, R. G.; Skrabalak, S. E., Seed-mediated co-reduction in a large lattice mismatch system: synthesis of Pd–Cu nanostructures. *Nanoscale* **2017,** *9* (22), 7570-7576.
68. Cho, B.; Lee, J.; Roh, I. P.; Lee, M. H.; Yu, T., A facile aqueous-phase synthesis method for small PdCu alloy nanocatalysts to enhance electrochemical CO2 reduction reactivity. *Journal of Alloys and Compounds* **2022,** *911*, 164990.
69. Yang, Y.; Cao, Y.; Yang, L.; Huang, Z.; Long, N. V., Synthesis of Pt-Pd Bimetallic Porous Nanostructures as Electrocatalysts for the Methanol Oxidation Reaction. *Nanomaterials (Basel, Switzerland)* **2018,** *8* (4).
70. Xiao, X.; Kang, T.-U.; Nam, H.; Bhang, S. H.; Lee, S. Y.; Ahn, J.-P.; Yu, T., One-pot synthesis of PdAu bimetallic composite nanoparticles and their catalytic activities for hydrogen peroxide generation. *Korean Journal of Chemical Engineering* **2018,** *35* (12), 2379-2383.
71. Sun, S.; Anders, S.; Thomson, T.; Baglin, J. E. E.; Toney, M. F.; Hamann, H. F.; Murray, C. B.; Terris, B. D., Controlled Synthesis and Assembly of FePt Nanoparticles. *The Journal of Physical Chemistry B* **2003,** *107* (23), 5419-5425.
72. DeSantis, C. J.; Sue, A. C.; Bower, M. M.; Skrabalak, S. E., Seed-Mediated Co-reduction: A Versatile Route to Architecturally Controlled Bimetallic Nanostructures. *ACS Nano* **2012,** *6* (3), 2617-2628.
73. Han, G.-H.; Kim, K. Y.; Nam, H.; Kim, H.; Yoon, J.; Lee, J.-H.; Kim, H.-K.; Ahn, J.-P.; Lee, S. Y.; Lee, K.-Y.; Yu, T. Facile Direct Seed-Mediated Growth of AuPt Bimetallic Shell on the Surface of Pd Nanocubes and Application for Direct H2O2 Synthesis *Catalysts* [Online], 2020.

74. Cargnello, M.; Agarwal, R.; Klein, D. R.; Diroll, B. T.; Agarwal, R.; Murray, C. B., Uniform Bimetallic Nanocrystals by High-Temperature Seed-Mediated Colloidal Synthesis and Their Catalytic Properties for Semiconducting Nanowire Growth. *Chemistry of Materials* **2015,** *27* (16), 5833-5838.
75. Chee, S. W.; Tan, S. F.; Baraissov, Z.; Bosman, M.; Mirsaidov, U., Direct observation of the nanoscale Kirkendall effect during galvanic replacement reactions. *Nature Communications* **2017,** *8* (1), 1224.
76. Rehn, S. M.; Ringe, E., Controllably Hollow AgAu Nanoparticles via Nonaqueous, Reduction Agent-Assisted Galvanic Replacement. *Particle & Particle Systems Characterization* **2018,** *35* (5), 1700381.
77. Mohl, M.; Dobo, D.; Kukovecz, A.; Konya, Z.; Kordas, K.; Wei, J.; Vajtai, R.; Ajayan, P. M., Formation of CuPd and CuPt Bimetallic Nanotubes by Galvanic Replacement Reaction. *The Journal of Physical Chemistry C* **2011,** *115* (19), 9403-9409.
78. Zhang, H.; Jin, M.; Wang, J.; Li, W.; Camargo, P. H. C.; Kim, M. J.; Yang, D.; Xie, Z.; Xia, Y., Synthesis of Pd−Pt Bimetallic Nanocrystals with a Concave Structure through a Bromide-Induced Galvanic Replacement Reaction. *Journal of the American Chemical Society* **2011,** *133* (15), 6078-6089.
79. Jing, H.; Wang, H., Structural Evolution of Ag–Pd Bimetallic Nanoparticles through Controlled Galvanic Replacement: Effects of Mild Reducing Agents. *Chemistry of Materials* **2015,** *27* (6), 2172-2180.
80. Crawley, J. W. M.; Gow, I. E.; Lawes, N.; Kowalec, I.; Kabalan, L.; Catlow, C. R. A.; Logsdail, A. J.; Taylor, S. H.; Dummer, N. F.; Hutchings, G. J., Heterogeneous Trimetallic Nanoparticles as Catalysts. *Chemical Reviews* **2022,** *122* (6), 6795-6849.
81. Li, H.; Shin, K.; Henkelman, G., Effects of ensembles, ligand, and strain on adsorbate binding to alloy surfaces. *J Chem Phys* **2018,** *149* (17), 174705.
82. Wu, Z.; Wegener, E. C.; Tseng, H.-T.; Gallagher, J. R.; Harris, J. W.; Diaz, R. E.; Ren, Y.; Ribeiro, F. H.; Miller, J. T., Pd–In intermetallic alloy nanoparticles: highly selective ethane dehydrogenation catalysts. *Catalysis Science & Technology* **2016,** *6* (18), 6965-6976.
83. Gunji, T.; Wakabayashi, R. H.; Noh, S. H.; Han, B.; Matsumoto, F.; DiSalvo, F. J.; Abruña, H. D., The effect of alloying of transition metals (M = Fe, Co, Ni) with palladium catalysts on the electrocatalytic activity for the oxygen reduction reaction in alkaline media. *Electrochimica Acta* **2018,** *283*, 1045-1052.
84. Li, B.; Prakash, J., Oxygen reduction reaction on carbon supported Palladium–Nickel alloys in alkaline media. *Electrochemistry Communications* **2009,** *11* (6), 1162-1165.
85. Liu, Y.; Wang, L.; Wang, G.; Deng, C.; Wu, B.; Gao, Y., High Active Carbon Supported PdAu Catalyst for Formic Acid Electrooxidation and Study of the Kinetics. *The Journal of Physical Chemistry C* **2010,** *114* (49), 21417-21422.
86. Gu, J.; Zhang, G.-M.; Yao, R.; Yu, T.; Han, M.-F.; Huang, R.-S. High Oxygen Reduction Activity of Pt-Ni Alloy Catalyst for Proton Exchange Membrane Fuel Cells *Catalysts* [Online], 2022.
87. Ma, Z.; Cano, Z. P.; Yu, A.; Chen, Z.; Jiang, G.; Fu, X.; Yang, L.; Wu, T.; Bai, Z.; Lu, J., Enhancing Oxygen Reduction Activity of Pt-based Electrocatalysts: From Theoretical Mechanisms to Practical Methods. *Angewandte Chemie International Edition* **2020,** *59* (42), 18334-18348.
88. Troutman, J. P.; Li, H.; Haddix, A. M.; Kienzle, B. A.; Henkelman, G.; Humphrey, S. M.; Werth, C. J., PdAg Alloy Nanocatalysts: Toward Economically Viable Nitrite Reduction in Drinking Water. *ACS Catalysis* **2020,** *10* (14), 7979-7989.
89. Lam, E.; Luong, J. H. T., Carbon Materials as Catalyst Supports and Catalysts in the Transformation of Biomass to Fuels and Chemicals. *ACS Catalysis* **2014,** *4* (10), 3393-3410.
90. Waterhouse, G. I. N.; Chen, W.-T.; Chan, A.; Jin, H.; Sun-Waterhouse, D.; Cowie, B. C. C., Structural, Optical, and Catalytic Support Properties of γ-Al2O3 Inverse Opals. *The Journal of Physical Chemistry C* **2015,** *119* (12), 6647-6659.
91. Lang, M.; Klahn, M.; Strunk, J., Photophysical and Catalytic Properties of Silica Supported Early Transition Metal Oxides Relevant for Photocatalytic Applications. *Catalysis Letters* **2019,** *149* (8), 2291-2306.

92. Ivanova, A. S.; Slavinskaya, E. M.; Gulyaev, R. V.; Zaikovskii, V. I.; Stonkus, O. A.; Danilova, I. G.; Plyasova, L. M.; Polukhina, I. A.; Boronin, A. I., Metal–support interactions in Pt/Al2O3 and Pd/Al2O3 catalysts for CO oxidation. *Applied Catalysis B: Environmental* **2010,** *97* (1), 57-71.
93. Zhu, W.; Yang, H.; Chen, J.; Chen, C.; Guo, L.; Gan, H.; Zhao, X.; Hou, Z., Efficient hydrogenolysis of cellulose into sorbitol catalyzed by a bifunctional catalyst. *Green Chemistry* **2014,** *16* (3), 1534-1542.
94. Bordet, A.; Leitner, W., Metal Nanoparticles Immobilized on Molecularly Modified Surfaces: Versatile Catalytic Systems for Controlled Hydrogenation and Hydrogenolysis. *Accounts of Chemical Research* **2021,** *54* (9), 2144-2157.
95. Wagner, H. H.; Hausmann, H.; Hölderich, W. F., Immobilization of Rhodium Diphosphine Complexes on Mesoporous Al-MCM-41 Materials: Catalysts for Enantioselective Hydrogenation. *Journal of Catalysis* **2001,** *203* (1), 150-156.
96. Kim, J.; Song, B.; Chung, I.; Park, J.; Yun, Y., High-performance Pt catalysts supported on amine-functionalized silica for enantioselective hydrogenation of α-keto ester. *Journal of Catalysis* **2021,** *396*, 81-91.
97. Huerta, A.; Torralvo, M. J.; Tenorio, M. J.; Pérez, E.; Bermúdez, J.; Calvo, L.; Cabañas, A., Deposition of Au nanoparticles into mesoporous SiO2 SBA-15. *The Journal of Supercritical Fluids* **2022,** *184*, 105582.
98. Zhao, J.; Yuan, H.; Qin, X.; Tian, K.; Liu, Y.; Wei, C.; Zhang, Z.; Zhou, L.; Fang, S., Au Nanoparticles Confined in SBA-15 as a Highly Efficient and Stable Catalyst for Hydrogenation of Quinoline to 1,2,3,4-Tetrahydroquinoline. *Catalysis Letters* **2020,** *150* (10), 2841-2849.
99. Graf, N.; Yegen, E.; Gross, T.; Lippitz, A.; Weigel, W.; Krakert, S.; Terfort, A.; Unger, W. E. S., XPS and NEXAFS studies of aliphatic and aromatic amine species on functionalized surfaces. *Surface Science* **2009,** *603* (18), 2849-2860.
100. Anastas, P. T.; Warner, J. C., *Green Chemistry: Theory and Practice*. Oxford University Press: 1998.
101. Mutlu, H.; Barner, L., Getting the Terms Right: Green, Sustainable, or Circular Chemistry? *Macromolecular Chemistry and Physics* **2022,** *223* (13), 2200111.
102. Keijer, T.; Bakker, V.; Slootweg, J. C., Circular chemistry to enable a circular economy. *Nature Chemistry* **2019,** *11* (3), 190-195.
103. Thompson, R. C.; Moore, C. J.; vom Saal, F. S.; Swan, S. H., Plastics, the environment and human health: current consensus and future trends. *Philosophical transactions of the Royal Society of London. Series B, Biological sciences* **2009,** *364* (1526), 2153-66.
104. Bishop, G.; Styles, D.; Lens, P. N. L., Recycling of European plastic is a pathway for plastic debris in the ocean. *Environment International* **2020,** *142*, 105893.
105. Jambeck, J. R.; Geyer, R.; Wilcox, C.; Siegler, T. R.; Perryman, M.; Andrady, A.; Narayan, R.; Law, K. L., Plastic waste inputs from land into the ocean. *Science* **2015,** *347* (6223), 768-771.
106. CIEL, Plastic and climate: The hidden costs of a plastic planet. **2017**.
107. Schyns, Z. O. G.; Shaver, M. P., Mechanical Recycling of Packaging Plastics: A Review. *Macromolecular Rapid Communications* **2021,** *42* (3), 2000415.
108. Verma, R.; Vinoda, K. S.; Papireddy, M.; Gowda, A. N. S., Toxic Pollutants from Plastic Waste-A Review. *Procedia Environmental Sciences* **2016,** *35*, 701-708.
109. Lalhmangaihzuala, S.; Laldinpuii, Z.; Lalmuanpuia, C.; Vanlaldinpuia, K., Glycolysis of Poly(Ethylene Terephthalate) Using Biomass-Waste Derived Recyclable Heterogeneous Catalyst. *Polymers* **2021,** *13* (1).
110. Damayanti; Wu, H.-S., Strategic Possibility Routes of Recycled PET. *Polymers* **2021,** *13* (9).
111. Liu, Y.; Yao, X.; Yao, H.; Zhou, Q.; Xin, J.; Lu, X.; Zhang, S., Degradation of poly(ethylene terephthalate) catalyzed by metal-free choline-based ionic liquids. *Green Chemistry* **2020,** *22* (10), 3122-3131.
112. Stanica-Ezeanu, D.; Matei, D., Natural depolymerization of waste poly(ethylene terephthalate) by neutral hydrolysis in marine water. *Scientific Reports* **2021,** *11* (1), 4431.

113. Rubio Arias, J. J.; Thielemans, W., Instantaneous hydrolysis of PET bottles: an efficient pathway for the chemical recycling of condensation polymers. *Green Chemistry* **2021,** *23* (24), 9945-9956.
114. Yang, W.; Liu, R.; Li, C.; Song, Y.; Hu, C., Hydrolysis of waste polyethylene terephthalate catalyzed by easily recyclable terephthalic acid. *Waste Management* **2021,** *135*, 267-274.
115. Campanelli, J. R.; Cooper, D. G.; Kamal, M. R., Catalyzed hydrolysis of polyethylene terephthalate melts. *Journal of Applied Polymer Science* **1994,** *53* (8), 985-991.
116. George, N.; Kurian, T., Recent Developments in the Chemical Recycling of Postconsumer Poly(ethylene terephthalate) Waste. *Industrial & Engineering Chemistry Research* **2014,** *53* (37), 14185-14198.
117. Kurokawa, H.; Ohshima, M.-a.; Sugiyama, K.; Miura, H., Methanolysis of polyethylene terephthalate (PET) in the presence of aluminium tiisopropoxide catalyst to form dimethyl terephthalate and ethylene glycol. *Polymer Degradation and Stability* **2003,** *79* (3), 529-533.
118. Hofmann, M.; Sundermeier, J.; Alberti, C.; Enthaler, S., Zinc(II) acetate Catalyzed Depolymerization of Poly(ethylene terephthalate). *ChemistrySelect* **2020,** *5* (32), 10010-10014.
119. Pham, D. D.; Cho, J., Low-energy catalytic methanolysis of poly(ethyleneterephthalate). *Green Chemistry* **2021,** *23* (1), 511-525.
120. Gupta, P.; Bhandari, S., 6 - Chemical Depolymerization of PET Bottles via Ammonolysis and Aminolysis. In *Recycling of Polyethylene Terephthalate Bottles*, Thomas, S.; Rane, A.; Kanny, K.; V.K, A.; Thomas, M. G., Eds. William Andrew Publishing: 2019; pp 109-134.
121. Zhang, L.-n.; Liu, L.-z.; Yue, Q.-f.; Zhu, C.-c., From Aminolysis Product of Pet Waste to Value-Added Products of Polymer and Assistants. *Polymers and Polymer Composites* **2014,** *22* (1), 13-16.
122. Chen, J.-W.; Chen, L.-W.; Cheng, W.-H., Kinetics of glycolysis of polyethylene terephthalate with zinc catalyst. *Polymer International* **1999,** *48* (9), 885-888.
123. Chen, F.; Wang, G.; Shi, C.; Zhang, Y.; Zhang, L.; Li, W.; Yang, F., Kinetics of glycolysis of poly(ethylene terephthalate) under microwave irradiation. *Journal of Applied Polymer Science* **2013,** *127* (4), 2809-2815.
124. Arai, M.; Zhao, F. Metal Catalysts Recycling and Heterogeneous/Homogeneous Catalysis *Catalysts* [Online], 2015, p. 868-870.
125. Shukla, S. R.; Kulkarni, K. S., Depolymerization of poly(ethylene terephthalate) waste. *Journal of Applied Polymer Science* **2002,** *85* (8), 1765-1770.
126. López-Fonseca, R.; Duque-Ingunza, I.; de Rivas, B.; Flores-Giraldo, L.; Gutiérrez-Ortiz, J. I., Kinetics of catalytic glycolysis of PET wastes with sodium carbonate. *Chemical Engineering Journal* **2011,** *168* (1), 312-320.
127. Fang, P.; Liu, B.; Xu, J.; Zhou, Q.; Zhang, S.; Ma, J.; lu, X., High-efficiency glycolysis of poly(ethylene terephthalate) by sandwich-structure polyoxometalate catalyst with two active sites. *Polymer Degradation and Stability* **2018,** *156*, 22-31.
128. Chen, F.; Wang, G.; Li, W.; Yang, F., Glycolysis of Poly(ethylene terephthalate) over Mg–Al Mixed Oxides Catalysts Derived from Hydrotalcites. *Industrial & Engineering Chemistry Research* **2013,** *52* (2), 565-571.
129. Fuentes, C. A.; Gallegos, M. V.; García, J. R.; Sambeth, J.; Peluso, M. A., Catalytic Glycolysis of Poly(ethylene terephthalate) Using Zinc and Cobalt Oxides Recycled from Spent Batteries. *Waste and Biomass Valorization* **2020,** *11* (9), 4991-5001.
130. Wang, Q.; Geng, Y.; Lu, X.; Zhang, S., First-Row Transition Metal-Containing Ionic Liquids as Highly Active Catalysts for the Glycolysis of Poly(ethylene terephthalate) (PET). *ACS Sustainable Chemistry & Engineering* **2015,** *3* (2), 340-348.
131. Yue, Q. F.; Xiao, L. F.; Zhang, M. L.; Bai, X. F., The Glycolysis of Poly(ethylene terephthalate) Waste: Lewis Acidic Ionic Liquids as High Efficient Catalysts. *Polymers* **2013,** *5* (4), 1258-1271.

Chapter 2

Experimental

Chapter 2:

2.1 Introduction

This thesis has been drafted as thesis by publication. Chapter three outlines the work completed for a collaborative publication where second authorship has been attained. Chapter four has been accepted and published as a first author manuscript. Chapter five and six are in manuscript format as first author awaiting submission/in review.

This chapter will briefly outline the characterisation techniques used. Techniques such as transmission electron microscopy (TEM), scanning electron microscopy (SEM), energy dispersive x-ray analysis (EDX), and x-ray photoelectron spectroscopy (XPS), x-ray diffraction (XRD), Fourier transform infrared spectroscopy (FTIR). Nuclear magnetic resonance (NMR) and Solid-state NMR (ssNMR) was used to identify the molecular structure of products that were obtained from reactions.

2.2 Electron Microscopy

Electron microscopy is a technique used to obtain high resolution images from atomic and micro level structures. It reveals information about the structural integrity and size of nanomaterials. The technique has applications in many areas such as materials science, biomedical sector and in industry for quality control. By comparing electron microscopy to optical microscopy, it is advantageous as the source of imaging radiation coming from electrons allows for better spatial resolution (picometers scale), whereas the optical microscopy uses photons which is around 200 nm. It also reveals information about the crystallinity, chemical composition, and electrical properties through electron microscopy. The two categories of electron microscopy are: Scanning electron microscopy (SEM) and Transmission electron microscopy (TEM)

Scanning electron microscopy (SEM) is an electron microscopy technique that obtains detailed images of particles with high spatial resolution. The sample being investigated is exposed to an electron beam with high energy that is scanned in a raster pattern across the sample revealing information about morphology, and topography.[1] SEM uses the scattering of

secondary and back scattered electrons. The electron beam is scanned along the surface of the sample. As soon as the electrons hit the sample, signals that are detected form an image of the surface of the sample.[2] In this work, SEM was carried out on a FEI Helios NanoLab 600i operating at 30 kV and 0.69 nA, with an attached EDX Oxford X-Max 80 detector.

Transmission electron microscopy (TEM) is a technique where a high energy beam of electrons passes through the sample and forms a 2D high resolution image of the nanomaterials. The technique reveals information of the nanomaterial's morphology eg, structure and size. The samples are deposited onto a TEM grid usually by drop casting where a few drops of the solution containing the sample containing the nanomaterial is added and left to dry. This technique requires controlled sample preparation to ensure that the TEM grid is not overloaded which would hinder the analysis as they would not be transparent enough for the electron beam to pass through without causing issues from inelastic scattering. The TEM grid is then clipped into the sample holder arm and then passed into the TEM under ultra-high vacuum and the samples can be observed once focused. TEM was used in this work to obtain high resolution images of nanoparticles, nanosheets to confirm their size and crystallinity. The microscope used in this work was a JEOL 2100 electron microscope at an operating voltage of 200 kV and FEI Titan TEM, at an operating voltage of 300 kV. The image J software was used to determine diameters of each individual nanoparticle and the mean diameter was calculated through excel. For each size distribution, approximately 200 particles were used. The graphs are fitted with normal distribution.

2.3 Energy Dispersive X-Ray Analysis (EDX)

Energy dispersive x-ray analysis (EDX) is a characterisation tool where x-rays are used to identify the chemical composition of nanomaterials. This technique was employed to determine the metal composition and distribution throughout samples. This was completed by obtaining elemental mapping, line scans and point scans. Energy-dispersive X-ray (EDX) analysis was carried out on an FEI Titan TEM, at an operating voltage of 300 kV. The principle of EDX analysis is when x-rays are generated from the sample through the electron beam. When they are generated, they display characteristics of certain elements which are present in the sample. The results give quite accurate concentrations of the elements. EDX detector can be attached to either a TEM or SEM. There are three main components in an EDX set up, the x-ray detector, voltage processor and the PC system.[3] The x- ray is located to avoid x-rays emitting from the sample. The x-rays coming from the sample are identified by the x-ray detector and when they pass into the detector an x-ray forms a current that then converts to a voltage pulse which is dependent on the energy from the x-ray. From this, it's possible to obtain quantitative data, which represents the elemental analysis of the sample.

2.4 X-ray photoelectron spectroscopy (XPS)

X-ray photoelectron spectroscopy (XPS) is a surface sensitive technique that provides quantitative and qualitative information on the surface chemistry of a material. It measures the kinetic energy of electrons which are released from the sample after they are exposed to x-rays. These x-rays are usually from either a Al Kα or Mg Kα source. Kinetic energy of photoelectrons are converted to binding energy (BE). The intensity of the electrons that are produced from the surface of the sample the spectra can be obtained for the sample.[4] When running a sample on the XPS, the first step is to scan the whole area from 0-1400 eV, this is called a survey spectrum. It detects all elements present in the sample. Next, the core levels are scanned, eg, C 1s, O 1s, N s and any other elements that are believed to be in the sample that is under investigation. It is worth noting that when the spectra are obtained there needs to be a carbon calibration, in this case the C 1s refence peak was at 284.8 eV.

In order for the XPS to operate, the system needs to be under ultra-high vacuum to measure the maximum number of electrons present in the sample.[4] It calculates an approximation of elemental composition, identifies the chemical bonds present and the oxidation of the elements of the sample under investigation. The electron kinetic energy determines the elements present in the sample. A change in the binding energies of a sample can indicate the change in oxidation state of an element. Elements with a high oxidation state have higher binding energies and the ejected electrons have lower kinetic energies. These shifts are called chemical shifts, and they happen when core level of atoms change their environment. All XPS data was acquired using a KRATOS AXIS 165 monochromatized X-ray photoelectron spectrometer equipped with an Al Kα (hv = 1486.6 eV) X-ray source. Spectra were collected at a take-off angle of 90°.

2.5 X-ray diffraction (XRD)

X-ray diffraction is a characterisation tool used to analyse and determine the crystal structure of a material. XRD works by sending a beam of x-rays directly at the sample, the resulting elastic scattering of x-rays is due to the atomic arrangements of the material in the sample being identified at different angles. When the number of x-rays that are diffracted at each angle are counted the Braggs law equation $n\lambda = 2d \sin \theta$, can be applied to find the interplanar distance (d) of a crystal. Where λ is the wavelength of the x-rays and θ is the angle that the diffracted x-rays are found. An advantage of using XRD is that when the diffraction pattern is found for a material, it can be compared to literature results which are compiled in the library database from the XRD software which helps in determining the phase and composition of the sample. X-ray diffraction (XRD) was carried out using a Philips X'pert Pro MPD, equipped with a Panalytical Empyrean Cu X-ray tube and a Philips X'celerator detector.

2.6 Dynamic Light Scattering (DLS)

Dynamic light scattering (DLS) is a technique to study diffusion behaviour of materials in solutions whereby using the diffusion coefficient and the hydrodynamic radii which is calculated from it all depend on the size of the molecule in question.[5] DLS was used in this work to determine the nanoparticle size and to determine if the nanoparticles were agglomerated in colloidal solutions. It works by measuring the hydrodynamic size of particles, by which light scattering from a laser that is able to pass through the nanoparticles solution and analyses the scattered light intensity as a function of time. It was the Brownian motion theory which explained the molecular motion of particles, stating that particles were exposed to random forces because of constant collision with solvents which resulted in spontaneous movement of the particles and that the mean squared displacement of the particles was because of Brownian motion was proportional to time.[5] DLS measurements were conducted on a Malvern Panalytical Zetasizer Nano ZSP using non-invasive backscattering (NIBS) technology. The scattering angle was set at 173° and the measurement temperature was set to 20 °C. Samples were dispersed in ethanol and sonicated to give a stable solution prior to analysis

2.7 Fourier-transform infrared spectroscopy (FTIR)

Fourier-transform infrared spectroscopy (FTIR) is a fast, non-destructive technique used to retrieve structural information regarding a sample which is being examined. The process involves infrared radiation in the region of 4000-450 cm^{-1}. The structural determination is possible as radiation is absorbed by interatomic bonds in compounds. The FTIR process identifies functional groups present in the sample. Certain chemical bonds appear at a particular wavelength on the FTIR spectrum as the absorb different intensities and frequencies and therefore the peaks which appear at a particular wavelength can be assigned to bonds with the compound. There are several different movements a bond can vibrate, there can be more than one IR frequency for a bond. An IR spectrum is divided into two sections, 4000-2000 cm^{-1} where you find only a small number of peaks therefore easy to interpret

(usually O-H and CH_2 peaks) and then 2000-450 cm^{-1} which is called the fingerprint region with a large number of peaks with can be difficult to distinguish between. The FTIR used in the work was Fourier transform infrared (FTIR) spectra were recorded on a Perkin Elmer Spectrum Two FT-IR Spectrometer operating in the range of 4000-450 cm^{-1} with a resolution of 4 cm^{-1} and spectra were averaged from 20 scans.

2.8 Thermo-gravimetric analysis (TGA)

Thermogravimetric analysis is the technique used for monitoring the mass loss of a sample as a function of temperature over time. The technique produces quantitative and qualitative data and is carried out by placing the sample in a pan which hangs from a balance and enclosed inside a chamber. As the analysis proceeds, the weight loss is measured as a function of the temperature vs time. The technique is commonly used to measure decomposition of samples or evolution of water from porous materials. TGA was carried out in air at a heating rate of 10°C /min from 25°C to 600°C.

2.9 Nuclear magnetic resonance (NMR)

Nuclear magnetic resonance (NMR) is a sensitive characterisation tool used to reveal the molecular structure of a sample at atomic level.[6] NMR can also determine changes in the phase of a sample. Experimentally, NMR utilises the behaviour of nuclei when they interact with a magnetic field. It maps out the chemical state of a nuclei and from this information can be obtained. The principle of NMR spectroscopy is that all nucleus are charged and most display multiple spins. When an external magnetic field is applied it's possible to form energy transfer between the initial energy to higher energy level. The energy transfer occurs at a wavelength that corresponds to radio frequencies and when the spin returns to its initial level, energy is emitted at the same frequency. The signal that matches this transfer is measured in many ways and processed in order to yield an NMR spectrum for the nucleus concerned. The most common magnetic nuclei are ^{1}H, ^{13}C and ^{29}Si. All nuclear magnetic resonance (NMR) samples in this work were run in deuterated chloroform ($CDCl_3$) or dimethyl

sulfoxide (d6-DMSO). ^{1}H NMR spectra were recorded on Bruker Avance III 300 NMR spectrometers, in proton-coupled mode using tetramethylsilane (TMS) as the internal standard.

2.10 Solid state Nuclear magnetic resonance (ssNMR)

Solid state NMR was used for catalyst analysis. It is a technique used evaluate a solid sample at atomic level to identify and determine the chemical structure, 3D structure and dynamics. When compared to liquid state NMR spectroscopy the nuclear spin interactions and the effects of the magnetic fields and radiofrequency pulses were the same. Due to the orientation dependence of the nuclear spin interactions of the solid state, most of the high-resolution solid-state NMR is measured using magic angle spinning (MAS). This effects the type of radiofrequency pulse sequences needed to obtain the structural information of the sample and also reveals information of the dynamics.[7] Therefore, because of this solid state NMR can extract information which can be used to obtain quantitative data of the sample, this is not possible in by liquid state NMR.

The analysis was completed for ^{1}H and ^{13}C CPMAS NMR experiments and were recorded at B_0 = 14.09 T (ν_0 = 600 MHz for ^{1}H) with a wide-bore Varian magnet equipped with a 3.2 mm triple-resonance HXY magic angle spinning (MAS) probe, operated in double-resonance. The samples were spun at a MAS rate, ν_R = 14 kHz. The initial $\pi/2$ pulse lasted 2.17 µs corresponding to a rf of ~ 115 KHz and was followed by a CP contact time equal to 1 ms. Analysis as also carried out on ^{1}H and ^{13}C NMR experiments which were recorded at B_0 = 22.3 T (ν_0 = 950 MHz for ^{1}H) with a narrow-bore magnet equipped with a Bruker AVANCE III console, using a 1.3 mm triple resonance HXY magic angle spinning (MAS) probe operated in double resonance mode. ^{1}H MAS NMR spectra were acquired by averaging 32 transients separated by a recycle interval of 12 s, using the DEPTH pulse sequence for probe background suppression,[4] with $\nu_1 \approx$ 80 kHz. The samples were spun at n_R = 50 kHz. For all solid-state NMR experiments, rotors were packed in air. ^{1}H and ^{13}C chemical shifts were referenced using a solid sample of adamantane (^{1}H δ_{iso} = 1.85 ppm and ^{13}C δ_{iso} = 29.47 and 38.52 ppm). Data processing was carried out using Bruker TopSpin (version 4.1.3) and ssNake (version 1.3).

2.11 Synthesis of Surfactant Assisted Pd Nanosheets

Pd NSs were synthesized by adding 5 ml of a 0.025 M C_{22}-QA (Br^-) solution in a glass sample vial along with 0.8 ml of 10 mM H_2PdCl_4 aqueous solution. The mixture was left to stir until ion exchange had occurred (15 min). 1 ml of a freshly prepared 0.3 M aqueous solution of $_L$-ascorbic acid (AA) was injected slowly into the solution. The reaction solution was placed on an ice bath and left undisturbed at 0° C with reaction times between 1-6 h. Once the reaction had reduced, the product was sonicated with toluene and collected by centrifugation and washed with ethanol. This purification procedure was repeated three times and the NSs were re-dispersed in ethanol.

PdAu NSs were synthesized using the same procedure as the Pd NSs but with co-addition of the Pd and Au precursors with varying molar ratios.

2.12 References

1. Akhtar, K.; Khan, S. A.; Khan, S. B.; Asiri, A. M., Scanning Electron Microscopy: Principle and Applications in Nanomaterials Characterization. In *Handbook of Materials Characterization*, Sharma, S. K., Ed. Springer International Publishing: Cham, 2018; pp 113-145.
2. Yan, Y., 7 - Tribology and tribocorrosion testing and analysis of metallic biomaterials. In *Metals for Biomedical Devices (Second Edition)*, Niinomi, M., Ed. Woodhead Publishing: 2019; pp 213-234.
3. Raval, N.; Maheshwari, R.; Kalyane, D.; Youngren-Ortiz, S. R.; Chougule, M. B.; Tekade, R. K., Chapter 10 - Importance of Physicochemical Characterization of Nanoparticles in Pharmaceutical Product Development. In *Basic Fundamentals of Drug Delivery*, Tekade, R. K., Ed. Academic Press: 2019; pp 369-400.
4. Korin, E.; Froumin, N.; Cohen, S., Surface Analysis of Nanocomplexes by X-ray Photoelectron Spectroscopy (XPS). *ACS Biomaterials Science & Engineering* **2017,** *3* (6), 882-889.
5. Stetefeld, J.; McKenna, S. A.; Patel, T. R., Dynamic light scattering: a practical guide and applications in biomedical sciences. *Biophysical reviews* **2016,** *8* (4), 409-427.
6. Singh, M. K.; Singh, A., Chapter 14 - Nuclear magnetic resonance spectroscopy. In *Characterization of Polymers and Fibres*, Singh, M. K.; Singh, A., Eds. Woodhead Publishing: 2022; pp 321-339.
7. Reif, B.; Ashbrook, S. E.; Emsley, L.; Hong, M., Solid-state NMR spectroscopy. *Nature Reviews Methods Primers* **2021,** *1* (1), 2.

Chapter 3

Synthesis of Support Free Pd Nanoparticles for Heterogenous Catalysis

Chapter 3:

Synthesis of Support Free Pd Nanoparticles for Heterogeneous Catalysis

3.1 Introduction

Heterogeneous catalysis plays a vital role in modern day synthesis of chemicals and fuels. [1] Supported heterogeneous catalysts also allow the catalyst to be easily recovered after the reaction and recycled in sequential reactions, which is particularly attractive for expensive noble metal catalysts. Supported metal catalysts are extensively used in industry for a variety of organic reactions such as oxidation and hydrogenation.[2-5] Generally, materials for catalyst supports possess high surface area, good chemical and mechanical stability and are capable of dispersing the active catalyst e.g. metal nanoparticles (NPs) over the surface. Typical catalyst support materials include carbon-based supports such as activated carbon and various oxide supports e.g. SiO_2, Al_2O_3 and TiO_2.[6-9] The support material is more than just an anchor to enhance stability of the metal material, and the two components can interact giving rise to metal-support interactions (MSI). [10-11] The MSI can give rise to charge transfer from or to the metal NP, support-induced restructuring of metal NPs and formation of specific metal–support interfaces[12]. Tuning the nature of the MSI has been used to alter catalytic behaviour. For example, Magrez *et al.*[13] reported a simple and efficient catalyst activation process for catalytic chemical vapour deposition of carbon nanotubes. They demonstrated that altering the acidity or basicity of the Al_2O_3 support was found to have an impact on the activity and selectivity of the catalyst for the polymerisation of unsaturated hydrocarbons.

While there are many advantages to the use of a support, they can hinder the catalyst activity and limit the accessible surface area of metal NP due to the interaction and immobilised on the a support.[14] The use of unsupported NPs *i.e.* solubilised NPs in solution has attracted interest in recent years as several NP properties e.g. size, shape and chemical composition can be easily tailored. The application of NPs solubilised in solution for chemical synthesis reactions, such as those used in the

pharmaceutical industry, holds significant potential for application with flow through synthesis where the use of conventional commercial carbon support material is not suitable. [15-16]

In the absence of a solid support, metal NP catalysts are stabilised by organic ligands. A wide variety of surface-immobilised ligands can be used for NP stabilisation such as small organic molecules, polymers, dendrites and even biomolecules.[17-19] Surface capping ligands can play an important role in the catalyst selectivity by potentially directing a reaction pathway.[20-21] Capping ligands influence catalytic properties of NPs through a variety of mechanisms such as steric or passivation effects, charge transfer occurring at the organic-metal interface, competitive adsorption or molecular recognition.[22] Controlling the surface environment of heterogeneous catalyst to enhance selectivity has been most well developed for self-assembled monolayer (SAM)-modified NPs, in particular thiol stabilized metal NPs.[23] Densely passivated NP surfaces with strongly bound head groups such as thiols, and well-solvated tail groups will result in high colloidal stability. However, a strongly passivated NP will also have poor catalytic activity due to limited surface accessibility of the reactants. Therefore, the use of more weakly bound surface ligands offer potential for improved activity. Polymer ligands are commonly used stabilisers in colloidal synthesis and typically have a weaker affinity for the NP surface than small ligand stabilisers. The application of polymer stabilised NPs as solubilised catalysts has been less well explored. Provided NP stability is maintained throughout the catalytic reaction to prevent NP aggregation, the use polymer-protected NPs is attractive due to the many water-soluble polymers available. Due to its high stabilising ability, nontoxicity and good solubility in many polar solvents, polyvinylpyrrolidone (PVP) is one of the most and widely studied capping agents in the synthesis of metal NPs.[24-26]

This chapter will focus on the synthesis of Pd NPs for application in support-free heterogeneous catalysts for reductive amination. Reductive amination is the conversion of an aldehyde or a ketone into an amine via an intermediate imine.[27] It is a versatile chemical reaction, particularly useful to synthesise complex amines, and the majority of amines prepared in the pharmaceutical industry are

made by this method. Reductive amination is often proposed as a greener way of constructing amines as it avoids having to use potentially toxic reagents like alkyl halides and sulphonates used in traditional synthesis reactions of amines with alkylating reagents. The reaction requires a reducing agent *e.g.* hydrogen and usually takes place in the present of a catalyst.[28]

The impact of ligands and the role of steric and interfacial electronic effects on the selectivity behavior of Pd NPs stabilised with different surface capping ligands is evaluated to identify the best catalytic system. This work was in collaboration with Dr. Gerard McGlacken and Dr. David Jones who performed the organic synthesis, Dr. Andreas Larsson and Dr. Mikael Rasander who conducted modelling experiments for the project. The organic synthesis and computational aspects of this study are not reported in this chapter however the publication titled "A unified approach to the synthesis of amines through a highly selective and broadly applicable imine reduction using modified Pd-nanoparticles" can be found at: https://doi.org/10.26434/chemrxiv-2022-q72lk

3.2 Experimental

Palladium (II) chloride (H_2PdCl_4) (99.9%), potassium tetrachloropalladate (K_2PdCl_4) (98%) sodium tetrachloropalladate ($NaPdCl_4$) (98%) polyvinylpyrrolidone (PVP) (Mw= 10,000 k, 40,000 k, 55,000 k & 360,000 k), polyvinyl alcohol (PVA) (Mw= 10,000 k), polyallylamine (PAA) (20% wt solution in water), polyacrylonitrile (PAN), polyacrylic acid (PAA), polymethyl methacrylate (PMMA) (Mw= 15,000 k), N-methyl-2-pyyrolidone (NMP), $NaBH_4$ (99.9%), 16-mercaptohexadecanoic acid (90%), dodecanethiol (DDT)(99%), dodecylamine (DDA) (99%), tetraoctylammonium bromide (TOABr) (98%) ethanol (99%), methanol (99%), acetone (99%) hydrochloric acid (35%), phosphoric acid (H_3PO_4), tetrahydrofuran (THF) (99.9%), toluene (99%) dichloromethane (DCM) (99%) and commercial Pd/C were all purchased from Sigma Aldrich.

Synthesis of mercaptohexadecanoic acid stabilised Pd NPs

0.02 g of K_2PdCl_4 was dissolved in 2 ml of water and 10 ml of solvent THF. To the red coloured solution, 250 µl of H_3PO_4 (85 %) and 0.009 g of 16-mercaptohexadecanoic acid was added. The colour of the solutions changed from red to orange-yellow. The solution was stirred for 5 min at room temperature. The temperature was then adjusted to 0° C using an ice bath and stirred for a further 5 min. A freshly prepared solution of $NaBH_4$, prepared by adding 0.0232 g of $NaBH_4$ to 1 ml water, was rapidly added to the solution. The solution turned black instantaneously, indicating the formation of NPs. Stirring was continued at 0 °C for 5 min, followed by a stirring at room temperature for a further 5 min. The THF was evaporated via rotary evaporator. The NPs were briefly sonicated and collected by centrifugation with DCM and H_2O (10 ml) which was repeated three times before being redispersed in EtOH. Methanol and acetone were also screened as solvents for NP synthesis but were not effective due to poor solubility of the Pd precursor.

Synthesis of dodecanethiol (DDT) stabilised Pd NPs

Two synthesis method was used for the preparation of decanethiol (DDT) stabilised NPs, a two-pase synthesis and a single-phase synthesis. For the two phase synthesis, 0.25 g of K_2PdCl_4 was dissolved in water and transferred into the toluene phase via the addition of 50 ml water and 0.625 g of tetraoctylammonium bromide (TOABr), which is indicated by the colourless toluene layer becoming deep red. The aqueous layer is removed using a separating funnel. 94 µl of DDT was added to toluene solution under vigorous stirring, giving a 1:2 thiol/Pd molar ratio. The solution was cooled in an ice bath for 45 min. A freshly prepared solution of 0.30 g of $NaBH_4$ in 5 ml of water was added to the solution and stirred at 0 °C for 10 min. The solution was left stirring for a further 3 h at room temperature. The solution was transferred into a separating funnel and the water layer was discarded. The majority of the toluene was removed via rotary evaporation leaving ~15 ml. The remaining solution was washed with EtOH three times and collected by centrifugation. The cleaning procedure was repeated three times and the NPs were redispersed in

toluene. The same procedure as described above was used for the preparation of DDT stabilised NPs with a thiol:Pd molar ratio of 1:1 by using 0.125 g of K_2PdCl_4 to 94 µl of DDT in the reaction. For the reduction step, 0.15 g of $NaBH_4$ was dissolved in 2.5ml water. The NP separation and purification procedures were the same as described above.

A one phase synthesis of DDT capped Pd NP was carried out taking 0.02 g of Na_2PdCl_4 dissolved in 2ml H_2O and 18 ml of THF. 250 µl of H_3PO_4 (85%) was added along with 7.5 µl DDT (1:2 thiol/Pd ratio). The solution was stirred at room temperature for 5 min. A freshly prepared solution of 1 ml H_2O and 23.2 mg of $NaBH_4$ was added rapidly to the solution and stirred for 10 min. The Pd NP solution was washed with water, methanol and acetone (10 ml x 3 for each). Sonication and centrifuge occurred in between each wash cycle. The NPs were redispersed in THF.

Synthesis of dodecylamine (DDA) stabilised Pd NPs

A one phase synthesis of DDA stabilised NP was carried out taking 0.02 g of Na_2PdCl_4 dissolved in 2 ml H_2O and 18 ml THF. 250 µl H_3PO_4 was added along with 0.0057 g of DDA (1:2 amine/Pd ratio). The solution was stirred for 5 min. A freshly prepared mixture of 0.0232 g $NaBH_4$ in 1 ml of H_2O was added rapidly to the solution and stirred for 10 min. The Pd NP solution was washed with water, methanol and acetone (10 ml x 3 for each). Sonication and centrifugation were carried out in between each wash cycle. The NPs were redispersed in THF.

For the two-phase synthesis, 0.23 g of Na_2PdCl_4 was dissolved in 5 ml of water. Separately, 0.825 g of TOABr was dissolved in 35 ml of toluene. The two solutions were combined and stirred vigorously for 15 min. 1.705 g of DDA was added to the solution given an amine:Pd ratio of 12:1 and rapidly stirred for 45 min. The organic layer turned from red to light yellow and the aqueous layer became cloudy. A freshly prepared solution of 0.435 g of $NaBH_4$ in 5 ml of water was added rapidly and the solution was stirred for 90 min, during which time the aqueous layer turned clear. The aqueous layer was removed via separating funnel and the toluene was removed via rotary evaporation leaving ~15 ml of solvent. The remaining solution was transferred to centrifuge tubes and washed with ethanol three times and

and then redispersed in toluene.

Synthesis of Polymer Stabilised Pd NPs

All polymer stabilised NPs were prepared using a Pd precursor stock solution. A 2 mM Pd stock solution was prepared by dissolving 17.8 mg $PdCl_2$ in 1 ml of a 0.2 M HCl and 49 ml distilled water. Pd NPs were prepared using PVP, PMMA, PAN, and PAA. In a typical procedure, a mixture of 15 ml of H_2PdCl_4 (2mM), 26 mg of PVP (molecular weight ~40,000), 24.5 ml of water and 10.5 ml of EtOH were added to a 100 ml round bottom flask with a stir bar. The molar ratio of Pd:PVP was 1:7.8. This mixture was heated to reflux and aged for 3 h under air. The synthesis was repeated using PVP of different molecular weights, 10,000 and 360,000. The synthesis was also conducted with Pd:PVP molar ratio of 1:1 and 1:0.3. The synthesis of Pd NPs stabilised by PVA, PAN, PMMA was carried out using the same procedure but substituting for the relevant polymer. The synthesis of PAA protected Pd NPs was carried out using 15 ml of H_2PdCl_4 (2 mM), 0.13 g of PAA, 24.5 ml of water and 10.5 ml of EtOH were added into a 100 ml round bottom flask with a stir bar. The solution was heated to reflux for 3h under air. A freshly prepared solution of 0.0056 g of $NaBH_4$ in 0.5 ml of water was added for the reduction of Pd.

Synthesis of PVP Stabilised Icosahedra Pd NPs

30 µg PVP (molecular weight 40, 000) was dissolved in 2 ml ethylene glycol and heated in 160°C for 20 min. 1 ml of H_2PdCl_4 (50 mM) was added rapidly. 1.5 ml of a 0.2 M HCl solution was added, and the solution was left to stir at 160 °C for 3 h. The reaction mixture was immersed in an ice bath for crash cooling to occur. The NPs were washed with acetone and water three times and collected by centrifugation. The NPs were redispersed in water.

Reductive Amination reaction

To a stirred solution of the imine (0.5 mmol) in EtOH (2.5 mL) in Schlenk tube, equipped with magnetic stirring bar aqueous Pd-PVP solution (2.5 mL, 0.3 mol%) was added . The Schlenk tube was then sealed with a septum and was subjected three vacuum-refill cycles with hydrogen gas from a

balloon. The contents of the reaction flask were then warmed to 35 °C with the aid of an oil bath. The resulting solution/suspension was vigorously stirred at this temperature for 22 hours, after which time the imine product was typically fully consumed. The crude reaction mixture was then partitioned between dichloromethane (20 mL) and water (3 mL) and separated using a separatory funnel. The aqueous phase was further extracted with dichloromethane (2 x 10 mL) and the combined organic phases were dried over magnesium sulfate, filtered and concentrated *in vacuo* before purification by column chromatography to afford the product as an off-white solid (0.46 mmol).

Material characterisation

X-ray Photoelectron Spectroscopy (XPS) spectra were acquired using a KRATOS AXIS 165 monochromatized X-ray photoelectron spectrometer equipped with an Al Kα (hv = 1486.6 eV) X-ray source. Spectra were collected at a take-off angle of 90° and all spectra were referenced to the C 1s peak at 284.8 eV. Pd 3d core levels were fit with a Shirley backgrounds and Gaussian-Lorentzian profiles. To achieve best fit, the peak positions were allowed to float with a variable FWHM ranging from 1-1.5 for metallic Pd(0) and 1.2-1.7 for oxidised Pd components. Peaks shifted to binding energies (BEs) greater than +1.5 eV of the elemental Pd(0) peak were assigned to bulk oxide phases PdO. Transmission electron microscopy (TEM) analysis was performed using a JEOL 2100 electron microscope at an operating voltage of 200 kV and high-resolution TEM. Fourier transform infrared (FTIR) spectra were recorded on a Perkin Elmer Spectrum Two FT-IR Spectrometer operating in the range of 4000-450 cm^{-1} with a resolution of 4 cm^{-1} and spectra were averaged from 20 scans. Nuclear magnetic resonance (NMR) samples were run in deuterated chloroform ($CDCl_3$). 1H NMR spectra were recorded on a Bruker Avance III 300 NMR spectrometers, in proton-coupled mode using tetramethylsilane (TMS) as the internal standard.

3.3 Results and Discussion

3.3.1 Synthesis of Colloidal Nanoparticles as Support Free Catalysts

Small organic ligands such as thiols, amines and phosphines are commonly used as stabilising ligands for colloidal synthesis. Due to the strong Pd–thiol interaction, the synthesis of Pd NPs with thiolated ligands results in NPs which typically have excellent colloidal stability. To achieve successful NP formation, it is imperative that the metal precursor and the stabilising ligand are both soluble in the synthesis solvent. Metal NP precursors are usually simple salts and therefore water-soluble, while common stabilising ligands are long alkyl chain surfactants so are usually soluble in non-polar solvents. A phase transfer catalyst (PTC) is typically used to achieve solubility of both metal salt and the capping ligand in the organic phase. While effective, PTCs are often used at high concentrations (molar excess)

and so require lengthy cleaning procedures to ensure their removal. An alternative approach to a two-phase synthesis with a PTC is the use of a one-phase synthesis where both the metal precursor and ligand are dissolved in the same solvent. A one-phase synthesis methodology has the clear advantage of not requiring a PTC, however an appropriate solvent system to achieve solubility of all regents needs to be first identified. Figure 1 compares the reaction scheme for the one phase and two-phase synthesis methodologies.

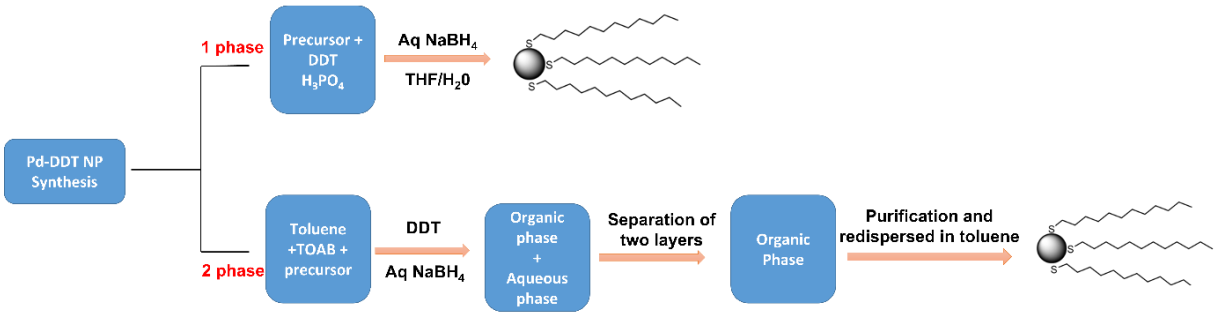

Figure 1: Reaction scheme of one phase vs two phase for the synthesis of DDT stabilised Pd nanoparticles

Thiol stabilised Pd NPs were prepared using a conventional two-phase synthesis with a PTC, trioctyl ammonium bromide, and a one-phase solvent system. A mixture of toluene and water in ratio of 10:1 for two phase method and THF:water in a ratio of 9:1 was determined to be a suitable solvent system for one phase . Figure 2 (a) and (b) shows the TEM image of DDT-stabilised Pd NPs prepared by a two-phase synthesis and one phase synthesis, respectively. Both synthesis methods produced well-defined, small diameter NPs. The mean diameter of the Pd NPs prepared by the conventional two-phase synthesis was 1.9 nm. The mean diameter of NPs prepared by the one-phase was 2.7 nm and was slightly less monodisperse. The molar ratio of Pd:thiol was altered to 1:1 for the two- phase synthesis during the reaction optimisation process, and it was observed that the NPs formed quickly aggregated. When using a 1:2 Pd:thiol molar ratio the NPs were more monodispersed and had a higher stability as excess thiols were stabilising the Pd NPs.

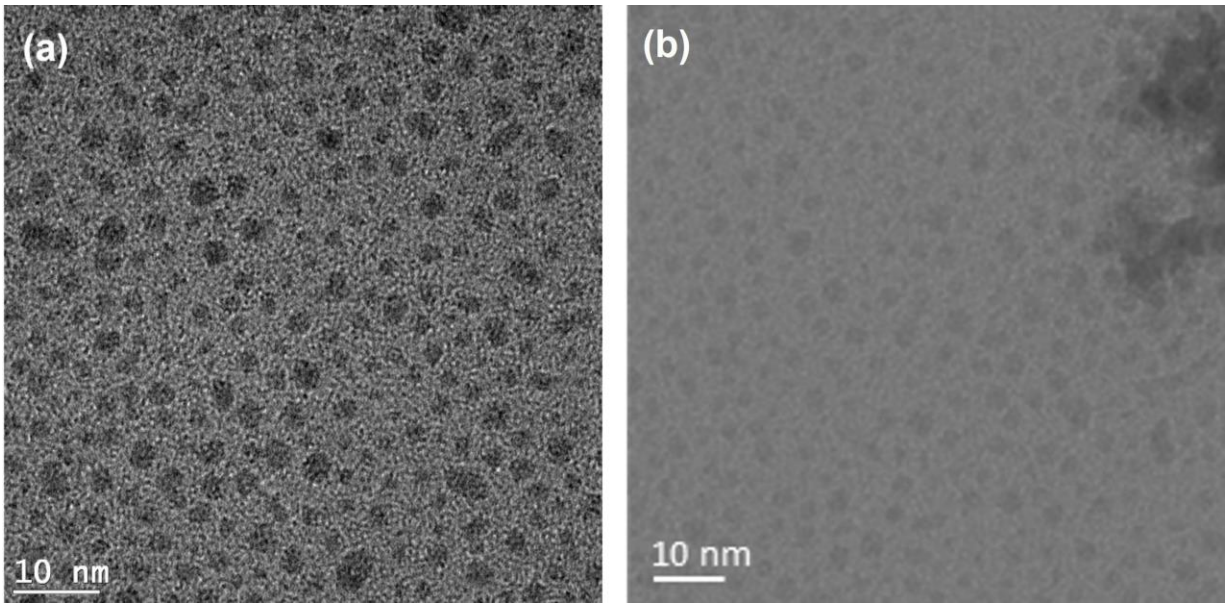

Figure 2: TEM images of DDT-stabilised Pd NPs prepared via (a) two phase and (b) one phase

Long chained alkane thiols *e.g.* dodecanethiol are most commonly used for NP synthesis and consequently the Pd NPs are soluble in non-polar solvent such as toluene and hexane and this limits their catalytic application to non-polar solvents. To enable NP solubility in polar and more green solvents *e.g.* water, polar functionalities must be incorporated into the thiol capping ligand. To achieve solubility in polar solvents, a bifunctional ligand, mercaptohexanoic acid (MHA) containing a terminal -SH group on one end and a carboxylic acid group on the other end was used. This ligand was used for the one-phase synthesis of MHA-capped Pd NPs. Acetone and methanol were evaluated as reaction solvents but resulted in precipitation of the metal after addition of the MHA. Water and THF in a ratio of 1:5 was successful for dissolving both precursor and ligand. Figure 3 shows a TEM image of the MHA-capped Pd NPs. The NPs had a mean diameter of 2 nm. The NPs were soluble in water and other polar solvents such as ethanol.

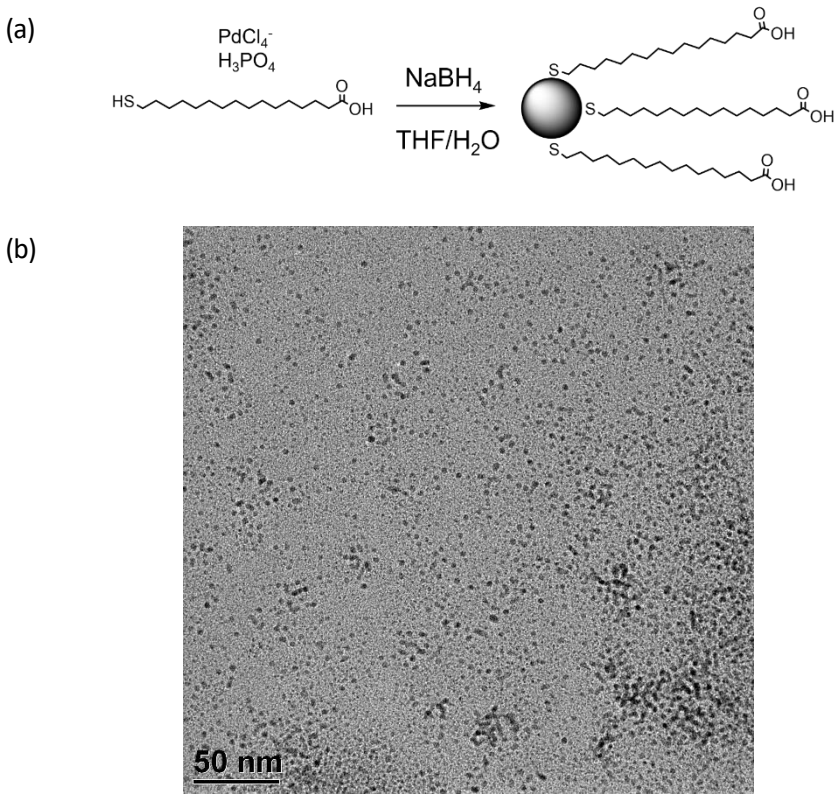

Figure 3: (a) Reaction scheme for the synthesis of mercaptohexanoic acid (MHA) stabilised Pd NPs, (b) TEM image of the MHA-capped Pd NPs.

Thiol capping ligands are highly effective for stabilising Pd NPs due to the high binding affinity of thiol functional groups to the Pd surface; however, thiols are also well-known to deactivate catalytic surfaces through strong coordination to catalytically active sites. Therefore, we synthesised Pd NPs with weaker binding amine ligands to compare their stability and catalytic activity. Similar to the DDT- stabilised Pd NPs, the DDA-Pd NPs were synthesised using both two phase and one phase methods. It was observed that the two-phase method produced more well-defined and monodisperse NPs. Figure 4(a) shows a TEM image of the well-defined DDA Pd NPs via two phase with the corresponding size distribution profile in the inset showing a mean diameter of 2.5 nm. The mean diameter is similar to previous reported DDA Pd NPs prepared using a two-phase synthesis.[29] Figure 4(b) shows the DDA-Pd NPs produced via the one phase method. The NPs are not as well defined and dispersed as the NPs produced by the two-phase method. The size distribution profile in the inset shows the mean diameter

of 2.5 nm which was similar to the diameter obtained in a two-phase NP synthesis. It was observed that the shelf life of the DDA-Pd NPs was shorter than the DDT-Pd nanoparticles, as they aggregated after 2 months. This is most likely due to the thiol-Pd interaction being stronger than that of amine-Pd, thereby resulting in NP agglomeration.

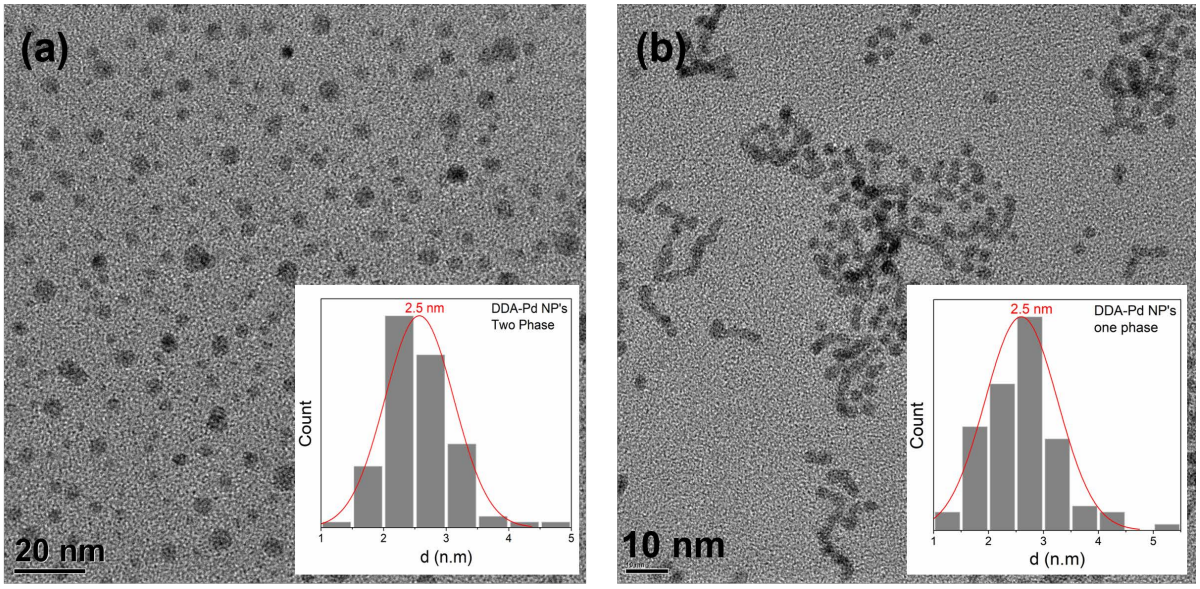

Figure 4: TEM images of DDA-Pd NPs with corresponding size distributions for (a) two phase and (b) one phase methods.

3.3.2 Synthesis of Polymer Stabilised Pd Nanoparticles as Support Free Catalysts

Pd NPs stabilised with numerous polymer capping ligands were synthesised to evaluate the effect on NP size and morphology. Figure 5 illustrates the polymers used, specifically polyvinylpyrrolidone (PVP), polyvinyl alcohol (PVA), polyacrylic acid (PAA), poly acrylonitrile (PAN), polyallylamine (PAH), poly (methyl methacrylate) (PMMA) and N-methyl-2-pyrrolidone (NMP). Polymer ligands typically have a weaker binding affinity for the NP surface, while their large size provides an effective steric barrier against NP aggregation. Due to its high stabilizing ability, nontoxicity and low cost, polyvinylpyrrolidone (PVP) is one of the most versatile and widely utilized capping agents and has been applied to the synthesis of all noble metal NPs.[24-26] As PVP contains a hydrophilic pyrrolidone ring and a hydrophobic alkyl backbone, it displays good solubility in both aqueous solutions and polar solvents

making it an attractive stabiliser for surface-modified heterogeneous catalysis. PVP prevents the aggregation of NPs by repulsive forces from the hydrophobic carbon chains that extend into solvents and interact with each other, this is known as the steric hinderance effect. Hirai *et al*.[30] demonstrated that the carbonyl groups of the PVP partly coordinate to the surface Pd atoms of the Pd nanoparticles. An important feature is the presence of carbonyl oxygen in PVP which are able to hydrogen bond solvent molecules.

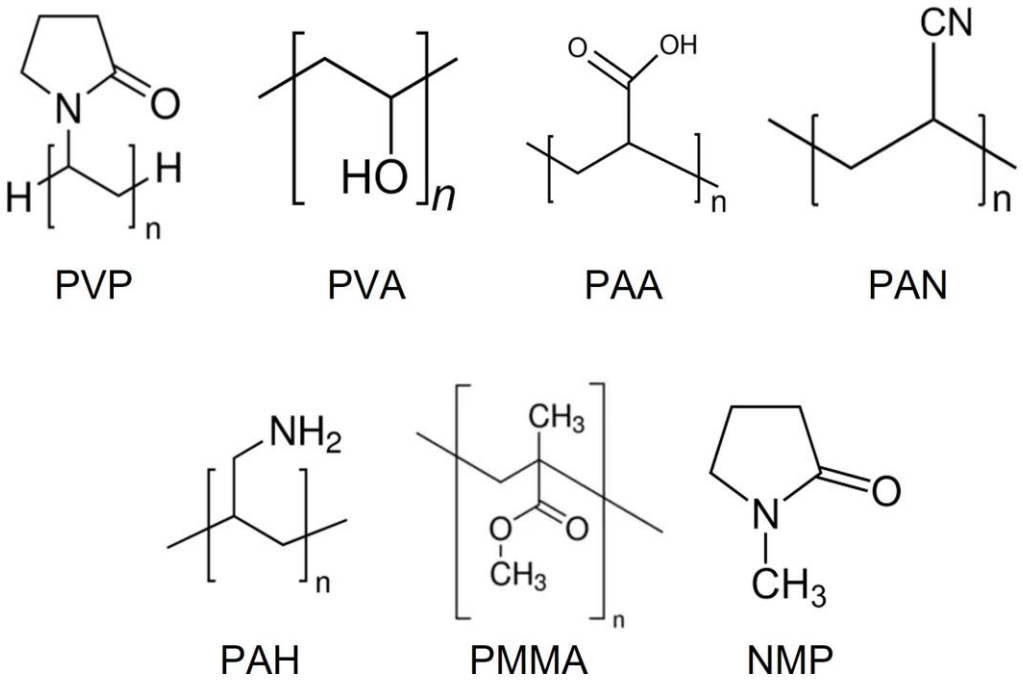

Figure 5: Polymers used to stabilize Pd NPs

Figure 6 (a) shows a TEM image of Pd NPs stabilized by PVP (Mw 40,000) synthesised using a Pd:PVP ratio of 1:7.8 (repeating unit). Figure 6 (b) shows the associated NP diameter distribution with a mean diameter of 2.1 nm. Dynamic light scattering (DLS) was used as a convenient method to verify the batch-to-batch reproducibility of PVP stabilised NP in solution. DLS is an easy method used to measure NP size, and also to evaluate their stability over time in solution. Unlike TEM, which measures the actual NP diameter DLS reports a hydrodynamic radius (R_H) of particles in a solution. The hydrodynamic radius is influenced by the thickness of the PVP coating and its interaction with the solvent. Well solvated ligands tend to have large hydrodynamic radius as the ligands extend into solution. A typical DLS spectrum can been seen in inset figure 6 revealing one peak which indicates

a single NP size. Capping ligands can significantly alter the chemical and physical properties of NPs.

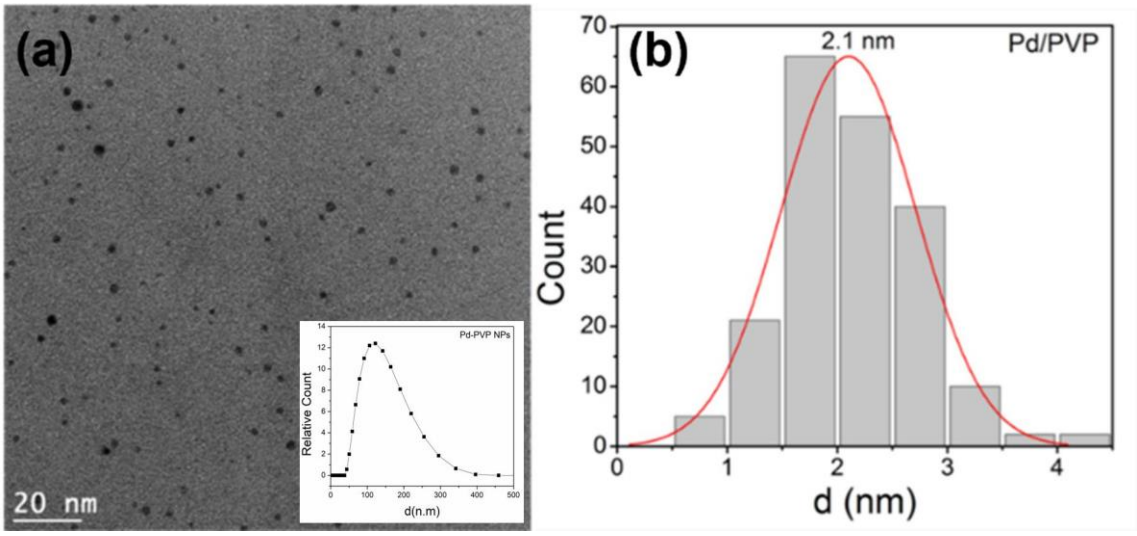

Figure 6: (a) TEM image and DLS size distribution of Pd NP stabilised by PVP and (b) corresponding size distribution profile from TEM.

Figure 7 shows TEM analysis and associated size distribution histograms of Pd NPs synthesized with a range of polymer capping ligands. PVA stabilised NPs, shown in Figure 7 (a) had a mean diameter of 5.2 nm. PAA produced well-defined Pd NPs with a mean diameter of 4.9 nm shown in Figure 7 (b), PAN stabilised NPs, shown in Figure 7(c) yielded a mixture of faceted NPs with a mean diameter of 14.7 nm. PAH was the only polymer ligand that did not undergo reduction by the ethanol solvent, which was attributed to the formation of a Pd:amine complex. Therefore, $NaBH_4$ was added to reduce the Pd precursor. The PAH-Pd NPs shown in figure 7(d) had a mean diameter of 1.9 nm. PMMA shown in Figure 7 (e) produced aggregated NPs attributed to the weak passivating ability of the ester group. PVP was replaced with the solvent NMP, to evaluate the role of a lactam ring in the absence of the polymer backbone. NMP formed poorly defined NPs as expected but could still sufficiently stabilise Pd NPs seen in fig 7 (f).

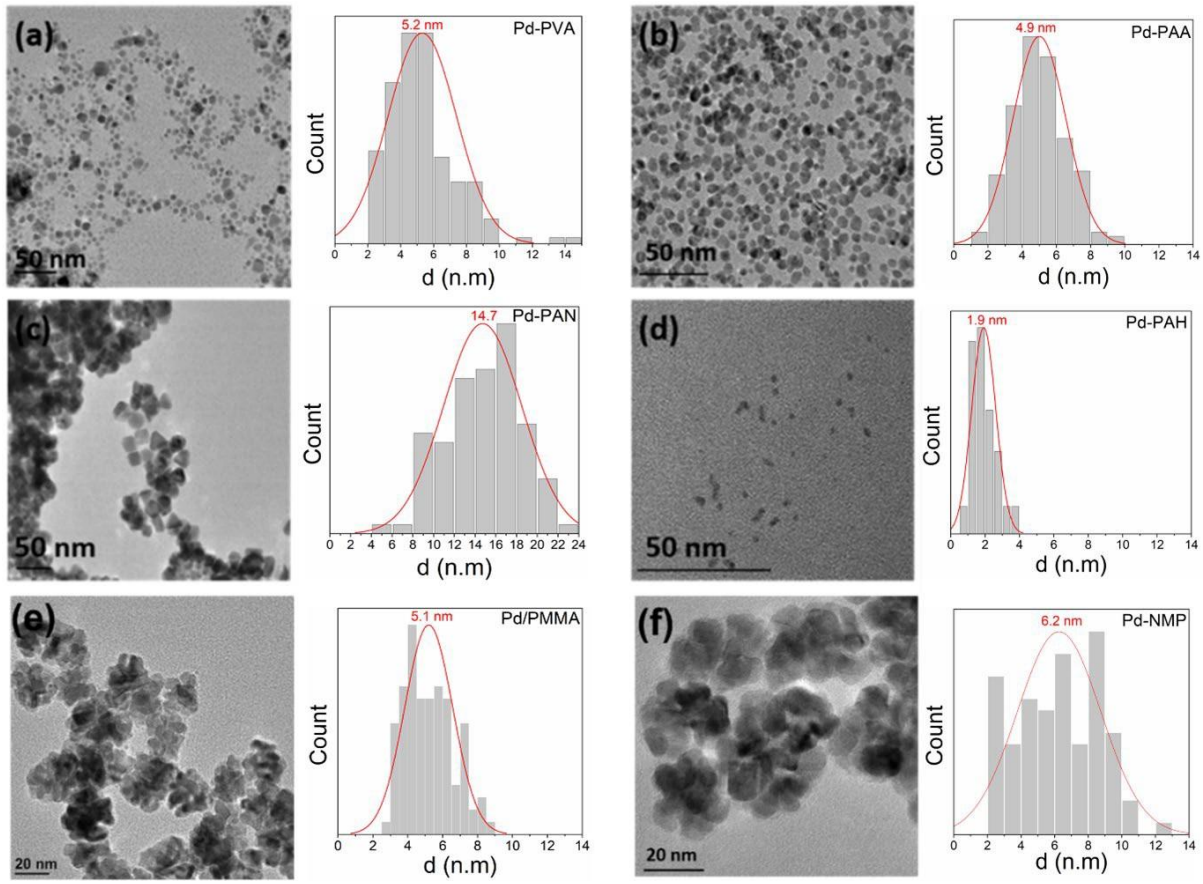

Figure 7: TEM images and associated size distribution analysis of Pd NPs stabilised with (a) PVA, (b) PAA, (c) PAN, (d) PAH, (e) PMMA and (f) NMP.

3.3.3 Catalytic Evaluation of colloidal Nanoparticles in Reductive Amination

Reductive amination is a methodology for the synthesis of amines from aldehydes or ketones. The reaction takes place in two parts. The first is the nucleophilic addition of the carbonyl group to form an imine, followed by reduction of the imine to an amine using a reducing agent. The imine is often formed and reduced *in situ* but in this catalytic study the imine was pre-formed and isolated, which was reduced to the secondary amine using molecular H_2 in the presence of the Pd NP catalysts, as shown in Figure 8. The desired product is the formation of a 2° amine but undesired products including over-reduction to the aniline, aldehyde and alcohol formation can also occur. The ligand-stabilised *i.e.* alkanethiol and alkylamine capped NPs and polymer stabilised NPs were screened in the reductive

amination reaction to identify the most suitable catalyst system. The hydrogenation of an imine was conducted in aqueous ethanol solvent at 35°C under 1 atm of H_2 gas.

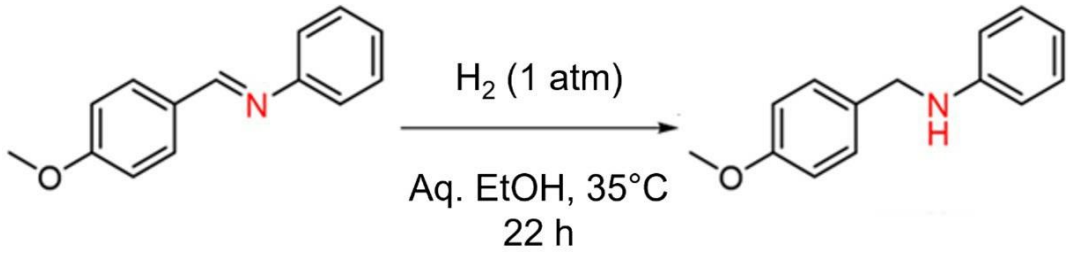

Figure 8: Reaction scheme for the reductive amination catalysed by Pd NPs

The DDT-stabilised Pd NPs failed to catalyse the reaction to any extent. The amine stabilised Pd NP produced low yields ~10%. The poor reactivity of the ligand stabilised NPs may be due to their highly passivated surfaces. In contrast, the polymer stabilised NPs showed excellent catalytic activity, but the catalytic behaviour was influenced by the nature of the capping ligand. Figure 9 shows the imine conversion and yields of the 2° amine for the reductive amination reaction catalysed by different polymer stabilised Pd catalysts. The PVP stabilised NP were the best performing catalysts with the high yield of the amine (93%) and only trace undesired impurities. The PAA-Pd NPs also performed well, with the low side product formation. The poorest performing catalysts being PMMA-Pd NPs, which is most likely due to the size and poor stabilising ability of PMMA. The PVP NPs exhibited no side product formation such as the alcohol or, aldehyde or aniline. The enhanced selectivity of the PVP-protected Pd NPs is highly advantageous to pharmaceutical synthesis chemistry.

In addition, an extensive substrate scope was studied for the reductive amination reaction using the PVP NPs carried out by Dr. David Jones, which will not be discussed here. The Pd-PVP colloidal NPs showed excellent applicability for reductive amination with varying side groups. The PVP NPs were also successfully applied to pharmaceutically relevant compounds, Adaphostin and Laptinib, obtained in excellent yields.

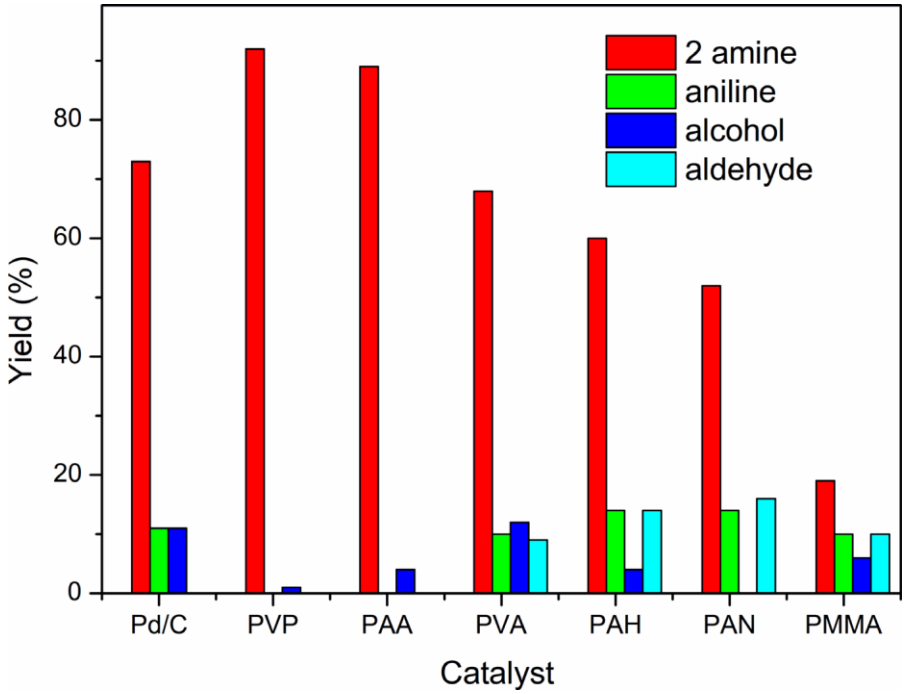

Figure 9: Comparison of catalytic performance of polymer stabilised Pd NP and Pd/C, for the reductive amination reaction using PVP, PAA, PAH, PAN and PMMA as the stabilizers for Pd NPs.

Water and ethanol are used as solvents for this transformation which are both classified as desirable solvents in a green chemistry context. The reaction also proceeded well in other solvents such as *N,N*-dimethylformamide and dimethyl sulfoxide although immiscible solvents such as dichloromethane, ethyl acetate and tetrahydrofuran led to aggregation of catalyst. The use of PVP as the stabiliser is also significant as it is non-toxic, cheap and widely available in most economic markets due to its numerous applications in other fields, including the food industry. In addition to the mild conditions under which this reaction proceeds, another benefit of this approach is that the PVP stabilised Pd NPs used are relatively straight-forward to prepare, utilising a highly robust, reproducible synthetic method which reliably yields NPs with a mean diameter of 2.5 nm.

Several synthesis parameters used for the colloidal catalyst solutions were varied to probe the role of steric effects on the reaction selectivity. As the PVP binding conformation is influenced by the metal: polymer molar ratio and the polymer molecular weight, NPs were prepared using PVP molecular weights of 10,000 and 360,000, and Pd:PVP molar ratios 1:1 and 1:0.3. Changing the solvent and shape

of NPs were also evaluated. Figure 10 shows TEM images and corresponding size distribution histograms of Pd-PVP 1:1, Pd-PVP 1:0.3, Pd-PVP 1:1 with MeOH as solvent and Pd icosahedral NPs.

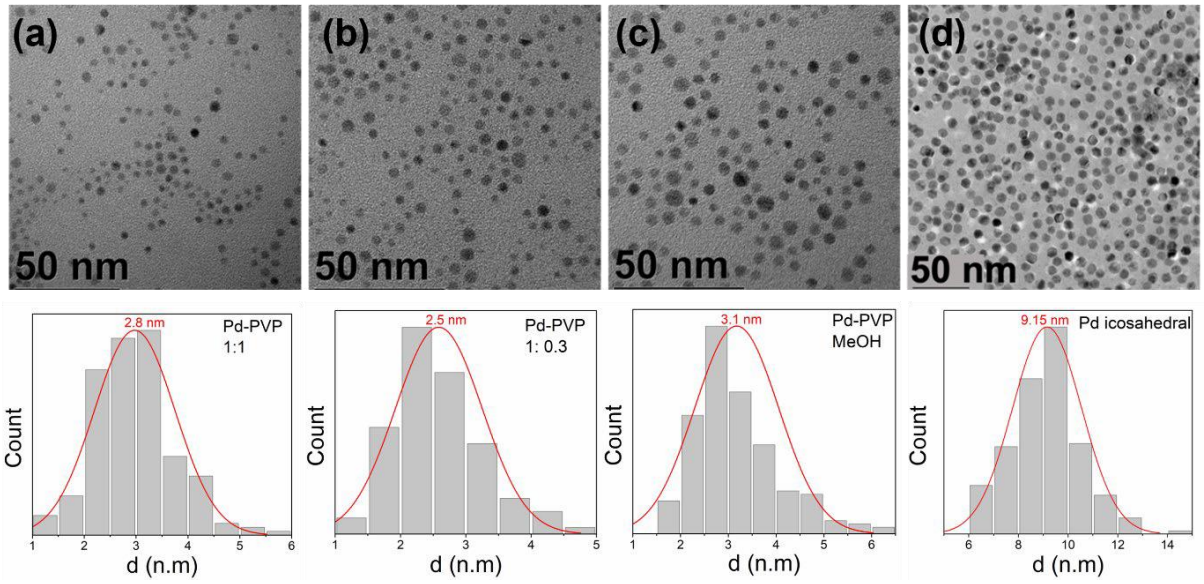

Figure 10: TEM images and corresponding size distribution histograms of (a) Pd-PVP 1:1, (b) Pd-PVP 1:0.3, (c) Pd-PVP with MeOH as solvent and (d) Pd icosahedral NPs

All the Pd-PVP colloidal solutions yield comparable results with almost identical selectivity to the original colloidal catalyst with a molecular weight of 40,000 and a Pd:PVP molar ratio of 1:7.8, indicating that steric effects in the length of the polymer backbone, choice of solvent and shape of NP do not play a dominate role. TEM analysis of the NPs and their associated size distributions before and after the reaction (Figure 11 (a)) show the NP diameter to be retained with a marginal increase in mean diameter from 2.1 nm to 2.5 nm.

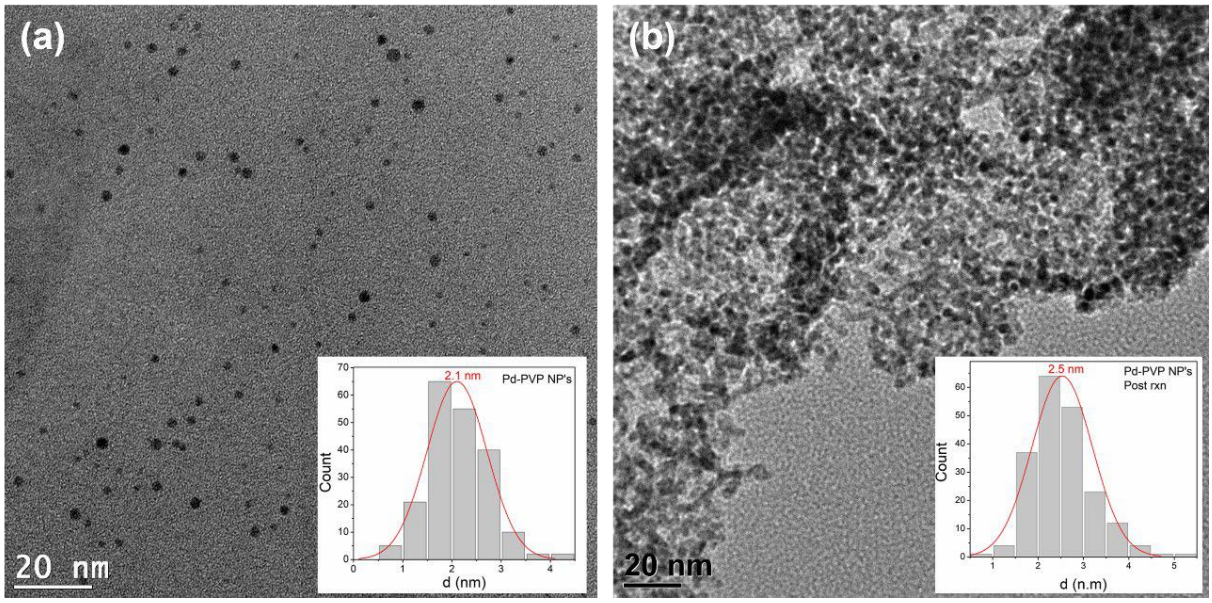

Figure 11: TEM images and corresponding size distribution of PdPVP NPs (a) pre reaction and (b) post reaction.

Changes to reaction selectivity are often associated with electronic effects arising from the metal-ligand interactions, therefore the interaction between PVP and the Pd NP, was analysed by XPS and ATR-FTIR before and after the reaction. The NPs recovered post-reaction could be redispersed in ethanol indicating at least some retention of the capping ligands. Based on the N:Pd XPS ratio, 77% of the PVP is lost from the catalyst. Despite its wide use in colloid synthesis, the interaction between adsorbed PVP molecules and metal surfaces remains controversial. Some studies have found that PVP adsorbs through the carbonyl O atom, with charge transfer occurring from PVP to the metal surface,[31] while others have found PVP to adsorb through the N atom.[32] PVP conformation and the direction of charge transfer is dependent on NP size[33], surface facet[34], metal oxidation state[35] and even the presence of solvent molecules can influence the adsorption behavior of PVP.[31] Analysis of the N 1s core level spectra of pure PVP and PVP-Pd NPs before and after the reaction are illustrated in Figure 12 (a). The binding energy (BE) of the N 1s peak for pure PVP polymer consists of a single component centered at 399.9 eV, characteristic of the pyrrolidone N.[36] The PVP stabilized NPs show a peak at

399.9 eV arising from unbound PVP, indicating that the majority of N groups do not interact with the Pd surface or their interaction does not modify the N electronic properties. The N 1s core level also consists of a second lower intensity peak at a higher B. E. of 400.4 eV, which is correlated to the presence of electron deficient N groups.[33] These species can arise from electron donation from the pyrrolidone N to the Pd or through resonance structure with O, as depicted in Figure 12. Pd NPs analysed after the reaction show only the N component at 400.4 eV, indicating that the unbound PVP is removed during the reaction. Analysis of the O 1s core level presents further evidence of electron donation from the O to Pd which shows a positive shift of + 0.5 eV in the O 1s B. E. for the PVP-Pd NPs compared to pure PVP. Similarly, the Pd 3d core level also confirms charge transfer from PVP to Pd. As the BEs are size dependent, a freshly reduced Pd on carbon catalyst was used as a reference for bare Pd. The Pd $3d_{5/2}$ peak for the PVP-stabilized NPs displays a shift to lower B. E. centered at 335.0 eV, consistent with electron donation from PVP to the Pd surface. The upward shift in the used catalyst is associated with oxidation of the surface due to loss of capping ligands.

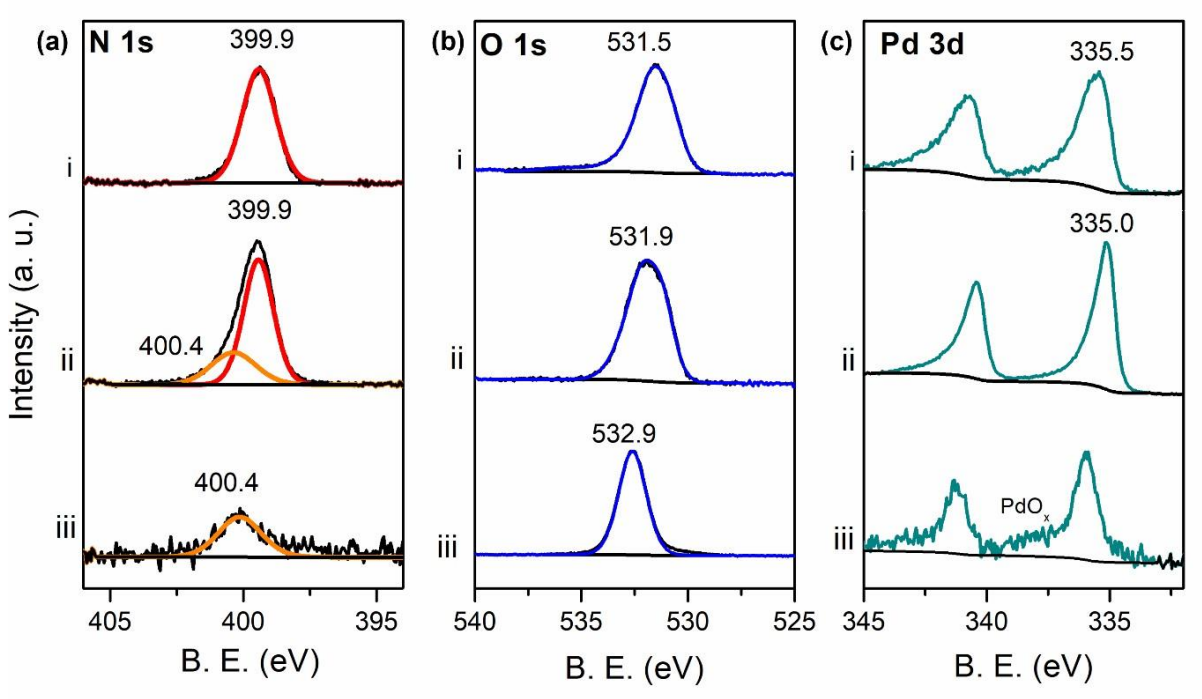

Figure 12: XPS Analysis of (i) PVP, (ii) freshly prepared catalyst and (iii) catalyst recovered post-reaction

Further confirmation of PVP binding through the carbonyl group is provided by FTIR analysis shown in Figure 13, which compares the FTIR spectra of PVP and PVP-stabilized Pd NPs. The two stretching vibrations for the N-C bonds are observed around 1780 cm^{-1}. The strongest absorption is seen at 1654 cm^{-1} assigned to the carbonyl stretching vibration and this peak is red shifted to 1643 cm^{-1} for the Pd NPs, attributed to charge transfer from the carbonyl O, correlating well with the XPS data. Notably, the shift in the carbonyl vibration is considerably smaller than that observed for other metal NPs such as Pt, Rh and Au, suggesting a weaker PVP-Pd interaction.[35, 37]

The PVP polymer was replaced with NMP during the synthesis of the colloidal catalyst and while the morphology of the resultant NPs were poorly defined, as can be excepted from the low stabilising power of NMP, the colloidal catalyst solution still displayed high selectivity suggesting the enhanced catalytic selectivity is not solely attributed to the steric effects of the organic ligand and that coordination of the head group contributes to the reactivity behaviour. Increased electron density of metal NPs by electron donating ligands results in weaker adsorption of electron rich intermediates which has been shown to influence product selectively in a number of hydrogenation reactions.[38-39]

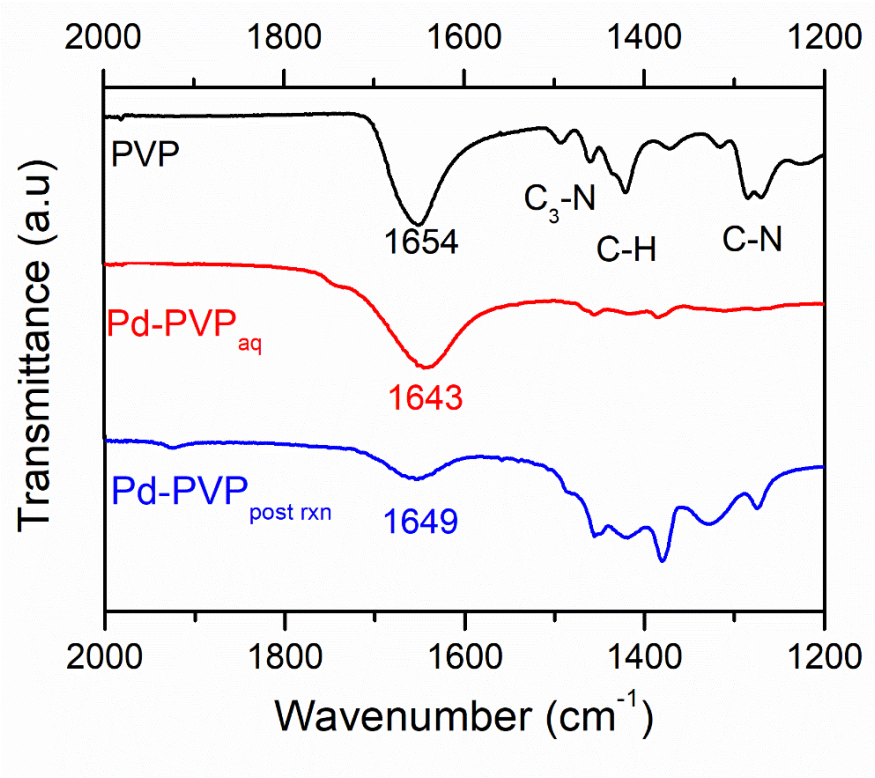

Figure 13: FTIR of PVP polymer, Pd-PVP aqueous solution and Pd-PVP post reaction.

Although PVP capping ligands gave superior performance, PAA-Pd NPs also displayed high selectivity, which was further assessed by FTIR and XPS to identify the ligand conformation. Figure 14 shows the FTIR spectra of Pd NPs stabilized by PAA and pure PAA. The carbonyl absorption of pure PAA located at 1703 cm^{-1} is broadened considerably and downshifted to 1647 cm^{-1} for the PAA-Pd NPs, again consistent with electron donation from the carbonyl group. Some contribution of the asymmetric stretching vibration $\nu_{as}(COO^-)$ at 1567/1517 cm^{-1} also appears, indicating the presence of ligands adsorbed as the carboxylate (COO^-)[40].

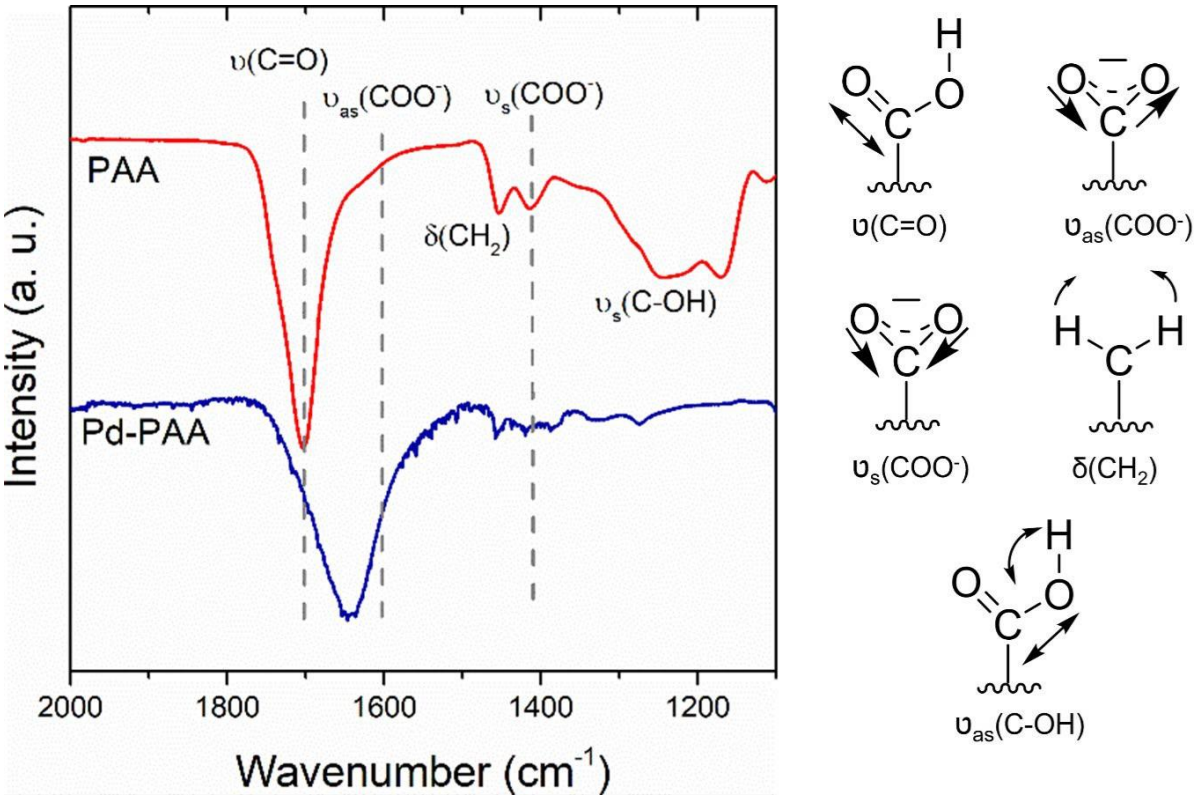

Figure 14: FTIR spectra of Pd NPs stabilized by PAA and pure PAA and corresponding binding modes.

This binding mode is also supported by XPS analysis of the Pd-PAA NPs as shown in Figure 15. Figure 15(a) shows the O 1s core level XPS spectra of pure PAA and PAA-Pd NP where the O=C-O peak in the pure PAA is observed at 530.8 eV and C-O-H peak at 533.2 eV. A considerable decrease in the peak intensity associated with the C-O-H bonds are observed in the O 1s core level of PAA bound the Pd NPs compared to pure PAA, as shown in Figure 15(a). Changes are also observed the C 1s core level with the appearance of an additional peak at a BE of 289.1 eV, associated with electron deficient carbon, is observed for the PAA-Pd NPs.[41]

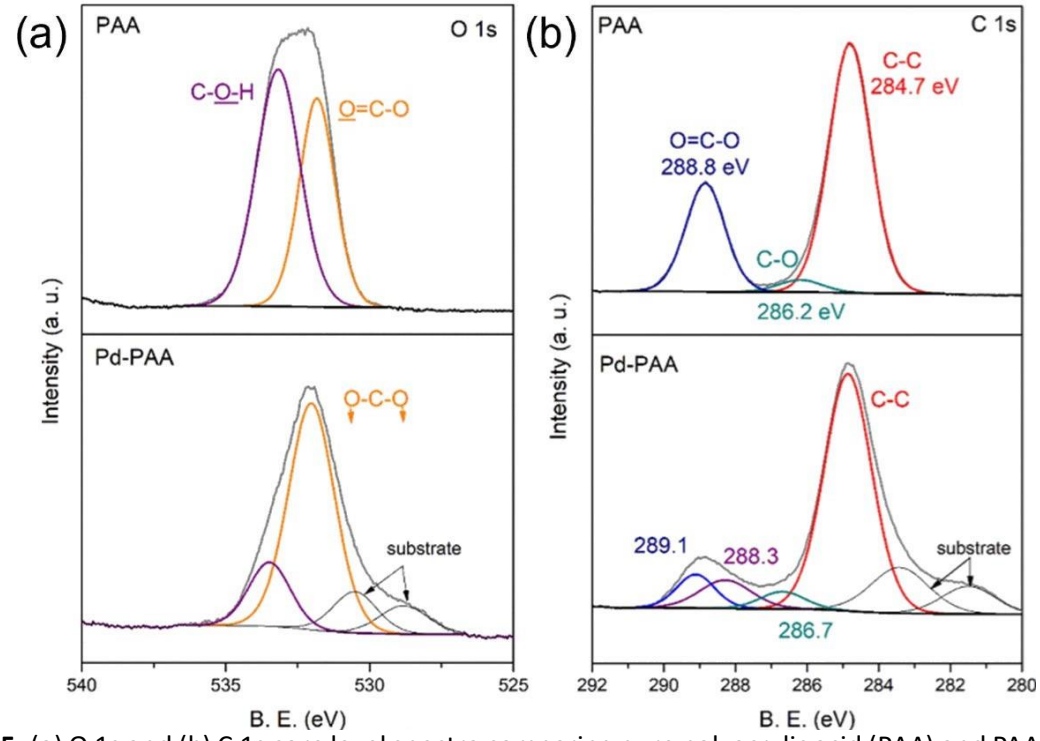

Figure 15: (a) O 1s and (b) C 1s core level spectra comparing pure polyacrylic acid (PAA) and PAA-stabilised NPs and FTIR analysis of PAA and PAA-stabilised Pd NPs

The adsorption of the substrates to be hydrogenated compete with the pre-adsorbed PVP molecules on the Pd surface. Selective hydrogenation of alkynes to alkene was shown to be controlled by the binding energy of the capping ligand, and when the adsorption energy of capping agents on the catalyst surface is higher than that of alkene intermediates, the reaction could proceed with high selectivity[56]. In this study, polymeric ligands which give rise to electron donation from the ligand to Pd display superior chemoselectivity compared to weakly co-ordinating ligands. Despite the ubiquitous use of PVP in colloidal synthesis, the exact nature of the interaction with the surface remains elusive. While both XPS and FTIR provide evidence of charge transfer from PVP to Pd, the electronic interaction appears to be weaker compared to other metal NPs.

Density functional theory (DFT) was employed to further elucidate the molecular conformation of PVP on a model Pd surface and determine the binding energy of PVP compared to the reaction intermediates. Computational work was carried out by Dr Råsander. Computation studies reveal that PVP is not chemisorbed to the Pd surface but physisorbed with a binding energy of 1.13 eV. The BE of

PVP is higher than the reaction intermediates that could be hydrogenated to result in undesired side products. The computational study (not presented here) support the experimental findings in that the strong adsorption of PVP inhibits the reaction pathway of undesired side products through a surface passivation effect leading the enhanced selectivity observed for the reductive amination.

3.4 Conclusion

In this chapter a variety of Pd NPs stabilised with a range of small organic ligands and polymers where prepared and evaluated as solubilised *i.e.* support-free heterogeneous catalysts. TEM, XPS and FTIR analysis was used to understand the steric effect of the capping ligands. The catalytic activity of the NPs was evaluated in the reductive amination. This chemistry proceeds in excellent yields under mild conditions and can be considered as a green process as it uses benign solvents and low catalyst loading. The ligands most effective in minimising undesired side products demonstrated charge transfer from the ligand to the Pd, in contrast, weakly coordinating polymers, in particular PVA afforded undesired side products. The PVP-stabilised NPs also displayed the highest reaction selectivity compared to commercial Pd/C. The presence of PVP ligands at the Pd NP surface gives rise to a combination of steric and electronic effects. XPS coupled with FTIR analysis show electron donation from the PVP carbonyl group to the Pd NP. This work shows the enormous potential of judiciously choosing stabilising ligands for surface functionalised heterogeneous catalysts and their application to organic synthesis.

3.5 References

1. Gunasekar, G. H.; Shin, J.; Jung, K.-D.; Park, K.; Yoon, S., Design Strategy toward Recyclable and Highly Efficient Heterogeneous Catalysts for the Hydrogenation of CO2 to Formate. *ACS Catalysis* **2018,** *8* (5), 4346-4353.
2. Wu, D.; Baaziz, W.; Gu, B.; Marinova, M.; Hernández, W. Y.; Zhou, W.; Vovk, E. I.; Ersen, O.; Safonova, O. V.; Addad, A.; Nuns, N.; Khodakov, A. Y.; Ordomsky, V. V., Surface molecular imprinting over supported metal catalysts for size-dependent selective hydrogenation reactions. *Nature Catalysis* **2021,** *4* (7), 595-606.
3. Kato, K.; Deng, D.; Kita, Y.; Kamata, K.; Hara, M., Primary amine synthesis by hydrogen-involving reactions over heterogeneous cobalt catalysts. *Catalysis Science & Technology* **2022**.
4. Soszka, E.; Jędrzejczyk, M.; Lefèvre, C.; Ihiawakrim, D.; Keller, N.; Ruppert, A. M., TiO2-supported Co catalysts for the hydrogenation of γ-valerolactone to 2-methyltetrahydrofuran: influence of the support. *Catalysis Science & Technology* **2022**.
5. Dong, Q.; Yin, S.; Guo, C.; Sato, T., Ce0.5Zr0.4Sn0.1O2/Al2O3 catalysts with enhanced oxygen storage capacity and high CO oxidation activity. *Catalysis Science & Technology* **2012,** *2* (12), 2521-2524.
6. Jüntgen, H., Activated carbon as catalyst support: A review of new research results. *Fuel* **1986,** *65* (10), 1436-1446.
7. Dagle, V. L.; Flake, M. D.; Lemmon, T. L.; Lopez, J. S.; Kovarik, L.; Dagle, R. A., Effect of the SiO2 support on the catalytic performance of Ag/ZrO2/SiO2 catalysts for the single-bed production of butadiene from ethanol. *Applied Catalysis B: Environmental* **2018,** *236*, 576-587.
8. Wang, C. H., Al2O3-supported transition-metal oxide catalysts for catalytic incineration of toluene. *Chemosphere* **2004,** *55* (1), 11-7.
9. Bagheri, S.; Muhd Julkapli, N.; Bee Abd Hamid, S., Titanium dioxide as a catalyst support in heterogeneous catalysis. *TheScientificWorldJournal* **2014,** *2014*, 727496.
10. Sankar, M.; He, Q.; Engel, R. V.; Sainna, M. A.; Logsdail, A. J.; Roldan, A.; Willock, D. J.; Agarwal, N.; Kiely, C. J.; Hutchings, G. J., Role of the Support in Gold-Containing Nanoparticles as Heterogeneous Catalysts. *Chemical Reviews* **2020,** *120* (8), 3890-3938.
11. Lokteva, E. S.; Golubina, E. V., Metal-support interactions in the design of heterogeneous catalysts for redox processes. *Pure and Applied Chemistry* **2019,** *91* (4), 609-631.
12. Li, Y.; Zhang, Y.; Qian, K.; Huang, W., Metal–Support Interactions in Metal/Oxide Catalysts and Oxide–Metal Interactions in Oxide/Metal Inverse Catalysts. *ACS Catalysis* **2022,** *12* (2), 1268-1287.
13. Magrez, A.; Smajda, R.; Seo, J. W.; Horváth, E.; Ribic, P. R.; Andresen, J. C.; Acquaviva, D.; Olariu, A.; Laurenczy, G.; Forró, L., Striking Influence of the Catalyst Support and Its Acid–Base Properties: New Insight into the Growth Mechanism of Carbon Nanotubes. *ACS Nano* **2011,** *5* (5), 3428-3437.
14. Ali, M. E.; Rahman, M. M.; Sarkar, S. M.; Hamid, S. B. A., Heterogeneous Metal Catalysts for Oxidation Reactions. *Journal of Nanomaterials* **2014,** *2014*, 192038.
15. Alam, A. M.; Shon, Y. S., Water-Soluble Noble Metal Nanoparticle Catalysts Capped with Small Organic Molecules for Organic Transformations in Water. *ACS applied nano materials* **2021,** *4* (4), 3294-3318.
16. Sole, R.; Buranello, C.; Bardella, N.; Di Michele, A.; Paganelli, S.; Beghetto, V., Recyclable Ir Nanoparticles for the Catalytic Hydrogenation of Biomass-Derived Carbonyl Compounds. *Catalysts* **2021,** *11* (8).
17. Juttukonda, V.; Paddock, R. L.; Raymond, J. E.; Denomme, D.; Richardson, A. E.; Slusher, L. E.; Fahlman, B. D., Facile Synthesis of Tin Oxide Nanoparticles Stabilized by Dendritic Polymers. *Journal of the American Chemical Society* **2006,** *128* (2), 420-421.
18. Auría-Soro, C.; Nesma, T.; Juanes-Velasco, P.; Landeira-Viñuela, A.; Fidalgo-Gomez, H.; Acebes-Fernandez, V.; Gongora, R.; Almendral Parra, M. J.; Manzano-Roman, R.; Fuentes, M., Interactions of

Nanoparticles and Biosystems: Microenvironment of Nanoparticles and Biomolecules in Nanomedicine. *Nanomaterials (Basel, Switzerland)* **2019,** *9* (10).
19. Garnweitner, G.; Ghareeb, H. O.; Grote, C., Small-molecule in situ stabilization of TiO2 nanoparticles for the facile preparation of stable colloidal dispersions. *Colloids and Surfaces A: Physicochemical and Engineering Aspects* **2010,** *372* (1), 41-47.
20. Marshall, S. T.; O'Brien, M.; Oetter, B.; Corpuz, A.; Richards, R. M.; Schwartz, D. K.; Medlin, J. W., Controlled selectivity for palladium catalysts using self-assembled monolayers. *Nature Materials* **2010,** *9* (10), 853-858.
21. Collins, G.; Holmes, J. D., Engineering Metallic Nanoparticles for Enhancing and Probing Catalytic Reactions. *Advanced Materials* **2016,** *28* (27), 5689-5695.
22. Pang, S. H.; Schoenbaum, C. A.; Schwartz, D. K.; Medlin, J. W., Directing reaction pathways by catalyst active-site selection using self-assembled monolayers. *Nature Communications* **2013,** *4* (1), 2448.
23. Rossi, L. M.; Fiorio, J. L.; Garcia, M. A. S.; Ferraz, C. P., The role and fate of capping ligands in colloidally prepared metal nanoparticle catalysts. *Dalton Transactions* **2018,** *47* (17), 5889-5915.
24. Koczkur, K. M.; Mourdikoudis, S.; Polavarapu, L.; Skrabalak, S. E., Polyvinylpyrrolidone (PVP) in nanoparticle synthesis. *Dalton Transactions* **2015,** *44* (41), 17883-17905.
25. Graham, L.; Collins, G.; Holmes, J. D.; Tilley, R. D., Synthesis and catalytic properties of highly branched palladium nanostructures using seeded growth. *Nanoscale* **2016,** *8* (5), 2867-2874.
26. Collins, G.; Schmidt, M.; O'Dwyer, C.; Holmes, J. D.; McGlacken, G. P., The Origin of Shape Sensitivity in Palladium-Catalyzed Suzuki–Miyaura Cross Coupling Reactions. *Angewandte Chemie International Edition* **2014,** *53* (16), 4142-4145.
27. Abdel-Magid, A. F.; Carson, K. G.; Harris, B. D.; Maryanoff, C. A.; Shah, R. D., Reductive Amination of Aldehydes and Ketones with Sodium Triacetoxyborohydride. Studies on Direct and Indirect Reductive Amination Procedures1. *The Journal of Organic Chemistry* **1996,** *61* (11), 3849-3862.
28. Irrgang, T.; Kempe, R., Transition-Metal-Catalyzed Reductive Amination Employing Hydrogen. *Chemical Reviews* **2020,** *120* (17), 9583-9674.
29. Moreno, M.; Kissell, L. N.; Jasinski, J. B.; Zamborini, F. P., Selectivity and Reactivity of Alkylamine- and Alkanethiolate-Stabilized Pd and PdAg Nanoparticles for Hydrogenation and Isomerization of Allyl Alcohol. *ACS Catalysis* **2012,** *2* (12), 2602-2613.
30. Hirai, H.; Yakura, N., Protecting polymers in suspension of metal nanoparticles. *Polymers for Advanced Technologies* **2001,** *12* (11-12), 724-733.
31. Ren, M.; Jin, Y.; Chen, W.; Huang, W., Rich Capping Ligand–Ag Colloid Interactions. *The Journal of Physical Chemistry C* **2015,** *119* (49), 27588-27593.
32. Niu, Z.; Li, Y., Removal and Utilization of Capping Agents in Nanocatalysis. *Chemistry of Materials* **2014,** *26* (1), 72-83.
33. Xian, J.; Hua, Q.; Jiang, Z.; Ma, Y.; Huang, W., Size-Dependent Interaction of the Poly(N-vinyl-2-pyrrolidone) Capping Ligand with Pd Nanocrystals. *Langmuir* **2012,** *28* (17), 6736-6741.
34. Collins, G.; Schmidt, M.; McGlacken, G. P.; O'Dwyer, C.; Holmes, J. D., Stability, Oxidation, and Shape Evolution of PVP-Capped Pd Nanocrystals. *The Journal of Physical Chemistry C* **2014,** *118* (12), 6522-6530.
35. Borodko, Y.; Humphrey, S. M.; Tilley, T. D.; Frei, H.; Somorjai, G. A., Charge-Transfer Interaction of Poly(vinylpyrrolidone) with Platinum and Rhodium Nanoparticles. *The Journal of Physical Chemistry C* **2007,** *111* (17), 6288-6295.
36. Collins, G.; Davitt, F.; O'Dwyer, C.; Holmes, J. D., Comparing Thermal and Chemical Removal of Nanoparticle Stabilizing Ligands: Effect on Catalytic Activity and Stability. *ACS Applied Nano Materials* **2018,** *1* (12), 7129-7138.
37. Borodko, Y.; Habas, S. E.; Koebel, M.; Yang, P.; Frei, H.; Somorjai, G. A., Probing the Interaction of Poly(vinylpyrrolidone) with Platinum Nanocrystals by UV−Raman and FTIR. *The Journal of Physical Chemistry B* **2006,** *110* (46), 23052-23059.

38. Guo, M.; Li, H.; Ren, Y.; Ren, X.; Yang, Q.; Li, C., Improving Catalytic Hydrogenation Performance of Pd Nanoparticles by Electronic Modulation Using Phosphine Ligands. *ACS Catalysis* **2018,** *8* (7), 6476-6485.
39. Chen, G.; Xu, C.; Huang, X.; Ye, J.; Gu, L.; Li, G.; Tang, Z.; Wu, B.; Yang, H.; Zhao, Z.; Zhou, Z.; Fu, G.; Zheng, N., Interfacial electronic effects control the reaction selectivity of platinum catalysts. *Nature Materials* **2016,** *15* (5), 564-569.
40. Zhang, X.; Chen, L.; Yuan, L.; Liu, R.; Li, D.; Liu, X.; Ge, G., Conformation-Dependent Coordination of Carboxylic Acids with Fe(3)O(4) Nanoparticles Studied by ATR-FTIR Spectral Deconvolution. *Langmuir* **2019,** *35* (17), 5770-5778.
41. López, G. P.; Castner, D. G.; Ratner, B. D., XPS O 1s binding energies for polymers containing hydroxyl, ether, ketone and ester groups. *Surface and Interface Analysis* **1991,** *17* (5), 267-272.

Chapter 4

PdAu Nanosheets for Visible Light Driven Suzuki Cross-Coupling Reactions

PdAu Nanosheets for Visible Light Driven Suzuki Cross-Coupling Reactions

Éadaoin Casey, Prof. Justin. D Holmes, Dr. Gillian Collins*

[1] School of Chemistry, University College Cork, Cork, T12 YN60, Ireland.

[2] AMBER Centre, Environmental Research Institute, University College Cork, Cork, T23 XE10, Ireland.

Keywords: 2D nanomaterials, Palladium Gold alloy nanosheets, visible light, photocatalysis, plasmonic, Suzuki reaction

Abstract

Combining a two-dimensional (2D) morphology and plasmonic photocatalysis represents an efficient design for light driven organic transformations. We report a one pot synthesis of surfactant templated PdAu nanosheets (NSs). Transmission electron microscopy (TEM) and x-ray photoelectron spectroscopy (XPS) analysis show the formation of 2D PdAu structures was initiated through nanoparticle seeds dispersed in the alkyl ammonium salt surfactant which acted as a template for the growth into NSs. The PdAu NSs were used for visible light enhanced Suzuki cross coupling. The PdAu bimetallic NSs outperformed monometallic Pd NSs and commercial Pd/C in room temperature Suzuki cross-coupling reactions. The high catalytic activity is attributed to a combination of the 2D morphology giving rise to plasmon enhanced catalysis, high density of surface atoms, the electron-rich Pd surface due to alloying and the presence of weakly bound amines. A comparative study of surfactant assisted NSs and CO-assisted NSs was also carried out to assess the influence of surface ligands on the catalytic and photocatalytic enhancement of NSs with similar morphology. The surfactant-assisted NSs showed substantially superior performance compared to the CO-assisted for room temperature Suzuki coupling reactions.

4.1 Introduction

Noble metals are ubiquitous in catalytic applications from chemical synthesis to energy storage and conversion. [1-3] The use of 2D metal nanosheets (NSs) for catalysis has attracted attention due to their unique chemical, physical and surface related properties. [1,4-5] As catalytically active sites are located on the surfaces or edges of catalysts, the presence of a high proportion of exposed atoms and large interfacial area of 2D metal NSs, enables them to operate with high atom utilisation efficiency, particularly advantageous to noble metal catalysts.[6-7] 2D metal NSs have been used for water splitting, CO_2 reduction and organic synthesis reactions.[8-9] Pd NSs prepared using layered double hydroxide templates display nearly 40 % higher turnover frequency compared to Pd nanoparticles (NPs) for the hydrogenation of nitrobenzene to aniline.[10] Rh NSs exhibited remarkably higher catalytic activity in the hydrogenation of phenol and cyclohexane compared to commercial Rh/C and PVP-Rh NPs and improved selectivity for aldehyde product in the hydroformylation of 1-octene.[11]

The intrinsic catalytic activity of noble metals such as Pd can also be significantly increased through alloying with plasmonic metals such as Au and Ag, by exploiting the local surface plasmon resonance (LSPR) of these nanostructures.[12-14] The development of noble metal catalysts with visible light enhancement has seen much interest in recent years with Pd and Pd alloy nanostructures used for an extensive range of organic transformations driven by visible light such as coupling reactions, hydrogenation and oxidation.[15-17] The main advantages of using light-harvesting catalysts are lower reaction temperatures compared to conventional thermal reactions, enhanced reaction rates and improved selectivity[18], enabling more energy efficient and greener route to chemical synthesis. The design of light harvesting heterogeneous catalysts are typically based on plasmonic metal-semiconductor junctions or multi-metallic nanostructures consisting of a plasmonic component (usually Au and Ag) and a catalytic component working synergistically, such as alloys or core shell nanostructures.[19-20] The ability to combine plasmonic enhancement with a 2D catalyst morphology represents an effective design for energy efficient catalyst driven by visible light. The LSPR peak of Pd

is typically located in the ultraviolet spectral range but 2D Pd NS have a LSPR that reside in the visible region of the spectrum.[21]

The synthesis of 2D metallic NSs is challenging due to tendency of metals to form three-dimensional close-packed structures but there have been advancements in this field in recent years.[22] Zheng *et al.*[21] was the first to report ultrathin Pd NSs with a thickness of 1.8 nm using CO as a structure directing agent. CO is highly effective in controlling the anisotropic growth of 2D metal NSs due to the strong adsorption of CO molecules on the Pd(111) planes which restricts growth along the [111] direction. CO can be replaced with $W(CO)_6$ which conveniently removes safety and toxicity issues associated with gaseous CO.[23] The CO-assisted synthesis method has also been applied to the formation of Pd alloy NSs such as PdFe, PdCo, PdNi, PtCu and PtPdAg [24-26]. While a CO-assisted route to 2D metal NSs is undoubtedly convenient for high yield and relatively low cost synthesis, a major drawback of using CO as a structure directing agent is that the surfaces of the NS are highly passivated which can be unfavourable or even detrimental for catalytic applications. Xu *et al.*[27] demonstrated the bottom-up synthesis of Pd NSs with controlled surface facets through a template-assisted solution-phase growth. By understanding the role of capping ligands, they can be tailored to enhance reactivity of metal nanostructure catalysts which has also been a topic gaining attention. Yang *et al.*[24] showed that replacing oleic acid ligands on CuPd NSs with ethylenediamine ligands led to a highly active catalyst for formic acid oxidation. Amine groups resulted in electron donation to the CuPd interface and is beneficial for the absorption of electron-deficient reactants like formic acid. A combination of amine capping ligands, a NS morphology giving a high electrochemically active surface area and synergistic effects between Cu and Pd, resulted in superior catalytic performance for formic acid oxidation compared to other Pd-based catalysts.

Here we report the one-pot synthesis of PdAu bimetallic NSs using an alkyl quaternary ammonium salt as a soft template. Time evolved TEM and XPS was used to understand the formation mechanism of the NSs and identify changes in the surface chemistry of the NSs. A Suzuki cross coupling reaction was

used to assess their catalytic performance under visible light irradiation. Both monometallic Pd and bimetallic PdAu NSs displayed catalytic enhancement with higher yields obtained when the reaction was carried out under visible light compared to conducting the reaction in the dark. The bimetallic NSs also outperformed the monometallic NSs, for example at a catalyst loading of 0.2 mol% Pd the PdAu NSs gave full conversion after 3 h at room temperature, while the Pd NSs gave a yield of 69% under the same conditions. The high performance of the surfactant assisted NSs is in part attributed and the presence of a weakly co-ordinating amine ligands at the surface. Stabilising ligands such as polymers, small organic molecules and inorganic species such as Br^- ions are commonly used in wet chemical synthesis, yet despite the many literature studies on light-enhanced Suzuki cross coupling, the catalytic role played by the capping ligands have been poorly addressed. To gain insight into ligand-enhanced catalytic and photocatalytic activity, surfactant-assisted NSs were compared with CO-assisted NSs. The surfactant assisted and CO-assisted NSs displayed markedly different performance profile for room temperature cross coupling reactions.

4.2 Experimental

Chemicals

Metal precursors palladium (II) chloride (H_2PdCl_4) (99.9 %), palladium acetylacetonate $Pd(acac)_2$ (99 %), silver nitrate ($AgNO_3$) (99.9 %), gold chloride ($HAuCl_4$) (99.9 %) and tungsten carbonyl $W(CO)_6$ were purchased from Sigma Aldrich. All other synthesis chemicals and solvents were purchased from Sigma Aldrich except for 1-bromodocosane (95 %) which was purchased from ABCR.

Synthesis of surfactant assisted nanosheets

Surfactant assisted Pd NSs were synthesized using a modified literature procedure.[27] Briefly, the long chain alkyl quaternary ammonium surfactant C_{22}-QA (Br^-) was first prepared by the addition of 1.95 g

of 1-bromodocosane (10 mmol) and 1.77 ml of trimethylamine (15 mmol) with 75 ml of acetonitrile and refluxed at 95 °C under N_2 for 22 h. After cooling, the solvent was removed via rotary evaporation. The crude product was washed with diethyl ether three times and dried overnight.

For the synthesis of Pd and PdAu NSs a 10 mM Pd precursor stock solution was prepared by dissolving 89 mg of $PdCl_2$ in 50 ml of a 0.2 M HCl. Pd NSs were synthesized by adding 5 ml of a 0.025 M C_{22}-QA (Br^-) solution in a glass sample vial along with 0.8 ml of 10 mM H_2PdCl_4 aqueous solution. The mixture was left to stir until ion exchange had occurred (15 min). 1 ml of a freshly prepared 0.3 M aqueous solution of L-ascorbic acid (AA) was injected slowly into the solution. The reaction solution was placed on an ice bath and left undisturbed at 0° C with reaction times between 1-6 h. Once the reaction had reduced, the product was sonicated with toluene and collected by centrifugation and washed with ethanol. This purification procedure was repeated three times and the NSs were re-dispersed in ethanol.

PdAu NSs were synthesized using the same procedure as the Pd NSs but with co-addition of the Pd and Au precursors. For example, PdAu NSs with a molar ratio of 5:1 were prepared by adding 5 ml of a 0.025 M C_{22}-QA (Br^-) solution along with 0.665 ml of a 10 mM H_2PdCl_4 and 0.135 ml of 10 mM $HAuCl_4$ aqueous solution. PdAu NSs with a molar ratio of 10:1 were synthesized using 0.728 ml of 10 mM H_2PdCl_4 and 0.072 ml of 10 mM $HAuCl_4$ aqueous solution. After the reaction, the product was sonicated with toluene and collected by centrifugation and washed with ethanol. This purification procedure was repeated three times and the NS were re-dispersed in ethanol.

Synthesis of CO assisted nanosheets

16 mg $Pd(acac)_2$, 30 mg PVP, 10 mg citric acid and 60 mg cetyltrimethylammonium bromide (98%) CTAB were placed in a test tube vial with 10 ml of DMF and the solution was bubbled with Ar for 15 min (solution 1). In a separate two neck round bottom flask, 100 mg of tungsten hexacarbonyl (97 %) $W(CO)_6$ was added and purged with Ar. Solution 1 was injected via cannula into the $W(CO)_6$ and heated to reflux at 80 °C. The reaction was left to age for 1 h. The product was collected by

centrifugation and washed with acetone (× 4) to remove excess reagents. The Pd NSs were redispersed in ethanol and used as seeds for the synthesis of PdAg and PdAu NSs. The synthesis was also conducted by changing the polymer ligand from PVP to polyvinyl alcohol (PVA) and exchanging the CTAB with other quaternary ammonium salts of different carbon change lengths C8, C12 and C22 *i.e. n*-octyltrimethylammonium bromide (98 %), dodecyltrimethylammonium bromide (98 %), and *n*-docosyltrimethylammonium bromide, respectively. CO-assisted alloy PdAg and PdAu NSs were synthesized using the same procedure as the Pd NSs but once the NSs were left to age, a solution containing 15 mg PVP and 0.692 ml of a 0.025 M $AgNO_3$ or 1.66 ml of a 0.01 M $AuCl_3$ was added and heated to reflux at 80 °C for a further 1h. The reaction vessel was wrapped in alumina foil as $AgNO_3$ is photosensitive. The product was collected by centrifugation and washed with acetone (× 4) to remove excess reagents and redispersed in ethanol.

Optimisation reactions: A number of reaction parameters such as the surfactant ligand, surfactant concentration, Au:Pd molar ratio, ascorbic acid concentration and temperature were altered to find the optimum reaction conditions for the formation of the NS.

Catalytic Evaluation: Suzuki Coupling reaction with and without illumination

Suzuki cross-coupling: In a typical experiment 0.026 g of phenylboronic acid (0.22 mmol). 0.046 g of 4-methoxyiodobenzene (0.2 mmol), 0.0553 g (0.4 mmol) of K_2CO_3 were added to 12 ml of ethanol/water (3:1) in a glass vial. The reactions were initiated by the addition of the catalyst (0.05-0.2 mol %) and stirred continuously using a magnetic stirrer. A LED light source was used for reactions carried out under visible light with broad band emission between 400 and 800 nm. The emission spectrum of the LED is given in Supporting Information, see Figure S1. Reactions were carried out in the dark by covering the entire reaction with foil. Reactions were carried out at room temperature (20 °C) or at 80 °C with reaction times between 1-6 h. Reactions were carried out in thermostated reactor to ensure temperature regulation and the reaction temperature was continually monitored. After the reaction was completed, the solution was filtered and washed with DCM (10 ml × 2), the aqueous layer was removed and washed with DCM (10 ml × 2) and then dried

with $MgSO_4$. The DCM was removed by rotary evaporation and product remained. The product was purified before NMR analysis with deuterated chloroform.

Materials Characterization

X-ray Photoelectron Spectroscopy (XPS) was acquired using a KRATOS AXIS 165 monochromatized X-ray photoelectron spectrometer equipped with an Al Kα (hv = 1486.6 eV) X-ray source. Spectra were collected at a take-off angle of 90° and all spectra were referenced to the C 1s peak at 284.8 eV. Pd 3d core levels were fit with a Shirley backgrounds and Gaussian-Lorentzian profiles. To achieve best fit, the peak positions were allowed to float with a variable FWHM ranging from 1-1.5 for metallic Pd(0) and 1.2-1.7 for oxidised Pd components. Peaks shifted to binding energies (BEs) greater than +1.5 eV of the elemental Pd(0) peak were assigned to bulk oxide phases PdO. Transmission electron microscopy (TEM) analysis was performed using a JEOL 2100 electron microscope at an operating voltage of 200 kV and high-resolution TEM and energy-dispersive X-ray (EDX) analysis was carried out on an FEI Titan TEM, at an operating voltage of 300 kV. Scanning electron microscopy (SEM) was carried out on a FEI Helios NanoLab 600i operating at 30 kV and 0.69 nA, with an attached EDX Oxford X- Max 80 detector. X-ray diffraction (XRD) was carried out using a Philips X'pert Pro MPD, equipped with a Panalytical Empyrean Cu X-ray tube and a Philips X'celerator detector. Fourier transform infrared (FTIR) spectra were recorded on a Perkin Elmer Spectrum Two FT-IR Spectrometer operating in the range of 4000-450 cm^{-1} with a resolution of 4 cm^{-1} and spectra were averaged from 20 scans. Nuclear magnetic resonance (NMR) samples were run in deuterated chloroform ($CDCl_3$). 1H NMR spectra were recorded on Bruker Avance III 300 NMR spectrometers, in proton-coupled mode using tetramethysilane (TMS) as the internal standard.

4.3 Results and Discussion

Synthesis of Alloy Surfactant Assistant Nanosheets

Bimetallic 2D NSs with extended sheet lengths were synthesized by reduction of Pd and Au precursor in the presence of long chain alkyl quaternary ammonium surfactant templates, as illustrated in Scheme 1. Figure 1(a) shows a TEM of NSs formed using a Pd:Au molar ratio of 5:1 and Figure 1(b) shows NSs produced using a molar ratio PdAu 10:1 NS, which have an irregular morphology. The TEM image shown in Figure 1(c) displays two overlapping sheets, with the inset figure showing the NSs to be crystalline. Figure 1(d) shows a high resolution image of a NS with a lattice spacing of 0.23 nm, which is close to that of (111) face centred cubic Pd, although the d-spacing of individual Au and Pd are quite close, *i.e.* 0.236 and 0.225 nm, respectively.[28] The TEM image also shows a high density of atomic steps along the edge of the NS. The mean thickness of the NS estimated by TEM, as shown in the inset of Figure 1(d), was *ca.* 5 nm, equivalent to over 20 atomic layers thick, which is greater than previously reported thickness of surfactant template monometallic Pd NSs *ca.* 2.5 nm.[27]

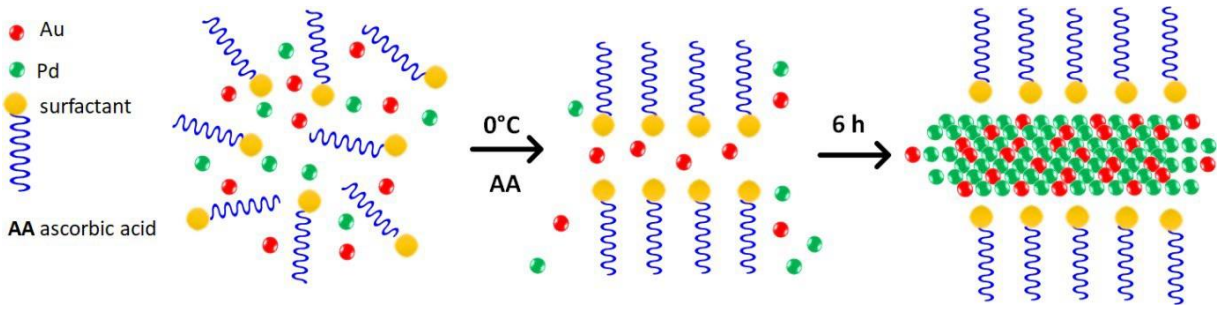

Scheme 1: Surfactant assisted synthesis of PdAu NSs.

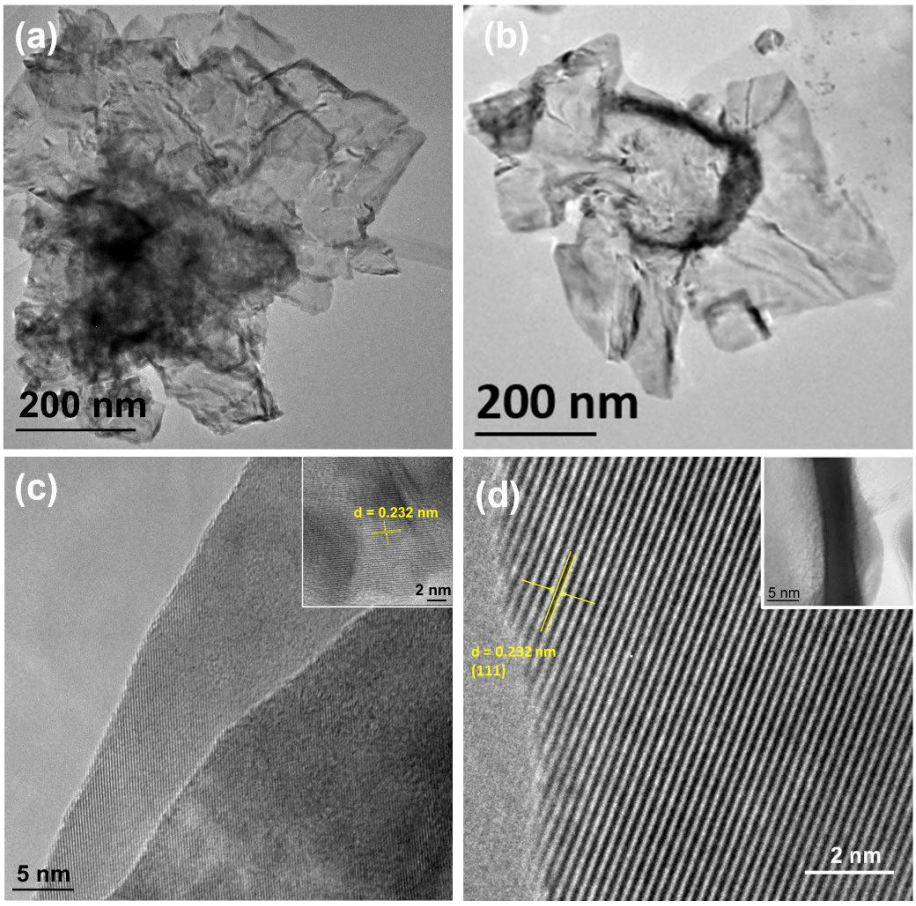

Figure 1: TEM images of (a) PdAu 5:1 NSs, (b) PdAu 10:1 NSs and (c) and (d) HRTEM with lattice planes of a PdAu 5:1 NS.

Elemental analysis was used to assess the distribution of Au and Pd in the NSs. Figure 2(a) and (b) show a low resolution TEM image and corresponding STEM image with EDX point analysis, respectively. The Pd:Au quantification data given in Figure 2(b) were consistent across different areas and also in good agreement with the Au and Pd precursor molar ratio used for the synthesis (5:1). Figure 2(c) displays an EDX line scan across a PdAu NS, and confirm the presence of both Au and Pd. Figures 2(d)-(f) shows the Pd, Au and the overlaid EDX maps for the PdAu 5:1 NS and Figures 2 (g)-(i) show the Pd, Au, and overlaid EDX maps for the 10:1 NS, respectively. The individual elemental EDX maps show uniform dispersion of Au and Pd, however closer evaluation of the overlaid maps reveals the presence of Pd-rich regions along the edges. Noticeably in Figure 2(h), which corresponds to the PdAu 10:1 NSs, the Au concentration along the edges is clearly lower than the central portion.

Additional EDX maps illustrating this pattern of dispersion are shown in the Supporting Information (see Figure S2). The presence of PdAu alloy and Pd-rich domain is also indicated by the XRD analysis. The XRD pattern shown in Supporting Information Figure S3 further supports the formation of crystalline NSs, with the characteristic peaks of Pd (111) and (200) observed at 2θ values of 40.1° and 46.6°, respectively for the monometallic Pd NSs.[29] The XRD pattern of the PdAu NSs shows a Pd (111) peak downshifted to 39.8 °, which was broader (FWHM = 0.46) compared to monometallic Pd NSs (FWHM = 0.32), typical of a PdAu alloy. An additional shoulder was also observed at 38.4°, attributed to the Au (111) peak but upshifted from the standard Au 111 diffraction peak.[30] A truly homogeneous alloy would be expected to display a single (111) diffraction peak for Au and Pd and the XRD analysis supports the EDX analysis indicating the presence of two alloy domains.

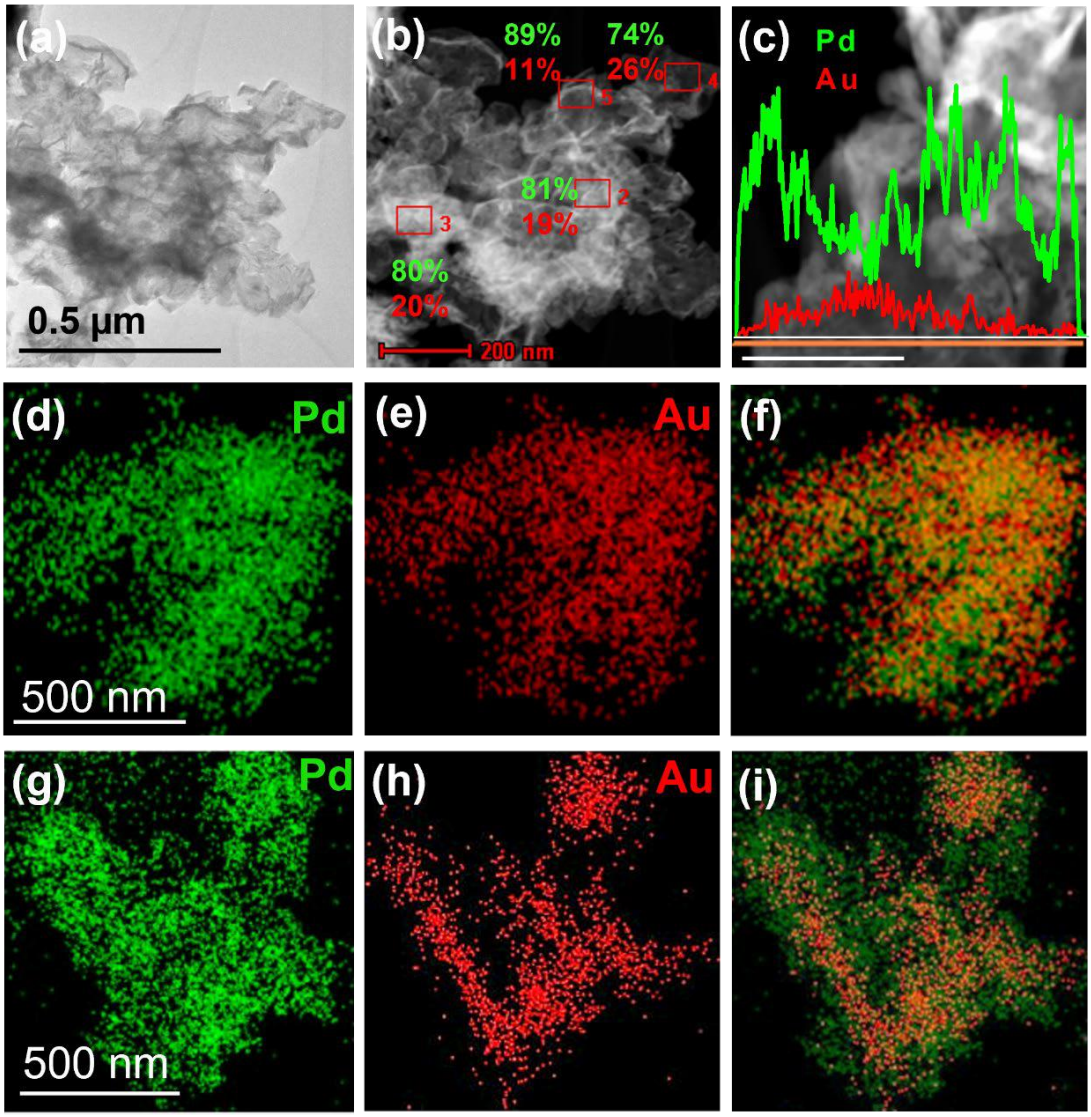

Figure 2: (a) TEM image of PdAu NSs 5:1, (b) STEM image and corresponding EDX quantification of atomic concentrations, (c) EDX line map of PdAu 5:1 NSs (scale bar is 100 nm), (d-f) Pd, Au and overlaid EDX maps for PdAu 5:1, (g-i) Pd, Au and overlaid EDX maps for PdAu 10:1 NSs.

XPS analysis was carried out to provide further insight into the modified electronic properties of the bimetallic NSs. Figure 3(a) compares the Pd 3d core level spectra of Pd, PdAu 10:1 and PdAu 5:1 NSs. The Pd $3d_{5/2}$ core level of the monometallic Pd NSs was centred at a BE of 335.3 eV, consistent with Pd(0). Minor oxide contributions were observed at 336.4 eV, corresponding to PdO and surface oxide species and a smaller shoulder peak at 337.8 eV, which is assigned to PdO_2.[29] The BE of Pd 3d was

negatively shifted from 335.3 eV in the Pd NSs to 334.9 eV in the PdAu NSs. These BE shifts indicate a change in the electronic structure and *d*-band modification of Pd, due to charge transfer between Au and Pd when they are alloyed. Peaks shifts were also observed in the Au 4f core level, shown in Figure 3(b). No Au was detected in the Pd NSs, as expected. The BE for Au(0) is usually reported at 84 eV[31] and the Au $4f_{7/2}$ peak of the Pd:Au 10:1 was centred at 83.9 eV, while the Pd:Au 5:1 peak was centred at 83.6 eV. This negative peak shift in the Au 4f BE can be attributed to the electronic modification of Au species by Pd.

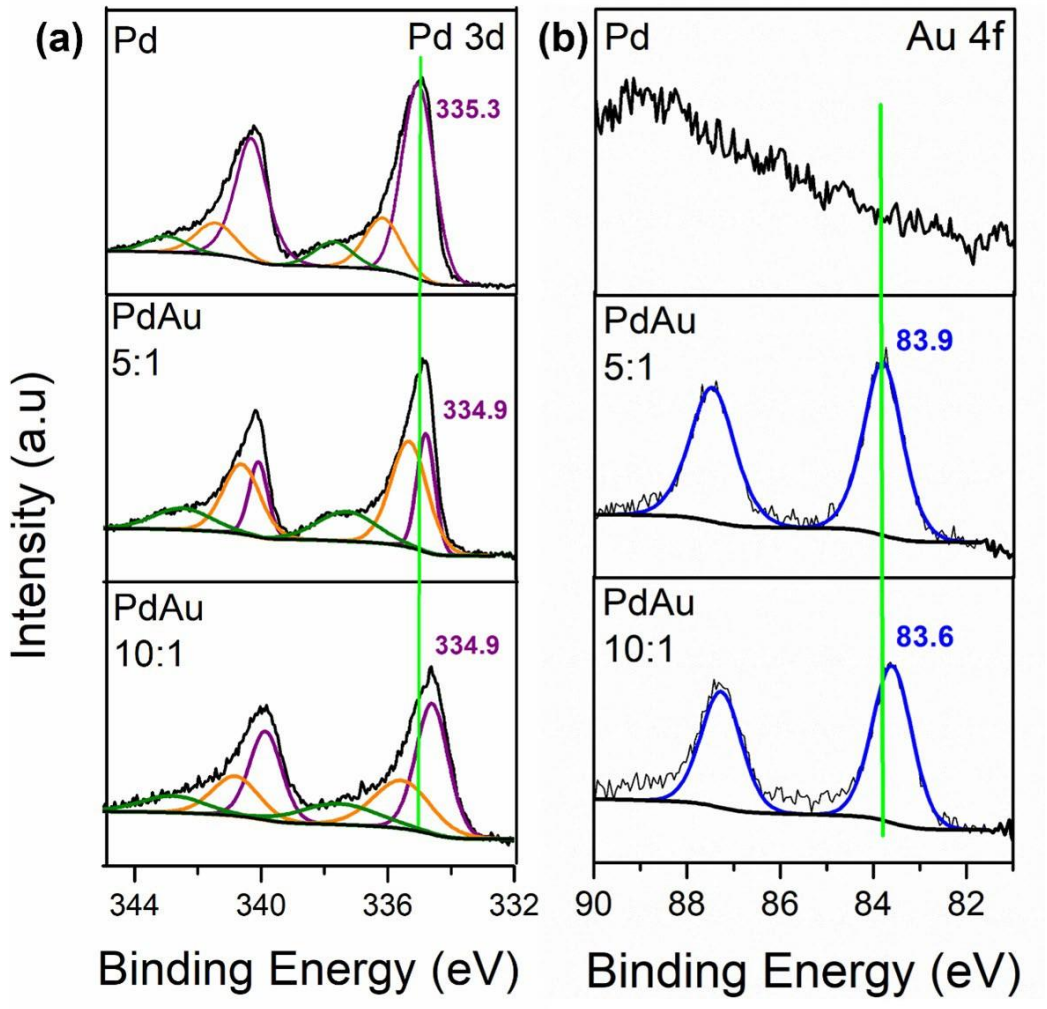

Figure 3: XPS analysis of (a) Pd 3d and (b) Au 4f core levels of Pd, PdAu 5:1 and 10:1 NS.

A number of reaction parameters such as the surfactant ligand, surfactant concentration, Au:Pd molar ratio, ascorbic acid concentration and temperature were altered to determine their effect on NS formation, which are summarised in Table S1 in Supporting Information. As outlined in Table S1 the optimal conditions for NS formation were using a C_{22}-QA surfactant at a concentration of 0.025 M, a surfactant:Pd molar ratio of 1:0.025, reaction temperature of 0 °C and 6 h. Under these conditions, tuning the Pd:Au molar ratio produces PdAu 10:1 or 5:1 NSs, as previously shown in Figures 1 and 2. Increasing the Au concentration further using a Pd:Au molar ratio of 2:1 gave a mixture of poorly defined NSs and NPs due to heterogeneous nucleation of the Au precursor, as shown in Figure S4 in the Supporting Information. Increasing the molar ratio of the Pd precursor relative to surfactant concentration (1:0.25) produced NSs but competitive growth of NPs was also evident as shown in Figure 4 (a)-(c). The higher surfactant concentration is required for surfactant templating growth of NSs and minimising the growth of NPs. Temperature was also a critical factor in the synthesis, with NSs only forming at an aging temperature of 0 °C and reactions at a higher temperature produced only irregular NPs. The head group of the surfactant also played a critical role in the synthesis. Xu *et al.*[27] reported that long chain alkyl ammonium salts with alkyl groups, carboxylates and pyridyl head groups all served as templates for Pd NSs, but this was not observed for the PdAu NSs, where the alkyl quaternary ammonium salt was the only capping agent successful in achieving a NS morphology. Substituting the methyl group on the ammonium salt for a carboxylic acid, formed irregular nanostructures, as shown in the TEM analysis, see Figure 4(d). While the carboxylic acid surfactant was not successful for the synthesis PdAu NSs it was effective for making monometallic Pd NS (Figure 4(e)), which may be attributed to the low coordinating ability of carboxylic acid groups towards Au. When the alkyl ammonium salt terminated with a pyridyl group was used, cuboctahedral nanocrystals were formed, as shown in Figure 4 (f).

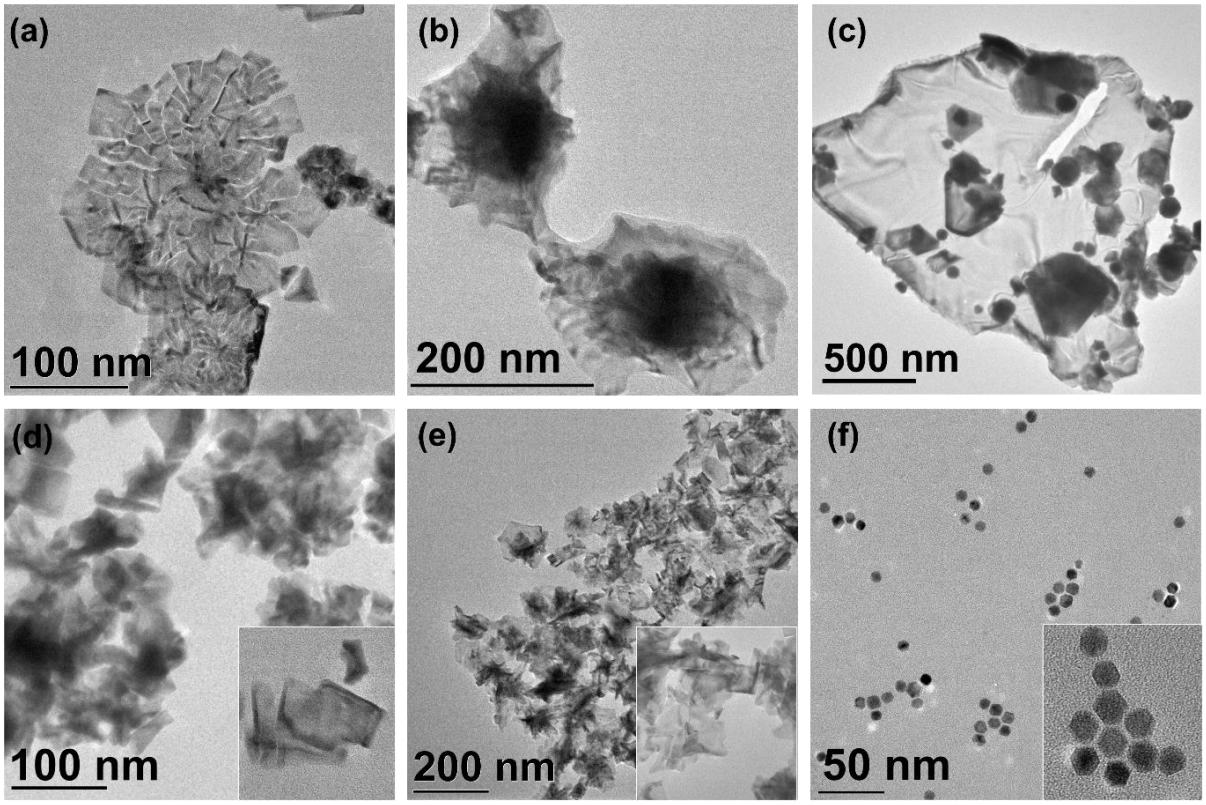

Figure 4: TEM images of nanostructures obtained with surfactant concentration of 0.025 M and Pd:Au molar ratio of (a) 5:1 (b) 2:1 and (c) 1:5. (d) PdAu nanostructures synthesized using C_{22}N-COOH (Br^-) surfactant, (e) Pd NSs synthesized using C_{22}-COOH (Br^-), (f) cuboctahedral NP formed using a C_{22}-Py (Br^-) surfactant.

Growth mechanism of PdAu alloy nanosheets

To understand the formation mechanism of the PdAu NSs, aliquots were taken from reaction solutions at various times and analysed by TEM. The TEM analysis was further correlated with XPS and EDX analysis of uncompleted reactions to determine changes in the chemical state and composition of the NSs. Figure 5(a) displays a TEM image 1 h after the reaction, using a Pd:Au molar ratio of 5:1, which shows the presence of small diameter NPs (~ 2 nm) dispersed in a carbon matrix consisting of the long chain alkyl ammonium salt. HR TEM of the NPs shown in Figure 5(a) inset show an interplanar distance of 0.235 nm which in is good agreement with the face centred cubic structure of Au (111).[32] As the reaction proceeds the formation of NSs is observed at 3 h, as shown in Figure 5(b).

EDX analysis of a NSs isolated from the incomplete reaction showed the presence of a Au-rich NSs, as shown in EDX the line scan in Figure 5(c). Correlating the TEM and EDX analysis with XPS analysis, (Figure 5(d)) this incomplete reaction mixture confirmed the presence of metallic Au, as indicated in the Au 4f spectra with the BE of 84 eV, consistent with Au^0 and indicating reduction of the Au precursor. The Pd 3d core level shows the presence of both metallic Pd^0 centred at 335.3 eV and Pd^{2+} centred at 337.8 eV, indicating partial reduction of the Pd precursor at this stage of the reaction.

Analysis of the peak areas in the deconvoluted Pd $3d_{5/2}$ core level determined that ~35 % of the Pd precursor had been reduced to Pd^0. In addition to Pd^0 and Pd^{2+} species there was a small peak at a BE of 336.5 eV, typically associated with electron deficient Pd species ($Pd^{\delta+}$) such as a surface oxide.[33] XPS analysis of NSs from the completed reaction (6 h) are also displayed in Figure 5(d). The Au 4f BE of the NSs after 6 h was downshifted with the Au $4f_{7/2}$ peak now centred at 83.6. eV. The corresponding Pd 3d core level of the NSs after 6 h showed primarily Pd^0, due to reduction of the remaining precursor and the Pd $3d_{5/2}$ peak position after 6 h was also downshifted to 334.9 eV, compared to the NS analysed at 3 h. This downshift is likely attributed to increased electron density of Pd associated with alloying. Negative shifts of both the Au 4f and Pd 3d core level bands in bimetallic species have been reported.[34]

Based on the ratio of the Au 4f to Pd 3d peaks, XPS analysis determined a Pd:Au ratio of 9.4:1 in the uncompleted reaction and 9:1 for the completed NS reaction, which is in excellent agreement with the starting molar ratio of the Pd and Au precursors (10:1). These studies imply that the formation mechanism of the PdAu NS is initiated by the formation of small diameter Au NP seeds dispersed in the long chain alkyl quaternary ammonium salt surfactant which serve as a template for the growth of NSs. The faster reduction of Au is understandable given the different standard reduction potential of Au and Pd ions ($AuCl_4^-$/Au, 1.002 V, $PdCl_4^{2-}$/Pd, 0.591 V).[35-36] Au-rich alloy NSs are initially formed and the Pd concentration increases with reduction of the precursor as the reaction proceeds. This mechanism accounts for the observed EDX mapping analysis showing the Pd-rich regions located around the NS edges, as after the Au precursor has been consumed, continued growth of the NS produces Pd-rich domains as identified by EDX.

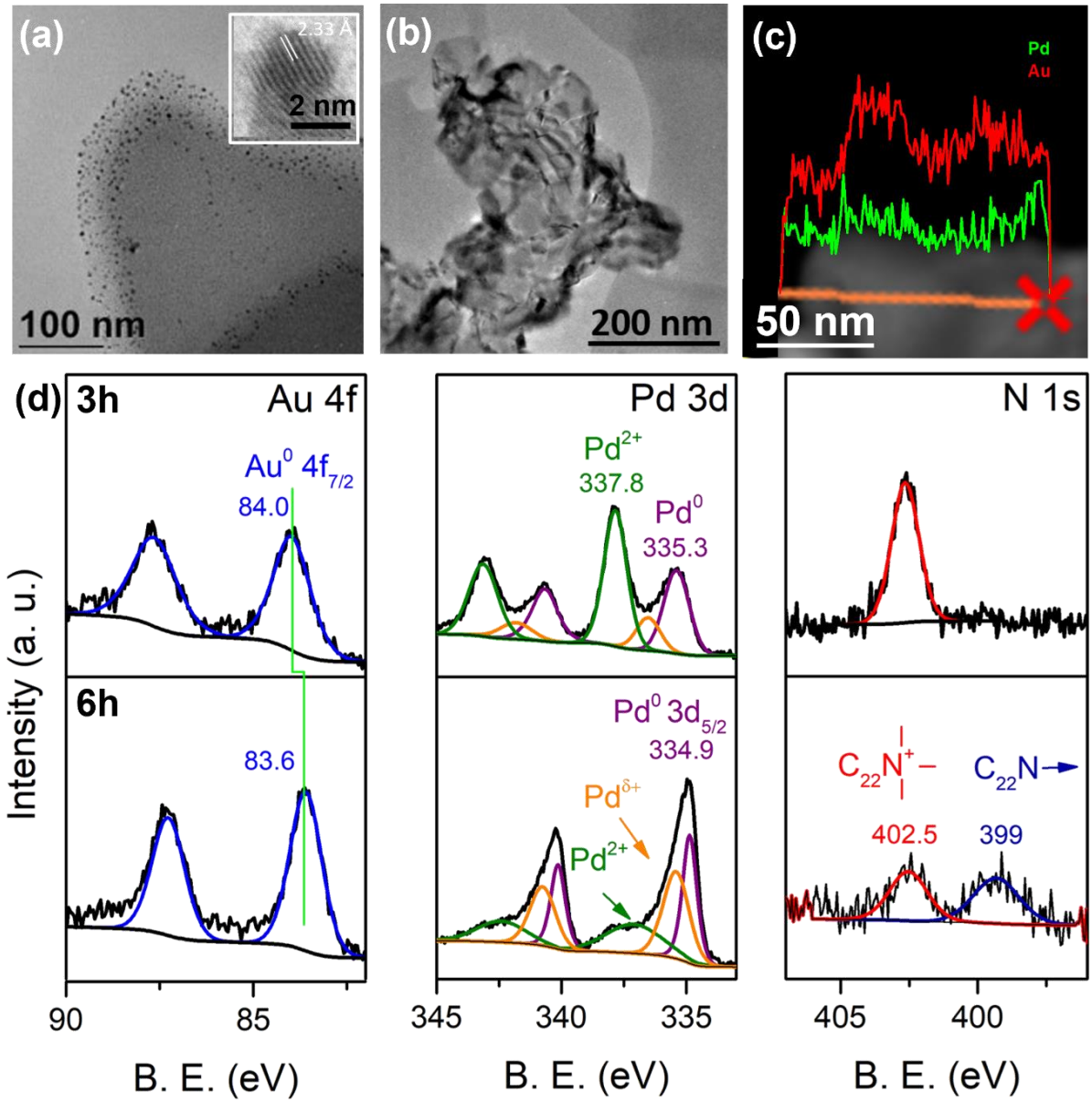

Figure 5: (a) TEM image 1 h after reaction showing NP formation, (b) TEM image from an incomplete reaction (3 h) showing formation of NSs, (c) EDX line map of NS after 3 h, (d) Au 4f, Pd 3d and N 1s XPS core levels from incomplete and complete NS reactions.

The evolution of changes to the NS surface chemistry during growth was also evaluated by assessing the N 1s core level which are shown in Figure 5(d). The N 1s core level of the incomplete reaction mixture showed a single peak at a BE of 402.5 eV, which is characteristic of the quaternary ammonium

salt.[37] The N 1s of the NSs formed showed the presence of two peaks, one centred at 402.5 eV due to the ammonium salt, and a second peak at a lower BE at 399 eV, which is characteristic of amine species or metal bound amines.[38] There are approximately equal amounts of these two N environments (52 % and 48 % attributed to species at a BE of 399 and 402.5 eV, respectively, based on the deconvoluted N 1s spectrum. As the reaction proceeds, there is also significant reduction in the Br^- ion species (see Supporting Information, Figure S5). Based on the N 1s and Br 3d signal the N:Br ratio in the incomplete reaction is 1:2.3 which falls to 1:0.54 in the NSs formed, suggesting that the surface of the NSs are passivated with a mixture of the non-coordinated quaternary ammonium salts (C_{22}-N^+Br^-) and a more electron-rich N functionality. Quaternary ammonium salts undergo C-N cleavage to form amines in the presence of many metals, which may explain the presence of the peak at 399 eV.[39] FTIR analysis of the surfactant and the NSs are shown in the Supporting Information Figure S6 and display significant peak broadening of the C-N vibration (950-1100cm^{-1}) for the Pd and PdAu NSs compared to the bulk quaternary ammonium salt.

Catalytic evaluation of nanosheets

The catalytic performance of the NSs was assessed in the Suzuki cross-coupling reaction of 4-iodoanisole (4-methoxyiodobenzene) and phenylboronic to give 4-methoxybiphenyl. Table S2 in the Supporting Information summaries some literature reports of Suzuki cross coupling reactions under conventional heating and light driven catalysts.[40-49]

The photocatalytic enhancement was evaluated by conducting reactions under visible light irradiation using an LED light source and in the dark (see Experimental Section for further details). NMR analysis confirmed no homocoupling of the boronic acid occurred and the cross coupled biphenyl was the only product formed in the reaction (See Supporting Information, Figure S7). The effect of catalyst concentration, temperature and reaction time were also evaluated. To investigate the effect of the NS surface chemistry, NSs prepared via a CO-assisted route were also synthesized and their catalytic

performance was studied as a comparison to the surfactant-assisted NSs. The catalytic activity of the Pd and PdAu (5:1) NSs in the Suzuki cross-coupling reaction show two distinct enhancement effects, one attributed to the alloy effect and the other to a photocatalytic enhancement. Figures 6(a) and (b) show reaction yields obtained for Pd and PdAu NSs, respectively, under light illumination and in the dark, at reaction times of 1, 2 and 3 h. The Pd catalyst concentration in both reactions was 0.1 mol % *i.e.* the Pd concentration was equivalent in the reactions catalysed by monometallic and bimetallic NSs. Both Pd and PdAu NSs showed improved yields under light illumination. After 3 h the yield obtained for the Pd NSs increased from 0 to 51 % under light illumination, while the PdAu NSs increased from 30 % (dark) to 98 % (LED). One notable difference between the Pd and PdAu NSs was the longer induction period displayed by the Pd catalysts compared to the bimetallic catalyst. Induction periods are commonly observed with nanoparticle catalysed Suzuki reactions and often attributed to the formation of active Pd species that are generated from the surface.[50] After 1 h at a 0.1 mol % Pd loading, no product was formed using Pd NSs, compared to a 32 % yield after 1 h for the PdAu NSs. The higher performance of Pd alloys toward Suzuki coupling has been reported in numerous alloys and be may attributed to the increased electron density of the Pd, which correlates with XPS analysis, indicating the Pd is more electron-rich in the bimetallic NSs.[51-52] The increased electron of the Pd facilitates oxidative addition of the aryl halide.[53]

Nanoparticle catalysed Suzuki reactions are known to depend on catalyst concentration. Increasing the catalyst concentration can sometimes decrease the activity due to catalyst aggregation. The reaction was evaluated at catalyst concentrations of 0.1 and 0.2 mol %. The same reactivity trend was observed using 0.2 mol % loading, with the bimetallic NSs outperforming the monometallic Pd NSs and yields were greater under visible light irradiation compared to reactions carried out in the dark, as shown in Figures 6 (c) and (d). The higher catalyst loading improved yields generally, *e.g.* Pd NSs showed no activity in the dark at 0.1 mol % but this increased to 38 % at 0.2 mol %. For the PdAu NSs there was an even larger yield improvement under light irradiation, increasing from 44 % at 0.1 mol %

to 93 % at 0.2 mol% after a 2 h reaction time. A yield of 93 % after 2 h for a Suzuki reaction carried out at room temperature is significant.

Figures 6 (e) and (f) highlight the effect of using a bimetallic catalyst compared to a monometallic catalyst. The PdAu NSs display better photocatalytic enhancement compared to the monometallic NSs having higher yields at all reaction times. Even in the absence of light, the PdAu NSs produce higher yields that the Pd NSs, indicating the presence of the alloy enhancement. XPS analysis revealed that the surface is electron rich in the PdAu NSs, which is known to favour the oxidative addition of the aryl halide and this may account for the higher activity of the PdAu NSs even in the absence of light. The combined catalytic enhancement effect when using light and a bimetallic catalyst is significant; at a Pd concentration of 0.1 mol % using monometallic Pd NSs in the dark, no product was formed after 3 h. Keeping the same Pd concentration, but using the PdAu NSs and under visible light illumination, the reaction goes to completion in the same time period. Commercial Pd on carbon was also evaluated as a reference catalyst to compare performance improvement when using a NS morphology. At a catalyst concentration of 0.2 mol % the yield obtained at room temperature was only 16 % after 3 h with commercial Pd/C.

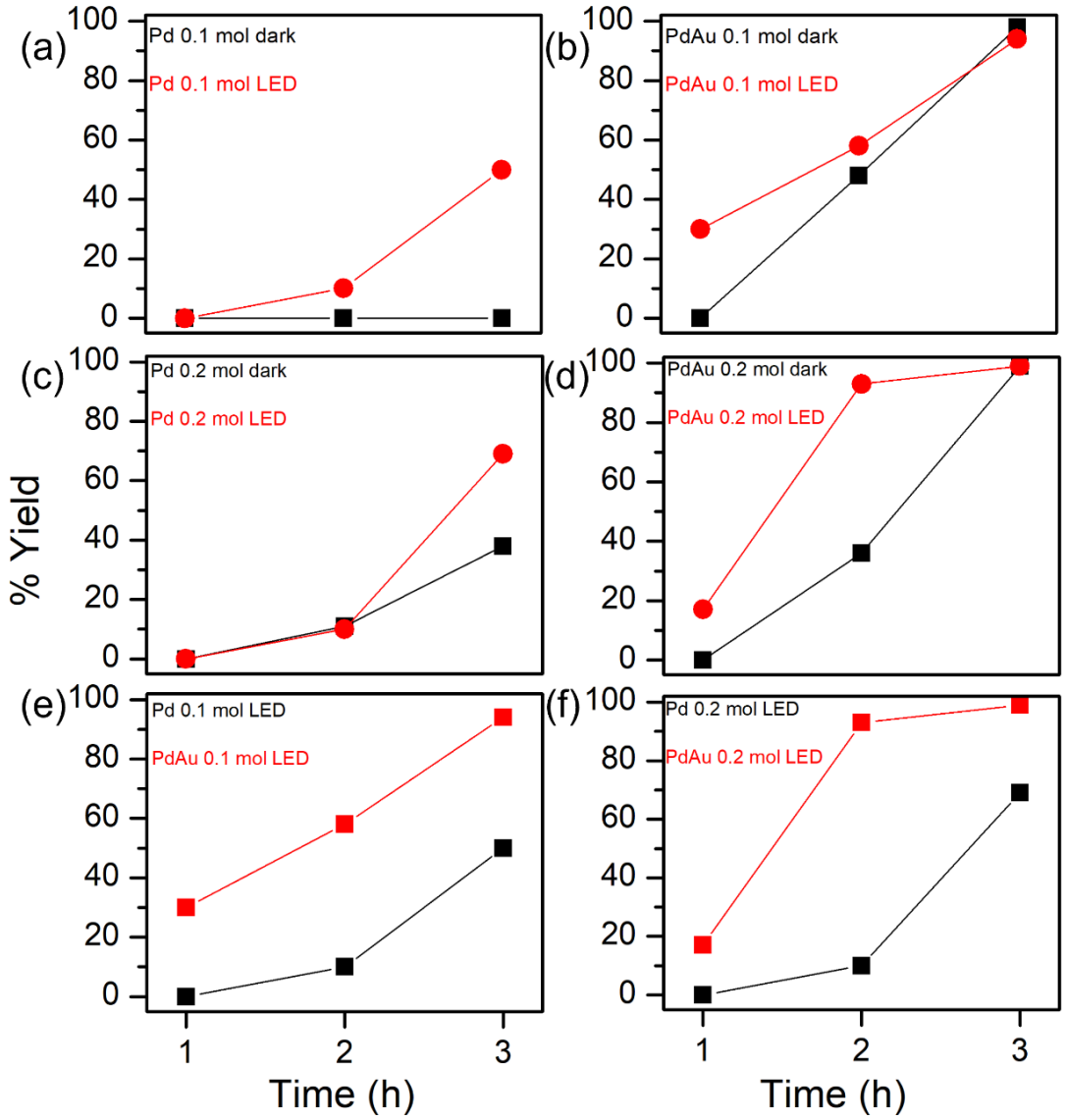

Figure 6: (a-f) Catalytic evaluation plots of the cross-coupling Suzuki reaction catalysed using Pd and PdAu NSs at 0.1 and 0.2 mol% under visible light irradiation and in the dark.

Catalysis by plasmonic nanostructures can be attributed to hot carriers or photothermal effects, and both have been observed in Suzuki cross-coupling reactions.[16, 54] Teranishi and co workers showed that plasmon enhanced catalytic activity of Pd hexagonal nanoplates was dominantly driven by hot electron injection.[49] In AuPd nanostructures photothermal effects can be significant and give rise to considerable increases in the solution temperature e.g. Buskens *et al.*[55], reported Pd NP tipped Au

nanorods increased the solution temperature from 25 to 60 °C under illumination but the large heating effect was attributed to the photothermal heat generation by the Au nanorod. To assess photothermal effects in the nanosheets, the temperature of the reaction solvent (EtOH:water) in the presence of 0.2 mol% catalyst was monitored over a 3 h period. A small increase of 3 °C (average of 3 runs) was observed for AuPd NSs while negligible increase was observed for the Pd NSs. The minimal heating effect is attributed to the low absorption cross section of the NSs and the use of LED illumination.[56] While a photothermal contribution cannot be ruled out, as the bulk temperature of the reaction solution may differ substantially from the local surface temperature of the nanosheets, hot electrons that undergo oxidative addition with the aryl halide rather than a photothermal effect is likely the dominant mechanism of the photocatalyzed Suzuki reaction.

The high catalytic performance of the NSs can also be attributed to their 2D morphology, with a high density of surface atoms. The presence of weakly coordinating ammonium salts should play a role in influencing the catalyst activity. To further evaluate the role of capping ligands on the catalytic behaviour of the NSs in the Suzuki cross coupling reaction, CO-assisted Pd NSs alloyed with traditional plasmonic metals were synthesized. The strong adsorption of CO onto Pd (111) facets produces well defined hexagonal NSs, as showed in the low-resolution TEM image in Figure 7(a). In addition to CO, organic stabilising ligands PVP and the CTAB are also required to prevent aggregation of the NSs (see Experimental Section for further details). The inset shows the image of a NS solution which have a characteristic blue appearance. The UV-vis spectra of the surfactant-assisted and CO-assisted NSs are shown in Figure 7(b). The surfactant-assisted NSs show increasing absorption across the visible spectrum (400-900 nm). The Pd and AuPd and spectra are similar and is attributed to the relatively low Au concentration in the nanosheets.[57] Furthermore, the absence of a peak observed at 530 nm i.e. the LSPR for Au NPs further indicates that Au is present within the nanosheets with very few spherical Au NPs in the suspension.[58] In contrast, the PdAu CO-assisted NSs display an increase in absorption around 500 nm associated with the presence of the Au NPs that formed from heterogeneous nucleation of the Au precursor. TEM analysis confirmed that the synthesis of PdAu NS

using a CO-assisted method produced a mixture of NSs and nanoparticles, due to heterogeneous nucleation of the Au (see Supporting Information, Figure S8). The surface chemistry of the CO-assisted NS was investigated by XPS. Figure 7(c) shows the N 1s core level of the Pd, PdAg and PdAu NSs. The Pd NSs showed the presence of two N peaks, one at 398.8 eV attributed to the PVP ligands and another at402.6 eV, attributed to the quaternary ammonium salt surfactant.[59] The PdAu and PdAg NSs displayed primarily one peak associated with the PVP ligands, with minor peaks associated to the ammonium surfactant.

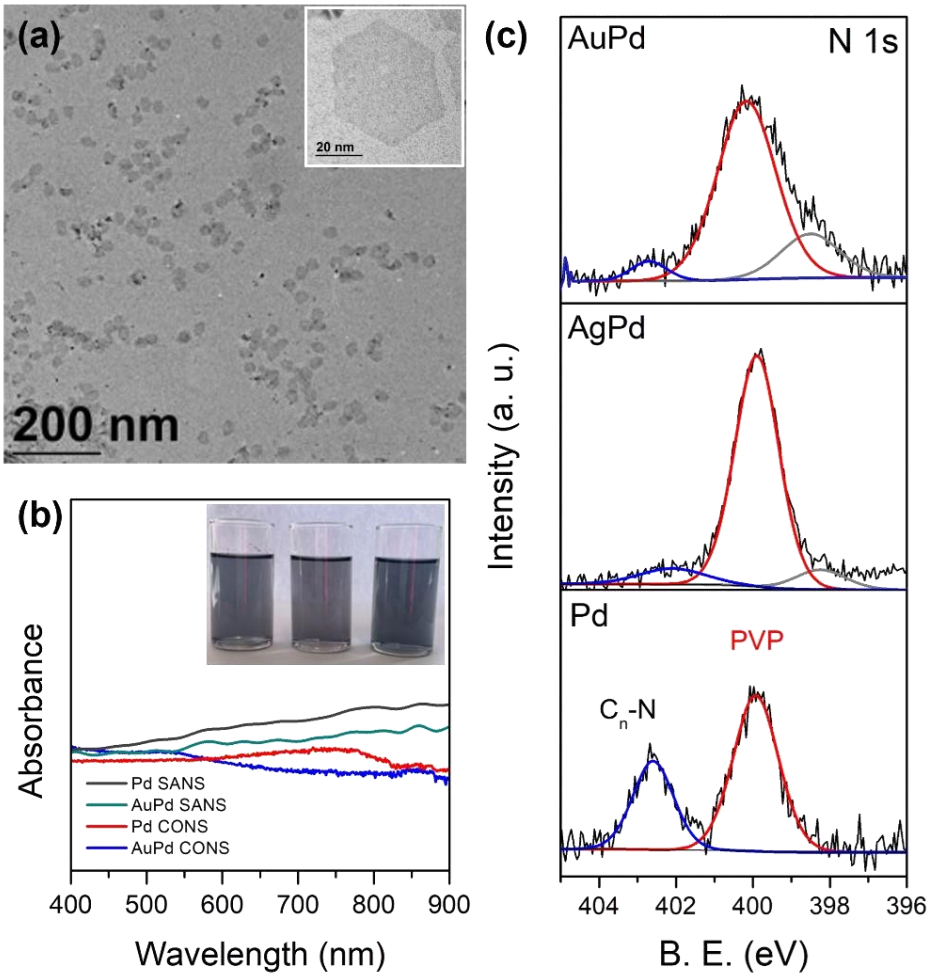

Figure 7: (a) Low resolution TEM image, (b) uv-visible spectra of surfactant-assisted and CO-assisted NSs and (c) N 1s core level of Pd, PdAg and PdAu CO-assisted NSs.

Figure 8(a) compares the reaction yields obtained for surfactant-assisted NSs and CO-assisted NSs in the Suzuki cross coupling reaction, carried out at 0.2 mol% in the dark and under light irradiation at

room temperature and at 80 °C. In contrast to the excellent activity observed for the surfactant-assisted NSs, the CO-assisted NSs showed no activity at room temperature and there was no impact of light illumination for reactions carried out at room temperature when catalysed by Pd, PdAg or PdAu. A catalyst concentration of at least 3 mol% was required before any product was formed at room temperature. While the surfactant-assisted and CO-assisted NSs have structural differences, *e.g.* the surfactant-assisted NSs are thicker and larger (~100 nm) compared to the CO-assisted NSs (45 nm),[23, 27] the poor catalytic activity of the CO-assisted NS is primarily attributed to the heavily passivated surface due to the presence of CO, PVP and CTAB. The reaction temperature was increased to 80 °C to promote remote removal of physisorbed surface ligands.[50] The elevated reaction temperature resulted in higher yields, as shown in Figure 8(a). The yield of the CO-assisted NSs synthesized at a temperature of 80 °C in the dark remained poor, at only 18%, but there was a significant photocatalytic enhancement in the presence of light, with a yield up to 99 % obtained. A similar photocatalytic enhancement was observed for the CO-assisted PdAg NSs, with the yield increasing to 40 % in the dark to 96 % under light. Although the PdAu CO-assisted NSs contained a mixture of sheets and Au NPs, a higher yield was obtained under illumination (71 %) compared to in the dark (26 %), due to the presence of a discreet plasmonic component (Au NPs) and a catalytic component (Pd NSs). As observed with the surfactant-assisted NSs, the bimetallic CO-assisted NSs showed superior performance to the monometallic Pd NS, both the absence and presence of light irradiation, attributed to the synergistic alloy effect.

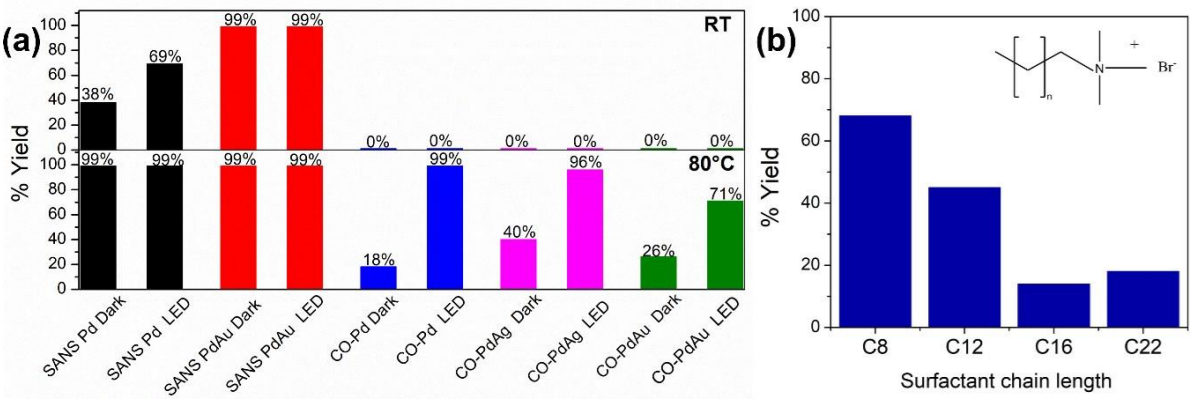

Figure 8: (a) Reaction yields obtained from surfactant assisted NSs (SANS) and CO-assisted NSs (CO-NS) after 3 h with 0.2 mol % Pd at room temperature (RT) and at a temperature of 80 °C. Note that the PdAu CO-assisted NSs is comprised of a mixture of Au NPs and NSs and (b) Reaction yields of biphenyl product obtained from CO-assisted Pd NSs synthesized using alkyl quaternary ammonium salts with different chain lengths (C8, C16, C12 and C22).

Efforts to partially remove surface ligands, which would be advantageous for catalysis, proved challenging. Solvent washing was ineffective, while chemical cleaning using $NaBH_4$ led to dissolution of the NSs as confirmed by TEM analysis (see Supporting Information Figure S10). By alternating the capping ligands used in the synthesis reaction it was found that the presence of CO, PVP and a long chain alkyl ammonium salt, *e.g.* CTAB, were all essential for successful NS formation. When the PVP was substituted for other polymers, such as PVA (polyvinylalcohol) no NSs formed due to the insufficient stabilising ability of the polymer. When the alkyl quaternary ammonium salt was removed from the synthesis, NSs did not form, however ammonium salts with different alkyl chain lengths could be exchanged. Changing the surfactant chain length did not impact on the 2D morphology of the NSs but there was as an increase in their mean size when synthesized using a shorter chain length surfactant. As shown in the size distribution analysis in Figure S11 (Supporting Information) the mean width for the NSs using C22, C16, C12 and C8 were 29 nm, 22 nm, 43 nm, 57 nm, respectively. Figure 8(b) shows the yield of the biphenyl after 3 h at 80 °C, using CO-assisted NSs prepared with different

alkyl chain lengths. The product yield increased with decreasing chain length going from 68 % for C8 to 18 % for C22. While it is difficult to disentangle a potential size effect on catalytic behaviour, the chain length of the ammonium salt surfactant has an impact on the catalytic behaviour. The higher performance of the shorter chain length is most likely attributed to the steric effect associated with a longer alkyl chain length impeding access to the surface of the NSs.[60] This study further highlights the importance of considering the impact of the capping ligands on the catalytic performance of the nanostructures with similar morphology.

4.4 Conclusions

We report a one pot synthesis of surfactant-templated PdAu NSs. TEM, EDX and XPS analysis indicate that the growth mechanism of the NSs is initiated through the formation of Au NP seeds dispersed within the quaternary ammonium salt surfactant. These NP seeds grow into 2D PdAu NSs and due to fast reduction of the Au precursor the edges of the NSs are Pd-rich as demonstrated by EDX. The catalytic and photocatalytic activity of the Pd and PdAu NSs were evaluated in room temperature Suzuki coupling reactions under light and dark conditions. A significant increase in product yields were observed under visible light illumination and the PdAu NSs showed the greatest photocatalytic enhancement compared to Pd NSs. The catalytic activity is attributed to the 2D morphology of the NSs, the electron rich Pd surface and the presence of weakly bound capping surface ligands. We further synthesized CO-assisted NSs to gain insight into the impact of surface chemistry using catalysts with a similar 2D morphology. A comparative study shows that the catalyst surface chemistry has a significant impact on both the catalytic and photocatalytic behaviour of ligand-stabilised NSs, with the heavily passivated CO-assisted NSs having poor reactivity. Both the surfactant-assisted and CO-assisted NSs showed the same trend with the bimetallic NSs displaying greater lighter enhancement compared to monometallic Pd NS. This work highlights the importance of considering the catalyst surface chemistry in addition to catalyst morphology for light enhanced reactions.

Author Information

*To whom correspondence should be addressed: Tel: +353 (0)21 4205143. E-mail: g.collins@ucc.ie

Orcid iD: 0000-0002-5950-2457

Notes

The authors declare no competing financial interest.

Supporting information

Additional analysis and results can be found in the supporting information. These include, TEM, XRD, EDX, FTIR and XPS survey scan of the surfactant assisted nanosheets, TEM and size distribution profiles of the CO assisted nanosheets, NMR spectra of the product of the Suzuki reaction, table of reaction parameters, literature results and TOF of each catalyst

Acknowledgements

This research was funded by Science Foundation Ireland (AMBER Grant No: 12/RC2278_P2). We thank Dr. Raman Bekarevich and Dr Eoin McCarthy from the Advanced Microscopy Laboratory at Trinity College Dublin and the Bernal Institute at University of Limerick for XPS.

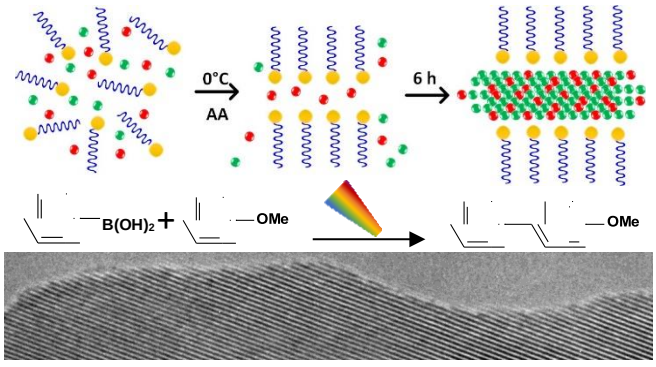

4.5 References

1. Ling, T.; Wang, J.-J.; Zhang, H.; Song, S.-T.; Zhou, Y.-Z.; Zhao, J.; Du, X.-W., Freestanding Ultrathin Metallic Nanosheets: Materials, Synthesis, and Applications. *Advanced Materials* **2015,** *27* (36), 5396-5402.
2. Feng, J.; Gao, C.; Yin, Y., Stabilization of noble metal nanostructures for catalysis and sensing. *Nanoscale* **2018,** *10* (44), 20492-20504.
3. Yang, T.-H.; Ahn, J.; Shi, S.; Wang, P.; Gao, R.; Qin, D., Noble-Metal Nanoframes and Their Catalytic Applications. *Chemical Reviews* **2021,** *121* (2), 796-833.
4. Chen, Y.; Fan, Z.; Zhang, Z.; Niu, W.; Li, C.; Yang, N.; Chen, B.; Zhang, H., Two-Dimensional Metal Nanomaterials: Synthesis, Properties, and Applications. *Chem Rev* **2018,** *118* (13), 6409-6455.
5. Luo, M.; Yang, Y.; Sun, Y.; Qin, Y.; Li, C.; Li, Y.; Li, M.; Zhang, S.; Su, D.; Guo, S., Ultrathin two-dimensional metallic nanocrystals for renewable energy electrocatalysis. *Materials Today* **2019,** *23*, 45-56.
6. Ma, Y.; Li, B.; Yang, S., Ultrathin two-dimensional metallic nanomaterials. *Materials Chemistry Frontiers* **2018,** *2* (3), 456-467.
7. Gupta, A.; Sakthivel, T.; Seal, S., Recent development in 2D materials beyond graphene. *Progress in Materials Science* **2015,** *73*, 44-126.
8. He, C.; Tao, J.; Shen, P. K., Solid Synthesis of Ultrathin Palladium and Its Alloys' Nanosheets on RGO with High Catalytic Activity for Oxygen Reduction Reaction. *ACS Catalysis* **2018,** *8* (2), 910-919.
9. Fan, Z.; Huang, X.; Tan, C.; Zhang, H., Thin metal nanostructures: synthesis, properties and applications. *Chemical Science* **2015,** *6* (1), 95-111.
10. Wang, J.; Du, C.; Wei, Q.; Shen, W., Two-Dimensional Pd Nanosheets with Enhanced Catalytic Activity for Selective Hydrogenation of Nitrobenzene to Aniline. *Energy & Fuels* **2021,** *35* (5), 4358-4366.
11. Yin, J.; Wang, J.; Ma, Y.; Yu, J.; Zhou, J.; Fan, Z., Recent Advances in the Controlled Synthesis and Catalytic Applications of Two-Dimensional Rhodium Nanomaterials. *ACS Materials Letters* **2021,** *3* (1), 121-133.
12. Zhang, Z.; Zhang, C.; Zheng, H.; Xu, H., Plasmon-Driven Catalysis on Molecules and Nanomaterials. *Accounts of Chemical Research* **2019,** *52* (9), 2506-2515.
13. Li, S.; Miao, P.; Zhang, Y.; Wu, J.; Zhang, B.; Du, Y.; Han, X.; Sun, J.; Xu, P., Recent Advances in Plasmonic Nanostructures for Enhanced Photocatalysis and Electrocatalysis. *Advanced Materials* **2021,** *33* (6), 2000086.
14. Liu, D.; Xue, C., Plasmonic Coupling Architectures for Enhanced Photocatalysis. *Advanced Materials* **2021,** *33* (46), 2005738.
15. Gu, Q.; Jia, Q.; Long, J.; Gao, Z., Heterogeneous Photocatalyzed C−C Cross-coupling Reactions Under Visible-light and Near-infrared Light Irradiation. *ChemCatChem* **2019,** *11* (2), 669-683.
16. Gellé, A.; Jin, T.; de la Garza, L.; Price, G. D.; Besteiro, L. V.; Moores, A., Applications of Plasmon-Enhanced Nanocatalysis to Organic Transformations. *Chemical Reviews* **2020,** *120* (2), 986-1041.
17. Wang, F.; Li, C.; Chen, H.; Jiang, R.; Sun, L.-D.; Li, Q.; Wang, J.; Yu, J. C.; Yan, C.-H., Plasmonic Harvesting of Light Energy for Suzuki Coupling Reactions. *Journal of the American Chemical Society* **2013,** *135* (15), 5588-5601.
18. Quiroz, J.; Barbosa, E. C. M.; Araujo, T. P.; Fiorio, J. L.; Wang, Y.-C.; Zou, Y.-C.; Mou, T.; Alves, T. V.; de Oliveira, D. C.; Wang, B.; Haigh, S. J.; Rossi, L. M.; Camargo, P. H. C., Controlling Reaction Selectivity over Hybrid Plasmonic Nanocatalysts. *Nano Letters* **2018,** *18* (11), 7289-7297.
19. Verma, P.; Mori, K.; Kuwahara, Y.; Raja, R.; Yamashita, H., Plasmonic nanocatalysts for visible-NIR light induced hydrogen generation from storage materials. *Materials Advances* **2021,** *2* (3), 880-906.

20. Collins, G.; Lonergan, A.; McNulty, D.; Glynn, C.; Buckley, D.; Hu, C.; O'Dwyer, C., Semiconducting Metal Oxide Photonic Crystal Plasmonic Photocatalysts. *Advanced Materials Interfaces* **2020,** *7* (8), 1901805.
21. Huang, X.; Tang, S.; Mu, X.; Dai, Y.; Chen, G.; Zhou, Z.; Ruan, F.; Yang, Z.; Zheng, N., Freestanding palladium nanosheets with plasmonic and catalytic properties. *Nature Nanotechnology* **2011,** *6* (1), 28-32.
22. Yu, Q.; Yang, Y., Synthesis of Two-dimensional Metallic Nanosheets: From Elemental Metals to Chemically Complex Alloys. *ChemNanoMat* **2020,** *6* (12), 1683-1711.
23. Li, Y.; Yan, Y.; Li, Y.; Zhang, H.; Li, D.; Yang, D., Size-controlled synthesis of Pd nanosheets for tunable plasmonic properties. *CrystEngComm* **2015,** *17* (8), 1833-1838.
24. Yang, N.; Zhang, Z.; Chen, B.; Huang, Y.; Chen, J.; Lai, Z.; Chen, Y.; Sindoro, M.; Wang, A.-L.; Cheng, H.; Fan, Z.; Liu, X.; Li, B.; Zong, Y.; Gu, L.; Zhang, H., Synthesis of Ultrathin PdCu Alloy Nanosheets Used as a Highly Efficient Electrocatalyst for Formic Acid Oxidation. *Advanced Materials* **2017,** *29* (29), 1700769.
25. Fan, J.; Yu, S.; Qi, K.; Liu, C.; Zhang, L.; Zhang, H.; Cui, X.; Zheng, W., Synthesis of ultrathin wrinkle-free PdCu alloy nanosheets for modulating d-band electrons for efficient methanol oxidation. *Journal of Materials Chemistry A* **2018,** *6* (18), 8531-8536.
26. Hong, J. W.; Kim, Y.; Wi, D. H.; Lee, S.; Lee, S.-U.; Lee, Y. W.; Choi, S.-I.; Han, S. W., Ultrathin Free-Standing Ternary-Alloy Nanosheets. *Angewandte Chemie International Edition* **2016,** *55* (8), 2753-2758.
27. Xu, D.; Liu, X.; Lv, H.; Liu, Y.; Zhao, S.; Han, M.; Bao, J.; He, J.; Liu, B., Ultrathin palladium nanosheets with selectively controlled surface facets. *Chemical Science* **2018,** *9* (19), 4451-4455.
28. Yang, M.; Wang, Z.; Wang, W.; Liu, C.-j., Synthesis of AuPd alloyed nanoparticles via room-temperature electron reduction with argon glow discharge as electron source. *Nanoscale Research Letters* **2014,** *9* (1), 405.
29. Pramanick, B.; Kumar, T.; Halder, A.; Siril, P. F., Engineering the morphology of palladium nanostructures to tune their electrocatalytic activity in formic acid oxidation reactions. *Nanoscale Advances* **2020,** *2* (12), 5810-5820.
30. Dong, Y.; Chen, Q.; Cheng, X.; Li, H.; Chen, J.; Zhang, X.; Kuang, Q.; Xie, Z., Optimization of gold–palladium core–shell nanowires towards H2O2 reduction by adjusting shell thickness. *Nanoscale Advances* **2020,** *2* (2), 785-791.
31. Anderson, D. P.; Alvino, J. F.; Gentleman, A.; Qahtani, H. A.; Thomsen, L.; Polson, M. I. J.; Metha, G. F.; Golovko, V. B.; Andersson, G. G., Chemically-synthesised, atomically-precise gold clusters deposited and activated on titania. *Physical Chemistry Chemical Physics* **2013,** *15* (11), 3917-3929.
32. Shi, Y.; Huang, J.-K.; Jin, L.; Hsu, Y.-T.; Yu, S. F.; Li, L.-J.; Yang, H. Y., Selective Decoration of Au Nanoparticles on Monolayer MoS2 Single Crystals. *Sci Rep* **2013,** *3* (1), 1839.
33. Maize, M.; El-Boraey, H. A.; Ayad, M. I.; Holmes, J. D.; Collins, G., Controlled morphology and dimensionality evolution of NiPd bimetallic nanostructures. *Journal of Colloid and Interface Science* **2021,** *585*, 480-489.
34. Zhu, X.; Guo, Q.; Sun, Y.; Chen, S.; Wang, J.-Q.; Wu, M.; Fu, W.; Tang, Y.; Duan, X.; Chen, D.; Wan, Y., Optimising surface d charge of AuPd nanoalloy catalysts for enhanced catalytic activity. *Nature Communications* **2019,** *10* (1), 1428.
35. Polotnyanko, N. A.; Khodakovskii, I. L., Thermodynamic properties of Pd chloride complexes and the Pd2+(aq) ion in aqueous solutions. *Geochemistry International* **2014,** *52* (1), 46-56.
36. Lingane, J. J., Standard potentials of half-reactions involving + 1 and + 3 gold in chloride medium: Equilibrium constant of the reaction AuCl4− + 2Au + 2Cl− = 3AuCl2−. *Journal of Electroanalytical Chemistry (1959)* **1962,** *4* (6), 332-342.
37. Graf, N.; Yegen, E.; Gross, T.; Lippitz, A.; Weigel, W.; Krakert, S.; Terfort, A.; Unger, W. E. S., XPS and NEXAFS studies of aliphatic and aromatic amine species on functionalized surfaces. *Surface Science* **2009,** *603* (18), 2849-2860.

38. Truica-Marasescu, F.; Wertheimer, M. R., Nitrogen-Rich Plasma-Polymer Films for Biomedical Applications. *Plasma Processes and Polymers* **2008,** *5* (1), 44-57.
39. Wang, Z.-X.; Yang, B., Chemical transformations of quaternary ammonium salts via C–N bond cleavage. *Organic & Biomolecular Chemistry* **2020,** *18* (6), 1057-1072.
40. Xu, J.; Wilson, A. R.; Rathmell, A. R.; Howe, J.; Chi, M.; Wiley, B. J., Synthesis and Catalytic Properties of Au–Pd Nanoflowers. *ACS Nano* **2011,** *5* (8), 6119-6127.
41. Swain, S.; M. B, B.; Kandathil, V.; Bhol, P.; Samal, A. K.; Patil, S. A., Controlled Synthesis of Palladium Nanocubes as an Efficient Nanocatalyst for Suzuki–Miyaura Cross-Coupling and Reduction of p-Nitrophenol. *Langmuir* **2020,** *36* (19), 5208-5218.
42. Xiao, Q.; Sarina, S.; Jaatinen, E.; Jia, J.; Arnold, D. P.; Liu, H.; Zhu, H., Efficient photocatalytic Suzuki cross-coupling reactions on Au–Pd alloy nanoparticles under visible light irradiation. *Green Chemistry* **2014,** *16* (9), 4272-4285.
43. Koohgard, M.; Hosseini-Sarvari, M., Enhancement of Suzuki–Miyaura coupling reaction by photocatalytic palladium nanoparticles anchored to TiO2 under visible light irradiation. *Catalysis Communications* **2018,** *111*, 10-15.
44. Chatterjee, S.; Bhattacharya, S. K., Size-Dependent Catalytic Activity and Fate of Palladium Nanoparticles in Suzuki-Miyaura Coupling Reactions. *ACS Omega* **2018,** *3* (10), 12905-12913.
45. Xiao, Q.; Sarina, S.; Bo, A.; Jia, J.; Liu, H.; Arnold, D. P.; Huang, Y.; Wu, H.; Zhu, H., Visible Light-Driven Cross-Coupling Reactions at Lower Temperatures Using a Photocatalyst of Palladium and Gold Alloy Nanoparticles. *ACS Catalysis* **2014,** *4* (6), 1725-1734.
46. Raza, F.; Yim, D.; Park, J. H.; Kim, H.-I.; Jeon, S.-J.; Kim, J.-H., Structuring Pd Nanoparticles on 2H-WS2 Nanosheets Induces Excellent Photocatalytic Activity for Cross-Coupling Reactions under Visible Light. *Journal of the American Chemical Society* **2017,** *139* (41), 14767-14774.
47. Hosseini-Sarvari, M.; Bazyar, Z., Visible Light Driven Photocatalytic Cross-Coupling Reactions on Nano Pd/ZnO Photocatalyst at Room-Temperature. *ChemistrySelect* **2018,** *3* (6), 1898-1907.
48. Huang, X.; Li, Y.; Chen, Y.; Zhou, H.; Duan, X.; Huang, Y., Plasmonic and catalytic AuPd nanowheels for the efficient conversion of light into chemical energy. *Angewandte Chemie (International ed. in English)* **2013,** *52* (23), 6063-7.
49. Trinh, T. T.; Sato, R.; Sakamoto, M.; Fujiyoshi, Y.; Haruta, M.; Kurata, H.; Teranishi, T., Visible to near-infrared plasmon-enhanced catalytic activity of Pd hexagonal nanoplates for the Suzuki coupling reaction. *Nanoscale* **2015,** *7* (29), 12435-12444.
50. Collins, G.; Davitt, F.; O'Dwyer, C.; Holmes, J. D., Comparing Thermal and Chemical Removal of Nanoparticle Stabilizing Ligands: Effect on Catalytic Activity and Stability. *ACS Applied Nano Materials* **2018,** *1* (12), 7129-7138.
51. Collins, G.; Rahme, K.; O'Connell, J.; Holmes, J. D., Embedding colloidal nanoparticles inside mesoporous silica using gas expanded liquids for high loading recyclable catalysts. *Catalysis Science & Technology* **2016,** *6* (19), 7212-7219.
52. Singh, A. K.; Xu, Q., Synergistic Catalysis over Bimetallic Alloy Nanoparticles. *ChemCatChem* **2013,** *5* (3), 652-676.
53. McMullin, C. L.; Fey, N.; Harvey, J. N., Computed ligand effects on the oxidative addition of phenyl halides to phosphine supported palladium(0) catalysts. *Dalton Transactions* **2014,** *43* (36), 13545-13556.
54. Kazuma, E.; Kim, Y., Mechanistic Studies of Plasmon Chemistry on Metal Catalysts. *Angewandte Chemie International Edition* **2019,** *58* (15), 4800-4808.
55. Verkaaik, M.; Grote, R.; Meulendijks, N.; Sastre, F.; Weckhuysen, B. M.; Buskens, P., Suzuki-Miyaura Cross-Coupling Using Plasmonic Pd-Decorated Au Nanorods as Catalyst: A Study on the Contribution of Laser Illumination. *ChemCatChem* **2019,** *11* (19), 4974-4980.
56. Sarhid, I.; Abdellah, I.; Martini, C.; Huc, V.; Dragoe, D.; Beaunier, P.; Lampre, I.; Remita, H., Plasmonic catalysis for the Suzuki–Miyaura cross-coupling reaction using palladium nanoflowers. *New Journal of Chemistry* **2019,** *43* (11), 4349-4355.

57. Sun, D.; Zhang, G.; Huang, J.; Wang, H.; Li, Q., Plant-Mediated Fabrication and Surface Enhanced Raman Property of Flower-Like Au@Pd Nanoparticles. *Materials* **2014,** *7* (2), 1360-1369.
58. Kim, J.; Song, B.; Chung, I.; Park, J.; Yun, Y., High-performance Pt catalysts supported on amine-functionalized silica for enantioselective hydrogenation of α-keto ester. *Journal of Catalysis* **2021,** *396*, 81-91.
59. Hu, X.; Lin, X.; Zhao, H.; Chen, Z.; Yang, J.; Li, F.; Liu, C.; Tian, F., Surface Functionalization of Polyethersulfone Membrane with Quaternary Ammonium Salts for Contact-Active Antibacterial and Anti-Biofouling Properties. *Materials (Basel)* **2016,** *9* (5), 376.
60. Gao, M.; Yang, Y.; Guo, J., Revealing the Role of Chain Length of Ligands on Gold Nanoparticles Surface in the Process for Catalysis Reduction of 4-Nitrophenol. *Catalysis Letters* **2019,** *149* (8), 2110-2118.

4.6 Supporting Information

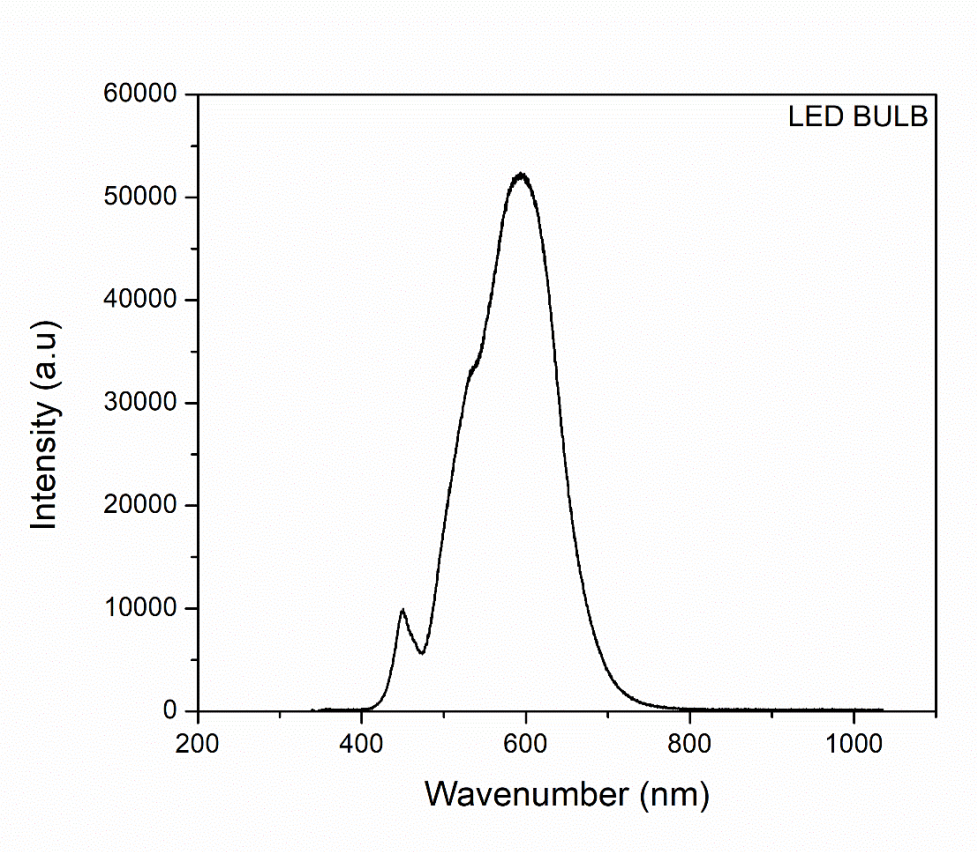

Figure S1: Emission Spectra of LED light

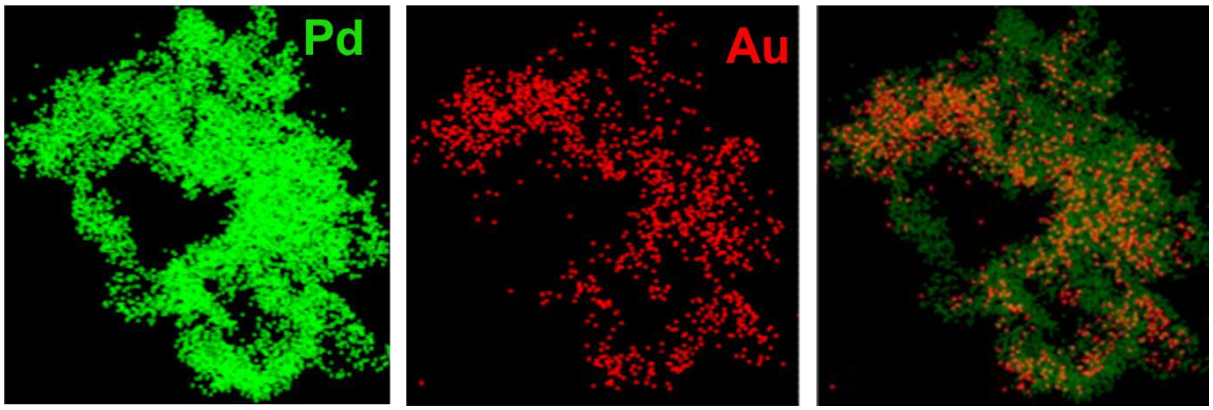

Figure S2: EDX of PdAu 10:1 NS's.

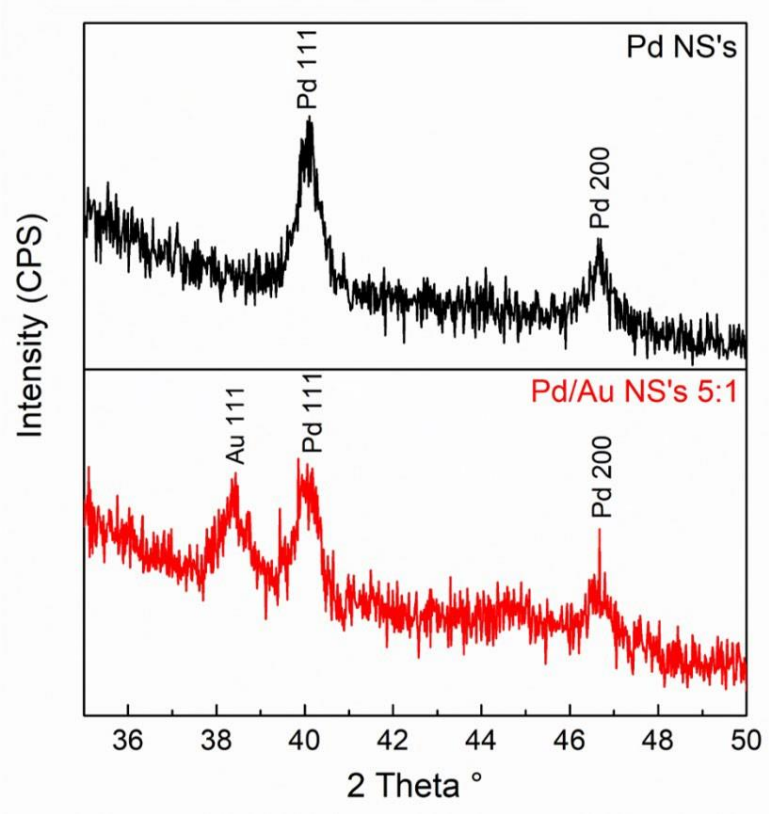

Figure S3: XRD of Pd and PdAu 5:1 NS's

Table S1: Reaction parameters

Moles of Pd	Moles of Au	Moles of surfactant	Moles of AA	Temp (c)	Time	Results
$1.6x10^{-5}$	-	$2.5x10^{-4}$	$3x10^{-4}$	0°C	6h	Nanoparticle formation
$1.6x10^{-5}$	-	$5x10^{-4}$	$3x10^{-4}$	0°C	6h	Nanoparticle formation
$1.6x10^{-5}$	-	$2.5x10^{-4}$	$3x10^{-4}$	0°C	3h	No reduction
$1.6x10^{-5}$	-	$5x10^{-4}$	$3x10^{-4}$	0°C	3h	No reduction
$8x10^{-6}$	-	$2.5x10^{-4}$	$3x10^{-4}$	0°C	6h	NS formation
$8x10^{-6}$	-	$5x10^{-4}$	$3x10^{-4}$	0°C	6h	NS and NP
$8x10^{-6}$	-	$2.5x10^{-4}$	$3x10^{-4}$	0°C	3h	NS and NP
$8x10^{-6}$	-	$5x10^{-4}$	$3x10^{-4}$	0°C	3h	NS and NP
$1.6x10^{-5}$	-	$2.5x10^{-4}$	$6x10^{-4}$	0°C	6h	No reduction
$8x10^{-6}$	-	$2.5x10^{-4}$	$6x10^{-4}$	0°C	6h	No reduction
$1.33x10^{-5}$	$2.66x10^{-6}$	$2.5x10^{-4}$	$3x10^{-4}$	0°C	6h	Nanoparticle formation
$1.33x10^{-5}$	$2.66x10^{-6}$	$5x10^{-4}$	$3x10^{-4}$	0°C	6h	Nanoparticle formation
$1.33x10^{-5}$	$2.66x10^{-6}$	$2.5x10^{-4}$	$3x10^{-4}$	0°C	3h	NS and NP
$1.33x10^{-5}$	$2.66x10^{-6}$	$5x10^{-4}$	$3x10^{-4}$	0°C	3h	NS and NP
$6.65x10^{-6}$	$1.35x10^{-6}$	$5x10^{-4}$	$3x10^{-4}$	0°C	6h	NS and NP
$6.65x10^{-6}$	$1.35x10^{-6}$	$2.5x10^{-4}$	$3x10^{-4}$	0°C	6h	NS formation
$6.65x10^{-6}$	$1.35x10^{-6}$	$2.5x10^{-4}$	$3x10^{-4}$	0°C	3h	NS and NP
$6.65x10^{-6}$	$1.35x10^{-6}$	$5x10^{-4}$	$3x10^{-4}$	0°C	3h	NS and NP
$1.33x10^{-5}$	$2.66x10^{-6}$	$2.5x10^{-4}$	$6x10^{-4}$	0°C	6h	No reduction
$6.65x10^{-6}$	$1.35x10^{-6}$	$2.5x10^{-4}$	$6x10^{-4}$	0°C	6h	No reduction
$7.28\ x10^{-6}$	$7.2\ x10^{-7}$	$2.5x10^{-4}$	$3x10^{-4}$	0°C	6h	NS formation
$1.456x10^{-5}$	$1.44x10^{-6}$	$5x10^{-4}$	$3x10^{-4}$	0°C	6h	NS and NP
$1.456x10^{-5}$	$1.44x10^{-6}$	$2.5x10^{-4}$	$3x10^{-4}$	0°C	3h	NS and NP
$1.456x10^{-5}$	$1.44x10^{-6}$	$5x10^{-4}$	$3x10^{-4}$	0°C	3h	NS and NP
$1.456x10^{-5}$	$1.44x10^{-6}$	$2.5x10^{-4}$	$6x10^{-4}$	0°C	6h	No reduction
$1.456x10^{-5}$	$1.44x10^{-6}$	$2.5x10^{-4}$	$6x10^{-4}$	0°C	6h	No reduction
$8x10^{-6}$	-	$2.5x10^{-4}$	$3x10^{-4}$	35°C	6h	No reduction
$6.65x10^{-6}$	$1.35x10^{-6}$	$5x10^{-4}$	$3x10^{-4}$	35°C	6h	No reduction
$1.456x10^{-5}$	$1.44x10^{-6}$	$2.5x10^{-4}$	$3x10^{-4}$	0°C	6h	No reduction

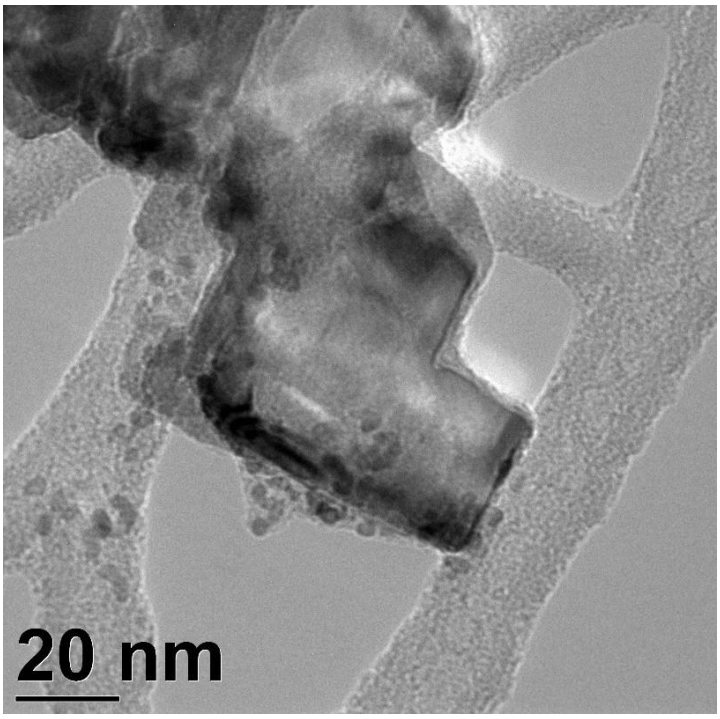

Figure S4: TEM image of PdAu 2:1 NS's.

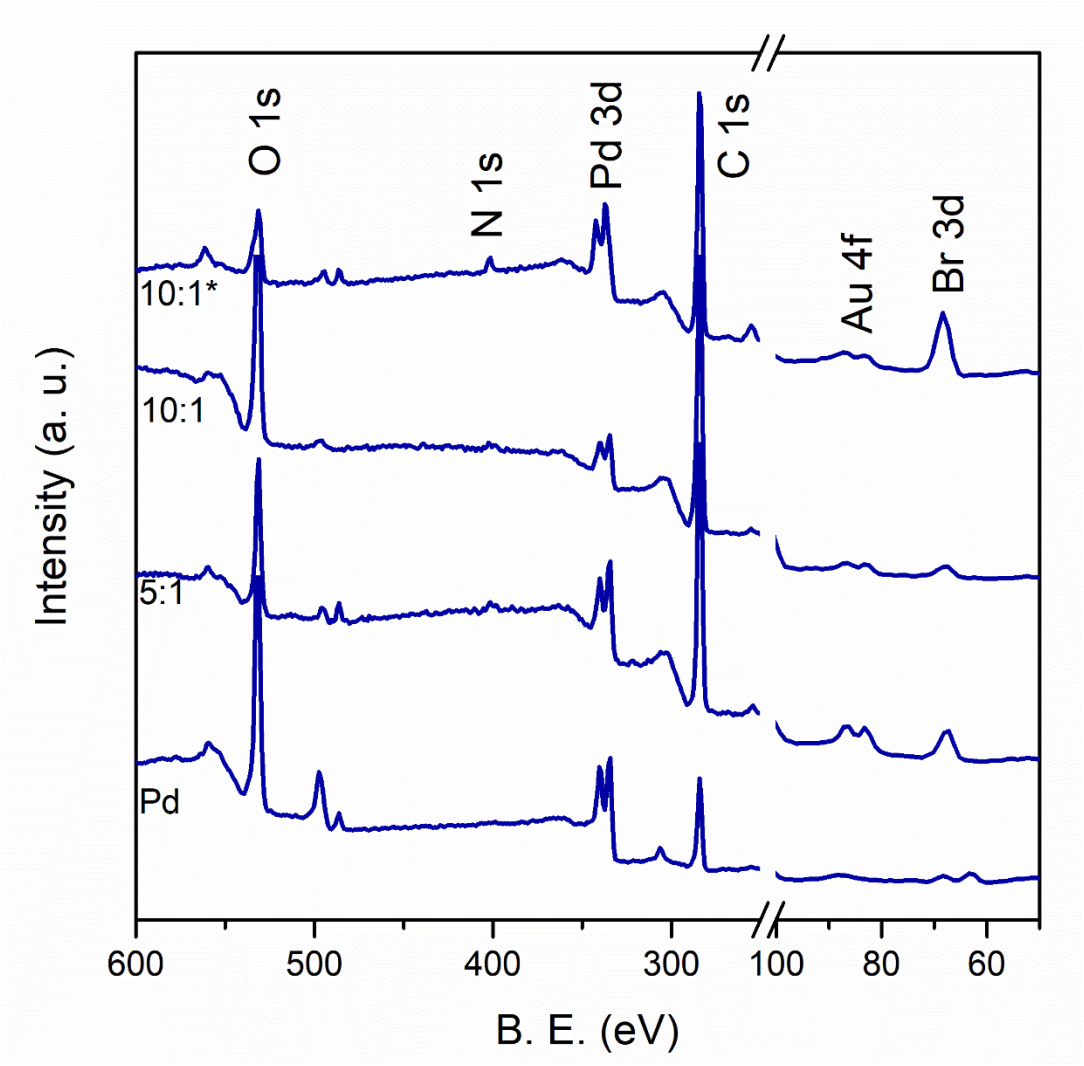

Figure S5: Survey scan of Pd NS, PdAu 5:1 NS and PdAu 10:1 NS with incomplete* and complete reduction.

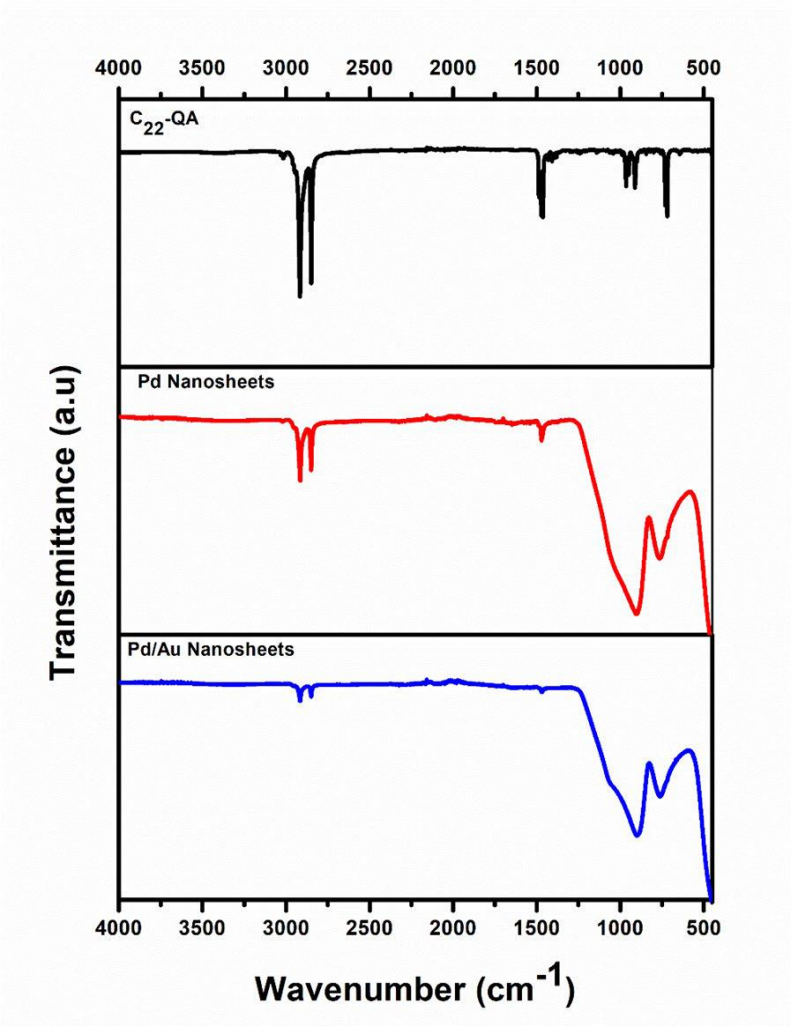

Figure S6: FTIR of the surfactant C_{22}-QA(Br^-), Pd and PdAu nanosheets.

Table S2: Summary of literature reports of catalysts used for Suzuki cross coupling under conventional (thermal) and light driven catalysis.

Catalyst	Surface Ligand	Reaction conditions	% Yield	Ref
Conventional Suzuki Cross Coupling				
PdAu nanoflower	PVP	80°C, 15 min, 0.3 wt%	93 %	[1]
Pd Nanocube	CTAB	Room temperature, 30 min, 4 wt%,	95 %	[2]
AuPd Nanoparticles	N/A	30 °C, 6 h, 3 wt%	96 %	[3]
Pd NP-TiO_2		28 °C, 4 h, 5 wt%	93 %	[4]
Pd nanoparticles	PVA	60 °C, 30 min, 0.2 mol%	79 %	[5]
Light-driven Suzuki Cross Coupling				
PdAu NPs on ZrO_2		45°C, 24h , Visible light	80 % light 10 % Dark	[6]
Pd NP on 2H-WS_2	PVP	RT, 3h, 60 W LED, 2.85 µg catalyst	90%	[7]
Pd/ZnO		RT, 1.5 h, visible light	96 % Light Trace Dark	[8]
AuPd nanowheels		50 °C, 90 min, Xe lamp, 0.2 mg catalyst	100 % Light 18 % dark	[9]
Pd hexagonal nanoplates	PVP	25°C, 3 h, Xe lamp 0.005 mmol catalyst loading	90 %	[10]
Pd/Au nanosheets	C_{22}-QA	0°C, 6h, Visible light, 0.2 mol% catalyst loading	99%	*This work*

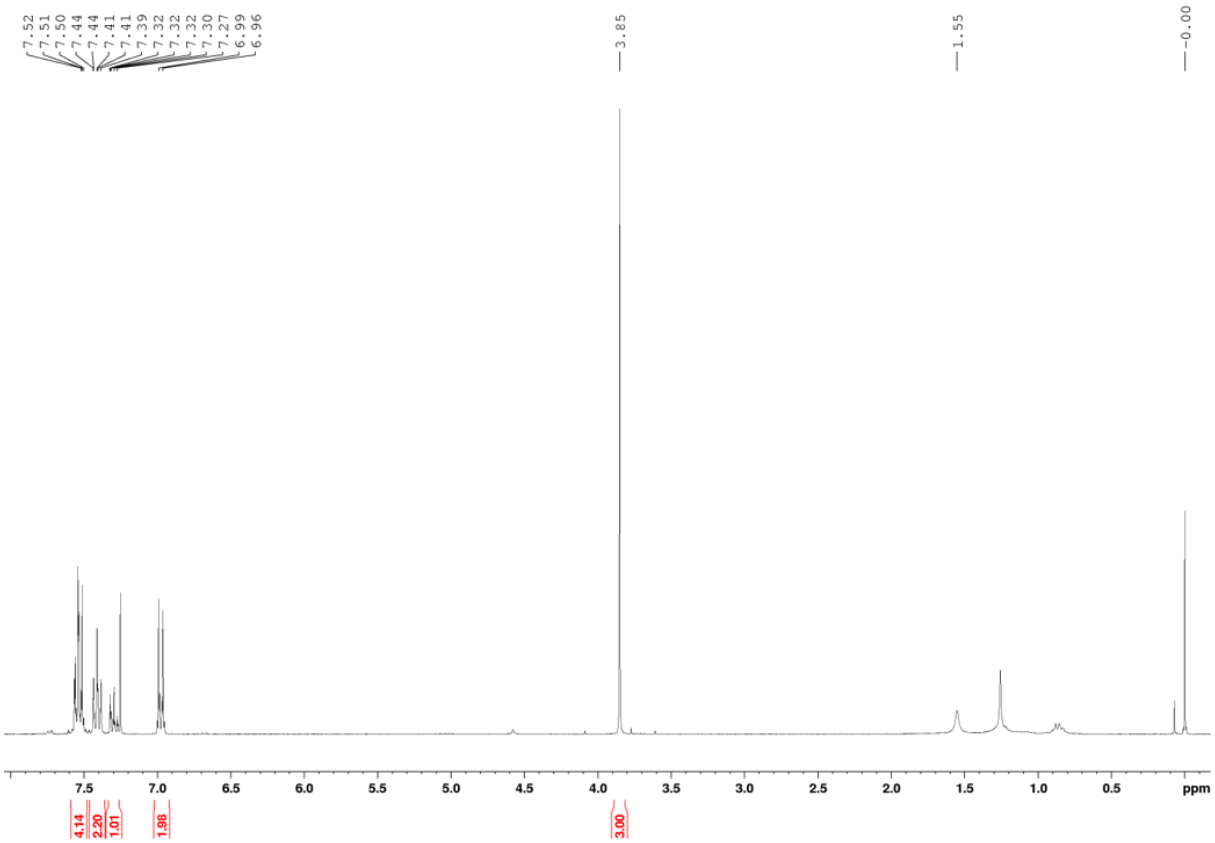

Figure S7: NMR of 4-methoxybiphenyl from the Suzuki cross couple reaction.

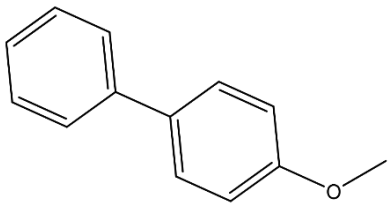

4-methoxybiphenyl: white solid, ^{1}H NMR (300 MHz $CDCl_3$)

δ= 7.56-7.55 (m, 4H), 7.41 (t, J=7.35Hz, 1H), 6.99 (d, J=8.8 Hz, 2H), 3.85 (s, 3H) ppm all in agreement with literature reports.

Catalyst	mol %	℃	Time	% Conversion	TON[(a)]	TOF(h^{-1})[(b)]
Pd Dark	0.1	25	2 h	0	0	0
Pd LED	0.1	25	2h	10	100	50
Pd Dark	0.2	25	2h	11	55	27.5
Pd LED	0.2	25	2h	10	50	25
PdAu Dark	0.1	25	2h	48	480	240
PdAu LED	0.1	25	2h	58	580	240
PdAu Dark	0.2	25	2h	36	180	90
PdAu LED	0.2	25	2h	93	465	232.5

Table S3: TOF for Pd and PdAu catalysts in the dark and under LED light at 0.1 and 0.2 mol% where [(a)] TON= moles of product x conversion/moles of Pd) and [(b)] TOF= TON/time (h)

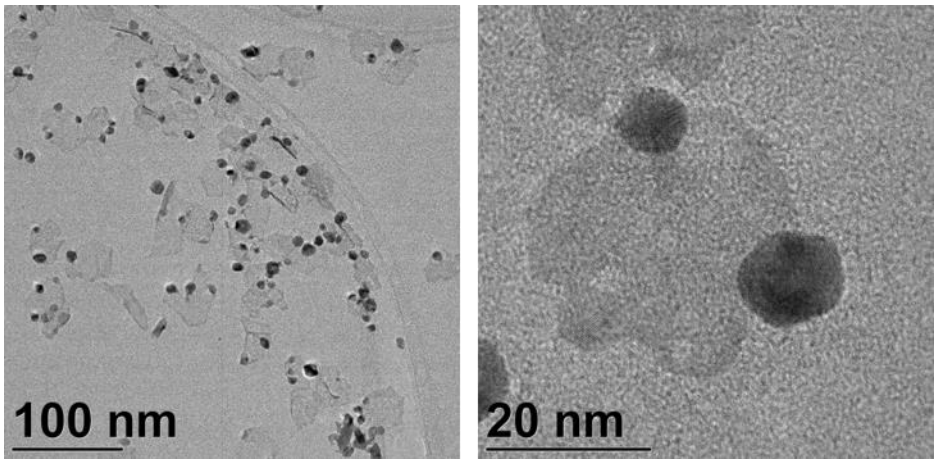

Figure S8: TEM images of CO-assisted Pd/Au nanosheets

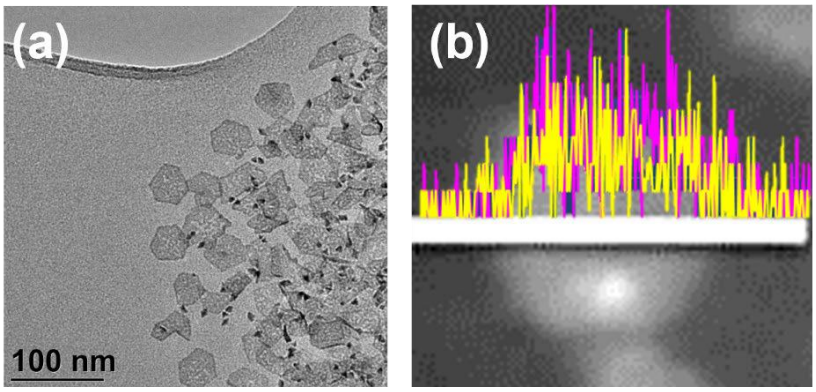

Figure S9: (a)TEM image and (b) EDX line scan of PdAg NS.

The CO-assisted methodology was successful for PdAg NSs. Supporting information, Figure S9 (a) shows a TEM image of PdAg NSs with a well-defined morphology and a mean length of 24 nm. It shows a single PdAg NS and alloy formation was confirmed by EDX analysis, as displayed in Figure 9 (b), showing a homogenous distribution of Pd and Ag across the NS.

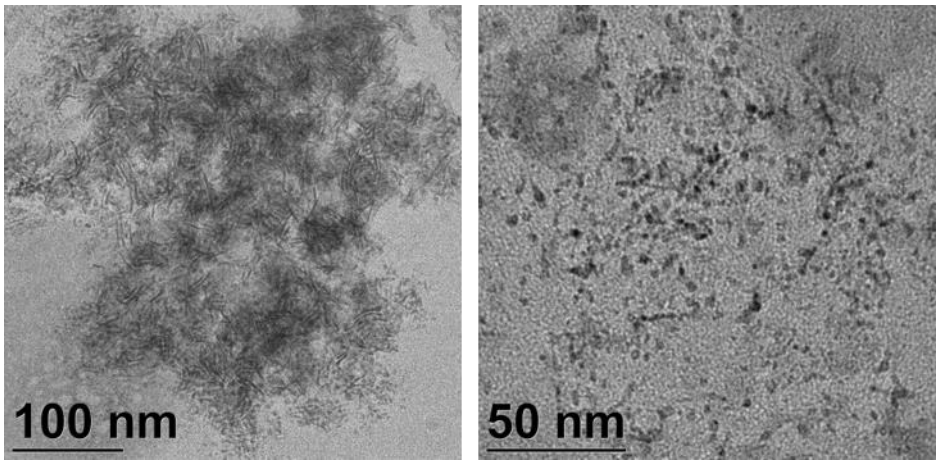

Figure S10: TEM images of nanosheets which were destroyed by chemically cleaned using $NaBH_4$

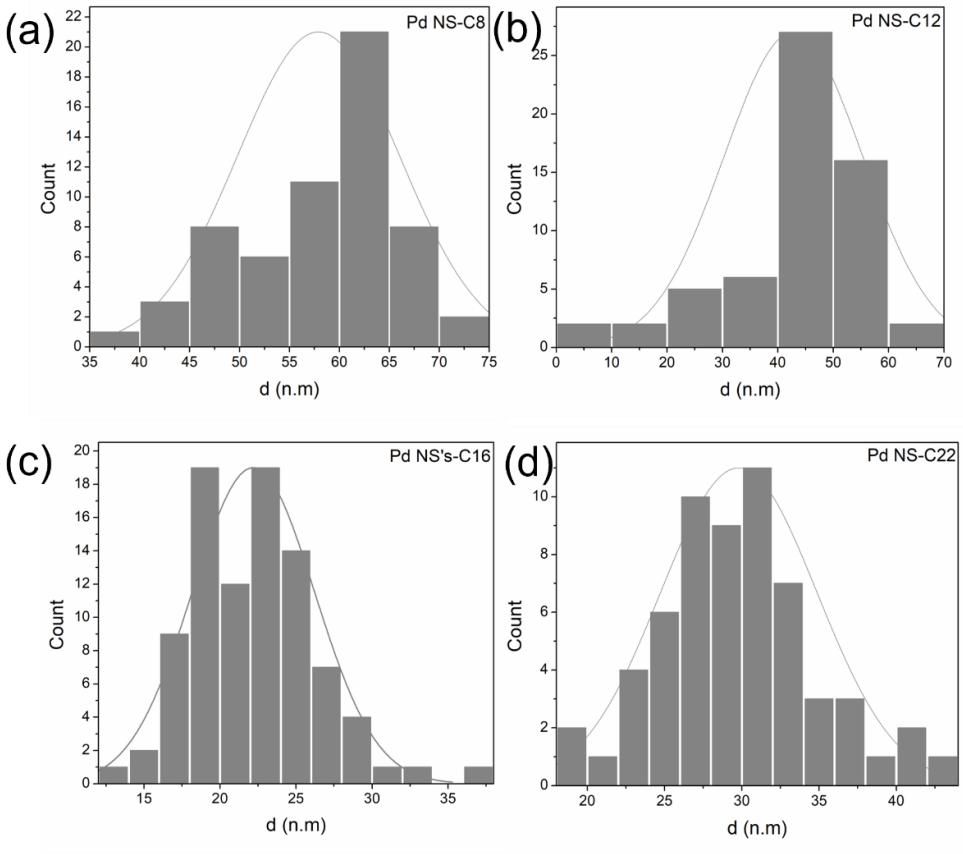

Figure S11: Size distribution profile of Pd NS with chain lengths (a) C8, (b) C12, (c) C16 and (d) C22

References

1. Xu, J.; Wilson, A. R.; Rathmell, A. R.; Howe, J.; Chi, M.; Wiley, B. J., Synthesis and Catalytic Properties of Au–Pd Nanoflowers. *ACS Nano* **2011,** *5* (8), 6119-6127.
2. Swain, S.; M. B, B.; Kandathil, V.; Bhol, P.; Samal, A. K.; Patil, S. A., Controlled Synthesis of Palladium Nanocubes as an Efficient Nanocatalyst for Suzuki–Miyaura Cross-Coupling and Reduction of p-Nitrophenol. *Langmuir* **2020,** *36* (19), 5208-5218.
3. Xiao, Q.; Sarina, S.; Jaatinen, E.; Jia, J.; Arnold, D. P.; Liu, H.; Zhu, H., Efficient photocatalytic Suzuki cross-coupling reactions on Au–Pd alloy nanoparticles under visible light irradiation. *Green Chemistry* **2014,** *16* (9), 4272-4285.
4. Koohgard, M.; Hosseini-Sarvari, M., Enhancement of Suzuki–Miyaura coupling reaction by photocatalytic palladium nanoparticles anchored to TiO2 under visible light irradiation. *Catalysis Communications* **2018,** *111*, 10-15.
5. Chatterjee, S.; Bhattacharya, S. K., Size-Dependent Catalytic Activity and Fate of Palladium Nanoparticles in Suzuki-Miyaura Coupling Reactions. *ACS Omega* **2018,** *3* (10), 12905-12913.
6. Xiao, Q.; Sarina, S.; Bo, A.; Jia, J.; Liu, H.; Arnold, D. P.; Huang, Y.; Wu, H.; Zhu, H., Visible Light-Driven Cross-Coupling Reactions at Lower Temperatures Using a Photocatalyst of Palladium and Gold Alloy Nanoparticles. *ACS Catalysis* **2014,** *4* (6), 1725-1734.
7. Raza, F.; Yim, D.; Park, J. H.; Kim, H.-I.; Jeon, S.-J.; Kim, J.-H., Structuring Pd Nanoparticles on 2H-WS2 Nanosheets Induces Excellent Photocatalytic Activity for Cross-Coupling Reactions under Visible Light. *Journal of the American Chemical Society* **2017,** *139* (41), 14767-14774.
8. Hosseini-Sarvari, M.; Bazyar, Z., Visible Light Driven Photocatalytic Cross-Coupling Reactions on Nano Pd/ZnO Photocatalyst at Room-Temperature. *ChemistrySelect* **2018,** *3* (6), 1898-1907.
9. Huang, X.; Li, Y.; Chen, Y.; Zhou, H.; Duan, X.; Huang, Y., Plasmonic and catalytic AuPd nanowheels for the efficient conversion of light into chemical energy. *Angewandte Chemie (International ed. in English)* **2013,** *52* (23), 6063-7.
10. Trinh, T. T.; Sato, R.; Sakamoto, M.; Fujiyoshi, Y.; Haruta, M.; Kurata, H.; Teranishi, T., Visible to near-infrared plasmon-enhanced catalytic activity of Pd hexagonal nanoplates for the Suzuki coupling reaction. *Nanoscale* **2015,** *7* (29), 12435-12444.

Chapter 5

Ligand-Aided Glycolysis of PET using Ultrasmall Fe_2O_3 Nanoparticles as Heterogeneous catalysts

Ligand-Aided Glycolysis of PET using Ultrasmall Fe_2O_3 Nanoparticles as Heterogeneous catalysts

Éadaoin Casey, Rachel Breen, Prof Arno Kentgens, Dr. Jennifer Gómez-Badillo, Dr. Albert Rimola Gibert, Dr. Gerard Pareras Niell, Prof. Justin. D Holmes, Dr. Gillian Collins*

[1] School of Chemistry, University College Cork, Cork, T12 YN60, Ireland.

[2] AMBER Centre, Environmental Research Institute, University College Cork, Cork, T23 XE10, Ireland.

Abstract

The development of efficient catalysts for the chemical recycling of PET is essential to tackling the global issue of plastic waste. Heterogeneous catalysts have the advantage of being easier to remove and reused in the reaction. In this work, we develop ligand assisted Fe_2O_3 nanoparticle (NP) catalysts supported on SiO_2. The ligand-Fe_2O_3 NP catalyst achieve full PET conversions and high BHET yields (70%) compared to bare Fe_2O_3 NPs, Fe^{3+} ion immobilised catalyst and homogenous $FeCl_3$ salts, with equivalent Fe loading. DFT calculations revealed the reactivity of the ion immobilised catalysts is strongly correlated to the ligand binding energy. DFT studies further showed that the products in the glycolysis reaction catalysed by the NP catalysts are stabilised showing a significant exergonic character compared to single ion immobilised Fe^{3+} ions. XPS analysis indicates charge transfer between the ligands and Fe_2O_3 NPs and the electron donating ability of N containing groups likely plays a role in the higher performance of the ligand-Fe_2O_3 catalysts. This work demonstrates the significant potential of tuning the electronic structure of heterogeneous catalyst for enhanced activity.

5.1 Introduction

In recent years, research into developing pathways to convert plastic waste polymers into monomers or value-added products has grown exponentially with the key goal of achieving a circular economy in the polymer life cycle.[1] Polyethylene terephthalate (PET) is a very useful polymer in our everyday life. It is a high-volume thermoplastic polyester and the reason for selecting recycling of PET in this work is because it has the largest market for textiles, packaging, high strength fibres, photographic films and most importantly for us bottles used for water/other beverages.[2-3] However, it is also one of the largest components of the postconsumer plastics waste in landfills highlighting the need for effective recycling strategies for this polymer. This has gained huge interest for researchers to find low cost, and environmentally friendly way of degrading it to a useful monomer for other uses with the final goal of achieving a circular economy in the polymer life cycle.[2, 4] There are a variety of methods of chemical recycling of plastic, these include, hydrolysis[5-6], alcoholysis[7-8] and glycolysis.[3, 9] Glycolysis is the most effective method for recycling as it is low cost, mild reaction conditions and uses low volatility solvents. The process involves the transesterification reaction of PET with excess glycol, (usually ethylene glycol) to obtain bis-(hydroxyethyl) terephthalate (BHET).[10] BHET can be repolymerised to PET and it is also used in the synthesis of unsaturated polyesters, rigid or flexible polyurethanes, and other fine chemicals.[11]

The factors which can influence the outcome of the glycolysis reaction are temperature, time, catalyst loading, and PET:EG ratio. The degradation of PET is usually performed in the presence of a catalyst as the transformation of PET using any of the mentioned methods are very stagnant in the absence of catalysts.[12-13] Homogenous catalysts such as metal salts[14-16], metal oxides[17-18] and ionic liquids.[2, 12, 19] are most commonly used, however, this leads to issues regarding catalyst recovery and recycling and contamination of the product.

Numerous heterogeneous catalysts have been developed for PET glycolysis. Biomass derived heterogeneous catalysts have been prepared from waste orange peel ash,[20] waste bamboo leaf ash

and calcium oxide based catalysts made from eggshells and seafood shells.[21-22] Cobalt nanoparticles (3 nm) stabilised by tannic acid ligands showed high activity for PET glycolysis with 96% conversion and 77% BHET yield.[23] Various metal oxides nanostructures have been reported as successful heterogeneous catalysts for depolymerising PET to BHET. Son et al.[24] reported the use of their exfoliated manganese oxide nanosheets which were able to catalyse the glycolysis of PET leading to full conversion of PET and 100% yield of BHET at 0.01 wt % catalyst, at 200 °C after 30 min. Mo-doped ultrathin ZnO nanosheets were reported as excellent catalysts by Cao and co-workers[25], for the depolymerisation reaction as it displays far superior yields of BHET than standard Zn catalysts which have been previously reported in literature. They report that undoped ZnO yields 54.7 % BHET which increases to 94.5 % when the ZnO was doped with Mo. The Mo atoms replace Zn atoms at defect sites forming Mo-Zn bonds, influencing the electronic structure of the catalyst and promoted electron transfer of the glycolysis reaction. Mesoporous SBA-15 catalysts doped with ZnO gave a 91% BHET yield, and the catalyst displayed good stability and high catalytic activity when recycled. Ion based heterogeneous catalysts such as metal organic frameworks (MOFs)[26-27] and zeolites[28] have also been reported as good catalysts for the depolymerisation reaction of PET due to their highly ordered structures, high surface areas and porosity.[27] Yang *et al*.[29] reported the use of metal azolate framework-6 catalyst (a sub class of MOFs) with a high density of zinc ion species immobilised on the surface achieving 92.4% conversion of PET and 81.7 % yield of BHET. Ionic liquids have become very topical in recent years especially in the glycolysis of PET. Wang et al.[30] investigated the use of metal ions immobilised on polymer ionic liquids as a potential catalyst for the glycolysis of PET. By using the catalyst [[BVim]NTf_2-Zn^{2+}, the PET conversion was reported to be 95.4 % and they obtained 77.8 % BHET.

It is evident from the literature that a wide variety for catalyst are effective for PET depolymerisation. The aim of this work is to find the optimum heterogeneous catalyst design for PET glycolysis with a particular focus on the immobilization of metal ion and nanoparticle-based catalysts. Surface modification of a catalyst support with organic linkers is a convenient strategy to immobilise transition

metal ions and can achieve high density of ions dispersed on the support material. The nature of the organic linker used to tether the ion can influence the steric and the electronic environment with the metal centre, which in turn can influence catalytic activity. [31] In this work metal ions were immobilised onto porous silica functionalised with different organic linkers, which are illustrated in scheme 1. The ion-based catalysts were then converted to NP catalysts either by calcination, which removed the organic ligands or by $NaBH_4$-treatment (reduced) which preserves the ligand. Functionalisation of the SiO_2 support enables the formation of well-dispersed small diameter Fe_2O_3 NP. The heterogeneous catalysts were evaluated for PET glycolysis to gain insight into how the immobilisation of the metal species and the organic ligands influenced catalytic performance. DFT calculations was used to correlate experimental observations.

5.2 Experimental

Chemicals

Mesoporous cellular foam (MCF) was obtained from Glantreo. 3-aminopropylytrimethoxysilane (APTMS), 3-(2-aminoethyl-aminopropyl)trimethoxysilane (AEAPTMS), 2-pyridine carboxaldehyde, cyanuric chloride (CNC), N,N diisopropylethylamine (DIEA), sodium borohydride ($NaBH_4$), iron (III) chloride ($FeCl_3.4H_2O$), ammonium hydroxide solution (30-33%), methanol, ethanol, toluene, acetonitrile, tetrahydrofuran and ethylene glycol were all purchased from Sigma Aldrich. PET was obtained from waste water bottles after labels and lids being removed were cut into 1 mm x 1 mm pieces for glycolysis experiments. Repeating unit of 192.68 g mol^{-1} was used as the molecular weight of PET.

Synthesis of surface modified mesoporous cellular foam SiO_2.

Synthesis of SiO_2-NH_2: 2 g of MCF SiO_2 was placed in a round bottom flask along with 4 ml of 3-ATPMS and 75 ml toluene. The mixture was refluxed at 120 °C for 12 h under argon. Once reaction had

completed, the solid product (SiO_2-NH_2) was suction filtered and washed with ethanol before being dried at 60 °C.

Synthesis of SiO_2-NH_2-SB: 1 g of the SiO_2-NH_2 prepared in the previous step, was placed in a round bottom flask along with 1.2 ml 2-pyridinecarboxaldehyde and 50 ml ethanol. The reaction mixture was refluxed at 60°C for 24 h. Once completed, the solid product (SiO_2-NH-SB) was filtered and washed with ethanol before being dried at 60 °C.

Synthesis of SiO_2-$NHNH_2$: 2 g of MCF SiO_2 was placed in a round bottom flask along with 4 ml of AEAPTMS and 75 ml toluene. Mixture was refluxed at 120 °C for 12 h under argon. Once reaction had completed, the solid product (SiO2-$NHNH_2$) was vacuum filtered and washed with ethanol before dried at 60 °C.

Synthesis of SiO_2-$NHNH_2$ SB: 1 g SiO_2-$NHNH_2$ prepared in the previous step, was placed in a round bottom flask along with 1.2 ml 2-pyridinecarboxaldehyde and 50 ml ethanol. The reaction mixture was refluxed at 60 °C for 24 h. Once completed, solid product (SiO_2-$NHNH_2$ SB) was filtered and washed with ethanol before being dried at 60 °C.

Synthesis of SiO_2-Pincer

1.4 g SiO_2-NH_2, 1.8 g cyanuric chloride (CNC), 1.8 ml DIEA and 40 ml THF were added to a round button flask. The reaction mixture was left to stir in an ice bath under argon for 8 h. The product SiO_2-CNC was filtered off and washed with THF (5 x 20 ml) and dried overnight. In a three-neck round bottom flask, 1.5 g of the SiO_2-CNC was dispersed in 30 ml dry acetonitrile, 2 g 2-aminopyridine and 2 ml DIEA were added and refluxed for 2 days. After completion, the solid product (SiO_2-Pincer) was filtered off and washed with methanol (5 x 30 ml) and dried at 50 °C overnight.

Fe ion immobilisation onto ligand modified SiO_2

Fe species were immobilised onto each of the functionalised SiO_2 supports by stirring 2 g $FeCl_3.4H_2O$ and 1 g of the ligand modified SiO_2 with 50 ml H_2O for 1 h. Once completed, 1 ml ammonium hydroxide

solution was added and pH of the solution adjusted from 2 to 12. The product was filtered off and washed with copious amounts of H_2O.

Synthesis of Fe_2O_3 NP on SiO_2

The Fe ion-based catalysts were converted into iron oxide nanoparticle catalysts by calcination or chemical reduction. Catalysts were annealed in a tube furnace at 450°C for 3 h in air.

For the $NaBH_4$-treated method, 0.5 g of the Fe-ion immobilised SiO_2 were placed in a 50 ml beaker. A freshly prepared solution of $NaBH_4$ (0.095g, 2.5 mmol) and 2 ml H_2O was rapidly added under vigorous stirring, turning the catalyst from orange to brown-black. The solution was stirred for 1 h before filtering and washing with copious amounts of H_2O.

Glycolysis reaction of PET to BHET

In a typical procedure, 1 g of PET, 0.1 g catalyst and 5 ml of ethylene glycol were refluxed at 190 °C for 3 h. Once reaction was complete, 5 ml of ice-cold H_2O was added to the reaction filtered off and dried. The catalyst was separated by filtration. The filtrate was placed in the fridge overnight after which the BHET crystallised out the solution. The BHET crystals were collected be filtration, washed with water and dried overnight before being weighed. During reaction optimisation, a number of reaction parameters were altered to understand their impact, such as temperature, time, catalyst loading and PET:EG ratio. The percentage PET conversion and isolated BHET yield calculated be the equations below.

% Conversion of PET: $\frac{W_0 - W_1}{W_0}\ x\ 100$ **eqn. 1**

Where W_0 is the initial weight of the PET used and W_1 is the weight of the unreacted PET after the reaction.

% Yield of BHET: $\frac{W_{BHET}/M_{BHET}}{W_0/M_{PET}}\ x\ 100$ **eqn 2:**

Where, W_{BHET} is weight of the BHET product after recrystallization, M_{BHET} is the molecular weight of BHET, W_0 is the initial weight of PET used and M_{PET} is the repeating unit of PET.

NMR analysis confirmed that no formation of dimers or oligomers occurred and that BHET was the only product formed in the reaction. The ^{1}H NMR spectrum of BHET can be seen in supplementary information Figure S1, where the four main peaks were a singlet at 8.12 ppm corresponding to an aromatic ring, an OH triplet at 5.01 ppm, CH_2 triplet at 4.32 ppm and CH_2 quartet at 3.77 ppm. Residual solvent d_6-DMSO was located at 2.51 ppm. The results are in good agreement with literature values of BHET.[32]

Materials Characterisation

X-ray Photoelectron Spectroscopy (XPS) was acquired using a KRATOS AXIS 165 monochromatized X-ray photoelectron spectrometer equipped with an Al Kα (hv = 1486.6 eV) X-ray source. Spectra were collected at a take-off angle of 90° and all spectra were referenced to the C 1s peak at 284.8 eV. Transmission electron microscopy (TEM) analysis was performed using a JEOL 2100 electron microscope at an operating voltage of 200 kV and high-resolution TEM and energy-dispersive X-ray (EDX) analysis was carried out on an FEI Titan TEM, at an operating voltage of 300 kV. Fourier transform infrared (FTIR) spectra were recorded on a Perkin Elmer Spectrum Two FT-IR Spectrometer operating in the range of 4000-450 cm^{-1} with a resolution of 4 cm^{-1} and spectra were averaged from 20 scans. Nuclear magnetic resonance (NMR) samples were run in deuterated chloroform ($CDCl_3$). 1H NMR spectra were recorded on Bruker Avance III 300 NMR spectrometers, in proton-coupled mode using tetramethysilane (TMS) as the internal standard.

Density functional theory (DFT) simulations were carried out using the CP2K package.[33] The SiO_2 studied here has been computationally represented as a periodic amorphous silica (SiO_2) surface. The surface selected showed a silanol density of 7.2 OH/nm^2 assuring the maximum number of Si atoms available to be functionalized in the unit cell.[34] In order to relax both geometry parameters and cell parameters, a cell optimization has been performed only with the SiO_2 surface, dimensions of the optimized unit cell are 13.34 x 13.73 x 49.21 $Å^3$. The following optimizations have been performed only relaxing the geometry parameters. Both cell and geometry optimizations of the periodic systems

were carried out with the CP2K package. The semi-local Perdew–Burke–Ernzerhof (PBEsol) functional was adopted[35] combined with a double-ζ basis set (DZVP-MOLOPT-SR-GTH gaussian basis set) for all the atom types, together with the Grimme D3BJ correction term to the electronic energy,[36] and a cutoff set at 500 Ry for the plane wave auxiliary basis set. Core electrons were described with the Goedecker–Teter–Hutter pseudopotentials[37] and valence ones with a mixed Gaussian and plane-wave (GPW) approach.[38] Single point calculations have been performed to correct the energies considering solvation effect. Solvation has been calculated using the self-consistent continuum solvation (SCCS) model as implemented in CP2K, in order to reproduce experimental conditions water and ethylene glycol have been used as solvents.[39] Binding energies (BE) have been then calculated considering basis-set superimposition errors (BSSE). In CP2K the interaction energy can be calculated defining 2 fragments **A** and **B**,

$$\boldsymbol{E_{int(s)} = E_{AB(s)} - (E_{A(s)} + E_{B(s)})} \qquad \textbf{Eqn. 3}$$

where $\mathbf{E_{int(s)}}$ is the interaction energy, **E** is energy, $\mathbf{E_{AB}}$ is energy of the SiO_2/metal structure, $\mathbf{E_A}$ corresponds to the energy of silica, $\mathbf{E_B}$ is energy of metal**.** All completed in a solvent. **A** corresponds to the SiO_2 functionalized surface with the organic ligands and **B** the Fe^{+3} ion, all of them considering water as solvent. Finally, in order to elucidate the local minima and transition states, vibrational harmonic frequencies were calculated at the PBE-D3BJ/DZVP level using the finite differences method. A partial Hessian approach was used to reduce the computational cost of the calculations. Thus, the vibrational frequencies were calculated on the optimized geometries only for a fragment of the entire system, which included the metal centre and the organic ligands for the single atom (SA) Fe^{+3} structures and, the nano-metal-cluster and the adsorbates for the FeO nanoparticle structures.

5.3 Results and discussion

Catalyst design

Silica is an excellent catalytic support material that allows the surface chemistry to be easily altered through surface functionalisation using silylation chemistry. Mesoporous cellular foam SiO_2 is a three-dimensional (3D) connected pore structure and it was chosen as it has a relatively large pore diameter (100 nm) in comparison to other porous silicas. Scheme 1 (a) shows the synthesis pathways to prepare mesoporous SiO_2 with five different capping ligands SiO_2-NH_2 (1), SiO_2-NH_2-SB (2), SiO_2-NH-NH_2 (3), SiO_2-NH-NH_2-SB (4) and SiO_2-pincer (5) (see Experimental section for reaction details).

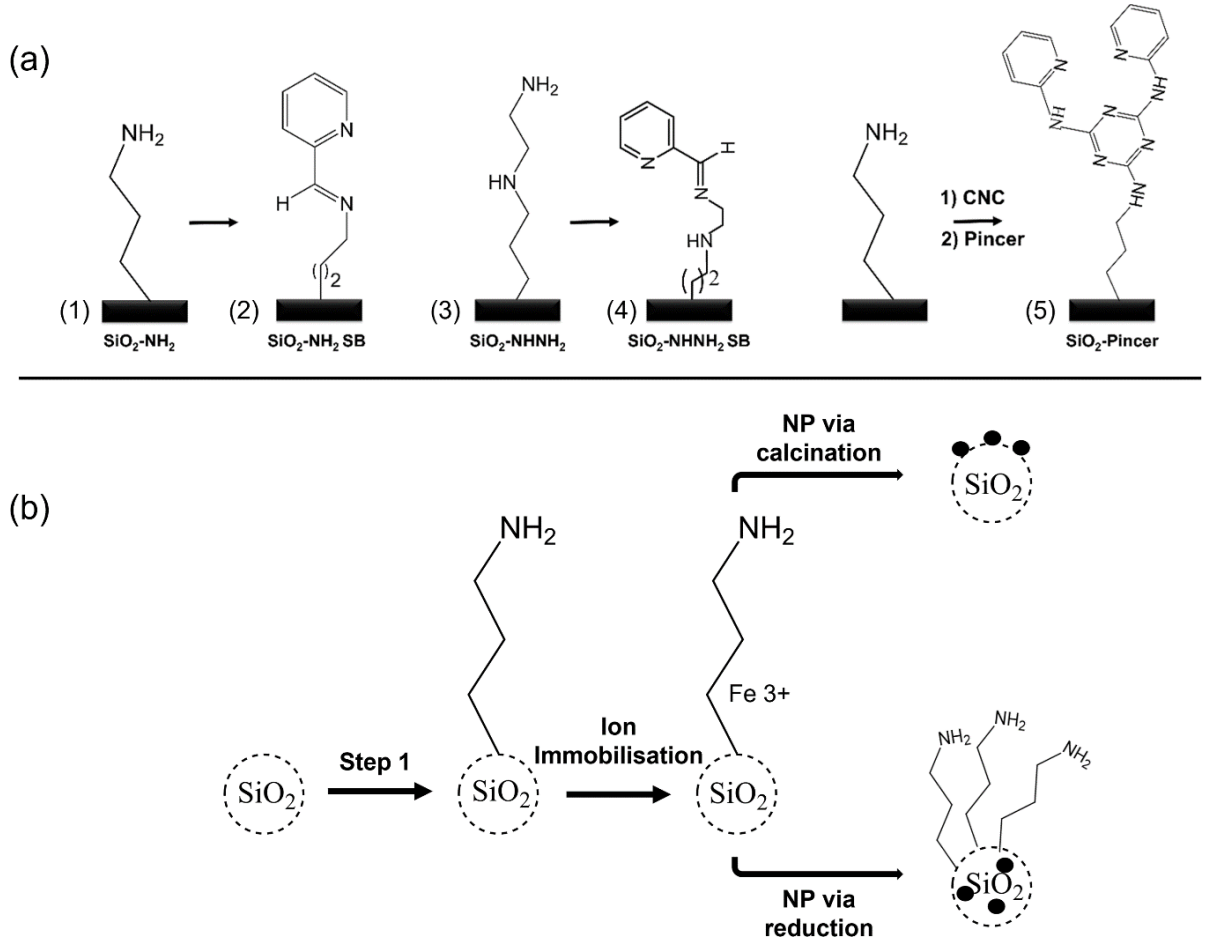

Scheme 1: (a) Synthesis pathways to prepare mesoporous SiO_2 with five different capping ligands SiO_2-NH_2 (1); SiO_2-NH_2-SB(2); SiO_2-NH-NH_2(3), SiO_2-NH-NH_2-SB (4) and SiO_2-pincer (5) and (b) the catalysts preparation scheme

XPS was employed to verify successful functionalisation of the SiO_2 support with each of the five ligands. After functionalisation, a N signal appeared in all the N 1s core levels as shown in Figure 1 (a) All catalysts displayed a dominant peak at a BE of 399 eV, attributed to the amine functional group and a shoulder peak at ~400-402 eV, attributed to protonated amines typically observed on modified SiO_2.[40] No N was detected in the bare SiO_2. The O 1s core level, in Figure 1 (b) also confirms functionalisation with the BE of the bare silica centred at 533.75 eV is downshifted to 532.5 eV, associated with the loss of Si-OH groups after surface modification.[41] The Si 2p core level, of bare SiO_2, shown in the Supporting Information Figure S2, shows a single peak at 104.25 eV and after functionalisation, the Si 2p peak can be deconvoluted in several peaks associated with different Si environments.

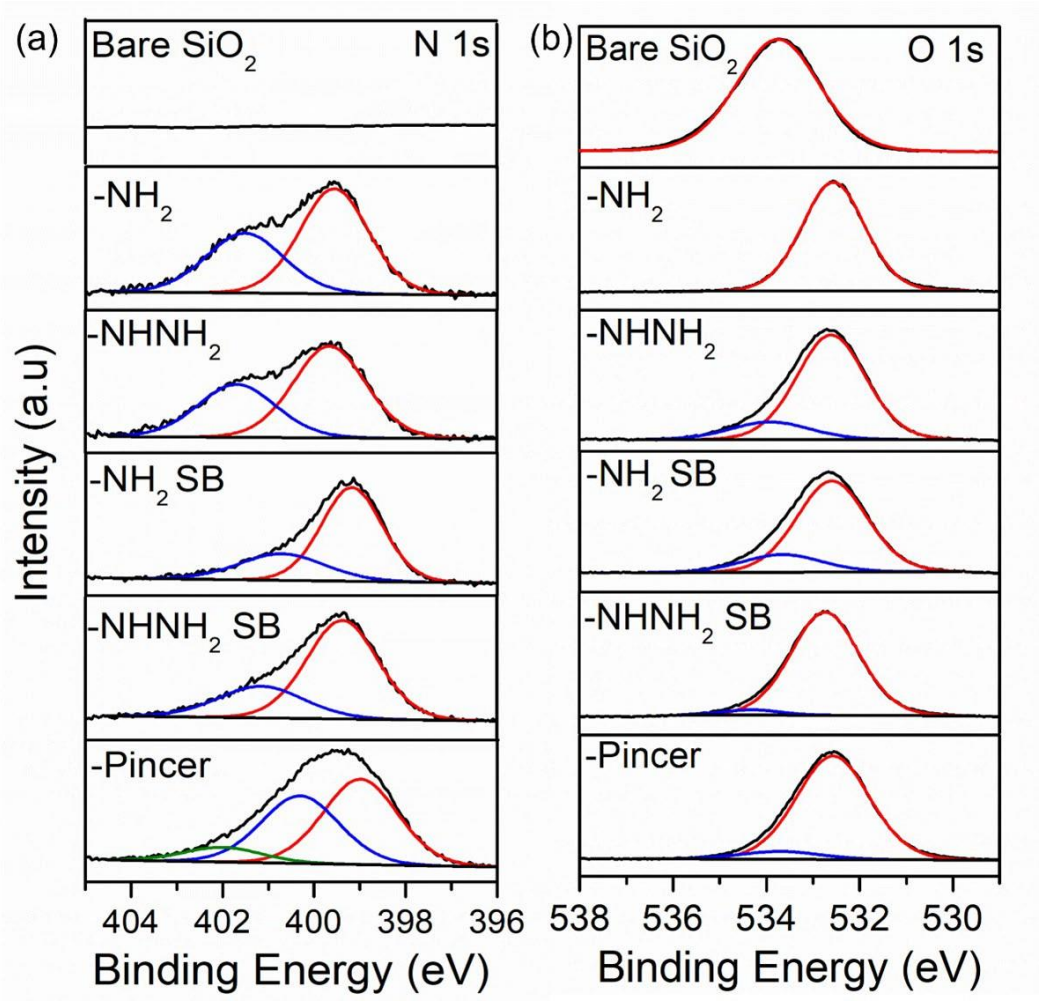

Figure 1: XPS analysis of the (a) N 1s spectra and (b) O 1s core level for bare silica, the functionalised SiO_2 with $-NH_2$, $-NH_2$ SB, $-NHNH_2$, $-NHNH_2$ SB and pincer respectively

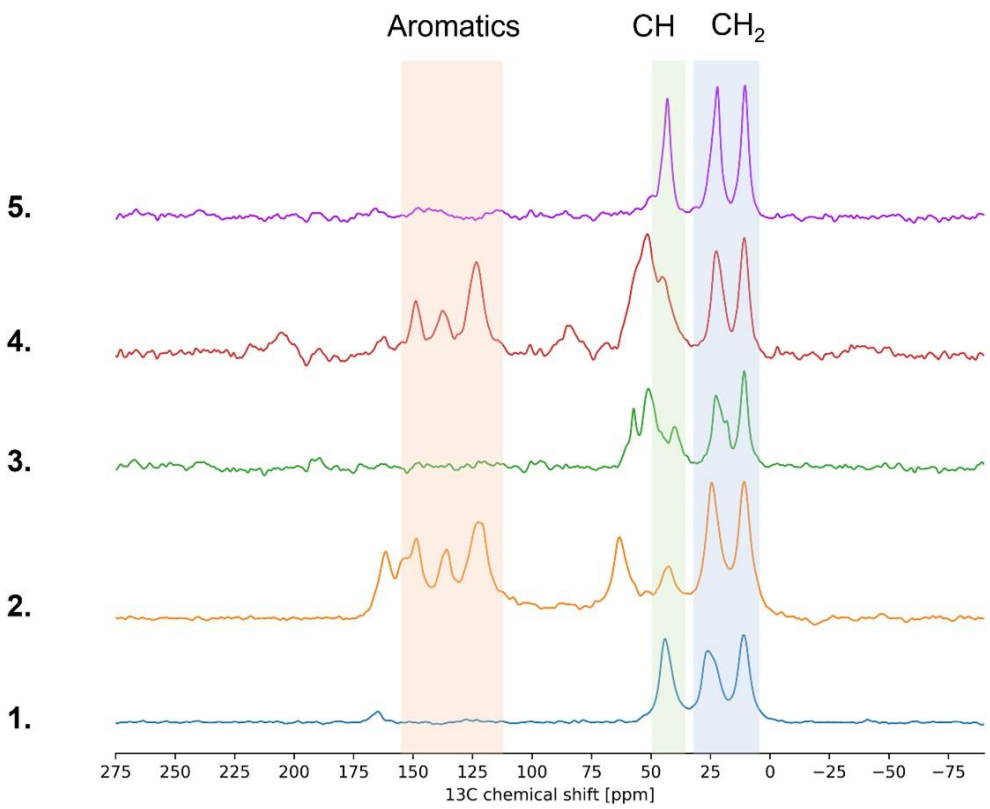

Figure 2: ^{13}C CPMAS of SiO_2 with five different capping ligands SiO_2-NH_2 (1); SiO_2-NH_2-SB (2); SiO_2-NH-NH_2 (3), SiO_2-NH-NH_2-SB (4) and SiO_2-pincer (5).

Solid state NMR was used to further evaluate the surface chemistry of the modified SiO_2. Solid state cross-polarisation magic angle spinning carbon-13 nuclear magnetic resonance (CPMAS ^{13}C NMR) of SiO_2 functionalised with five different capping ligands; SiO_2-NH_2 (1); SiO_2-NH_2-SB (2); SiO_2-NH-NH_2 (3), SiO_2-NH-NH_2-SB (4) and SiO_2-pincer (5), are shown in Figure 2. The presence of the alkyl groups appearing in SiO_2-NH_2 (1) and SiO_2-NH-NH_2 (3) catalysts (from 60 to 10 ppm) confirms successful grafting of the NH_2 and NH-NH_2 ligands onto SiO_2. The SiO_2-NH_2 SB (2) and SiO_2-NH-NH_2 SB (4) catalysts are prepared from catalysts 1 and 3 respectively, show the presence of aromatic peaks between 175-100 ppm confirming successful functionalisation with the Schiff base ligands. The alkyl groups were observed in the SiO_2-pincer catalyst; however, aromatic groups were not detected. The absence of the aromatic groups could possibly be due to the low concentration as attachment of the pincer ligand occurs over two synthesis steps, therefore the concentration of the alkyl groups would be higher as that attachment occurs first, then the bulky aromatic rings are attached last.

The N 1s XPS spectra clearly indicates changes to the N environment, and an increase in the N:Si ratio. Detailed spectra ^{13}C CPMAS spectra for each catalyst are found in the supplementary information Figure S3.

After organic functionalisation, Fe ions were immobilised onto the SiO_2 (see Experimental section for details). We chose iron as the metal catalyst as iron salts are effective for glycolysis of PET and have lower environmental impact compared to other effective metal ion catalysts such as Zn^{2+}. ICP-MS analysis was used to determine the Fe loading in each of the catalysts. Table S1 displays the quantitative results with the Fe loadings for each ligand, with the highest loading for the simple amine ligand SiO_2-NH_2 (4172.8 ppm) and lowest for the SiO_2-pincer ligand (3904 ppm) which can be expected given the bulky nature of the ligand.

The Fe ion immobilised catalysts were then converted to iron oxide nanoparticle catalysts by calcination at 450 °C, which removed the organic ligands on the SiO_2 surface or with $NaBH_4$ treatment (reduced) which persevered the organic ligands, as represented in scheme 1(b). XPS analysis of the NP catalyst were carried out to determine the chemical states of the iron oxide NP and assess the interaction of the ligand and the NPs. Figure 3(a) shows the Fe 2p spectrum for the SiO_2-NH_2-SB NP calcinated (C) and $NaBH_4$ treatment (R) catalysts. The Fe $2p_{3/2}$ is located at a BE of 711 eV and is good agreement with that reported for Fe_2O_3.[42] The Fe $2p_{3/2}$ also has a clear satellite peak at 718 eV, characteristic of Fe^{3+}, further indicating Fe_2O_3. The Fe 3p shown in the supporting information Figure S4 is fit to a single peak a BE of 55 eV, again indicating the presence of Fe^{3+} only. Magnetite (Fe_3O_4) does not have a satellite peak and the Fe 3p is usefully deconvoluted into the Fe^{3+} and Fe^{2+} species. Figure 3 (b) shows the O 1s core level before Fe adsorption with a dominant peak at 532.6 eV associated with the SiO_2. After NP formation an additional peak at a BE of 530.2 eV appears in the O 1s of both NP catalysts, which is in excellent agreement with the BE for Fe-O-Fe, consistent with the formation of NPs.[43] The O 1s core level of the other NP catalysts, shown in the Supporting Information figure S5, display the same trend with the appearance of the Fe-O-Fe peak after NP formation. Figure 3(c) shows the N 1s core level of the SiO_2-NH_2-SB catalyst, with a dominant peak at a BE of 399 eV, attributed to the amine functional group and a shoulder peak at 401 eV, attributed to protonated amines, as

aminosilane protonation occurs from the support Si-OH.[40] The peak intensity of the N 1s in the calcined catalyst decreases substantially, as excepted due to loss of the ligand but there are residual ligands present. The Si:N ratio estimate that ~85% of the ligands are removed. The N 1s peak of both the calcined and $NaBH_4$-treated catalysts is upshifted to a BE of 339.8 eV, indicating charge transfer from the organic ligand to the Fe_2O_3 NPs. XPS analysis of the other catalysts also show the same trend with the N 1s core level shifting upward (see supporting information figure S6)

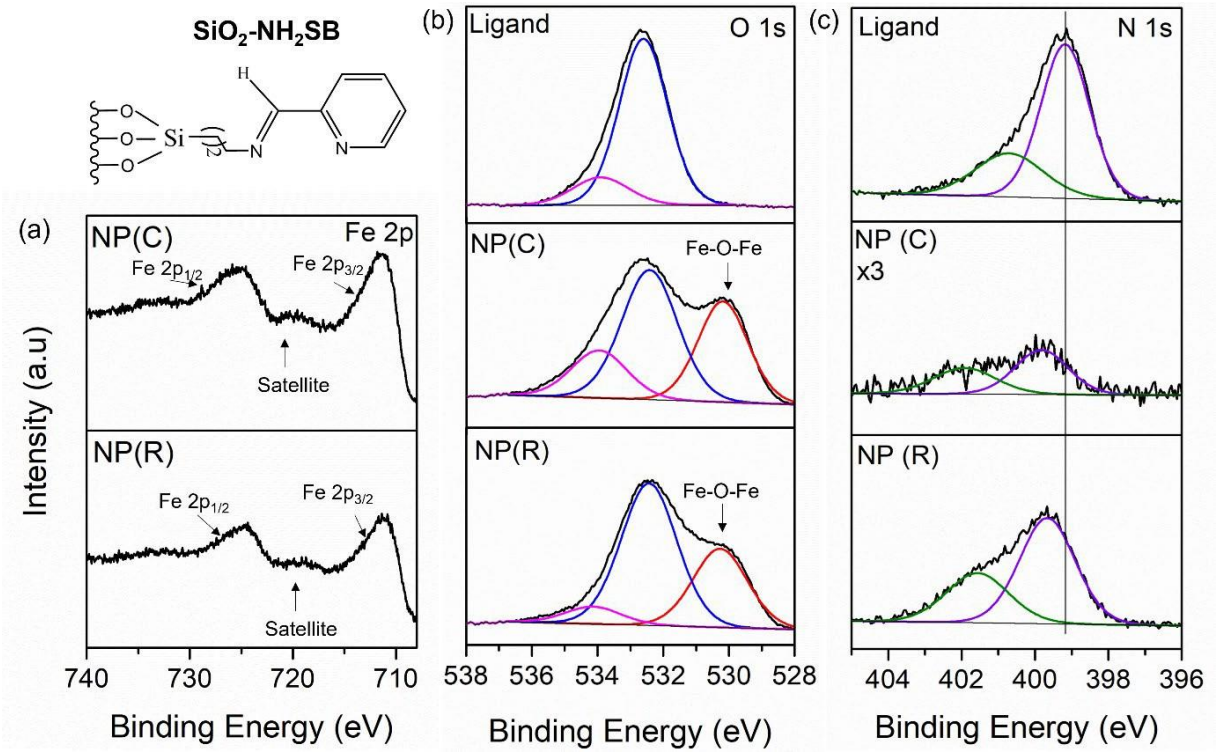

Figure 3: XPS core level scans of Fe 2p, O 1s and N 1s for the SiO_2-NH-SB and the corresponding Fe_2O_3 NP catalysts prepared via calcination (C) and $NaBH_4$-treated (R) methods.

Screening of catalysts

The catalytic performance of all twenty catalysts for the glycolysis of PET was investigated under the same reaction conditions. Figure 4 (a-d) compares the catalytic performance of the ligand modified catalysts, the Fe ion-based catalysts, the NP-calcined catalysts, and the NP-reduced catalysts, respectively, showing the PET conversion and isolated yields of BHET. Interestingly, some of the ligand only catalysts display good PET conversion as shown in Figure 4(a). Good catalyst activity corresponded to the ligands with terminal primary amines *i.e.* the NH_2 and NH-NH_2 ligands, having a conversion of 61% and 75%, respectively. The activity is associated with the ligands being organic bases. The bare SiO_2 support did not catalyse the reaction to any extent.

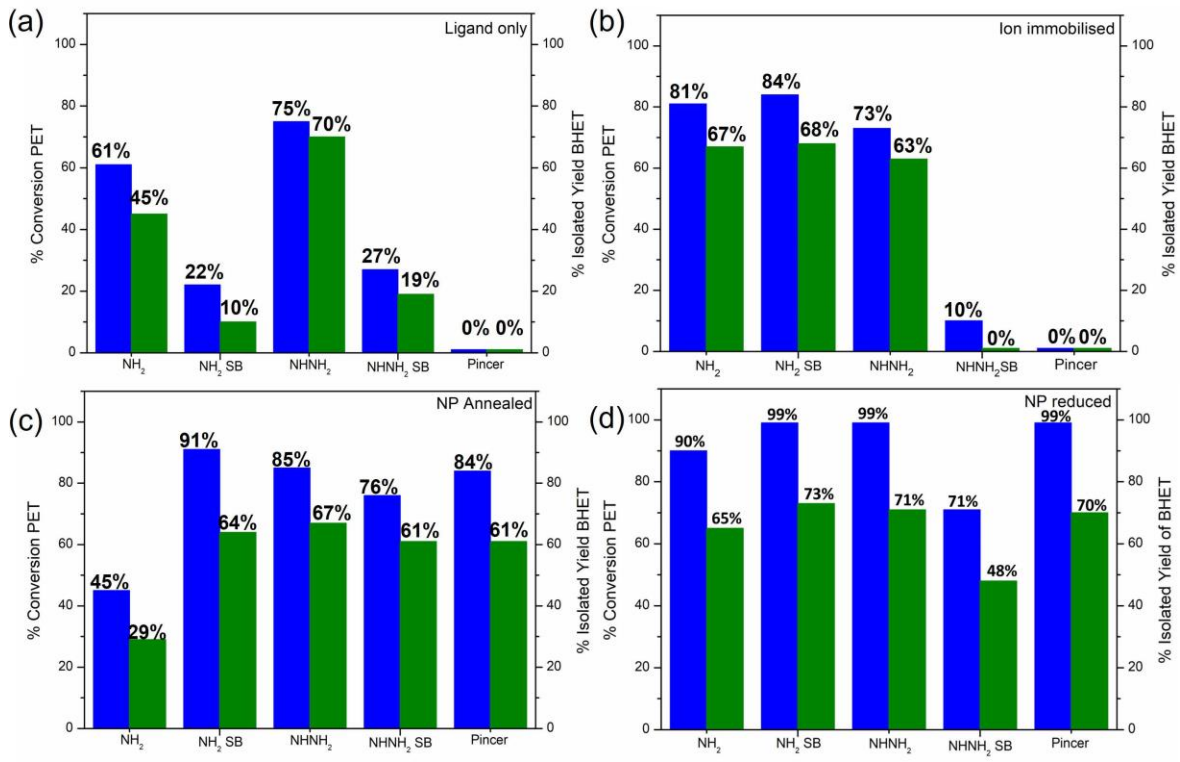

Figure 4: % conversion of PET and % yield of BHET obtained from glycolysis reaction for the catalysts which are ligand only, ion immobilised, NP via calcination and NP via $NaBH_4$ treated (reduced).

Figure 4 (b) compares the catalytic results after Fe ion immobilisation. The PET conversion increased for Fe immobilised on the SiO_2-NH_2, and SiO_2-NH_2-SB, with conversions of 81 % and 84 %, respectively, which is expected due to the presence of Fe^{3+} ions. A notable conclusion from Figure 4(b) is the considerable difference in activity observed between the Fe ions immobilised onto SiO_2 using the two Schiff base ligands. High conversion was observed for Fe ion immobilised using the SiO_2-NH_2–SB ligand (84%), however only a 10 % conversion was observed when using a SiO_2-NH-NH_2-SB ligand. The Fe loading on both catalysts is very similar indicating that the coordination chemistry of the iron on the surface modified SiO_2 plays a crucial role in the observed catalytic behaviour. The Fe^{3+} ions immobilised using the pincer ligand did not catalyse the reaction to any extent, which was attributed to the tight binding the Fe ions to the ligand.

Figure 4(c) and (d) show the PET conversion and isolated yields obtained using the NP catalysts obtained by calcination or $NaBH_4$-treatment, respectively. Generally, the NP catalysts displayed similar or higher PET conversions and BHET yields compared to their ion-immobilised version, regardless of whether they were prepared by calcination or $NaBH_4$-treatment, with exception of one catalyst: SiO_2-NH_2. The conversion of PET decreased from 81% in the ion SiO_2-Fe^{3+}-NH_2 catalyst to 45% when the catalyst was converted to NPs by calcination. However, when the catalyst was prepared by $NaBH_4$ treatment, a conversion of 90% was obtained. This trend is attributed to dual catalytic depolymerisation from the preservation of the amine ligands which are catalytically active in the reaction, as seen in Figure 4(a). All of the NP catalysts prepared by $NaBH_4$ treatment were superior to catalysts prepared by calcination. We rationalised that the size of the NPs formed may differ depending on the nature of the ligand and whether a calcination or $NaBH_4$-treated method was used, but this was not supported by TEM analysis. Figure 5 shows TEM analysis of the catalysts prepared by calcination and $NaBH_4$-treatment, which also confirms the formation of small diameter (~1-2 nm) Fe_2O_3 NPs well dispersed throughout the SiO_2 support. Due to the small size of the NPs and being embedded into the amorphous SiO_2 support it was challenging to obtain accurate size distributions, however it is clear from the TEM analysis that the diameter of the NPs was similar for catalysts prepared by $NaBH_4$ treatment and calcination. Their similar NP size indicates that the higher activity of the $NaBH_4$

treated catalysts may be attributed to the presence of the organic ligand. Synergistics effects have been shown between metal salts and organic bases for PET glycolysis.[44] However, several of the ligands used here are not bases, yet clearly have a beneficial impact on the catalytic performance. A recent report demonstrated that the addition of anisole to alkali metals salt catalysed PET glycolysis, facilitated a lower reaction temperature. DFT calculations suggested that the electron donating methoxy group in anisole transfers electron density to carbonyl O atom making it more nucleophilic and thereby susceptible to attack by metal ion species.[45] The electron donating ability of N containing groups in the ligands may have a similar effect in aiding glycolysis.

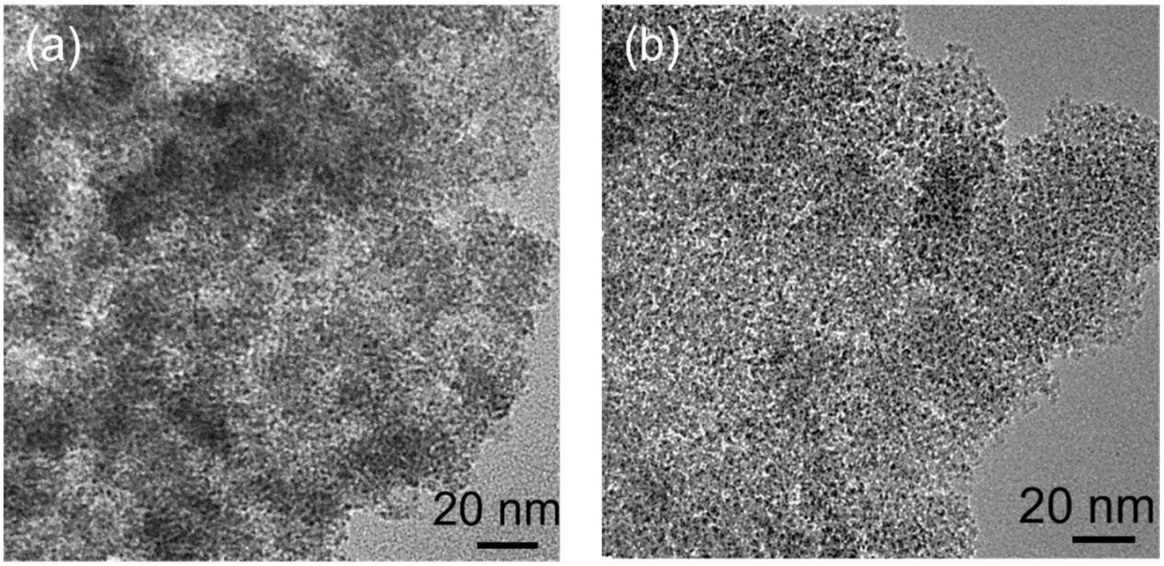

Figure 5: TEM images of Fe_2O_3 NPs supported on SiO_2 prepared by (a) calcination and (b) chemical reduction.

The catalytic evaluation highlights some important features on catalytic design in this system. The organic ligand used to bind the metal ion can significantly impact the catalytic performance as illustrated by the different reactivity behaviour. The metal oxide NP catalysts are in general superior to metal ion immobilised catalysts and the presence of both the organic ligand and metal oxide NP (i.e. catalysts prepared by $NaBH_4$-treatment) gave the best performance. We used DFT to rationalise the observed catalytic trends. Firstly, to analyse the strength of the interaction between the iron ion and the functionalized surface, binding energies (BEs) have been calculated (see Experimental Section for details).

We performed optimisations of the functionalised SiO_2 surface in the presence of Fe^{3+} considering three possible spin states translated to three different multiplicities (M = 2, 4, 6), showing that the high-spin M=6 is the ground state for the Fe^{+3} ion. Once the localized ground state for the Fe^{3} ion, had been determined binding energies have been calculated. The nature of the surface under study allows the SiO_2 surface to be functionalised with up to three organic linkers in the same unit cell. Binding energies represented in Table 1 are for the different organic linkers containing one, two, or three ligands (1L, 2L and 3L, respectively).

The organic ligands present a similar trend, with BEs dramatically decreasing as fewer ligands are involved, meaning that the iron ion is trapped within a net of coordinating bonds between the organic ligands (see Figure 6). The two poorest performing catalysts, Fe^{3+} immobilised on SiO_2-NH-NH_2-SB and SiO_2-pincer, had the highest binding energies as shown in Table 1, which effectively traps the ion in between the three sterically bulky organic ligands. For the SiO_2-pincer catalyst, the Fe^{3+} is coordinated with six N groups of the three pyridine rings. For SiO_2-NH-NH_2-SB catalyst the Fe^{3+} is coordinated to the three imine and the three pyridinic N groups. For these ligands, Fe had the largest BEs with Fe^{3+} coordinated in an octahedral geometry, and so the metal centre is sterically blocked from reacting, giving poor performance as observed. In the SiO_2-NH_2-SB catalyst the Fe ion is coordinated between three pyridinic Ns and two imine groups but unlike the SiO_2-NH-NH_2-SB catalyst, the metal ion is not octahedrally coordinated, resulting in a slightly lower binding energy. This lower binding energy and coordination geometry results in a less sterically hindered Fe^{3+} centre likely explains the significantly better catalytic performance of the SiO_2-NH_2-SB catalyst (84% conversion) compared to SiO_2-NH-NH_2-SB catalyst (10% conversion). A high metal ion BE is also attributed to why the performance for the SiO_2-NH-NH_2 catalyst did not improve after Fe ion immobilisation. In this system, the ligand only catalyst demonstrated relatively good reactivity with 75% conversion. After Fe ion immobilization (loading 4043.3 ppm), there was no change in the PET conversion (73%). In this ligand system, Fe^{3+} is coordinated to six amine groups, combining three primary amines and three secondary amines, in an octahedral geometry. The high BE limits the participation of the Fe^{3+} in the reaction and furthermore,

the presence of Fe^{3+} also prevents the terminal amine groups from catalysing the reaction. This contrasts with the SiO_2-NH_2 catalyst where Fe^{3+} is coordinated only by three amine groups giving it a lower BE and so the PET conversion increased after Fe^{3+} immobilisation.

Table 1: Binding energies (in kcal·mol^{-1}) of Fe^{+3} ion coordination with the organic ligands in the solvent phase (water).

Structure	1L	2L	3L
SiO_2-NH_2	-1.66	-80.73	-143.30
SiO_2-NH-NH_2	-123.83	-173.80	-258.27
SiO_2-NH_2-SB	-40.90	-172.47	-200.58
SiO_2-NH-NH_2-SB	-84.48	-227.11	-303.82
SiO_2-Pincer	-132.54	-273.49	-290.01

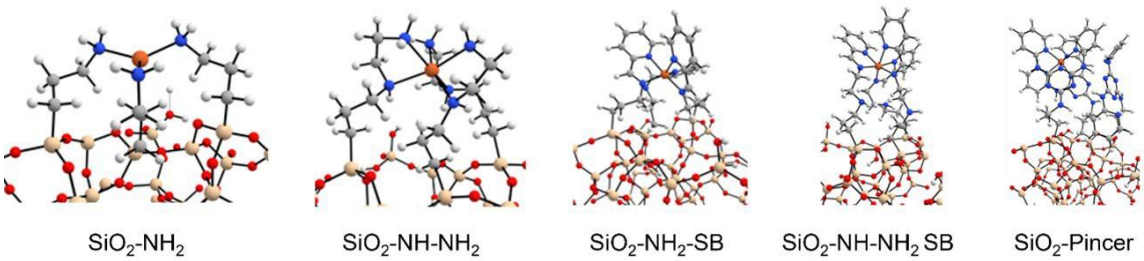

Figure 6: Representation of the optimized geometries for the different ligands coordinating the Fe^{+3} ion. Colour scheme: grey (C), white (H), blue (N), orange (Fe), red (O) and beige (Si).

The glycolysis reaction using the ion and NP catalysts were also modelled. The glycolysis of PET is the molecular degradation of the polymer by EG through a trans-esterification reaction where the ester linkage breaks and is replaced with hydroxyl groups. The reaction process starts with the coordination of PET to the metal centre by the oxygen of the carbonyl group of the ester. Since both ester groups are only separated by two -CH_2 it is possible to face the coordination of both adjacent ester groups. The following step is the transesterification of the ester by the EG where the carbonyl carbon is attacked by the free electron pair present on the hydroxyl group of EG. This is followed by the binding

between the hydroxyl ethyl group of EG with the carbonyl carbon of PET, resulting in breaking the long polymer chain into two short oligomers. The subsequent glycolysis will break this oligomer forming the BHET product.

The same mechanism for PET depolymerisation was modelled by constructing a molecular cluster that includes two repetitive units of the PET polymer (**A**) (See Figure 7(c)). The reaction was evaluated without a catalyst, and catalysed both by a single Fe^{+3} ion immobilised catalyst and the FeO NP catalyst in Figure 7 (a) and (b) respectively. In modelling the Fe^{+3} ion immobilised catalyst, it is important to consider the availability of the metal centre as the active site. Therefore, systems where the Fe^{+3} ion is fully coordinated or trapped between the most voluminous ligands will not perform well due to steric hindrance (e.g., SiO_2-$NHNH_2$-SB and SiO_2-Pincer), as experimentally demonstrated. Therefore, the system selected to represent the single Fe^{+3} ion catalysts was the SiO_2-NH_2 catalyst (Figure 7). Although this is the system presenting the lowest BEs, it is the structure presenting the least steric impediments. To model the NP catalyst, in order to keep the model simple and affordable in terms of computational resources it has been modelled a FeO nanocluster adsorbed onto the amorphous SiO_2 seen in Figure 7 (b), obtained using the Bulk Cut Nanoparticle Model (BCN-M), a computational tool that automatically generates Wulff-like models for binary materials with controlled stoichiometry.[46]

As shown in figure S7, PET fragment coordinates with the metal centre through the carbonyl group [Fe-O=C]. The trans-esterification reaction mechanism proposed here goes through one four-centred transition state ($\mathbf{TS_{A\text{-}B}}$) where the carbonyl carbon of the PET molecular cluster is attacked by the hydroxyl group of the EG subsequently forming the hydroxyl-carbonyl bond.

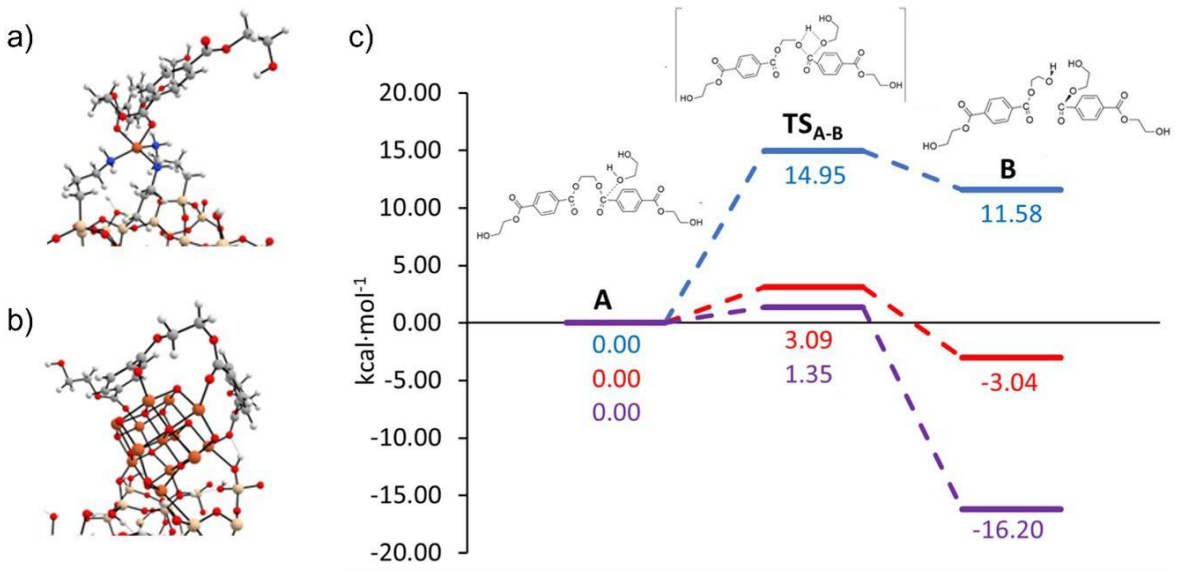

Figure 7: (a) Optimized geometry of the adsorbed PET molecular cluster over the Fe^{+3} ion. (b) Optimized geometry of the adsorbed PET over the FeO NP. Colour scheme: grey (C), white (H), blue (N), orange (Fe), red (O) and beige (Si). (c) Relative Gibbs energy profile at 190 °C (in kcal·mol^{-1}) for PET glycolysis considering EG as a solvent, via uncatalyzed (blue colour), catalysed by a single atom Fe^{3+} (red colour) and catalysed by a FeO NP (purple colour).

Figure 7 (c) depicts the potential energy surfaces (PES) for the reaction catalysed by single Fe^{3+} immobilised on SiO_2-NH_2 and the FeO NP catalyst. The PES show clear differences between the Fe ion and NP based catalysts structures under study. Energetic values show that the uncatalysed reaction not only goes through a higher barrier but also it presents and endergonic character and as expected, the activation energy is significantly reduced when performing the reaction with a catalyst. Interestingly, activation energies for both the Fe^{+3} and the FeO NP catalysts are similar (3.09 kcal mol^{-1} vs 1.35 kcal mol^{-1}, respectively), however there is an important difference in the thermodynamics. Products in the reaction catalysed by the NP catalyst are stabilized showing a significant exergonic character. Therefore, when performing the glycolysis reaction catalysed by the NP based catalysts, it is enhanced not only kinetically as the activation energy is lower but also, thermodynamically. The increased exergonic character is the main difference between the single Fe^{3+} ion catalyst and the NP

system, due to stabilization of the products and so therefore the metal oxide NP catalyst show superior catalytic activity. The product (BHET) for each reaction is the same, the differences are the catalysts and their environments which is the reason for the energy differences.

Optimisation of reaction conditions

Finally, we used the best performing catalyst as identified by the evaluation study i.e. the Fe_2O_3 NP catalysts prepared by $NaBH_4$-treatment using the SiO_2-NH_2-SB and SiO_2-pincer ligands, to further study the impact of reaction parameters such as temperature, time, catalyst loading and PET:EG ratio. Figure 8(a) compares the effect of reaction temperature and catalyst concentration. The PET conversions increased with higher catalyst loading reaching full conversion at 100 mg. The optimal temperature of the reaction was found to be 190 °C, with PET conversions decreasing at lower temperatures. Figure 8(b) shows the ratio of PET: EG was critical for the reaction with a ratio of 1:5 being optimal for full PET conversion. On decreasing the ratio to 1:3, there was insufficient EG to cover the PET for the reaction to proceed smoothly. Figure 8 (c) shows a reaction time series ranging from one to three hours of the heterogeneous catalysts compared with using a homogeneous $FeCl_3$ catalyst. The reactions were carried out under the same conditions and iron loading. Both the heterogeneous catalysts display higher PET conversions compared to the homogeneous catalyst. It is clear that under these conditions the Fe_2O_3 NPs catalyst outperformed the ion-immobilised catalyst but also a homogenous catalyst of equivalent loading. This is attributed to the high dispersion of the NP on the SiO_2 support and the presence of the organic ligand. An additional benefit of using a heterogeneous catalyst was the absence of the metal contamination in the BHET product, which was clearly evident in the isolated BHET using the homogeneous iron catalyst. Finally, the use of additives and colorants are commonly found in post-consumer plastic and their impact on catalyst performance is not always explored. The Fe_2O_3 NP catalyst was used to depolymerise black and green coloured PET as shown in Figure 8 (d), giving high PET conversions of 94 % for both black and green plastic showing that this catalyst can effectively be used for coloured plastic.

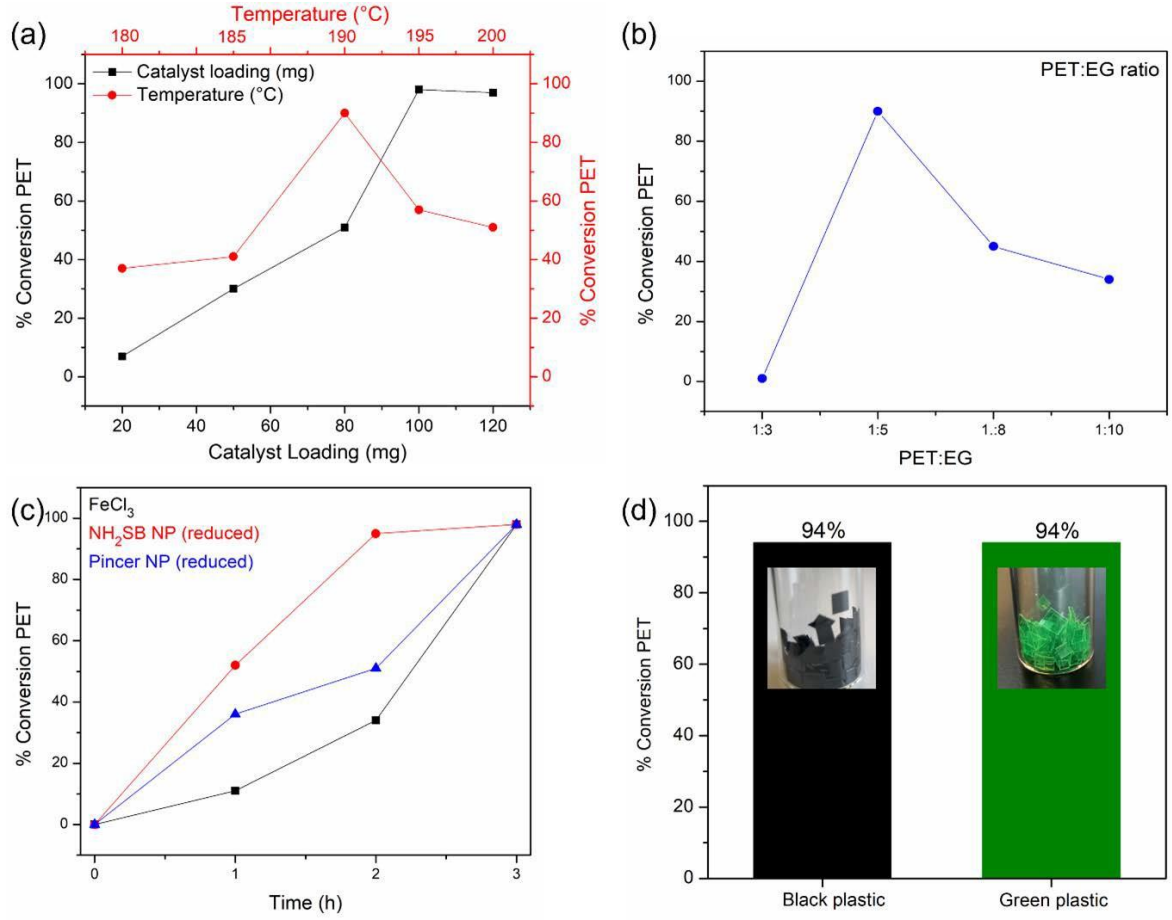

Figure 8: (a) Optimisation reactions and, (b) PET:EG ratio optimisation, (c) time series of $FeCl_3$, Fe pincer NP reduced and Fe NH_2 SB NP $NaBH_4$-treated (reduced) (d) coloured plastic.

5.4 Conclusions

In conclusion, we investigated the catalyst design for the glycolysis of PET using heterogeneous mesoporous SiO_2 catalysts. The SiO_2 support was modified with a range of nitrogen containing ligands used for the immobilised of Fe ions. The Fe immobilised catalysts were then converted into Fe_2O_3 NPs via calcination or $NaBH_4$-treatment (reduction) to find the optimum catalyst for the depolymerisation of PET to BHET. The NP based catalyst performed better than ion immobilised catalysts and that the presence of both the metal oxide NP and organic ligand display the best performance giving full PET conversion and high BHET yields, which was attributed to synergistic effects between the ligand and the NP.

This work also demonstrates the potential role of using organically modified SiO_2 supports for PET glycolysis without the presence of an active metal species. The SiO_2 support functionalised with simple organic ligands, such as primary amines showed relatively good PET conversion (70 %). It was this observation that led to the motivation of the next results chapter which was to develop metal-free heterogeneous catalysts based on surface modification with highly basic organic ligands.

5.5 References

1. Johansen, M. R.; Christensen, T. B.; Ramos, T. M.; Syberg, K., A review of the plastic value chain from a circular economy perspective. *Journal of Environmental Management* **2022,** *302*, 113975.
2. Liu, Y.; Yao, X.; Yao, H.; Zhou, Q.; Xin, J.; Lu, X.; Zhang, S., Degradation of poly(ethylene terephthalate) catalyzed by metal-free choline-based ionic liquids. *Green Chemistry* **2020,** *22* (10), 3122-3131.
3. Siddiqui, M. N.; Redhwi, H. H.; Al-Arfaj, A. A.; Achilias, D. S., Chemical Recycling of PET in the Presence of the Bio-Based Polymers, PLA, PHB and PEF: A Review. *Sustainability* **2021,** *13* (19).
4. Hou, Q.; Zhen, M.; Qian, H.; Nie, Y.; Bai, X.; Xia, T.; Rehman, M. L. U.; Li, Q.; Ju, M., Cell Reports Phys. *Sci* **2021,** *2*, 100514.
5. Stanica-Ezeanu, D.; Matei, D., Natural depolymerization of waste poly(ethylene terephthalate) by neutral hydrolysis in marine water. *Scientific Reports* **2021,** *11* (1), 4431.
6. Yang, W.; Liu, R.; Li, C.; Song, Y.; Hu, C., Hydrolysis of waste polyethylene terephthalate catalyzed by easily recyclable terephthalic acid. *Waste Management* **2021,** *135*, 267-274.
7. Chen, J.; Lv, J.; Ji, Y.; Ding, J.; Yang, X.; Zou, M.; Xing, L., Alcoholysis of PET to produce dioctyl terephthalate by isooctyl alcohol with ionic liquid as cosolvent. *Polymer Degradation and Stability* **2014,** *107*, 178-183.
8. Scremin, D. M.; Miyazaki, D. Y.; Lunelli, C. E.; Silva, S. A.; Zawadzki, S. F., PET Recycling by Alcoholysis Using a New Heterogeneous Catalyst: Study and its Use in Polyurethane Adhesives Preparation. *Macromolecular Symposia* **2019,** *383* (1), 1800027.
9. Wang, L.; Nelson, G. A.; Toland, J.; Holbrey, J. D., Glycolysis of PET Using 1,3-Dimethylimidazolium-2-Carboxylate as an Organocatalyst. *ACS Sustainable Chemistry & Engineering* **2020,** *8* (35), 13362-13368.
10. Chen, F.; Wang, G.; Shi, C.; Zhang, Y.; Zhang, L.; Li, W.; Yang, F., Kinetics of glycolysis of poly(ethylene terephthalate) under microwave irradiation. *Journal of Applied Polymer Science* **2013,** *127* (4), 2809-2815.
11. Vollmer, I.; Jenks, M. J. F.; Roelands, M. C. P.; White, R. J.; van Harmelen, T.; de Wild, P.; van der Laan, G. P.; Meirer, F.; Keurentjes, J. T. F.; Weckhuysen, B. M., Beyond Mechanical Recycling: Giving New Life to Plastic Waste. *Angewandte Chemie International Edition* **2020,** *59* (36), 15402-15423.
12. Yue, Q. F.; Xiao, L. F.; Zhang, M. L.; Bai, X. F., The Glycolysis of Poly(ethylene terephthalate) Waste: Lewis Acidic Ionic Liquids as High Efficient Catalysts. *Polymers* **2013,** *5* (4), 1258-1271.
13. Duque-Ingunza, I.; López-Fonseca, R.; de Rivas, B.; Gutiérrez-Ortiz, J. I., Process optimization for catalytic glycolysis of post-consumer PET wastes. *Journal of Chemical Technology & Biotechnology* **2014,** *89* (1), 97-103.
14. Shukla, S. R.; Kulkarni, K. S., Depolymerization of poly(ethylene terephthalate) waste. *Journal of Applied Polymer Science* **2002,** *85* (8), 1765-1770.
15. López-Fonseca, R.; Duque-Ingunza, I.; de Rivas, B.; Flores-Giraldo, L.; Gutiérrez-Ortiz, J. I., Kinetics of catalytic glycolysis of PET wastes with sodium carbonate. *Chemical Engineering Journal* **2011,** *168* (1), 312-320.
16. Fang, P.; Liu, B.; Xu, J.; Zhou, Q.; Zhang, S.; Ma, J.; lu, X., High-efficiency glycolysis of poly(ethylene terephthalate) by sandwich-structure polyoxometalate catalyst with two active sites. *Polymer Degradation and Stability* **2018,** *156*, 22-31.
17. Chen, F.; Wang, G.; Li, W.; Yang, F., Glycolysis of Poly(ethylene terephthalate) over Mg–Al Mixed Oxides Catalysts Derived from Hydrotalcites. *Industrial & Engineering Chemistry Research* **2013,** *52* (2), 565-571.
18. Fuentes, C. A.; Gallegos, M. V.; García, J. R.; Sambeth, J.; Peluso, M. A., Catalytic Glycolysis of Poly(ethylene terephthalate) Using Zinc and Cobalt Oxides Recycled from Spent Batteries. *Waste and Biomass Valorization* **2020,** *11* (9), 4991-5001.

19. Wang, Q.; Geng, Y.; Lu, X.; Zhang, S., First-Row Transition Metal-Containing Ionic Liquids as Highly Active Catalysts for the Glycolysis of Poly(ethylene terephthalate) (PET). *ACS Sustainable Chemistry & Engineering* **2015,** *3* (2), 340-348.
20. Lalhmangaihzuala, S.; Laldinpuii, Z.; Lalmuanpuia, C.; Vanlaldinpuia, K., Glycolysis of Poly(Ethylene Terephthalate) Using Biomass-Waste Derived Recyclable Heterogeneous Catalyst. *Polymers (Basel)* **2020,** *13* (1).
21. Yunita, I.; Putisompon, S.; Chumkaeo, P.; Poonsawat, T.; Somsook, E., Effective catalysts derived from waste ostrich eggshells for glycolysis of post-consumer PET bottles. *Chemical Papers* **2019,** *73* (6), 1547-1560.
22. Laldinpuii, Z.; Lalhmangaihzuala, S.; Pachuau, Z.; Vanlaldinpuia, K., Depolymerization of poly(ethylene terephthalate) waste with biomass-waste derived recyclable heterogeneous catalyst. *Waste Management* **2021,** *126*, 1-10.
23. Veregue, F. R.; Pereira da Silva, C. T.; Moisés, M. P.; Meneguin, J. G.; Guilherme, M. R.; Arroyo, P. A.; Favaro, S. L.; Radovanovic, E.; Girotto, E. M.; Rinaldi, A. W., Ultrasmall Cobalt Nanoparticles as a Catalyst for PET Glycolysis: A Green Protocol for Pure Hydroxyethyl Terephthalate Precipitation without Water. *ACS Sustainable Chemistry & Engineering* **2018,** *6* (9), 12017-12024.
24. Son, S. G.; Jin, S. B.; Kim, S. J.; Park, H. J.; Shin, J.; Ryu, T.; Jeong, J.-M.; Choi, B. G., Exfoliated manganese oxide nanosheets as highly active catalysts for glycolysis of polyethylene terephthalate. *FlatChem* **2022,** *36*, 100430.
25. Cao, J.; Lin, Y.; Jiang, W.; Wang, W.; Li, X.; Zhou, T.; Sun, P.; Pan, B.; Li, A.; Zhang, Q., Mechanism of the Significant Acceleration of Polyethylene Terephthalate Glycolysis by Defective Ultrathin ZnO Nanosheets with Heteroatom Doping. *ACS Sustainable Chemistry & Engineering* **2022,** *10* (17), 5476-5488.
26. Suo, Q.; Zi, J.; Bai, Z.; Qi, S., The Glycolysis of Poly(ethylene terephthalate) Promoted by Metal Organic Framework (MOF) Catalysts. *Catalysis Letters* **2017,** *147* (1), 240-252.
27. Wu, Y.; Wang, X.; Kirlikovali, K. O.; Gong, X.; Atilgan, A.; Ma, K.; Schweitzer, N. M.; Gianneschi, N. C.; Li, Z.; Zhang, X.; Farha, O. K., Catalytic Degradation of Polyethylene Terephthalate Using a Phase-Transitional Zirconium-Based Metal–Organic Framework. *Angewandte Chemie International Edition* **2022,** *61* (24), e202117528.
28. Shukla, S. R.; Palekar, V.; Pingale, N., Zeolite catalyzed glycolysis of poly(ethylene terephthalate) bottle waste. *Journal of Applied Polymer Science* **2008,** *110* (1), 501-506.
29. Yang, R.-X.; Bieh, Y.-T.; Chen, C. H.; Hsu, C.-Y.; Kato, Y.; Yamamoto, H.; Tsung, C.-K.; Wu, K. C. W., Heterogeneous Metal Azolate Framework-6 (MAF-6) Catalysts with High Zinc Density for Enhanced Polyethylene Terephthalate (PET) Conversion. *ACS Sustainable Chemistry & Engineering* **2021,** *9* (19), 6541-6550.
30. Wang, T.; Shen, C.; Yu, G.; Chen, X., Metal ions immobilized on polymer ionic liquid as novel efficient and facile recycled catalyst for glycolysis of PET. *Polymer Degradation and Stability* **2021,** *194*, 109751.
31. Kim, J.; Song, B.; Chung, I.; Park, J.; Yun, Y., High-performance Pt catalysts supported on amine-functionalized silica for enantioselective hydrogenation of α-keto ester. *Journal of Catalysis* **2021,** *396*, 81-91.
32. Li, M.; Huang, Y.; Yu, T.; Chen, S.; Ju, A.; Ge, M., Chemical recycling of waste poly(ethylene terephthalate) fibers into azo disperse dyestuffs. *RSC Advances* **2014,** *4* (87), 46476-46480.
33. Hutter, J.; Iannuzzi, M.; Schiffmann, F.; VandeVondele, J., cp2k: atomistic simulations of condensed matter systems. *WIREs Computational Molecular Science* **2014,** *4* (1), 15-25.
34. Ugliengo, P.; Sodupe, M.; Musso, F.; Bush, I. J.; Orlando, R.; Dovesi, R., Realistic Models of Hydroxylated Amorphous Silica Surfaces and MCM-41 Mesoporous Material Simulated by Large-scale Periodic B3LYP Calculations. *Advanced Materials* **2008,** *20* (23), 4579-4583.
35. Perdew, J. P.; Ruzsinszky, A.; Csonka, G. I.; Vydrov, O. A.; Scuseria, G. E.; Constantin, L. A.; Zhou, X.; Burke, K., Restoring the Density-Gradient Expansion for Exchange in Solids and Surfaces. *Physical Review Letters* **2008,** *100* (13), 136406.

36. Grimme, S.; Antony, J.; Ehrlich, S.; Krieg, H., A consistent and accurate ab initio parametrization of density functional dispersion correction (DFT-D) for the 94 elements H-Pu. *The Journal of Chemical Physics* **2010,** *132* (15), 154104.
37. Goedecker, S.; Teter, M.; Hutter, J., Separable dual-space Gaussian pseudopotentials. *Physical Review B* **1996,** *54* (3), 1703-1710.
38. Lippert, B. G.; Parrinello, J. H.; Michele, A hybrid Gaussian and plane wave density functional scheme. *Molecular Physics* **1997,** *92* (3), 477-488.
39. Andreussi, O.; Dabo, I.; Marzari, N., Revised self-consistent continuum solvation in electronic-structure calculations. *J Chem Phys* **2012,** *136* (6), 064102.
40. Graf, N.; Yegen, E.; Gross, T.; Lippitz, A.; Weigel, W.; Krakert, S.; Terfort, A.; Unger, W. E. S., XPS and NEXAFS studies of aliphatic and aromatic amine species on functionalized surfaces. *Surface Science* **2009,** *603* (18), 2849-2860.
41. Paengjun, N.; Vibulyaseak, K.; Ogawa, M., Heterostructural transformation of mesoporous silica–titania hybrids. *Scientific Reports* **2021,** *11* (1), 3210.
42. Yamashita, T.; Hayes, P., Analysis of XPS spectra of Fe2+ and Fe3+ ions in oxide materials. *Applied Surface Science* **2008,** *254* (8), 2441-2449.
43. Poulin, S.; França, R.; Moreau-Bélanger, L.; Sacher, E., Confirmation of X-ray Photoelectron Spectroscopy Peak Attributions of Nanoparticulate Iron Oxides, Using Symmetric Peak Component Line Shapes. *The Journal of Physical Chemistry C* **2010,** *114* (24), 10711-10718.
44. Delle Chiaie, K. R.; McMahon, F. R.; Williams, E. J.; Price, M. J.; Dove, A. P., Dual-catalytic depolymerization of polyethylene terephthalate (PET). *Polymer Chemistry* **2020,** *11* (8), 1450-1453.
45. Le, N. H.; Ngoc Van, T. T.; Shong, B.; Cho, J., Low-Temperature Glycolysis of Polyethylene Terephthalate. *ACS Sustainable Chemistry & Engineering* **2022**.
46. González, D.; Camino, B.; Heras-Domingo, J.; Rimola, A.; Rodríguez-Santiago, L.; Solans-Monfort, X.; Sodupe, M., BCN-M: A Free Computational Tool for Generating Wulff-like Nanoparticle Models with Controlled Stoichiometry. *The Journal of Physical Chemistry C* **2020,** *124* (1), 1227-1237.

5.6 Supplementary information

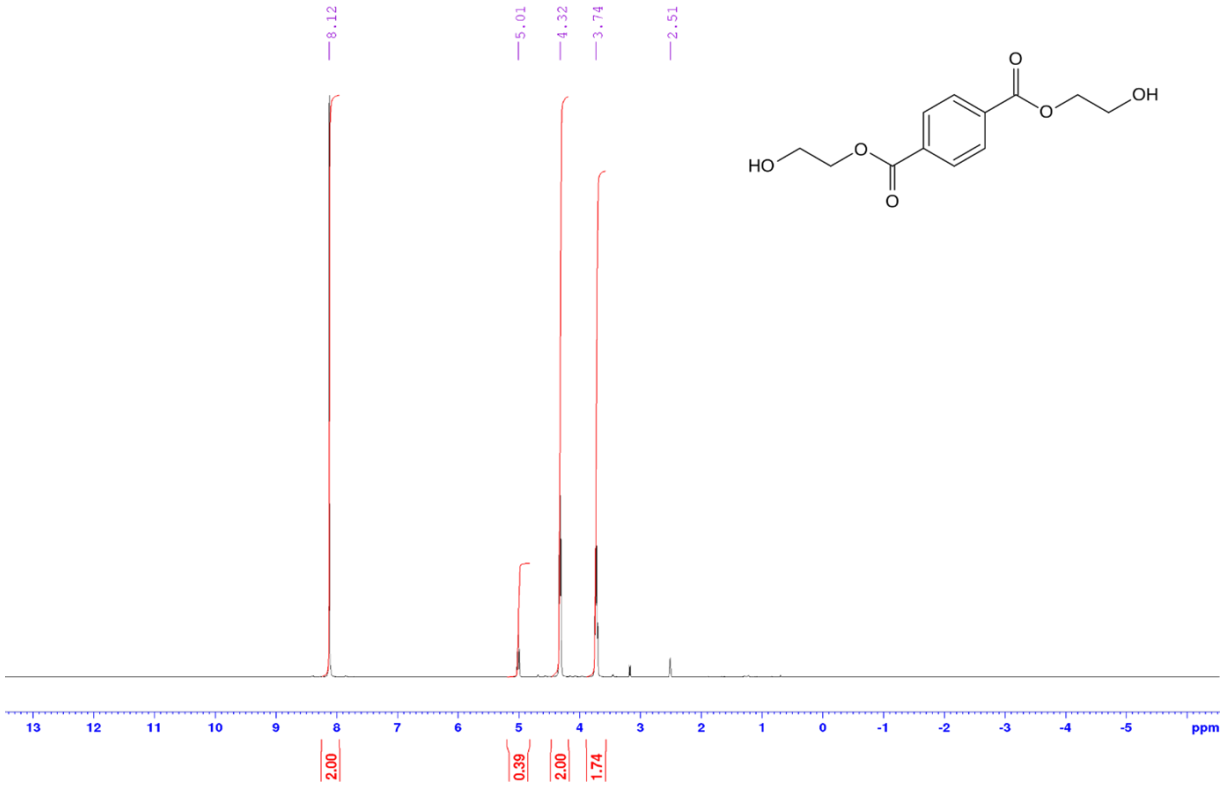

Figure S1: ^{1}H NMR of the BHET product formed from the glycolysis of PET

NMR analysis confirmed that no formation of dimers or oligomers occurred and that BHET was the only product formed in the reaction. The 1H NMR spectrum of BHET can be seen in figure 11, where the four main peaks were a singlet at 8.12 ppm corresponding to an aromatic ring, an OH triplet at 5.01 ppm, CH_2 triplet at 4.32 ppm and CH_2 quartet at 3.77 ppm. Residual solvent d_6-DMSO was located at 2.51 ppm. The results are in good agreement with literature values of BHET.

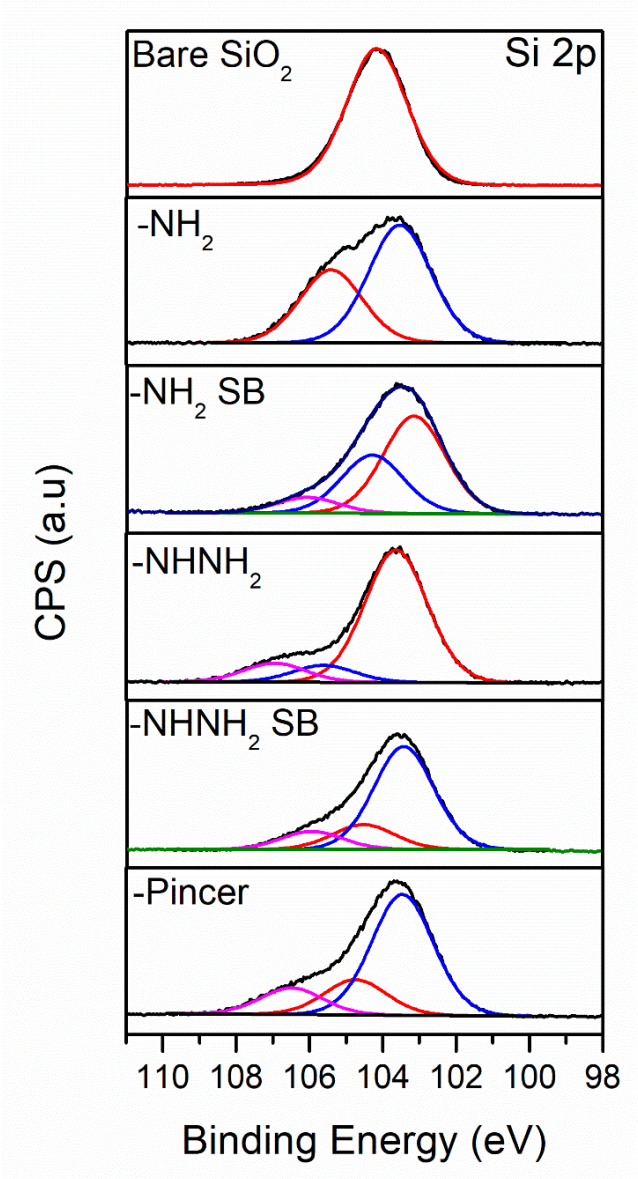

Figure S2: XPS analysis of the Si 2p core level for bare silica, the functionalised SiO_2 with $-NH_2$, $-NH_2$ SB, $-NHNH_2$, $-NHNH_2$ SB and pincer respectively

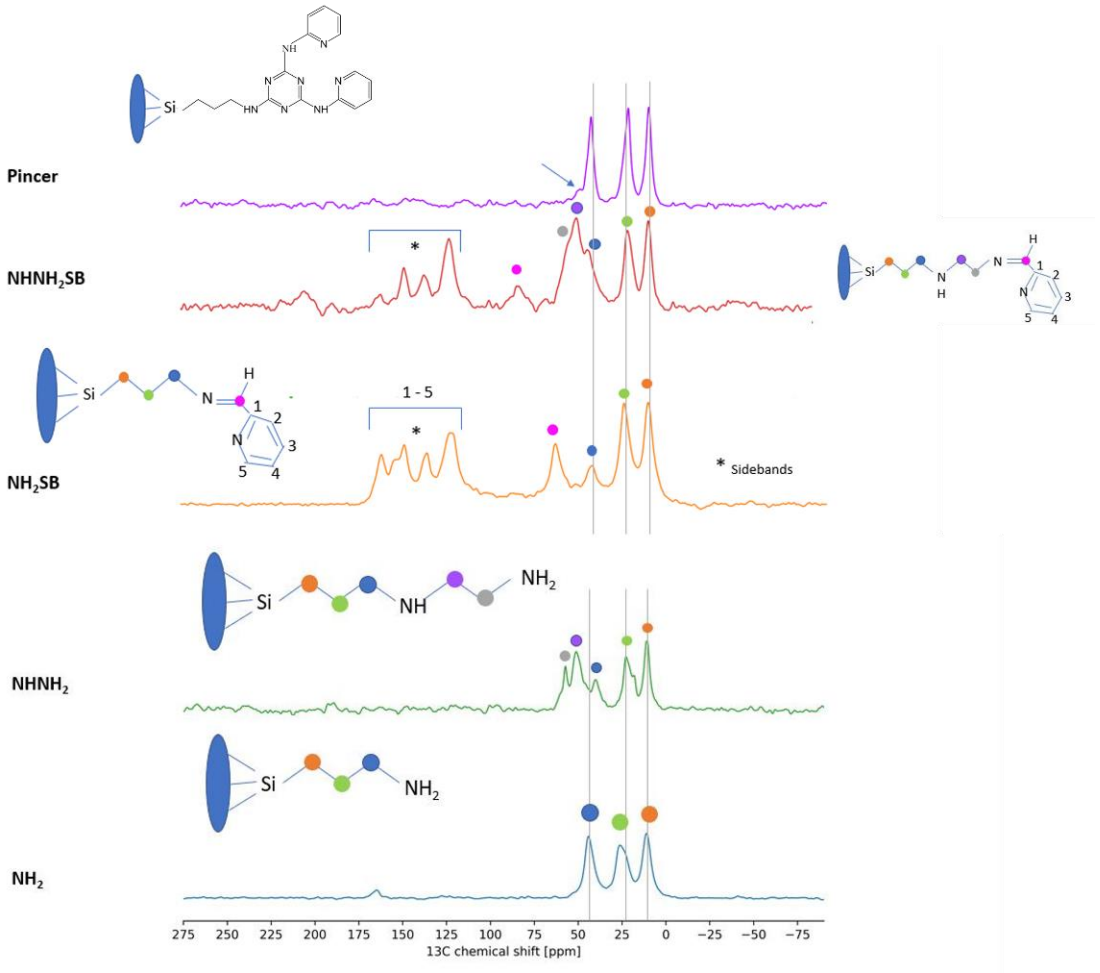

Figure S3: ^{13}C CPMAS solid state NMR of each functionalised SiO_2 catalyst.

Table S1: ICP-MS results showing the Fe loading for each ion immobilised catalyst.

Catalyst	Fe Loading
Fe NH_2	4173 ppm
Fe NH_2SB	4981 ppm
Fe $NHNH_2$	4043 ppm
Fe $NHNH_2$ SB	3964 ppm
Fe pincer	3904 ppm

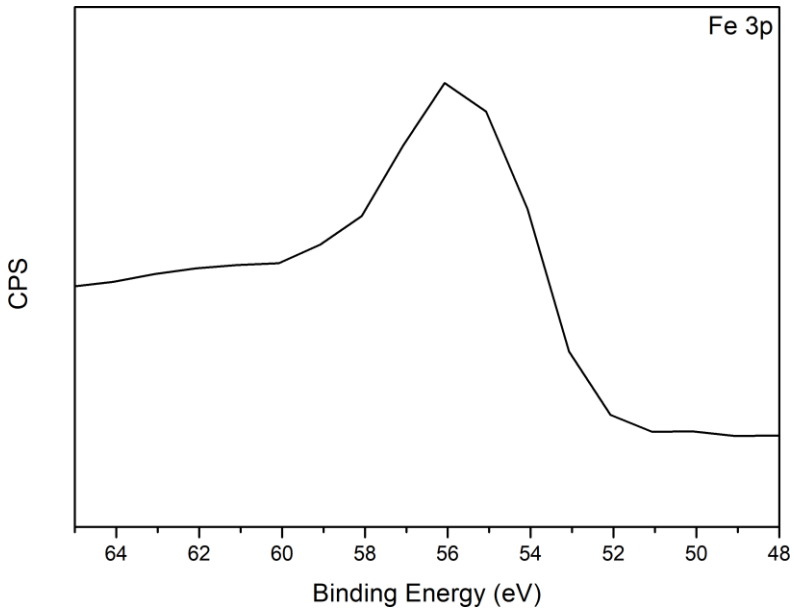

Figure S4: Fe 3p spectrum of Pincer NP via $NaBH_4$-treatment.

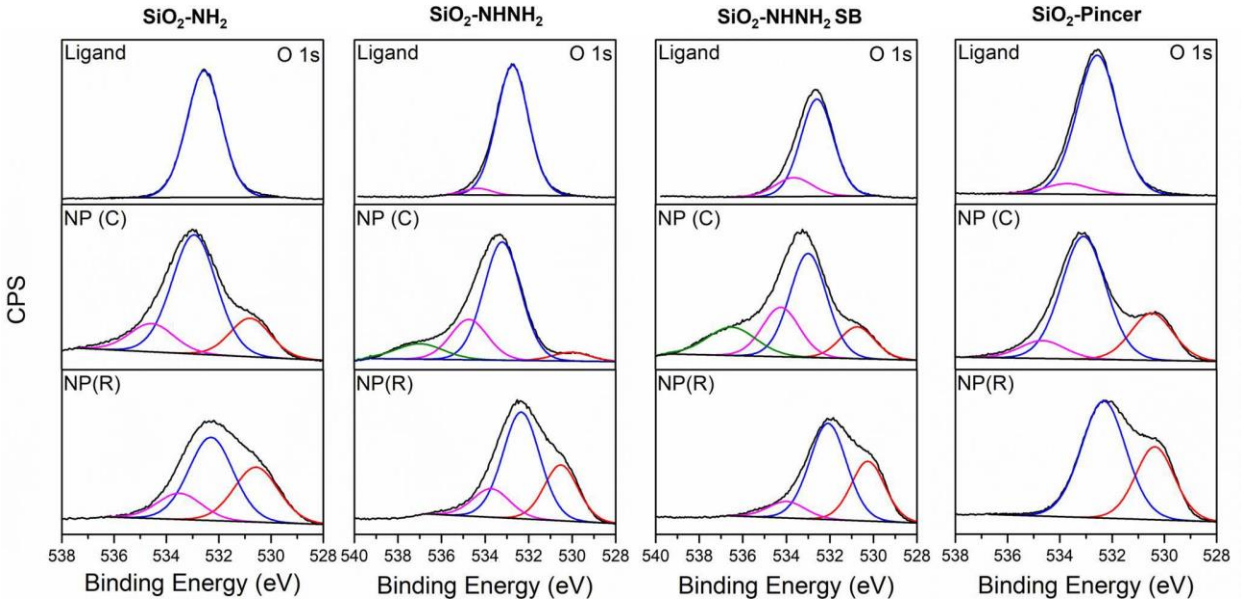

Figure S5: O 1s core level spectra of ligand only and both calcined and $NaBH_4$-treated (reduced) NP catalysts for SiO_2-NH_2, SiO_2- NH-NH_2, SiO_2-NH-NH_2 SB and SiO_2-pincer ligands.

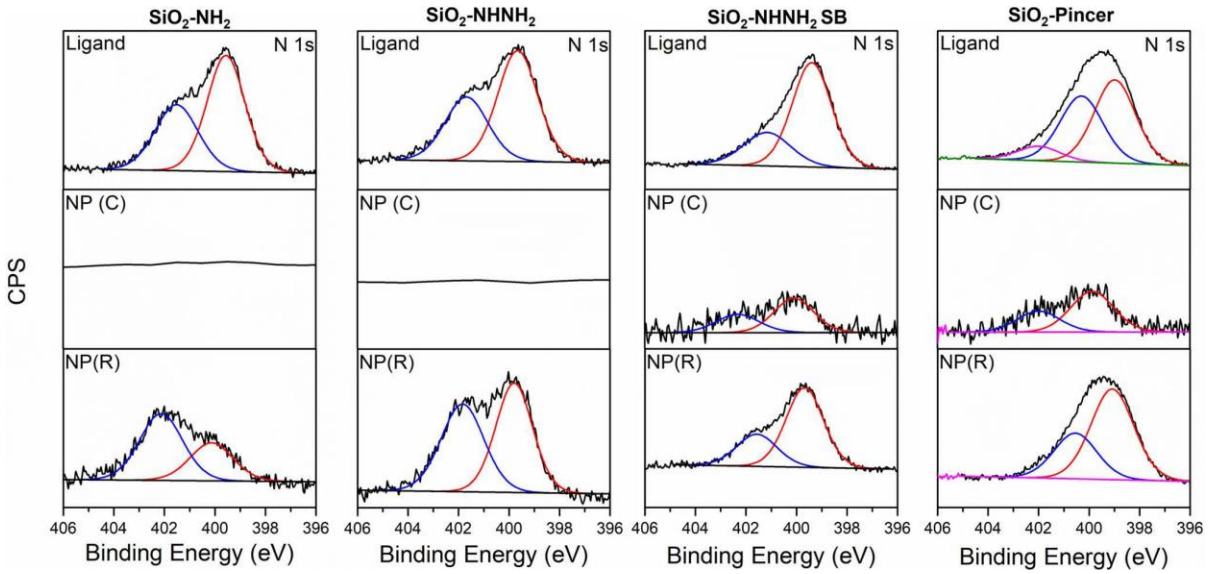

Figure S6: N 1s core level spectra of ligand only and both calcined and $NaBH_4$-treated (reduced) NP catalysts for SiO_2-NH_2, SiO_2- NH-NH_2, SiO_2-NH-NH_2 SB and SiO_2-pincer ligands.

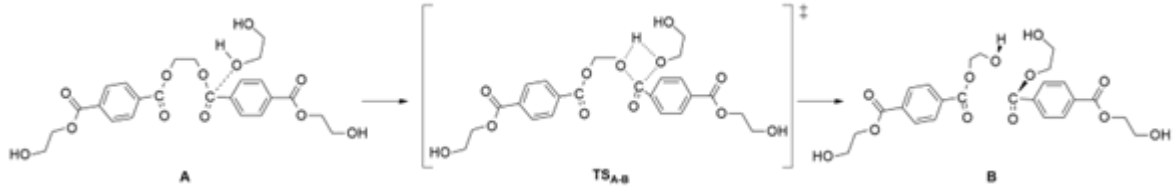

Figure S7: Proposed mechanism for the PET glycolysis reaction.

Chapter 6

Metal free heterogeneous catalysts for chemical Degradation of PET and PLA

Metal Free Heterogeneous Catalysts for Chemical Degradation of PET and PLA

Éadaoin Casey, Rachel Breen, Eleanor Noonan, Prof. Justin. D Holmes, Dr. Gillian Collins*

[1] School of Chemistry, University College Cork, Cork, T12 YN60, Ireland.

[2] AMBER Centre, Environmental Research Institute, University College Cork, Cork, T23 XE10, Ireland.

Abstract

Chemical recycling is an important strategy to tackle the growing global problem of plastic waste pollution. The development of metal-free catalysts for depolymerisation of plastics is attractive as it avoids the use of metal salts which are potentially damaging to the environment. Here we report a metal-free heterogeneous catalyst for the glycolysis of polyethylene terephthalate (PET) to form the monomer bis(2-hydroxyethyl) terephthalate (BHET) and methanolysis of polylactic acid (PLA) to form methyl lactate (MeLa). The catalysts are based on covalent surface modification of mesoporous silica (SiO_2) with guanidine ligands. The depolymerisation reactions were carried out under conventional thermal and microwave-assisted heating. Under thermal conditions the catalyst which gave the highest PET conversion in the shortest time was SiO_2-DCD. The SiO_2-DCD was also the best-performing catalyst under microwave conditions. We also observed that the role of the support material influenced catalyst performance under microwave conditions. For methanolysis of PLA, the SiO_2-DCD catalyst gave the highest yield of MeLa. The work illustrates that surface-bound organocatalysts based on guanidine catalysts are versatile catalysts for plastic depolymerisation.

6.1 Introduction

Plastics are ubiquitous to our everyday lives as it one of the most used materials around the world owing to their low cost, versatility, and ease of production.[1] Their uses range from lifelong plastic materials for household appliances, building materials and electronics to the single use plastics such as shopping bags, straws, food packaging and water bottles.[2] The main issues arising in these single use items as that there is such high demand as the production has already increased dramatically in the last 50 years from 15 to 311 million tons and is expected to double by 2035, this leads to a drastic increase in waste produced.[3] Depending on the type of plastic, it can take anywhere from 20-500 years to degrade, and this waste usually ends up in our landfills which it will inevitability not be able to withstand the increase waste over time. According to the Department of the Environment, Climate, and Communications[4], 70% of all marine litter in the EU are found from the 10 most common single uses plastic items. The Irish Government have set obligations in a directive which will enforce PET plastic bottles (up to 3 litres in size) being banned from the Irish market from January 2025 unless the PET bottles contain a minimum of 25% recycled plastic. By January 2030, they must contain at least 30% recycled plastic. In recent years, researchers have been developing pathways to convert plastic waste polymers into monomers or value-added products forming a circular economy in the polymer life cycle.[5]

Polyethylene terephthalate (PET) is a thermoplastic polyester and used in wider ranging applications such as textiles, food packaging and water bottles.[6] It is the most common polymer for single used plastics and a key contributor to the problem of post-consumer plastic waste. This polymer has been heavily researched in recent years to find an effective, environmentally friendly method to transform it to a useful monomer with the final goal of achieving a circular economy in the polymer life cycle rather than incineration which is harmful to the environment.[7] Glycolysis is the most effective method for depolymerisation of PET to its monomer BHET as it can be achieved under mild conditions with a relatively low cost.[8] [9] The method involves a reaction between PET, excess ethylene glycol and a catalyst with the product BHET being obtained. The degradation occurs at relatively high temperature

(> 200 °C) in the absence of a catalyst but typically proceeds ~190°C in the presence of a catalyst.[10] Zinc acetate is one of the most commonly used catalysts as it can achieve excellent conversions (> 90%) of PET.[11-12] A wide variety of catalyst are effective for PET glycolysis such as metal oxides[13-14], metal salts[11, 15], and organocatalysts.[3, 9, 16-17]

Metal free catalysts are particularly attractive, as a green and sustainable alternative to metal based catalysts. It also avoids potential metal ion contamination in the end product. Guanidines have gained attention in catalysis as they are strong organic bases . Fukushima and co-workers[18] reported the use of commercially available guanidine catalyst 1,5,7-triazabicyclo[4.4.0]dec-5-ene (TBD) as highly effective catalyst for the glycolysis of PET in the presence of ethylene glycol. PET was fully converted and an isolated yield of 78 % was obtained at 190 °C, 10 mol % catalyst, 1:5 ratio PET:EG after 325 min. For comparison, when the reaction was completed in the absence of TBD, PET was fully converted after 40 h at 190 °C. Le *et al*.[19] reported the catalytic activity of TBD in a co-solvent assisted glycolysis reaction were 100 % conversion of PET and 82 % yield of BHET was achieved at 153 °C after 2 h.

Chipurici *et al.*[20] demonstrated a synthesis of heterogeneous catalysts with guanidine superbases chemically grafted on silica-coated Fe_3O_4 magnetic nanoparticles for microwave-assisted transesterification reaction of waste oil. They report that their three guanidine base catalysts performed well in the transesterification reactions yielding over 80 % fatty acid methyl ester. Fehér *et al*. [16] reported the novel synthesis of TBD supported on silica gel as an eco-friendly organocatalyst for PET glycolysis depolymerisation. They also tested three commercially available functionalised silicas for comparison with their newly designed catalyst in the same reaction. The Si-TBD catalyst had the highest catalytic activity achieving 100 % conversion of PET and 88 % yield of BHET. The optimal reaction conditions were 190 °C, 15.5 mol % catalyst, EG: PET molar ratio of 12.6, and 1.7 h reaction time.

The use of microwave assisted glycolysis has seen a huge interest due to the significant reduction in reaction time and energy consumption, potentially improving the energy efficiency of the PET

glycolysis.[21] The main advantage of microwave heating over existing conventional heating methods is, rapid heating rates and high temperatures, which is commonly known as “thermal effects”. This occurs through dielectric heating mechanism and can result in an increased reaction rates, product selectivity and increased yields over conventional thermal methods.[22] Thermal effects in microwave assisted methods occur through hotspot generation, and selective species heating which is a unique characteristic of microwave-assisted heating. The most common catalysts reported for microwave assisted reaction glycolysis for the PET depolymerisation reaction are metal salts and metal oxides.[23]

Recently, there has been great interest in biodegradable plastics such as polylactic acid (PLA) as an alternative to fossil-fuel derived plastics material and the environmental issues regarding the waste from other plastic products. The PLA market has increased exponentially in recent years as the physical properties are similar to that of the current plastics PET, PP and HDPE and is able to be used as an alternative without having the waste disposal issues. While often branded as an eco-friendly biogradable plastic, PLA only degrades at an appreciable rate under specific conditions such as those generated in industrial composing facilities. In the natural environment, PLA persists for hundreds of years.[24] Furthermore, designing a plastic to degrade in the environment affiliates with a linear plastics economy model and does not align to a circular model. Therefore, instead of disposing of PLA to composting sites, upcycling strategies are needed to enable a more sustainable use of the PLA. Methanolysis is a common method for the transformation from PLA to MeLa – which is a green solvent. There has been several reports of inorganic metal salts such as $FeCl_3$ and ZnAc catalysts, however these salts are deemed environmentally damaging. Román-Ramírez et al.[24] produced MeLa from chemical degradation of PLA using an ethylenediamine Zn(II) complex. They trialled three PLA sources during their study, including a cup, a toy, and a 3D printing material at 70, 90 and 110 °C. They report achieving high selectively and yields (>94%). Petrus and co workers[25], synthesised multiple alkyl lactates using metal containing catalysts with temperatures ranging from 80 to 260 °C and they reported that a combination of high temperatures and pressure with excess alcohol leads to an increase in the lactate production and yield.

Previously, we reported metal NP based catalysts and through that study we were surprised to find SiO_2 functionalised with simple amine ligands displayed relatively good PET conversion (~70%). Building on this, we aimed to develop more powerful organo heterogeneous catalysts. In this work, we prepare guanidine based heterogeneous catalysts by surface functionalised of SiO_2 support. The catalyst were characterised by XPS, FTIR, TGA and BET and evaluated for conventional thermal and microwave assisted glycolysis of PET and methanolysis of PLA. The catalyst showed excellent activity for PET glycolysis with full PET conversion under both conventional thermal and microwave assisted heating. The catalysts were used in the methanolysis of PLA to MeLa under thermal and microwave heating with full conversions of PLA. Microwave assisted degradation of PLA was superior over thermal heating. DFT calculations was used to model the geometries of each of the ligands on the SiO_2 surface and the reactivity of both the PET and PLA degradation reactions.

6.2 Experimental

Chemicals

Mesoporous cellular foam (MCF) SiO_2 was obtained from Glantreo. (APTES), N,N dicyclohexylcarbodimine (DCC), 1-ethyl-3-(3-dimethylaminopropyl) carbodiimide (EDC), dicyandiamide (DCD) , methanol, ethanol, toluene, tetrahydrofuran and ethylene glycol were all purchased from Sigma Aldrich. Commercial PET bottles were obtained from waste water bottles. Commercial PLA was obtain from Vegware lids. The plastics were cut into 1 mm x 1 mm pieces for glycolysis and methanolysis experiments. Repeating unit of 192.68 g/mol was used as the molecular weight of PET.

Synthesis of SiO_2-DCG

In a 100 ml round bottom flask, 2.1 g (10 mmol) N,N dicylcohexylcarbodimine (DCC) was dissolved in 20 ml of dry toluene under argon. 2.1 ml of 3-aminopropyltriethoxylsilane (APTES) was added, and the reaction was refluxed at 100 °C for 24 h under Ar. Next 1 g of SiO_2 was added and the reaction was left to reflux for a further 24 h. When the reaction had completed, the resulting mixture was filtered and washed with copious amounts of ethanol and the product, SiO_2-DCG ((1,3-(dicyclohexyl) 2-(3-(triethoxysilyl)propyl) guanidine) was a solid powder dried at 60°C in an oven.

Synthesis of SiO_2-EDG

In a 100 ml round bottom flask, 1.55 g (10 mmol) of 1-ethyl-3-(3-dimethylaminopropyl) carbodiimide (EDC) was dissolved in 20 ml of dry toluene under Ar. 2.1 ml of APTES was added, and the reaction was refluxed at 100 °C for 24 h under argon. Next 1g of SiO_2 was added and the reaction was left to refluxed for a further 24 h. When the reaction had completed, the resulting mixture was filtered and washed with copious amounts of ethanol and the product SiO_2-EDG (1- ethyl, 3 (3-(3-dimethylamino propyl)) 2-(3-(triethoxysilyl)propyl) guanidine) was a solid powder was dried at 60 °C in an oven.

Synthesis of SiO_2-DCD

In a 100 ml round bottom flask, 0.8408 g (10 mmoles) dicyandiamide (DCD) was dissolved in 20 ml of dry toluene under argon. 2.1 ml of APTES was added, and the reaction was refluxed at 100 °C for 24 h under argon. Next, 1 g of SiO_2 was added and the reaction was left to refluxed for a further 24 h. When the reaction had completed, the resulting mixture was filtered and washed with copious amounts of ethanol and the product SiO_2-DCD (imidocarbonimidic diamide- 2-(3-(triethoxysilyl)propyl) guanidine) was a solid powder was dried at 60 °C in an oven.

Thermal glycolysis of PET

In a typical procedure, 1 g of PET, 0.1 g catalyst and 5 ml of ethylene glycol were refluxed at 190 °C for 3 h. Once reaction was complete, 5 ml of ice-cold H_2O was added to the reaction filtered off and dried. The catalyst was separated by filtration. The filtrate was placed in the fridge overnight after which the BHET crystallised out the solution. The BHET crystals were collected be filtration, washed with water and dried overnight before being weighed to calculate the % yield. PET conversion and yield were calculated be the equations below.

Calculations

% Conversion of PET: $\frac{W_0 - W_1}{W_0} \; x \; 100$ **eqn. 1**

Where W_0 is the initial weight of the PET used and W_1 is the weight of the unreacted PET after the reaction.

% Yield of BHET: $\frac{W_{BHET}/M_{BHET}}{W_0/M_{PET}} \; x \; 100$ **eqn. 2**

Where, W_{BHET} is weight of the BHET product after recrystallisation, M_{BHET} is the molecular weight of BHET, W_0 is the initial weight of PET used and M_{PET} is the repeating unit of PET

Repeating unit of 192.68 g/mol was used as the molecular weight of PET.

Methanolysis of PLA

0.5 g PLA, 50 mg catalyst, 5 ml MeOH and 7.5 ml THF was placed in a 23 ml teflon vessel autoclave from Parr instrument Company and sealed tight. Autoclave was placed into oven at 130 °C for 20 h. Once reaction had completed, the resulting mixture was filtered and washed with excess MeOH, and the solvent was removed via rotary evaporation leaving the product MeLa. The unreacted plastic was collected from the filter paper and dried and weighed to calculate the PLA mass loss.

Microwave assisted glycolysis of PET

1 g of PET, 0.1 g catalyst and 10 ml ethylene glycol were added to the Milestone Flexiwave SK-15 high pressure digestion rotors and the reactions were carried out at between 10-60 min ranging from 190-220 °C with a stir speed of 960 rpm, ramp time of 5 min and at 800 W. The recrystallisation step post-reaction was the same as for thermal glycolysis.

Microwave assisted methanolysis of PLA

0.5 g PLA, 50 mg catalyst, and a ratio of 2:3 methanol:THF were added to Teflon tubes and reaction takes place in the flexiwave microwave at 130°C with a ramp time of 5 min for times ranging from 10-60 min and at 800 W.

Optimsation reactions

For the degradation of PET and PLA under both thermal and microwave assisted heating methods, a number of reaction parameters were altered, these include, time, temperature, catalyst loading, ratio of plastic to solvent and stir speed.

Calculations

% Conversion of PLA: $\frac{W_0 - W_1}{W_0} \; x \; 100$ **eqn 3:**

Where W_0 is the initial weight of the PLA used and W_1 is the weight of the unreacted PLA after the reaction.

Materials Characterisation

X-ray Photoelectron Spectroscopy (XPS) was acquired using a KRATOS AXIS 165 monochromatized X-ray photoelectron spectrometer equipped with an Al Kα (hv = 1486.6 eV) X-ray source. Spectra were collected at a take-off angle of 90° and all spectra were referenced to the C 1s peak at 284.8 eV. Transmission electron microscopy (TEM) analysis was performed using a JEOL 2100 electron microscope at an operating voltage of 200 kV and high-resolution TEM and energy-dispersive X-ray (EDX) analysis was carried out on an FEI Titan TEM, at an operating voltage of 300 kV. Fourier transform infrared (FTIR) spectra were recorded on a Perkin Elmer Spectrum Two FT-IR Spectrometer operating in the range of 4000-450 cm^{-1} with a resolution of 4 cm^{-1} and spectra were averaged from 20 scans. Nuclear magnetic resonance (NMR) samples were run in deuterated chloroform ($CDCl_3$). 1H NMR spectra were recorded on Bruker Avance III 300 NMR spectrometers, in proton-coupled mode using tetramethylsilane (TMS) as the internal standard. Microwave reactions were performed in Teflon vessels in a milestone Flexiwave microwave synthesis platform with a SK-15 high pressure rotor equipped with an IR temperature sensor.

6.3 Results and discussion

The use of porous SiO_2 as a support enables surface modification via functionalisation with organic ligands. The aim of this work was to synthesise mesoporous SiO_2 with three different guanidine capping ligands, DCG, EDG and DCD. All catalysts were synthesised in a one pot method which is advantageous. The structure of each catalyst can be seen in figure 1.

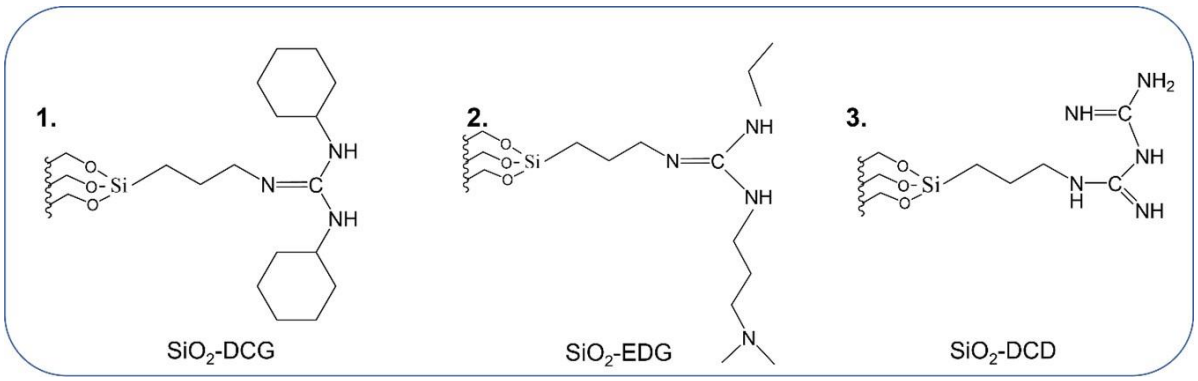

Figure 1: Modified SiO_2 with three different capping ligands 1) SiO_2-DCG, 2) SiO_2-EDG and 3) SiO_2-DCD

XPS was employed to verify successful functionalisation of the guanidine ligands to the SiO_2 support. O 1s core level scans for each functionalised SiO_2 catalyst is shown in Figure 2(a). O 1s core level scans indicate functionalisation with the binding energy (BE) of the bare silica centred at 533.8 eV is downshifted to 532 eV, associated with the loss of Si-OH groups due to covalent modification of the surface.[26] Attachment of the ligands is also indicated by the appearance of a N 1s signal, as shown in Figure 2 (b). No N was detected in the bare SiO_2. The N 1 s of the three catalysts revealed the presence of a dominant peak at 400.2, 400.2 and 399.78 eV, for SiO_2-DCG, EDG and DCD catalysts, respectively, which is characteristic of amine species[27]. A small shoulder peak is observed at a higher BE assigned

to protonated N species. The Si:N ratio for the SiO_2-DCD catalyst was greater than the DCG and EDG catalysts, which was expected as it has the most nitrogen environments.

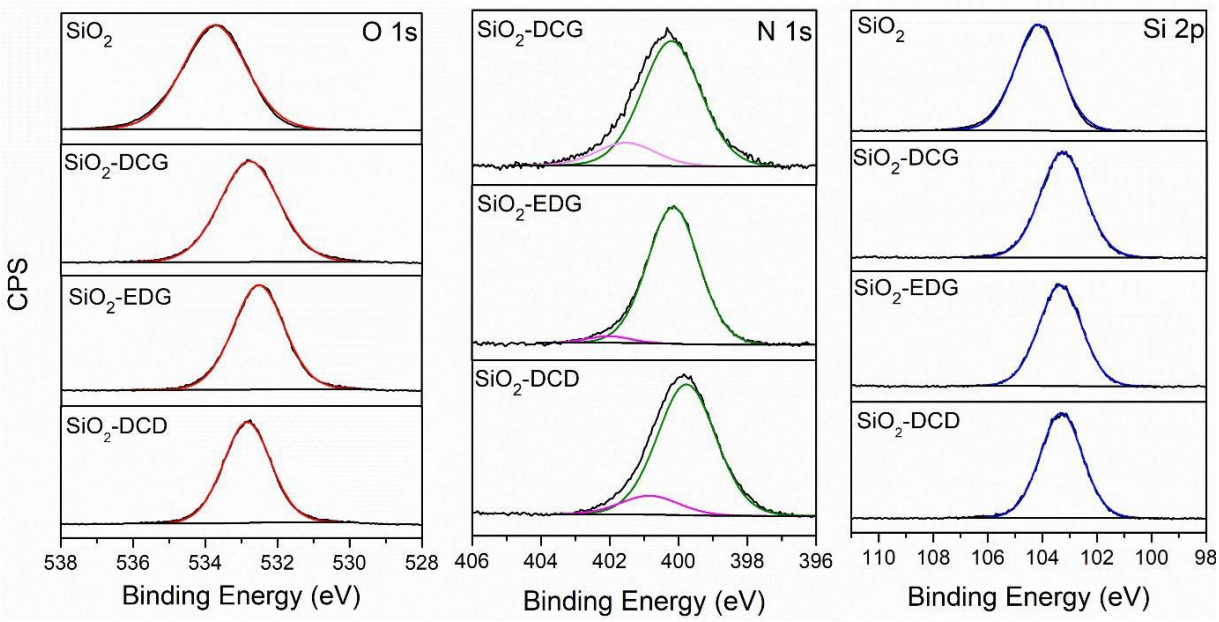

Figure 2: XPS analysis of core level scans (a) O 1s, (b) N1s and (c) Si 2p for SiO_2, SiO_2-DCG, SiO_2-EDG and SiO_2-DCD.

Si 2p core level scans are seen in figure 2(c). Si 2p of bare SiO_2 shows a single peak at 104.2 eV and after functionalisation, the Si 2p peak downshifts to 103.3 eV which is indicative of successful grafting of the guanidine ligands to the SiO_2 support through reaction with the surface Si-OH groups. Survey scans for bare SiO_2, SiO_2-DCG, SiO_2-EDG and SiO_2-DCD are seen in Figure S1.

TEM analysis of the guanidine catalyst, shown in Figure 3(a) confirmed the morphology of the SiO_2 was not affected by the functionalisation procedure. FTIR was employed to investigate the surface of the modified SiO_2, as seen in Figure 3(b). Post functionalisation, there is a decrease in the peak intensity for the Si-OH bond around 955 cm^{-1} for each of the SiO_2 guanidine catalysts, indicative of successful grafting of the guanidine ligands to the SiO_2 support.[28]

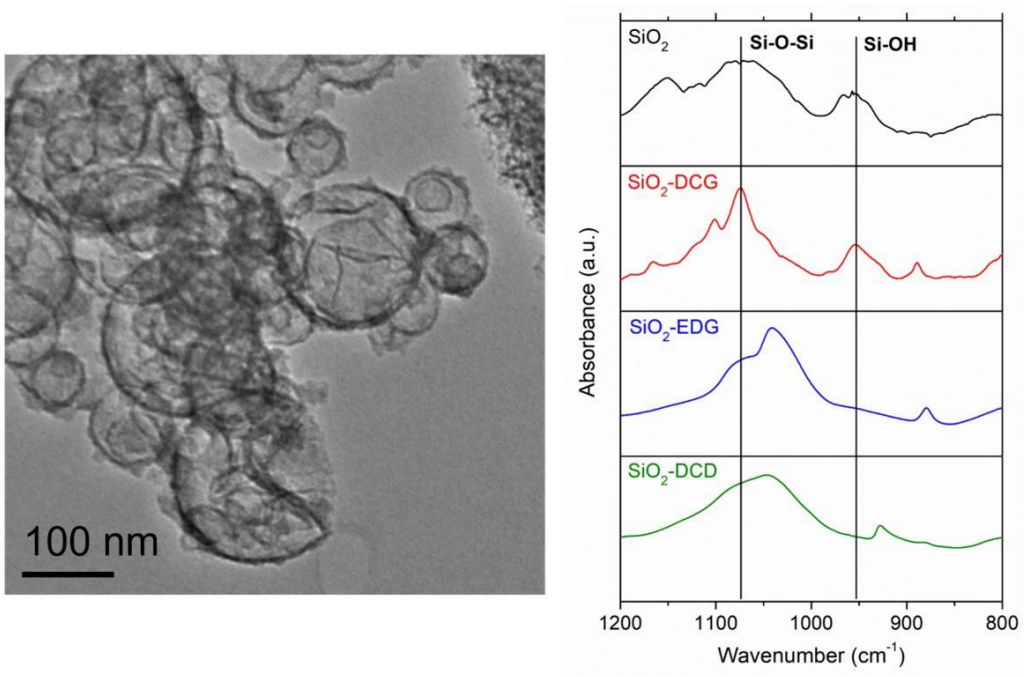

Figure 3: (a) TEM of SiO_2 post functionalisation and (b) FTIR spectra of bare SiO_2 and each SiO_2 functionalised by different guanidine.

TGA analysis was used to assess the thermal stability of each of the SiO_2 guanidine catalysts and to reveal the amount of organics that was present after functionalisation. The profile of the bare SiO_2 is substantially different from the functionalised catalysts. This can be seen in Figure S2, where the initial weight loss observed in all the guanidine grafted SiO_2 is attributed to water and residual solvent molecules on the surface. The second weight-loss step can be assigned to the release of the organosilanes and the guanidine derivatives from the silica surface. The weight loss step for each catalyst begins after 200 °C which suggest the chemical attachment of the organosilanes to the surface of the SiO_2. The EDG and DCD catalysts have a slightly higher thermal stability, with mass loss not occurring until ~250 °C, compared to the DCG ligand where mass loss starts to occur ~220°C. At 300 °C the mass loss for DCG was ~21% while both DCD and EDG catalysts obtained a mass loss of ~13%.

Screening of catalysts-thermal vs microwave irradiation

The catalytic performance of the three SiO_2 supported guanidine catalysts was investigated for the depolymerisation of PET to BHET under conventional thermal and microwave assisted glycolysis. Figure 4(a) compares the PET conversion and isolated BHET yields obtained from each catalyst under thermal conditions at 190°C for 3 h and 100 mg catalyst. It's worth noting that bare SiO_2 did not catalyse the reaction to any extent.

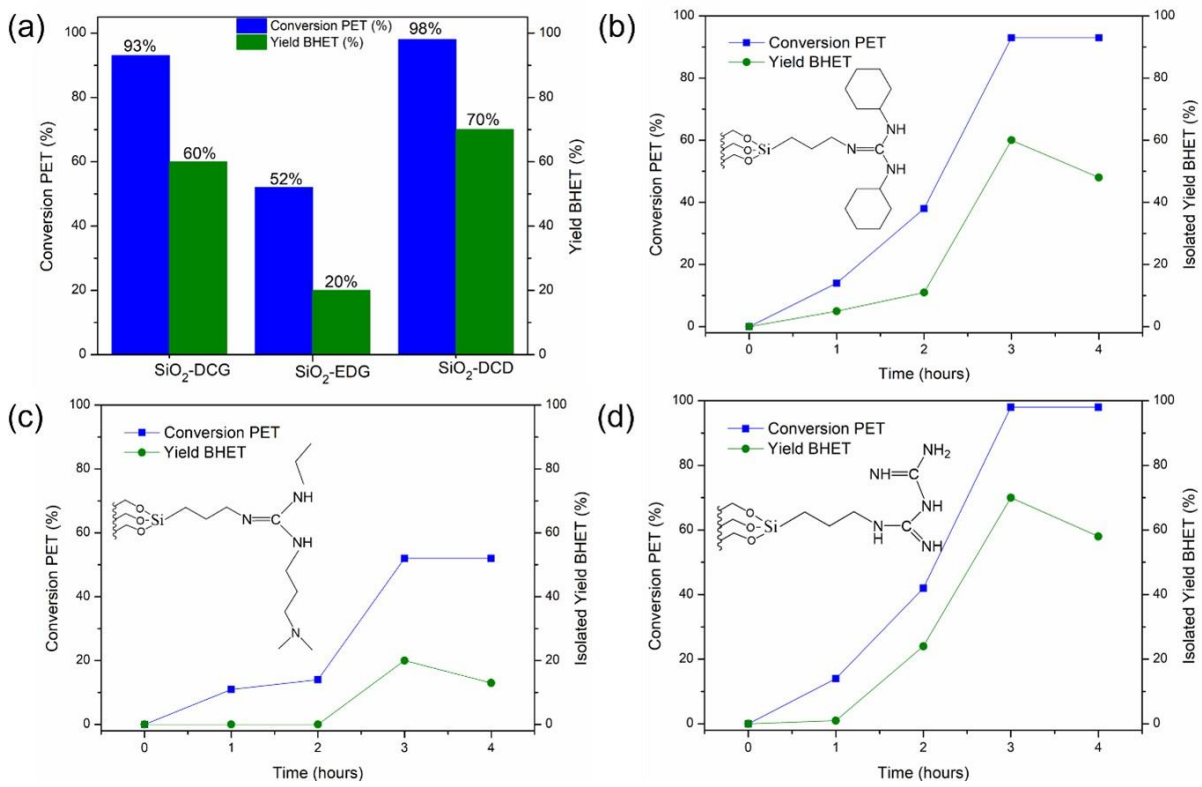

Figure 4: (a) DCG, EDG and DCD modified SiO_2 catalysts for the depolymerisation of PET to BHET under conventional thermal heating reaction, and time series for the thermal reactions using (b) SiO_2-DCG, (c) SiO_2-EDG and (d) SiO_2-DCD catalysts.

The SiO_2-DCD catalyst displayed the best catalytic activity giving full PET conversion and isolated yield of BHET was 70%. ^{1}H NMR of the isolated BHET can be found in Figure S3. Analysis of the filtrate after recrystallisation revealed residual BHET in the solution but no dimers were detected by NMR. The reason for SiO_2-DCD being the best performing catalyst could be due to the structure having more

nitrogen environments as it has been reported in the literature that amine rich ligands are known for increasing the catalytic activity.[29] The SiO_2-DCG catalyst also displayed good performance, giving a 93% conversion of PET. The SiO_2-EDG catalyst displayed the lowest activity with only 52% conversion of PET obtained after 3 h. The low performance of the EDG ligand is likely attributed bulky 3-(3-dimethylaminopropyl) group in the unsymmetrical guanidine, implying that steric effects play an important role in the activity of the heterogeneous catalysts. Figure 4(b-d) shows reaction time series for PET conversion and BHET yield obtained for each catalyst from 0-4 h. The SiO_2-DCG and SiO_2-DCD display similar reaction profiles with as at 3 h both catalysts obtained 100% PET conversions and isolated BHET yield of ~70%. At longer reaction times the BHET yield decreased, which is indicative of dimerization as mechanistically the glycolysis reaction undergoes an equilibrium reaction between the monomer and dimers which in turn lowers the yield of BHET.[30] In contrast, the sluggish behaviour of the EDG ligand is clear from the time series with only 16% conversion at 2 h but this increases to 52% at 3h.

Microwave assisted glycolysis has become popular due to the enhanced reaction rates, higher yields and increased energy efficiency compared to conventional thermal heating .[31] An optimisation study of the reaction parameter for microwave assisted glycolysis was performed, as shown in in Table 1. The optimal conditions under standard thermal depolymerisation were reactions using 0.1 g catalyst and a PET:EG ratio of 1:10, at 190 °C was the optimal reaction temperature of 190 °C. Under microwave irradiation, it was found that increasing the temperature greatly increased PET conversion while lowering reaction times (30 min). Each of the catalysts performed best at 210 °C. Sufficient agitation of the reaction mixture by using a high stirring speed was important to containing high PET conversion using heterogeneous catalyst. Reactions carried out using the SiO_2-DCD catalyst, at a stirring rate of 250 rpm gave 85% PET conversion, while 100% conversion was achieved using a stir speed of 960 rpm. It was found that the optimum reaction conditions were 210°C, 30 min, 960 rpm, 100 mg catalyst and 1:10 PET:EG ratio.

Figure 5 (a) compares the catalytic performance of the three catalysts in microwave assisted glycolysis of PET performed at 30 min. The catalyst reactivity trend observed under microwave assisted glycolysis was different to conventional thermal glycolysis. Similar to conventional thermal glycolysis, the SiO_2-DCD was the best performing catalyst and the time to achieve full PET conversion was significantly reduced from 3 h to 30 min, attributed to the microwave heating effect. The SiO_2-EDG catalyst also performed well, with 85 % PET conversion and lastly SiO_2-DCG had the lowest catalytic activity under microwave conditions converting only 50% PET. TGA analysis showed that the SiO_2-DCG ligand had the lowest thermal stability, and this may contribution to the poor performance of this ligand under microwave conditions.

Catalyst	Loading	Time	PET:EG	Stir Speed	Temperature	Conversion PET	Isolated Yield BHET
Si-DCG	0.1g	30 min	1:10	960rpm	190°C	6%	1%
Si-DCG	0.1g	30 min	1:10	960rpm	200°C	20%	11%
Si-DCG	0.1g	30 min	1:10	960rpm	210°C	50%	27%
Si-DCG	0.1g	40 min	1:10	960rpm	210°C	81%	48%
Si-DCD	0.1g	30 min	1:10	960rpm	190°C	23%	7%
Si-DCD	0.1g	30 min	1:10	960rpm	200°C	39%	16%
Si-DCD	0.1g	30 min	1:10	960rpm	210°C	93%	67%
Si-DCD	0.1g	40 min	1:10	960rpm	210°C	100%	56%
Si-DCD	0.1g	40 min	1:10	256rpm	210°C	85%	68%
Si-EDG	0.1g	30 min	1:10	960rpm	190°C	4%	0%
Si-EDG	0.1g	30 min	1:10	960rpm	200°C	16%	3%
Si-EDG	0.1g	30 min	1:10	960rpm	210°C	85%	58%
Si-EDG	0.1g	40 min	1:10	960rpm	210°C	100%	61%

Table 1: Optimisation of reaction parameters for microwave assisted glycolysis using SiO_2-DCG, SiO_2-EDG and SiO_2-DCD catalysts.

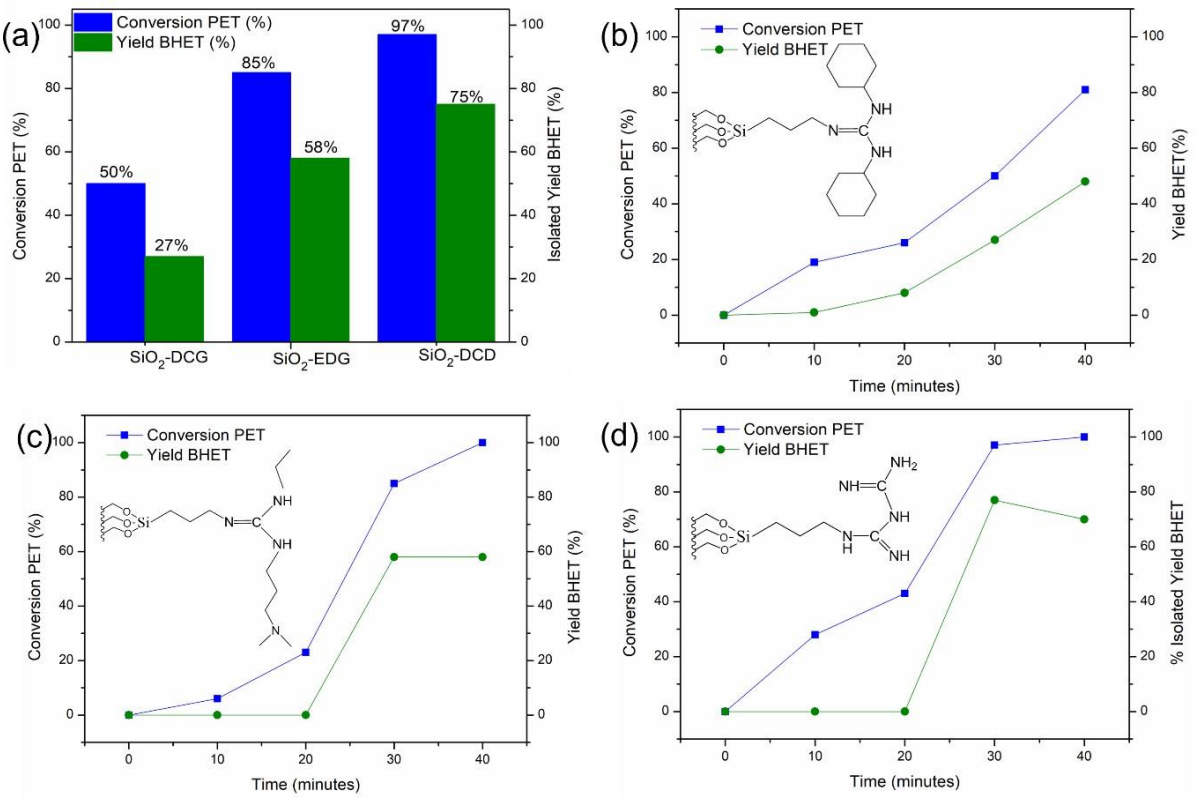

Figure 5: (a) DCG, EDG and DCD modified SiO_2 catalysts for the depolymerisation of PET to BHET 30 min microwave reaction, and time series for the microwave reactions using (b) SiO_2-DCG, (c) SiO_2-EDG and (d) SiO_2-DCD catalysts.

Figure 5 (b-d) shows the reaction time of the catalysts from 0-40 min for the SiO_2-DCG, SiO_2-EDG and SiO_2-DCD catalysts, respectively. Reaction conversions for each catalyst sharply increased between 20 and 30 min. The SiO_2-DCD and SiO_2-EDG catalysts had similar reaction profiles under microwave conditions and the SiO_2-DCG catalyst showed slower PET conversion. As it was observed, there seemed to be an induction period for the SiO_2-EDG, and this is similar to how the catalyst performed thermally and it was suggested that it was due to the thermal stability that was seen in the TGA analysis. Overall, it is interesting that the catalysts perform differently depending on the method used for the glycolysis reaction and that these metal free catalysts are effective in both thermal and microwave assisted methods.

The need for a higher temperature under microwave assisted heating may be attributed to support material. The best microwave-responsive catalysts are ideally those that can absorbed microwave

irradiation. While SiO_2 is a microwave absorber, carbon-based catalysts have been widely used in microwave assisted reaction such as biomass conversion, phenol oxidation NO_x reduction.[32] We grafted the poorest performing guanidine ligand, DCG on acid-treated activated carbon and evaluated the performance under the same reaction conditions. The performance of the DCG ligand increased the conversions from (50 %) on SiO_2 support to 100% PET conversion on activated carbon. This result demonstrates the important role of the support material on the catalytic behaviour of heterogeneous catalysts for microwave assisted glycolysis.

We next explored the application of the heterogeneous guanidine catalysts for methanolysis of PLA. Typical catalysts for this reaction are homogeneous metal complexes and as our metal free SiO_2-guanidine catalysts demonstrated good catalytic behaviour for PET glycolysis, we were interested in a proof of concept for the versatility of the catalysts in this reaction. The transesterification of commercial grade PLA from waste coffee lids to MeLa was assessed under both thermal and microwave assisted heating. The reaction scheme for depolymerisation of PLA to MeLa can be seen in figure 6, where methanol and tetrahydrofuran are used as the protic source and solvent respectively. Mechanistically, there is an equilibrium between the formation of the MeLa product and the oligomers. There have been a number of reports in literature, where they obtain full conversion of PLA and their product is a mix of the internal PLA methine, chain end methine oligomers and MeLa, which can be monitored by NMR. Typically, the methanolysis of PLA to MeLa is carried out in a pressurised vessel at 120°C with reaction times reported up to 3 days.[24, 33-34] As far we are aware, there are no reports for metal-free heterogeneous catalyst for PLA methanolysis.

Initially, an optimisation study was performed thermally to find the best reaction conditions. This included altering the solvent ratios of MeOH:THF, catalyst loading, time, temperature, stir speed and heating methods (including refluxing, sealed vessels in sand bath/oil bath and autoclave). These can be seen in the table S1. The role of the THF is to increase the solubility of the PLA and reaction did not

proceed in the absence of THF. The depolymerisation was carried out under standard reflux conditions but resulted in low PLA conversions which was attributed to the low boiling points of MeOH and THF. Therefore, sealed glass vessels were used to achieve higher temperatures for the reaction. Lamberti et al.[35] reported the mechanism is a two-step reversible reaction that the PLA chains quickly converted to chain end oligomers which then slowly forms the product MeLa. During the optimisation process, it was observed that as the reaction proceeded, the % of internal oligomers decreased as the polymer chains were broken up, producing more chain end oligomers and subsequently the MeLa monomer. Reactions with a higher yield of MeLa had a much lower % of internal oligomers and a higher % of chain end as the depolymerisation process had proceeded further. This can be observed with the NMR analysis used the evaluate the product distribution as shown in Figure 6. The ^{1}H NMR of the products matched previously reported values well. These are Internal (Int) methine (5.09–5.21 ppm), chain end methine (CE) (4.30–4.39 ppm/5.09–5.21 ppm), and MeLa (4.23–4.29 ppm).[24] This shows the equilibrium of the MeLa product and the intermediate oligomers. Using the sealed gas vessels, with reaction conditions of 130 °C, 3 h, 250 rpm and 2:3 ratio of MeOH:THF, full conversion of PLA was achieved with yield of MeLa and both chain end and internal methine oligomers being 17, 54, 29%, respectively. Román-Ramírez and co-workers,[24] achieved similar MeLa yield using a Zn catalyst under thermal conditions. The presence of the equilibrium reaction between the oligomers and MeLa, limits the yield of MeLa is to ~30 %. Removing the MeLa as it is formed can shift the reaction equilibrium and increase the yield. There have also been reports of using an autoclave to perform the degradation of PLA to MeLa, where the higher pressure can also increase MeLa yield.[24, 35]. Carrying out the reaction in an autoclave it was possible to get full conversion of PLA and a 42% yield of MeLa. The product distribution of MeLa, chain end oligomers and internal methine oligomers was 42, 54, and 4%, respectively with reaction conditions of 130°C, 0.05 g SiO_2-DCD, 2:3 MeOH:THF and 72 h. The higher MeLa yields and minimal internal methine oligomers demonstrate the beneficial impact of the high pressure in the autoclave reactor. Figure 6 shows stacked ^{1}H NMR spectra for the products

formed under the reactions conditions of (a) 4 h reaction using a sealed vessel, (b) 20 h using an autoclave and (c) 72 h reaction using an autoclave.

The reaction was also evaluated under microwave irradiation conditions and similar to the thermal reactions, the equilibrium between the intermediate oligomers and MeLa observed. Polylatic acid (PLA) was fully converted yielding 30, 62, 8%, MeLa, chain end and, respectively. The significant advantage of the microwave was the shorter reaction time as similar PLA mass loss and yields of MeLa were observed in 30 min. In contrast, the autoclave reaction required 20-72 h for comparable yields which makes microwave assisted methods more attractive.

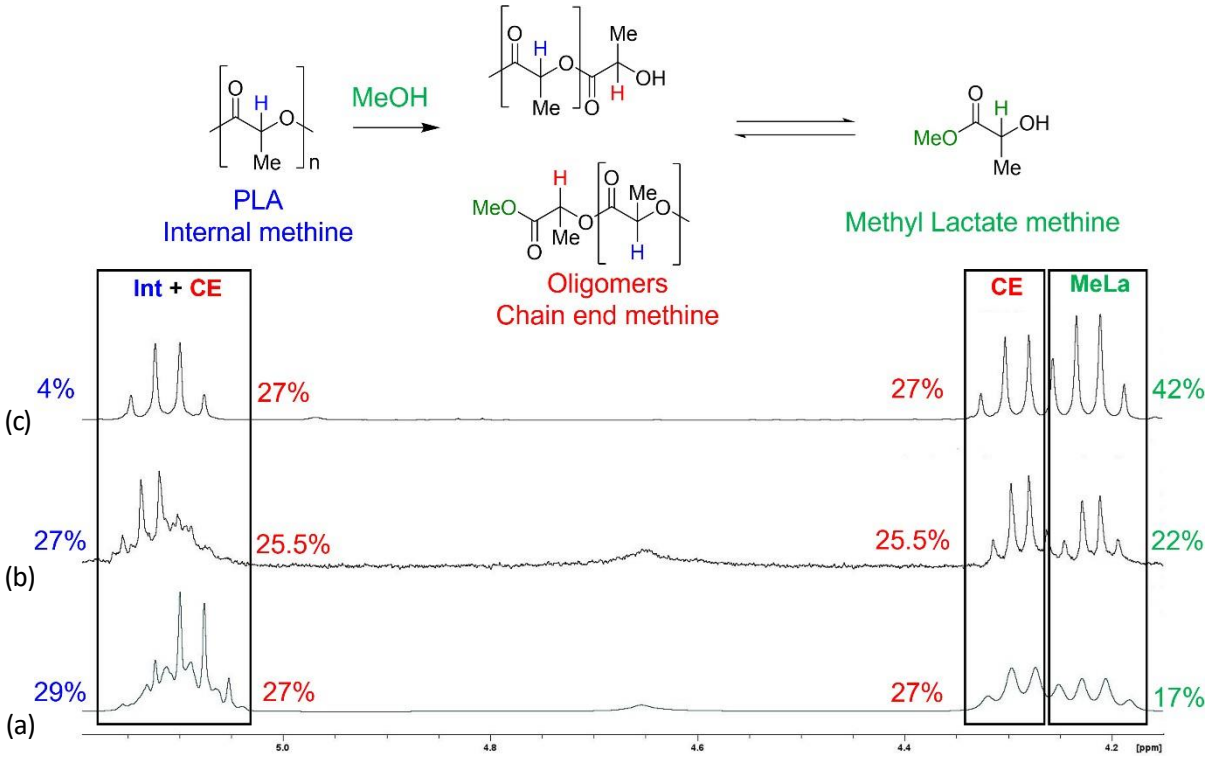

Figure 6: ^{1}H NMR stacked spectra of the products obtained from the methanolysis of PLA to MeLa for (a) sealed vessel reaction at 4 h, (b) 20 h reaction in an autoclave and (c) 72 h autoclave reaction. Each reaction was performed at 130°C with 0.05g catalyst loading.

The ^{1}H NMR of commercial MeLa the product formed from microwave reactions can be found in Figure S4 along with the optimisation results in table S2. PLA has been fully converted in both thermal and microwave assisted methods, but the microwave assisted method is more favourable. It has been reported in literature for increased yields of MeLa to be achieved the reaction must take place at higher temperatures/pressures, but our results are comparable to the yields reported using metal-based catalysts and this proves that these metal free guanidine catalysts have versatility as efficient catalysts for both the depolymerisation of PET and PLA.

6.4 Conclusions

SiO_2 was functionalised with different guanidine ligands for the study of heterogeneous metal free catalysts for the depolymerisation of PET to BHET monomer. The three catalysts displayed good catalytic activity with high PET conversions under both thermal and microwave assisted methods. The SiO_2-DCD catalyst performed best, and this is likely due to its nitrogen rich environment. To assess the versatility of our guanidine catalysts, we trialled them in a methanolysis of PLA to MeLa. 100 % conversion of PLA was achieved under both thermal and with microwave irradiation. The equilibrium between the internal and chain end oligomers was found to be challenging without the use of higher-pressure systems but overall it was possible to convert 100% PLA under both thermal and with microwave irradiation which proves that these guanidine based heterogeneous catalysts are effective for both recyclability of PET and PLA to high quality monomers.

6.6 References

1. Zhou, X., Research on Conversion of Waste Polyethylene Terephthalate into Value-Added Monomer replacing Landfill and Incineration for Environmental Pollution Control. *IOP Conference Series: Earth and Environmental Science* **2021,** *859* (1), 012097.
2. Soong, Y. V.; Sobkowicz, M. J.; Xie, D., Recent Advances in Biological Recycling of Polyethylene Terephthalate (PET) Plastic Wastes. *Bioengineering (Basel, Switzerland)* **2022,** *9* (3).
3. Jehanno, C.; Flores, I.; Dove, A. P.; Müller, A. J.; Ruipérez, F.; Sardon, H., Organocatalysed depolymerisation of PET in a fully sustainable cycle using thermally stable protic ionic salt. *Green Chemistry* **2018,** *20* (6), 1205-1212.
4. European Union (Single Use Plastics) Regulations 2021. http://vlex.com/vid/european-union-single-use-870566418 ed.
5. Liu, Y.; Yao, X.; Yao, H.; Zhou, Q.; Xin, J.; Lu, X.; Zhang, S., Degradation of poly(ethylene terephthalate) catalyzed by metal-free choline-based ionic liquids. *Green Chemistry* **2020,** *22* (10), 3122-3131.
6. Chen, F.; Wang, G.; Li, W.; Yang, F., Glycolysis of Poly(ethylene terephthalate) over Mg–Al Mixed Oxides Catalysts Derived from Hydrotalcites. *Industrial & Engineering Chemistry Research* **2013,** *52* (2), 565-571.
7. Hou, Q.; Zhen, M.; Qian, H.; Nie, Y.; Bai, X.; Xia, T.; Rehman, M. L. U.; Li, Q.; Ju, M., Cell Reports Phys. *Sci* **2021,** *2*, 100514.
8. Chen, F.; Wang, G.; Shi, C.; Zhang, Y.; Zhang, L.; Li, W.; Yang, F., Kinetics of glycolysis of poly(ethylene terephthalate) under microwave irradiation. *Journal of Applied Polymer Science* **2013,** *127* (4), 2809-2815.
9. Wang, L.; Nelson, G. A.; Toland, J.; Holbrey, J. D., Glycolysis of PET Using 1,3-Dimethylimidazolium-2-Carboxylate as an Organocatalyst. *ACS Sustainable Chemistry & Engineering* **2020,** *8* (35), 13362-13368.
10. Yue, Q. F.; Xiao, L. F.; Zhang, M. L.; Bai, X. F., The Glycolysis of Poly(ethylene terephthalate) Waste: Lewis Acidic Ionic Liquids as High Efficient Catalysts. *Polymers* **2013,** *5* (4), 1258-1271.
11. Khoonkari, M.; Haghighi, A. H.; Sefidbakht, Y.; Shekoohi, K.; Ghaderian, A., Chemical Recycling of PET Wastes with Different Catalysts. *International Journal of Polymer Science* **2015,** *2015*, 124524.
12. Viana, M. E.; Riul, A.; Carvalho, G. M.; Rubira, A. F.; Muniz, E. C., Chemical recycling of PET by catalyzed glycolysis: Kinetics of the heterogeneous reaction. *Chemical Engineering Journal* **2011,** *173* (1), 210-219.
13. Fuentes, C. A.; Gallegos, M. V.; García, J. R.; Sambeth, J.; Peluso, M. A., Catalytic Glycolysis of Poly(ethylene terephthalate) Using Zinc and Cobalt Oxides Recycled from Spent Batteries. *Waste and Biomass Valorization* **2020,** *11* (9), 4991-5001.
14. Yunita, I.; Putisompon, S.; Chumkaeo, P.; Poonsawat, T.; Somsook, E., Effective catalysts derived from waste ostrich eggshells for glycolysis of post-consumer PET bottles. *Chemical Papers* **2019,** *73* (6), 1547-1560.
15. López-Fonseca, R.; Duque-Ingunza, I.; de Rivas, B.; Arnaiz, S.; Gutiérrez-Ortiz, J. I., Chemical recycling of post-consumer PET wastes by glycolysis in the presence of metal salts. *Polymer Degradation and Stability* **2010,** *95* (6), 1022-1028.
16. Fehér, Z.; Kiss, J.; Kisszékelyi, P.; Molnár, J.; Huszthy, P.; Kárpáti, L.; Kupai, J., Optimisation of PET glycolysis by applying recyclable heterogeneous organocatalysts. *Green Chemistry* **2022,** *24* (21), 8447-8459.
17. Kamber, N. E.; Tsujii, Y.; Keets, K.; Waymouth, R. M.; Pratt, R. C.; Nyce, G. W.; Hedrick, J. L., The Depolymerization of Poly(ethylene terephthalate) (PET) Using N-Heterocyclic Carbenes from Ionic Liquids. *Journal of Chemical Education* **2010,** *87* (5), 519-521.
18. Fukushima, K.; Coulembier, O.; Lecuyer, J. M.; Almegren, H. A.; Alabdulrahman, A. M.; Alsewailem, F. D.; McNeil, M. A.; Dubois, P.; Waymouth, R. M.; Horn, H. W.; Rice, J. E.; Hedrick, J. L.,

Organocatalytic depolymerization of poly(ethylene terephthalate). *Journal of Polymer Science Part A: Polymer Chemistry* **2011,** *49* (5), 1273-1281.
19. Le, N. H.; Ngoc Van, T. T.; Shong, B.; Cho, J., Low-Temperature Glycolysis of Polyethylene Terephthalate. *ACS Sustainable Chemistry & Engineering* **2022**.
20. Chipurici, P.; Vlaicu, A.; Călinescu, I.; Vînătoru, M.; Busuioc, C.; Dinescu, A.; Ghebaur, A.; Rusen, E.; Voicu, G.; Ignat, M.; Diacon, A., Magnetic silica particles functionalized with guanidine derivatives for microwave-assisted transesterification of waste oil. *Scientific Reports* **2021,** *11* (1), 17518.
21. Gawande, M. B.; Shelke, S. N.; Zboril, R.; Varma, R. S., Microwave-Assisted Chemistry: Synthetic Applications for Rapid Assembly of Nanomaterials and Organics. *Accounts of Chemical Research* **2014,** *47* (4), 1338-1348.
22. Muley, P. D.; Wang, Y.; Hu, J.; Shekhawat, D., Microwave-assisted heterogeneous catalysis. In *Catalysis: Volume 33*, The Royal Society of Chemistry: 2021; Vol. 33, pp 1-37.
23. Scé, F.; Cano, I.; Martin, C.; Beobide, G.; Castillo, Ó.; de Pedro, I., Comparing conventional and microwave-assisted heating in PET degradation mediated by imidazolium-based halometallate complexes. *New Journal of Chemistry* **2019,** *43* (8), 3476-3485.
24. Román-Ramírez, L. A.; McKeown, P.; Jones, M. D.; Wood, J., Poly(lactic acid) Degradation into Methyl Lactate Catalyzed by a Well-Defined Zn(II) Complex. *ACS Catalysis* **2019,** *9* (1), 409-416.
25. Petrus, R.; Bykowski, D.; Sobota, P., Solvothermal Alcoholysis Routes for Recycling Polylactide Waste as Lactic Acid Esters. *ACS Catalysis* **2016,** *6* (8), 5222-5235.
26. Paengjun, N.; Vibulyaseak, K.; Ogawa, M., Heterostructural transformation of mesoporous silica–titania hybrids. *Scientific Reports* **2021,** *11* (1), 3210.
27. Truica-Marasescu, F.; Wertheimer, M. R., Nitrogen-Rich Plasma-Polymer Films for Biomedical Applications. *Plasma Processes and Polymers* **2008,** *5* (1), 44-57.
28. Otoufi, M. K.; Shahtahmasebi, N.; Kompany, A.; Goharshadi, E. K.; Roghani, A., Gradual Growth of Gold Nanoseeds on Silica for Silica@Gold Core–Shell Nano Applications by Two Different Methods: A Comparison on Structural Properties. *Journal of Cluster Science* **2014,** *25* (5), 1307-1317.
29. Zhang, J.; Huang, Z.; Xie, Y.; Jiang, X., Modulating the catalytic activity of gold nanoparticles using amine-terminated ligands. *Chemical science* **2022,** *13* (4), 1080-1087.
30. Lalhmangaihzuala, S.; Laldinpuii, Z.; Lalmuanpuia, C.; Vanlaldinpuia, K., Glycolysis of Poly(Ethylene Terephthalate) Using Biomass-Waste Derived Recyclable Heterogeneous Catalyst. *Polymers* **2021,** *13* (1).
31. de la Hoz, A.; Díaz-Ortiz, Á.; Moreno, A., Microwaves in organic synthesis. Thermal and non-thermal microwave effects. *Chemical Society Reviews* **2005,** *34* (2), 164-178.
32. Ji, T.; Zhu, J., Microwave-Responsive Nanomaterials for Catalysis. In *Responsive Nanomaterials for Sustainable Applications*, Sun, Z.; Liao, T., Eds. Springer International Publishing: Cham, 2020; pp 65-91.
33. Chen, J.-W.; Chen, L.-W.; Cheng, W.-H., Kinetics of glycolysis of polyethylene terephthalate with zinc catalyst. *Polymer International* **1999,** *48* (9), 885-888.
34. Song, X.; Zhang, X.; Wang, H.; Liu, F.; Yu, S.; Liu, S., Methanolysis of poly(lactic acid) (PLA) catalyzed by ionic liquids. *Polymer Degradation and Stability* **2013,** *98* (12), 2760-2764.
35. Lamberti, F. M.; Ingram, A.; Wood, J. Synergistic Dual Catalytic System and Kinetics for the Alcoholysis of Poly(Lactic Acid) *Processes* [Online], 2021.

6.6 Supporting Information

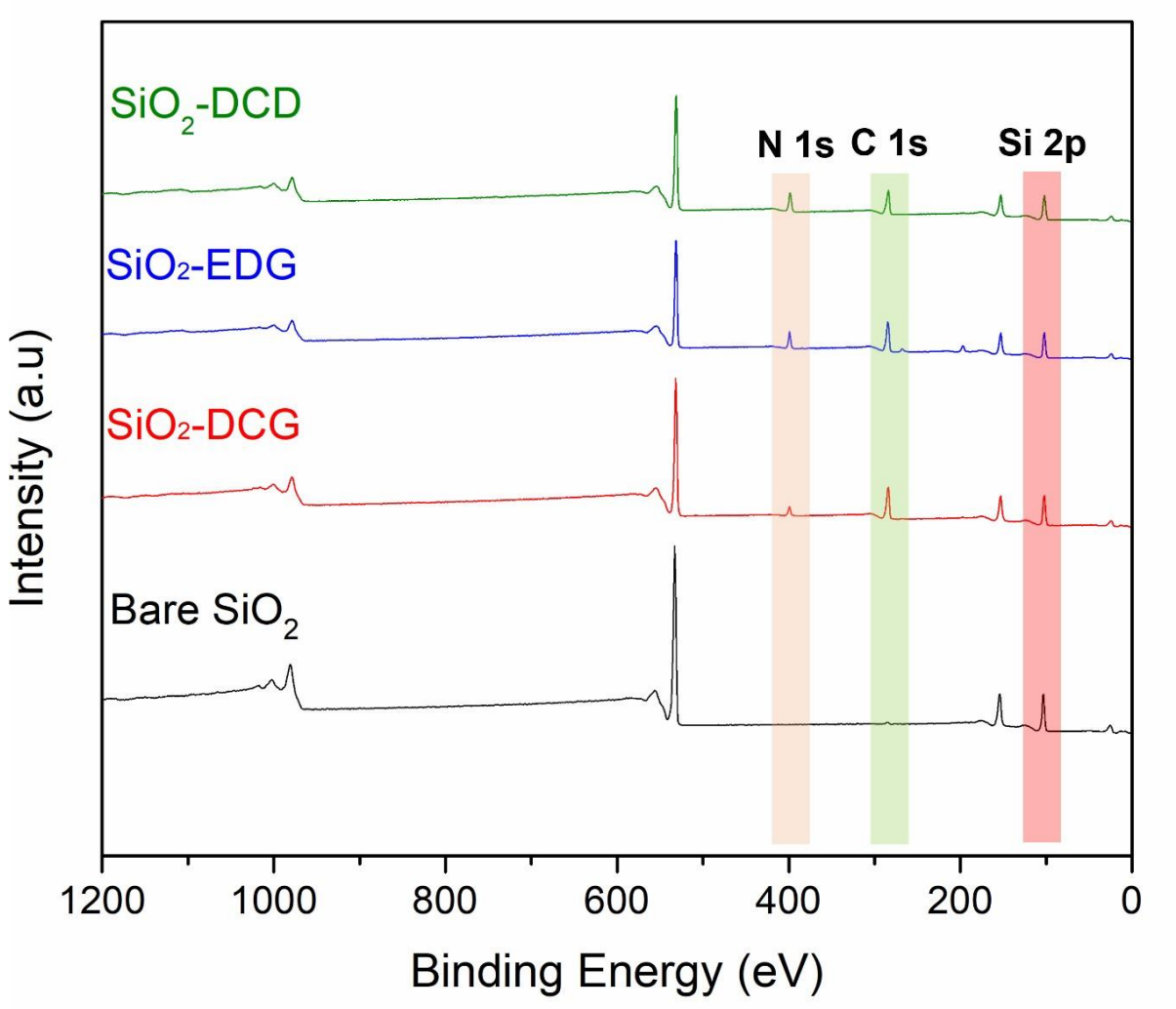

Figure S1: XPS Survey scan for bare SiO_2, SiO_2-DCG, SiO_2-EDG and SiO_2-DCD.

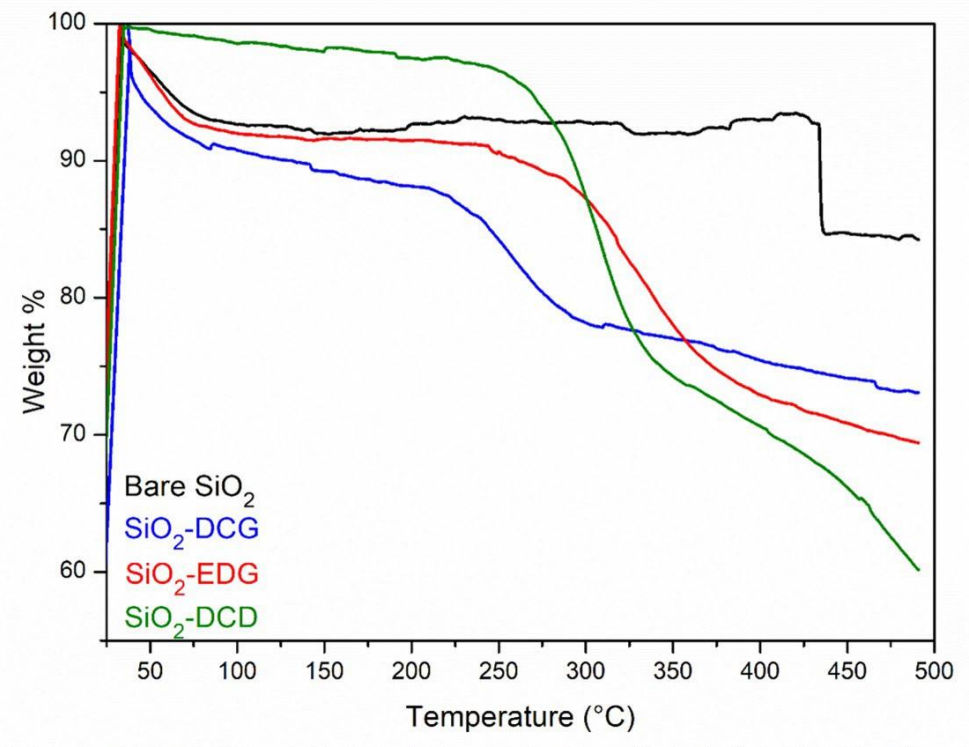

Figure S2: Thermogravimetric analysis of bare SiO_2, SiO_2-DCG, SiO_2-EDG and SiO_2-DCD.

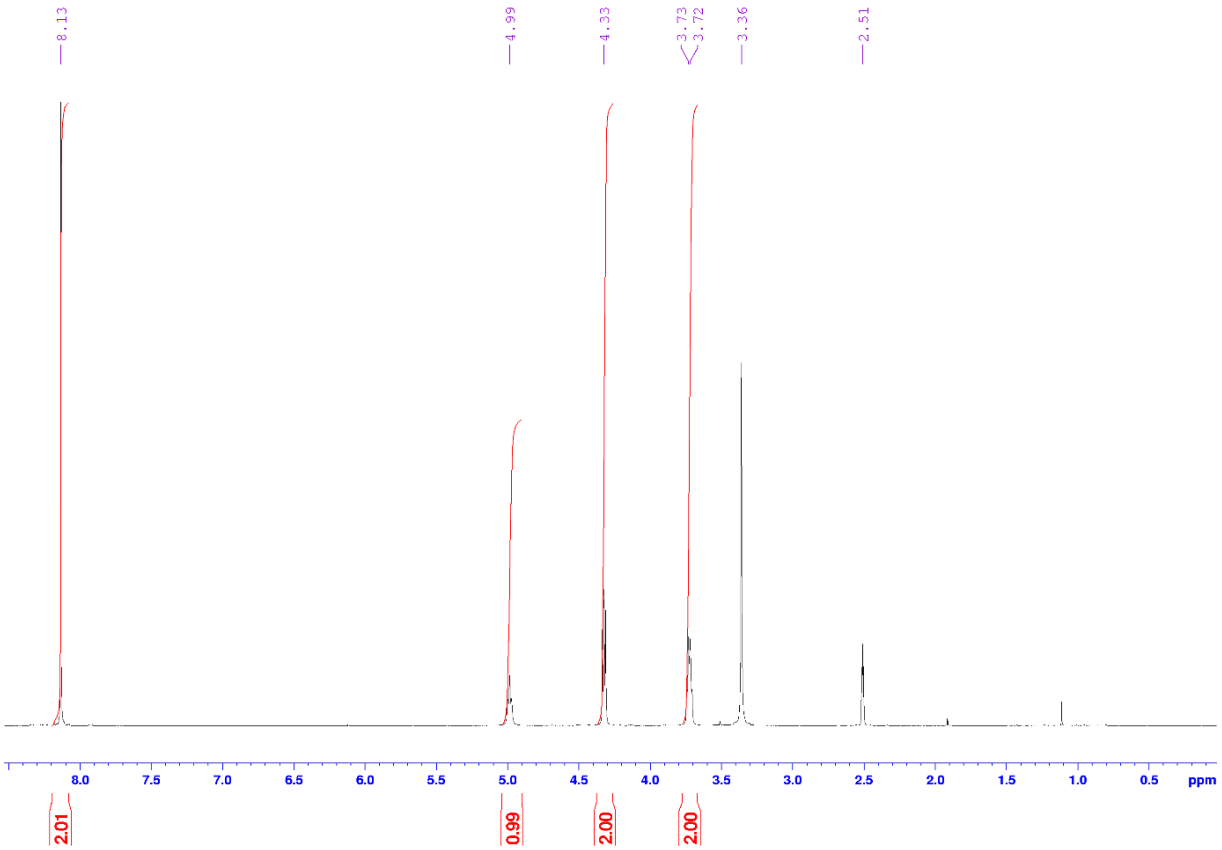

Figure S3: ^{1}H NMR of the product BHET

NMR analysis confirmed that no formation of dimers or oligomers occurred and that BHET was the only product formed in the reaction. The 1H NMR spectrum of BHET can be seen in figure 11, where the four main peaks were a singlet at 8.12 ppm corresponding to an aromatic ring, an OH triplet at 5.01 ppm, CH_2 triplet at 4.32 ppm and CH_2 quartet at 3.77 ppm. Residual solvent d_6-DMSO was located at 2.51 ppm. The results are in good agreement with literature values of BHET.

Table S1: Reaction optimisation of methanolysis of PLA under thermal conditions

Catalyst	Loading	PLA	MeOH	THF	Temperature	Thermal set up	Time	Mass loss PLA	Oligomers	MeLa
DCD	0.1 g	0.1g	5 ml	5 ml	70 °C	Reflux	3 h	43 %	100 %	-
DCD	0.1 g	0.1g	5 ml	5 ml	90 °C	Reflux	3 h	52 %	100 %	-
DCD	0.02 g	0.5 g	8 ml	-	130 °C	Sealed Vessel	4 h	71 %	100 %	-
DCD	0.04 g	0.5 g	8 ml	-	130 °C	Sealed Vessel	4 h	78 %	100 %	-
DCD	0.05 g	0.5 g	8 ml	-	130 °C	Sealed Vessel	4 h	82 %	100 %	-
DCD	0.08 g	0.5 g	8 ml	-	130 °C	Sealed Vessel	4 h	80 %	100 %	-
DCD	0.05 g	0.5 g	1 ml	7 ml	130 °C	Sealed Vessel	4 h	82 %	100 %	-
DCD	0.05 g	0.5 g	3 ml	5 ml	130 °C	Sealed Vessel	4 h	82 %	95 %	5 %
DCD	0.05 g	0.5 g	2 ml	6 ml	130 °C	Sealed Vessel	4 h	100 %	83 %	17 %
DCD	0.05 g	0.5 g	2 ml	6 ml	60 °C	Sealed Vessel	4 h	61 %	100 %	-
DCD	0.05 g	0.5 g	2 ml	6 ml	100 °C	Sealed Vessel	4h	50 %	100 %	-
DCD	0.05 g	0.5 g	12.5 ml	-	130 °C	Autoclave	4 h	79 %	100 %	-
DCD	0.05 g	0.5 g	12.5 ml	-	130 °C	Autoclave	5 h	73 %	100 %	-
DCD	0.05 g	0.5g	12.5 ml	-	130 °C	Autoclave	8 h	87%	100 %	-
DCD	0.05 g	0.5g	2.5 ml	10 ml	130 °C	Autoclave	5 h	87%	100 %	-
DCD	0.05 g	0.5g	4.5 ml	8 ml	130 °C	Autoclave	5 h	93%	100 %	-
DCD	0.05 g	0.5g	6.25 ml	6.25 ml	130 °C	Autoclave	4 h	91 %	100 %	-
DCD	0.05 g	0.5g	6.25 ml	6.25 ml	130 °C	Autoclave	5 h	93 %	100 %	-
DCD	0.05 g	0.5g	6.25 ml	6.25 ml	130 °C	Autoclave	8 h	99 %	96 %	4 %
DCD	0.05 g	0.5 g	5 ml	7.5 ml	130 °C	Autoclave	4 h	99 %	100 %	-
DCD	0.05 g	0.5g	5 ml	7.5 ml	130 °C	Autoclave	5 h	98 %	100 %	
DCD	0.05 g	0.5g	5 ml	7.5 ml	130 °C	Autoclave	8 h	100 %	97 %	3 %
DCD	0.05 g	0.5g	5 ml	7.5 ml	130 °C	Autoclave	12 h	100 %	94 %	6 %
DCD	0.05 g	0.5g	5 ml	7.5 ml	130 °C	Autoclave	20 h	100 %	78 %	22 %
DCD	0.05 g	0.5g	5 ml	7.5 ml	130 °C	Autoclave	72 h	100 %	58 %	42 %

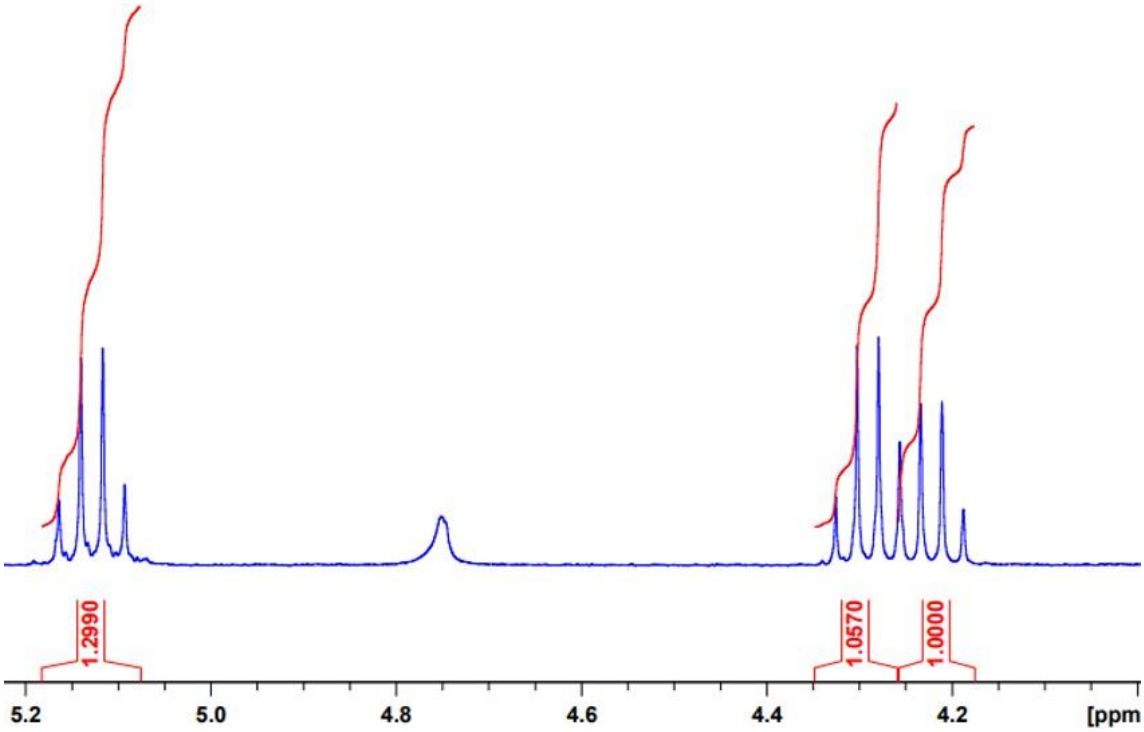

Figure S4: ^{1}H NMR of the product from the PLA degradation microwave reaction

Table S2: Reaction optimisation of methanolysis of PLA under microwave irradiation.

Catalyst	Loading	PLA	MeOH	THF	Ramp	Hold	Temp	Stirring	MW	Mass loss PLA	Oligomers	MeLa
DCG	0.05 g	0.5 g	5 ml	-	5 min	30 min	130°C	960 rpm	800 W	96 %	100 %	-
DCG	0.05 g	0.5 g	2 ml	3 ml	5 min	30 min	130°C	960 rpm	800 W	96 %	100 %	-
DCG	0.05 g	0.5 g	1 ml	4 ml	5 min	30 min	130°C	960 rpm	800 W	91%	100 %	-
EDG	0.05 g	0.5 g	2 ml	3 ml	5 min	30 min	130°C	960 rpm	800 W	84%	100%	-
DCG	0.05 g	0.5 g	2 ml	3 ml	5 min	30 min	130°C	960 rpm	800 W	100%	70 %	30 %
DCD	0.05 g	0.5 g	2 ml	3 ml	5 min	30 min	130°C	960 rpm	800 W	97%	88 %	12 %
DCD	0.05 g	0.5 g	2ml	3 ml	5 min	30 min	80°C	256 rpm	1000W	35%	100 %	-
DCG	0.05 g	0.5 g	2ml	3 ml	5 min	30 min	80°C	256 rpm	1000W	4%	100 %	-
EDG	0.05 g	0.5 g	2ml	3 ml	5 min	30 min	80°C	256 rpm	1000W	0%	100 %	-
DCD	0.05 g	0.5 g	2 ml	3 ml	5 min	45 min	130°C	256 rpm	1000 W	24%	100 %	-
DCG	0.05 g	0.5 g	2 ml	3 ml	5 min	45 min	130°C	256 rpm	1000 W	0%	100 %	-
EDG	0.05 g	0.5 g	2 ml	3 ml	5 min	45 min	130°C	256 rpm	1000 W	0%	100 %	-

Chapter 7

Conclusions

Conclusions

This thesis work highlights the need for optimal catalyst design for a range of applications in heterogeneous catalysis in terms of size, morphology, surface capping ligands and the role of the support material.

The aim for chapter 3 was to develop support-free polymer stabilised NPs for the application in pharmaceutical synthesis. This work highlighted the importance of choosing the correct capping ligand to stabilise NPs which was proven to be essential for achieving good catalytic activity in an organic transformation. Pd NPs stabilised by different stabilising ligands such as long chain thiols and amines and a variety of polymers were synthesised and evaluated as colloidal support- free heterogeneous catalyst for organic synthesis. The catalytic activity of the Pd NPs were examined for reductive amination a key industrial reaction in pharmaceutical synthesis. After each of the catalysts were screened, it was observed that the best performing stabiliser was PVP, giving a high yield of the desired amine with the least amount of undesired side product formation. The interaction between PVP molecules and the Pd metal surface has been a topic of controversy in the literature as some report that the PVP binds through the carbonyl O while others report that it occurs through the N atom. Materials characterisation methods such as XPS and FTIR were used access this interaction between PVP and the metal surface. It was revealed that the presence of PVP ligands at the NP surface gives rise to combination of steric and electronic effects and it was shown that electron donation from the PVP carbonyl group to the Pd NP occurred. The Pd-PVP NPs showed excellent applicability for reductive amination with varying side groups. It was also found that the Pd NPs were also successfully applied to pharmaceutically relevant compounds, Adaphostin and Laptinib, obtained in excellent yields. This work successfully demonstrated that the use of the polymer stabilised NPs were excellent candidates for hydrogenation catalysis. This work has future potential in flow synthesis.

Chapter 4 reports a new one pot synthesis of alloy PdAu nanosheets using a surfactant assisted soft template. The understanding of the formation mechanism of the nanosheets was an important feature of this work and this was investigated using a combination of characterisation techniques

such as, TEM, EDX and XPS analysis. It was found that the growth mechanism of the nanosheets was initiated from the production of Au NP seeds dispersed within a soft surfactant template. The NP seeds then grew into 2D PdAu nanosheets and because of the fast reduction of the Au precursor the edges of the nanosheets. This mechanism accounts for the observed EDX mapping analysis which showed that there was Pd- rich regions located around the NS edges, and after the Au precursor has been consumed, continued growth of the NS produced Pd-rich domains as identified by EDX. The alloy nanosheets showed enhanced catalyst activity under visible light for Suzuki cross coupling reaction. The bimetallic nanosheets display better activity compared to the monometallic nanosheets both in the dark and under light irradiation which was attributed to synergistic alloy effects of electron donation from Au to Pd as suggested by XPS. The excellent catalytic activity of the nanosheets was associated with the presence of weakly co-ordinating amine ligands from the surfactant at the surface. To gain further insight into the role of ligands in light assisted catalysis, nanosheets with a similar 2D morphology but different surface capping ligands were also synthesised and evaluated in the Suzuki reaction. The CO- assisted NS were found to be heavily passivated displaying poor reactivity. Both the surfactant- assisted and CO-assisted NSs showed the same trend with the bimetallic NSs displaying better lighter enhancement compared to monometallic Pd NS. This work highlights the importance of considering the catalyst surface chemistry in addition to catalyst morphology for light enhanced reactions. It is the first studying combining two-dimensional (2D) metal catalyst and plasmonic photocatalysis. Catalysts using visible light energy to drive chemical reactions have great potential for green synthesis.

Chapter 5 demonstrates the need for the development of efficient catalysts for the chemical recycling of PET to help tackling the global issue of plastic waste. The design the optimum heterogeneous catalyst for the depolymerisation of PET to more value-added monomer, BHET was the motivation for this work. Porous SiO_2 was functionalised by a range of different organic ligands using to immobilise the active Lewis acid catalyst. The ion immobilised catalysts were converted into Fe_2O_3 NP catalysts by calcination or $NaBH_4$-treatment to produced ~1-2 nm size NP embedded into the SiO_2 support. In total 20 catalysts were synthesised and further characterised by TEM, XPS, solid

state NMR along with DFT calculations. The NP catalysts were superior to the ion immobilised catalysts in the glycolysis reaction giving full PET conversion and high BHET yields. This was found to be due to the presence of both the Fe_2O_3 NP and organic ligand, due to the synergistic effects between the ligand and the NP which has been nicely shown through the combination of material chemistry, solid state NMR and DFT calculations.

The good catalytic activity of the organic ligand-based catalysts in Chapter 5 led to the motivation and aim for chapter 6, which was to synthesise metal-free heterogeneous using guanidine ligands which are highly basic organic compounds, anchored to a porous SiO_2 support. Three catalysts were prepared with varying steric and nitrogen environments and were evaluated in the depolymerisation of PET to BHET. They were studied under thermal and microwave conditions to find the most effective method of converting PET to BHET achieving a high yield. It was discovered that the nitrogen environment of the catalyst was key in the performance of the catalysts, as the more nitrogen environments available led to higher performing catalytic activity with the microwave assisted method being the most advantageous. The versatility of the catalysts was assessed in a methanolysis reaction for the conversion of PLA to methyl lactate. The studies conducted and seen in literature reported that presence of the equilibrium reaction between the oligomers and MeLa, limits the yield of MeLa which is a more complication reaction when compared to the depolymerisation of PET. It was observed that when these guanidine based heterogeneous catalysts were evaluated in the methanolysis reaction, PLA was fully converted yielding the predictable mixture of product, which aligns nicely with literature reports. The results are comparable with metal-based catalysts which have been previously reported in literature, which shows the enormous potential for metal free guanidine based catalysts in the future. These guanidine based heterogeneous catalysts are effective for both recyclability of PET and PLA to high quality monomers, with the microwave assisted method being able to achieve excellent conversion of both PET and PLA with less time and energy being required making it the more attractive method from a green chemistry point of view. Chapter 5 and 6 illustrate the huge potential for designing more active catalysts for plastic depolymerisation. Future work would be using these catalysts on other plastics such as polycarbonate and polyethylene.